**Universidade Federal de Santa Catarina**
**Centro Tecnológico**
**Programa de Pós-graduação em Engenharia Mecânica**

FELIPE GESSER BATTISTI

# TECHNICAL AND ECONOMIC ASSESSMENT OF TRANSIENT SUPERCRITICAL CARBON DIOXIDE BRAYTON CYCLES WITH THERMAL ENERGY STORAGE SYSTEMS

Florianópolis/SC – Brasil

2020

FELIPE GESSER BATTISTI

# TECHNICAL AND ECONOMIC ASSESSMENT OF TRANSIENT SUPERCRITICAL CARBON DIOXIDE BRAYTON CYCLES WITH THERMAL ENERGY STORAGE SYSTEMS

Tese submetida ao Programa de Pós-graduação em Engenharia Mecânica da Universidade Federal de Santa Catarina para a obtenção do título de Doutor em Engenharia Mecânica.
Orientador: Prof. Alexandre Kupka da Silva, Ph.D.

Florianópolis/SC – Brasil

2020

Ficha de identificação da obra elaborada pelo autor,
através do Programa de Geração Automática da Biblioteca Universitária da UFSC.

Battisti, Felipe Gesser
Technical and economic assessment of transient supercritical carbon dioxide Brayton cycles with thermal energy storage systems / Felipe Gesser Battisti ; orientador, Alexandre Kupka da Silva, 2020.
195 p.

Tese (doutorado) - Universidade Federal de Santa Catarina, Centro Tecnológico, Programa de Pós-Graduação em Engenharia Mecânica, Florianópolis, 2020.

Inclui referências.

1. Engenharia Mecânica. 2. Supercritical carbon dioxide. 3. Transient simulation. 4. Thermal energy storage. 5. Parametric analysis and optimization. I. da Silva, Alexandre Kupka . II. Universidade Federal de Santa Catarina. Programa de Pós-Graduação em Engenharia Mecânica. III. Título.

FELIPE GESSER BATTISTI

# TECHNICAL AND ECONOMIC ASSESSMENT OF TRANSIENT SUPERCRITICAL CARBON DIOXIDE BRAYTON CYCLES WITH THERMAL ENERGY STORAGE SYSTEMS

O presente trabalho em nível de doutorado foi avaliado e aprovado por banca examinadora composta pelos seguintes membros:

**Prof. Edson Bazzo, Dr.Eng.**
UFSC – Florianópolis/SC – Brasil

**Prof. Jader Riso Barbosa Junior, Ph.D.**
UFSC – Florianópolis/SC – Brasil

**Prof. Jose Antonio Perrella Balestieri, Dr.Eng.**
UNESP – Guaratinguetá/SP – Brasil

**Prof. Louis Gosselin, Ph.D.**
ULAVAL – Quebec/QC – Canadá

Certificamos que esta é a **versão original e final** da Tese que foi julgada adequada para obtenção do título de **Doutor em Engenharia Mecânica** na área de concentração **Engenharia e Ciências Térmicas**.

Documento assinado digitalmente
Jonny Carlos da Silva
Data: 06/08/2020 17:01:17-0300
CPF: 514.515.064-49

**Prof. Jonny Carlos da Silva, Dr.Eng.**
Coordenador do Programa de
Pós-Graduação em Engenharia Mecânica
UFSC – Florianópolis/SC – Brasil

Documento assinado digitalmente
Alexandre Kupka da Silva
Data: 05/08/2020 09:06:09-0300
CPF: 000.190.189-32

**Prof. Alexandre Kupka da Silva, Ph.D.**
Orientador
UFSC – Florianópolis/SC – Brasil

Documento assinado digitalmente
Felipe Gesser Battisti
Data: 05/08/2020 00:50:07-0300
CPF: 074.047.399-93

**Felipe Gesser Battisti, M.Eng.**

Florianópolis/SC, 03 de abril de 2020

Aos meus pais, Sirlei e Gilson,

pelos apoio e incentivo incessantes.

A todos os que de quaisquer formas,

direta ou indiretamente,

contribuíram para concretização deste trabalho.

## AGRADECIMENTOS

À minha família. De forma bastante especial, aos meus pais Gilson A. Battisti e Sirlei L. G. Battisti, à minha avó Lorena M. S. Gesser e à minha tia avó Lurdete M. Salm por terem me dado condições de seguir minha formação acadêmica, pela confiança, pelo apoio incondicional. À minha irmã Helena G. Battisti, que me aguenta há tantos anos. Ao meu querido e saudoso avô Aristides Battisti.

Ao Prof. Alexandre K. da Silva, meu orientador, por todo apoio, pela confiança, por ter me proporcionado esta oportunidade de crescer tanto na minha formação acadêmica.

À querida e insubstituível amiga Rosângela A. de Sousa por todas as ajudas, pelas conversas, pelos tantos conselhos.

Ao LEPTEN e ao Prof. Sergio Colle pelo apoio, pela infraestrutura.

Aos Julio N. Scussel, Luigi A. de Araujo Passos, Carlos J. Noriega Sánchez, Allan R. Starke, José M. Cardemil Iglesias, grandes amigos que fiz nesta jornada. Aos muitos outros antes membros do LEPTEN, e hoje meus amigos. Em especial, aos Arthur P. da Veiga, Vinicius K. Scariot, Giovanni S. Delsoto, Thaís D. Luz, Alex C. Santana, Olivia C. da Rosa, Leonardo F. L. Lemos, Gustavo M. Hobold, Bruno S. Emerick, Ruan C. Comelli, Thiago Cardias, Mateus Stahelin, Vinicius R. B. Bonini, Andrés P. Sarmiento Cajamarca, Paulo C. C. Galeano, Carolina M. Coelho, Vanessa R. Werle.

Ao Prof. Louis Gosselin pela sensacional experiência em Quebec.

Aos meus amigos De Sempre pela amizade de tantos anos.

Ao governo federal, à UFSC, ao POSMEC pela oportunidade de fazer parte deste e crescer neste programa de doutorado .

Aos que apoiaram financeiramente o desenvolvimento deste trabalho. A ANEEL/Petrobras através dos projetos de pesquisa 0050.0080593.12.9 e PD-00553-0042/2016. A Petrobras através do Programa Petrobras de Formação de Recursos Humanos (PFRH) – convênio 6000.0062072.10.4; a Agência Nacional do Petróleo, Gás Natural e Biocombustíveis (ANP); a Financiadora de Estudos e Projetos (FINEP); o Ministério da Ciência, Tecnologia e Inovação (MCTI) através do Programa de Recursos Humanos da ANP para o Setor Petróleo e

Gás (PRH-ANP/MCTI). O presente trabalho foi realizado com apoio do CNPq, Conselho Nacional de Desenvolvimento Científico e Tecnológico – Brasil. O presente trabalho foi realizado com apoio da Coordenação de Aperfeiçoamento de Pessoal de Nível Superior – Brasil (CAPES) – Código de Financiamento 001.

Enfim, a todos que contribuíram de quaisquer formas para a concretização deste trabalho.

*"If I have seen further it is by standing on the shoulders of giants"*

Isaac Newton

## RESUMO

Esta tese explora o comportamento transiente de plantas de produção de potência com fontes intermitentes de calor, dióxido de carbono supercrítico (s-$CO_2$) como fluido de transferência de calor (HTF), ciclos Brayton e sistemas de armazenamento de energia térmica (TES). Este documento compreende três estudos intercomplementares principais. Primeiro, a tese discute o comportamento transiente de um ciclo de Brayton recuperativo utilizando s-$CO_2$, que inclui TES sólido e sistema de armazenamento de massa. O comportamento transiente do ciclo é promovido através de um perfil de temperatura da fonte de calor que imita o de uma planta híbrida (usina solar assistida por combustível fóssil) – ou seja, um perfil idealizado de temperatura semelhante ao fluxo solar associado a uma linha base constante. Para permitir as discretizações espacial e temporal dos principais componentes do ciclo, foram desenvolvidas rotinas numéricas em volumes finitos. Em segundo lugar, o comportamento transiente de um sistema TES *packed-bed* cilíndrico com s-$CO_2$ é investigado. O modelo numérico 1-D desenvolvido é responsável pela troca de calor entre o meio poroso e o HTF através de uma formulação de duas temperaturas, permitindo o cálculo das perdas de carga e de calor para o ambiente derivadas do escoamento de fluido pelo do tanque do TES. A análise termo-hidráulica investiga, por pontos de vista paramétrico e de otimização, os efeitos de parâmetros operacionais e de projeto, como tamanho do tanque e sua razão de aspecto, tamanho das partículas do meio poroso, temperatura de carregamento, ciclos de carga e descarga. Em terceiro lugar, é apresentada uma avaliação econômica e ambiental da viabilidade de um sistema integrado composto por campo de energia solar concentrada (CSP), bloco de potência e sistema TES *packed-bed* considerando s-$CO_2$ como HTF. A análise considera dados de ano meteorológico típico (TMY) para determinar os custos anuais de produção de energia de uma usina de $\sim 10$ MW, também usando a abordagem do custo nivelado de energia (LCOE). Com base em análises paramétricas, combinações de tamanhos de campo solar e sistema TES são estudadas enquanto considerando custos de equipamentos, operação e manutenção, aquecimento auxiliar e ambientais. Sobre a primeira parte, a análise mostra que os efeitos inerciais térmicos são capazes de alterar drasticamente a produção das plantas, já que o sistema pode requerer vários dias para atingir um padrão operacional periódico representativo, e que as hipóteses de regime permanente e de processo quase estático devem ser cuidadosamente consideradas quando um sistema TES é empregado. Além disso, se utilizado um controle adequado para os processos de carga e descarga do TES, seu uso pode estender significativamente a produção da planta, permitindo um melhor ajuste ao perfil de demanda. Sobre a segunda parte, os resultados sugerem claramente as tendências de *design* para sistemas TES *packed-bed* com s-$CO_2$, mostrando que não apenas a eficiência termo-hidráulica combinada de carga-descarga do sistema TES é altamente dependente dos parâmetros de projeto e operação, mas também que ele pode ser otimizado com relação a tais parâmetros. Sobre a terceira parte, a avaliação exploratória encontrou tendências econômicas para a planta integrada. Embora as soluções com o sistema TES *packed-bed* possam não ter melhorado o LCOE em comparação com as respectivas referências, a avaliação geral revelou não apenas a possível viabilidade do sistema integrado usando essa opção de TES com s-$CO_2$, mas também evidenciou caminhos para exames mais aprofundados, como otimização multiobjetivo também considerando aspectos ambientais.



**Keywords**: Dióxido de carbono supercrítico, Simulação transiente, Armazenamento de energia térmica, *Packed-bed*, Análise paramétrica & otimização, Avaliação econômica.

## RESUMO EXPANDIDO

### Introdução

A importância de estudar, desenvolver e otimizar sistemas de produção de energia depende não apenas de aspectos econômicos e técnicos, mas também de preocupações ambientais. Consequentemente, o estudo sobre fluidos de trabalho para de ciclos de potência vem sendo impulsionado. Neste sentido, o dióxido de carbono supercrítico (s-$CO_2$) destaca-se cada vez mais devido às variações de suas propriedades termofísicas quando próximo do seu ponto crítico termodinâmico – o qual ocorre em baixa temperatura e pressão moderada ($\sim$31 °C e $\sim$7.4 MPa [1–4]) – ao seu baixo impacto ambiental – o $CO_2$ pode ser considerado como possuindo baixo potencial de aquecimento global e de destruição da camada de ozônio [1] – e a permitir altos níveis de compacticidade para sistemas térmicos [5–7].

Motivados pela crescente demanda de energia, numerosos estudos têm considerado ciclos de potência utilizando s-$CO_2$, com foco especial no atual estado da arte de equipamentos para altas pressão e temperatura [8]. Embora o s-$CO_2$ tenha sido proposto inicialmente como fluido de transferência de calor (HTF) para beneficiar sistemas nucleares [5], nos últimos anos, plantas de energia solar concentrada (CSP) começaram a focar tal HTF. Tal interesse visa aproveitar características inerentes ao uso do s-$CO_2$, as quais incluem altos valores de eficiência, escoamento monofásico, aquecimento direto, arrefecimento a seco [9–13]. Além disso, esse HTF é atóxico, térmica e quimicamente estável, apresenta baixo custo e características desejáveis em relação à transferência de calor e à perda de carga [14–17]. Além disso, o limite de temperatura operacional comumente atribuído a fluidos de transferência de calor comerciais para CSP (e.g., a temperatura de degradação de óleos térmicos) pode ser superado usando s-$CO_2$ [18, 19]. No entanto, desafios tecnológicos intrínsecos ainda estão presentes ao se considerar fluidos de trabalho em condições supercríticas, os quais impedem a completa implantação comercial de ciclos utilizando s-$CO_2$. Estudos já consideraram diferentes fontes de calor, configurações de ciclo e componentes [5,6,16,20–25] visando ao desenvolvimento de melhores ciclos de potência, e.g., Refs. [14, 21]. Entre as linhas de pesquisa que consideram s-$CO_2$, os estudos têm se concentrado na otimização de ciclos [26, 27], comparações com outros fluidos de trabalho [22], aspectos econômicos [28], análise exergética [14].

Considerando as possíveis variabilidade sazonal e incerteza de disponibilidade de fontes renováveis de energia, os precisos projeto e avaliação de sistemas alimentados por elas, como plantas solares, exigem que os ciclos térmicos sejam modelados em condições transientes. Apesar desta clara necessidade de modelagem dependente do tempo, a literatura mostra que esses sistemas são normalmente modelados como processos quase-estáticos ou em regime permanente, e.g., Refs. [16, 29]. Embora os resultados obtidos com tal formulação possam servir como indicadores do comportamento de um sistema ao longo do tempo, eles podem falhar para explicar completamente aspectos relacionados à resposta temporal.

Sistemas de armazenamento de energia térmica (TES) e hibridação com fontes de calor convencionais estão sendo estudados para melhorar a estabilidade produtiva de plantas térmicas de fontes intermitentes. Focando o primeiro, dentre várias abordagens, a literatura atual aponta sistemas *packed-bed* e de duplo tanque como duas alternativas promissoras para TES com s-$CO_2$. Especificamente sobre sistemas *packed-bed*, eles foram convencionalmente projetados para trabalhar com ar comprimido, o qual permite simulações mais fáceis

e apresenta desempenho termo-hidráulico bem documentado [30–33]. Então, aspectos particulares diretamente relacionados ao s-$CO_2$ ainda estão indisponíveis (por exemplo, parâmetros de design e operacionais), o que faz previsões técnicas e econômicas sobre o comportamento desse sistema serem ainda incertas. Embora estudos tenham indicado a compatibilidade de soluções TES *packed-bed* com s-$CO_2$, vários autores enfatizaram que essas aplicações ainda enfrentam grandes barreiras técnicas [34].

Tendo em vista os potenciais benefícios associados ao s-$CO_2$, esta tese pretende explorar e estudar o desempenho transiente de ciclos de potência e sistemas TES usando tal fluido com foco em aplicações CSP, por meio de simulação, análise e otimização. Assim, este documento compreende três estudos intercomplementares principais, os quais são apresentados em seis capítulos e um apêndice. O Capítulo 1 introduz e contextualiza o trabalho, apresentando seus objetivos e a estrutura do documento. O Capítulo 2 é dedicado à revisão da literatura, no qual, inicialmente, atenção especial é dada ao $CO_2$ como fluido de trabalho para ciclos térmicos e, depois, é apresentada uma revisão de trabalhos relevantes selecionados. O Capítulo 3 é dedicado a apresentar a metodologia e os resultados do primeiro estudo, o qual trata das análise e otimização transientes de um ciclo Brayton recuperativo auxiliado por sistemas TES sólido e de armazenamento de massa. Da mesma forma, o Capítulo 4 apresenta a metodologia e os resultados do segundo estudo, o qual trata do mapeamento de desempenho de um sistema TES *packed-bed* para plantas CSP utilizando s-$CO_2$. Consequentemente, o Capítulo 5 apresenta a metodologia e os resultados do terceiro estudo, o qual trata da avaliação econômica e ambiental de um campo solar integrado a um sistema TES *packed-bed* e a um bloco de potência, todos utilizando s-$CO_2$. Em seguida, o Capítulo 6 é dedicado às conclusões e sugestões para trabalhos futuros. E, finalmente, o Apêndice A apresenta detalhadamente o processo para obter a expressão geral da equação de energia usada nos três estudos que compõem esta tese.

**Objetivos**

O objetivo global desta tese é o desenvolvimento de conhecimento, sob pontos de vista termodinâmico e numérico, acerca do desempenho transiente de ciclos Brayton utilizando s-$CO_2$ acoplados a sistemas TES com foco em plantas CSP. A fim de alcançar o objetivo global deste trabalho, os seguintes objetivos específicos são considerados:

- Fornecer uma ampla visão geral sobre o desempenho termo-hidráulico transiente de plantas CSP utilizando s-$CO_2$ e sistemas TES;
- Contribuir com a literatura, explorando o *know-how* ainda incipiente sobre soluções TES com s-$CO_2$;
- Estudar numericamente o desempenho transiente de um ciclo Brayton utilizando s-$CO_2$ e sistema TES, incluindo aspectos-chave como estratégia de controle do sistema e parâmetros de construção do TES;
- Abordar, através de pontos de vista paramétrico e de otimização, a lacuna tecnológica sobre o desempenho termo-hidráulico de dispositivos TES *packed-bed* utilizando s-$CO_2$ para plantas CSP;
- Avaliar econômica e ambientalmente a viabilidade de uma planta CSP utilizando s-$CO_2$ e sistema TES *packed-bed* através de simulação numérica transiente, considerando dados meteorológicos reais.

**Metodologia**
Primeiro, a tese discute o comportamento transiente de um ciclo de Brayton recuperativo utilizando s-$CO_2$, que inclui TES sólido e sistema de armazenamento de massa. O comportamento transiente do ciclo é promovido através de um perfil de temperatura da fonte de calor que imita o de uma planta híbrida (e.g., usina solar assistida por combustível fóssil) – ou seja, um perfil idealizado de temperatura semelhante ao fluxo solar associado a uma linha base constante. Para permitir as discretizações espacial e temporal dos principais componentes do ciclo, foram desenvolvidas rotinas numéricas em volumes finitos. Em segundo lugar, o comportamento transiente de um sistema TES *packed-bed* cilíndrico com s-$CO_2$ é investigado. O modelo numérico 1-D desenvolvido é responsável pela troca de calor entre o meio poroso e o HTF através de uma formulação de duas temperaturas, permitindo o cálculo das perdas de carga e de calor para o ambiente derivadas do escoamento de fluido pelo do tanque do TES. A análise termo-hidráulica investiga, por pontos de vista paramétrico e de otimização, os efeitos de parâmetros operacionais e de projeto, como tamanho do tanque e sua razão de aspecto, tamanho das partículas do meio poroso, temperatura de carregamento, ciclos de carga e descarga. Em terceiro lugar, é apresentada uma avaliação econômica e ambiental da viabilidade de um sistema integrado composto por campo de energia solar concentrada (CSP), bloco de potência e sistema TES *packed-bed* considerando s-$CO_2$ como HTF. A análise considera dados de ano meteorológico típico (TMY) para determinar os custos anuais de produção de energia de uma usina de $\sim 10$ MW, também usando a abordagem do custo nivelado de energia (LCOE). Com base em análises paramétricas, combinações de tamanhos de campo solar e sistema TES são estudadas enquanto considerando custos de equipamentos, operação e manutenção, aquecimento auxiliar e ambientais.

**Resultados**
Sobre a primeira parte, a análise mostra que os efeitos inerciais térmicos são capazes de alterar drasticamente a produção das plantas, já que o sistema pode requerer vários dias para atingir um padrão operacional periódico representativo, e que as hipóteses de regime permanente e de processo quase estático devem ser cuidadosamente consideradas quando um sistema TES é empregado. Além disso, se utilizado um controle adequado para os processos de carga e descarga do TES, seu uso pode estender significativamente a produção da planta, permitindo um melhor ajuste ao perfil de demanda. Sobre a segunda parte, os resultados sugerem claramente as tendências de *design* para sistemas TES *packed-bed* com s-$CO_2$, mostrando que não apenas a eficiência termo-hidráulica combinada de carga-descarga do sistema TES é altamente dependente dos parâmetros de projeto e operação, mas também que ele pode ser otimizado com relação a tais parâmetros. Sobre a terceira parte, a avaliação exploratória encontrou tendências econômicas para a planta integrada. Embora as soluções com o sistema TES *packed-bed* possam não ter melhorado o LCOE em comparação com as respectivas referências, a avaliação geral revelou não apenas a possível viabilidade do sistema integrado usando essa opção de TES com s-$CO_2$, mas também evidenciou caminhos para exames mais aprofundados, como otimização multiobjetivo também considerando aspectos ambientais.

**Palavras-chave**: Dióxido de carbono supercrítico (s-$CO_2$), Simulação transiente, Armazenamento de energia térmica (TES), *Packed-bed*, Análise paramétrica & otimização, Avaliação econômica.

## ABSTRACT

This dissertation explores the transient behavior of intermittent-heat-sources-based power plants using supercritical carbon dioxide (s-$CO_2$) as heat transfer fluid (HTF), Brayton cycles, and thermal energy storage (TES) systems. This document comprises three main inter-complementary studies. First, this dissertation discusses the transient behavior of an s-$CO_2$ recuperative Brayton cycle, which includes solid TES and mass storage systems. The cycle time-dependent behavior is promoted through a heat source temperature profile mimicking that of a hybrid power plant (fossil-assisted solar plant) – i.e., an idealized solar-radiation-flux-like temperature profile on top of a constant baseline. For allowing spatial and temporal discretizations of key components of the cycle, finite-volume numerical routines were specifically developed. Secondly, the transient behavior of a cylindrical s-$CO_2$-based packed-bed TES system is investigated. The 1-D numerical model developed accounts for the heat exchange between the porous medium and the HTF through a two-temperature formulation, thus allowing the calculation of the pressure drop and the heat loss to the environment derived from the fluid flow through the TES tank. The thermal-hydraulic analysis investigates, from parametric and optimization standpoints, the effects of design and operational parameters, such as the tank size and aspect ratio, the porous medium particle size, the charging temperature, the charging-discharging cycling. Thirdly, an economic assessment on the feasibility of a concentrated solar power (CSP) plant composed of solar field, power block, and packed-bed TES system considering s-$CO_2$ as HTF is presented. The analysis considered typical meteorological year (TMY) data for determining the annual costs of producing energy in a $\sim$ 10 MW plant also using the levelized cost of energy (LCOE) approach. By drawing upon parametric analyses, combinations of solar field and TES sizes are studied while considering equipment, operation and maintenance, auxiliary heating, and environmental costs. From the first part, the analysis shows that the thermal inertial effects are capable of drastically changing the power delivery of the cycles because the overall system might require several days to reach a periodic representative operational pattern, which suggests that steady-state and quasi-steady-state hypotheses must be carefully considered when a TES system is employed. Moreover, if a proper control strategy is used for the TES charging and discharging processes, its use can significantly extend the cycle power output delivery allowing a better fitting to the demand profile. From the second part, the results clearly suggest design trends for s-$CO_2$-based systems, showing that not only the thermal-hydraulic charging-discharging combined efficiency of the TES unit is highly dependent on design and operation parameters, but also that it can be optimized with respect to such parameters. From the third part, the exploratory assessment found economic trends for the integrated plant. Although the solutions with the packed-bed TES system might have not improved the LCOE in comparison to the respective references, the overall examination revealed the possible feasibility of the integrated system using such a TES technology for s-$CO_2$ and evidenced several venues for further examination, such as multi-objective optimization also regarding environmental aspects.



**Keywords**: Supercritical carbon dioxide (s-$CO_2$), Transient simulation, Thermal energy storage, Packed-bed, Parametric analysis & optimization, Economic assessment.

## JOURNAL PUBLICATIONS

Methodologies, modeling, results, and discussions obtained during the development of this dissertation are already partially presented in the following journal paper:

- BATTISTI, F. G.; DELSOTO, G. S.; da SILVA, A. K. Transient analysis and optimization of a recuperative $sCO_2$ Brayton cycle assisted by heat and mass storage systems. Energy, v. 150, p. 979 – 991, 2018. ISSN 0360-5442.

Additional journal paper published during the period of development of this dissertation:

- da ROSA, O. C.; BATTISTI, F. G.; HOBOLD, G. M.; da SILVA, A. K. Enhancing heat rejection from electronic devices with a supercritical carbon dioxide minichannel heat exchanger. International Journal of Refrigeration, v. 106, p. 463-473, 2019. ISSN 0140-7007.

Author's remaining published journal papers:

- BATTISTI, F. G.; CARDEMIL, J. M.; da SILVA, A. K. A multivariable optimization of a Brayton power cycle operating with $CO_2$ as working fluid. Energy, v. 112, p. 908-916, 2016. ISSN 0360-5442.
- BATTISTI, F. G.; CARDEMIL, J. M.; MILLER, F. M.; da SILVA, A. K.. Normalized performance optimization of supercritical, $CO_2$-based power cycles. Energy, v. 82, p. 108-118, 2015. ISSN 0360-5442.

## LIST OF FIGURES

## LIST OF TABLES

## LIST OF SYMBOLS

### Abbreviations

| | |
|---|---|
| C | Compressor |
| CDS | Central differencing scheme |
| Co | Cooler |
| CSP | Concentrated solar power |
| DNI | Direct normal irradiation |
| He | Heater |
| HEx | Heat exchanger |
| HTF | Heat Transfer Fluid |
| HTR | High-temperature recuperator |
| LHS | Left-hand side |
| LHV | Lower heating value |
| LMTD | Logarithmic mean temperature difference |
| LTR | Low-temperature recuperator |
| MC | Main compressor |
| MS | Mass storage |
| NSR | Non-saturated region |
| PB | Power block |
| PCM | Phase change material |
| RC | Recompressor |
| Rec | Recuperator |
| RHS | Right-hand side |
| s-$CO_2$ | Supercritical carbon dioxide |

| | | |
|---|---|---|
| SF | Solar field | |
| T | Turbine | |
| TES | Thermal Energy Storage | |
| UDS | Upwind differencing scheme | |

**Greeks**

| | | |
|---|---|---|
| $\alpha$ | Generic interface indicator, solid internal energy linearization factor | [–] |
| $\beta$ | Kunii and Smith's solid effective conductivity correlation parameters | [–] |
| $\Delta$ | Difference, increment, step | [–] |
| $\delta$ | Improvement index | [%] |
| $\epsilon$ | Deviation, emissivity | [–] |
| $\eta$ | Efficiency | [–] |
| $\Gamma$ | Inefficiency ratio | [–] |
| $\gamma$ | Pfeffer's correlation coefficient | [–] |
| $\kappa$ | Ratio between solid and fluid thermal conductivities | [–] |
| $\Lambda$ | Distance to the origin point | [–] |
| $\lambda$ | Overall power deviation | [W] |
| $\mu$ | Dynamic viscosity | $[\mathrm{Pa} \cdot \mathrm{s}]$ |
| $\Omega$ | Generation term | $[\mathrm{W/m^3}]$ |
| $\omega$ | Fluid film effective thickness | [–] |
| $\omega$ | Ratio between effective fluid film thickness and particle diameter | [–] |
| $\Phi$ | Dissipation function | $[\mathrm{1/s^2}]$ |
| $\phi$ | Given arbitrary quantity | [–] |
| $\Psi$ | Particle sphericity | [–] |
| $\psi$ | Equation general coefficient | [–] |
| $\rho$ | Volume-specific mass | $[\mathrm{kg/m^3}]$ |

| | | |
|---|---|---|
| $\sigma$ | Yield strength | [MPa] |
| $\Theta$ | Heat flow area boundary angle for one contact point | [rad] |
| $\theta$ | Angle of incidence | [rad] |
| $\varepsilon$ | Porosity | [–] |
| $\varphi$ | Solid specific heat at constant pressure coefficient | [–] |
| $\xi$ | Modified Ergun's pressure drop correlation coefficient | [–] |
| $\zeta$ | Aspect ratio | [–] |

**Romans**

| | | |
|---|---|---|
| $\dot{E}$ | Thermal power | [W] |
| $\dot{m}$ | Mass flow rate | [kg/s] |
| $\dot{W}$ | Power produced/consumed | [W] |
| $\hbar$ | Volumetric convection heat transfer coefficient | [$\mathrm{W/(m^3 \cdot K)}$] |
| $A$ | Area | [$\mathrm{m^2}$] |
| $b$ | Specific cost | [US$/(kg or J)] |
| $C$ | Cost | [US$] |
| $c$ | Mass-specific heat at constant pressure | [$\mathrm{J/(kg \cdot °C)}$] |
| $D$ | Diameter, bed diameter | [m] |
| $d$ | Particle (sphere) diameter | [mm] |
| $DNI$ | Direct normal irradiation | [$\mathrm{W/m^2}$] |
| $dr$ | Discount rate | [%/yr] |
| $e$ | Friction factor, mass-specific internal energy | [–, J/kg] |
| $G$ | Mass flow rate per unit of cross section area | [$\mathrm{kg/(m^2 \cdot s)}$] |
| $g$ | Enthalpy-temperature coupling factor | [$\mathrm{(K \cdot kg)/J}$] |
| $h$ | Convection heat transfer coefficient | [$\mathrm{W/(m^2 \cdot K)}$] |
| $I$ | Solar irradiation | [$\mathrm{W/m^2}$] |

| | | |
|---|---|---|
| $i$ | Mass-specific enthalpy | [J/kg] |
| $j$ | Given time step | [–] |
| $k$ | Thermal conductivity | [W/(m · K)] |
| $L$ | Length | [m] |
| $l$ | Generic length | [m] |
| $LCOE$ | Levelized cost of energy | [US$/MWh] |
| $LHV$ | Lower heating value | [J/kg] |
| $LT$ | Lifetime | [yr] |
| $N$ | Number of divisions/tubes of the TES, number of elements | [–] |
| $n$ | Number of particles/scaling factor | [–] |
| $P$ | Pressure | [Pa] |
| $p$ | Perimeter | [m] |
| $R$ | Thermal resistance | [K/W] |
| $r$ | Radial length | [m] |
| $S$ | Size metric | [$m^2$, W, W/K] |
| $s$ | Mass-specific entropy | [J/(kg · K)] |
| $SM$ | Solar multiple | [–] |
| $T$ | Temperature | [K, °C] |
| $t$ | Time | [s] |
| $u$ | Velocity | [m/s] |
| $UA$ | Global conductance | [W/K] |
| $V$ | Volume | [$m^3$] |
| $v$ | Mass-specific volume | [$kg/m^3$] |
| $W$ | Energy produced/consumed | [J] |
| $x$ | Mass flow rate fraction | [–] |

| | | |
|---|---|---|
| $z$ | Axial distance | [m] |
| f | Factor | [–] |

**Subscripts and Superscripts**

| | |
|---|---|
| $\alpha$ | Equation general subindex |
| $\Delta P$ | Pressure drop |
| * | Normalized |
| 0 | Previous time step |
| 1,2,... | Counters |
| a | Approximated |
| ac | Acceleration |
| Adiab | Adiabatic |
| Aper | Aperture |
| Aux | Auxiliary |
| b | Iteration counter, indexer, beam |
| Bypass | Bypass |
| C | Compressor, charging |
| Cd | Conduction |
| Co | Cooler |
| Coll | Collector |
| Comb | Combined |
| Crit | Critical |
| Cv | Convection |
| D | Diameter/bed diameter as characteristic length, discharging |
| d | Particle (sphere) diameter as characteristic length |
| Dec | Decoupled |

| | |
|---|---|
| E | East node |
| e | East interface |
| eff | Effective |
| EG | Electric generator |
| Env | Environmental |
| eq | Equivalent |
| Equip | Equipment |
| Ext | External |
| F | Fluid |
| g | Ground |
| H | Hot |
| He | Heater |
| HEx | Heat exchanger |
| High | High |
| HSi | Heat sink |
| HSo | Heat source |
| HT | Heat transfer |
| Hyd | Hydraulic |
| I | Refers to the $1^{st}$ law of thermodynamics, idle |
| i | Indexer, insulation |
| In | Inlet |
| Int | Internal |
| Iso | Isentropic |
| Lid | Lid |
| LMTD | Logarithmic mean temperature difference |

| | |
|---|---|
| Loss | Loss |
| Low | Low |
| Max | Maximal |
| Min | Minimal |
| Mirror | Mirror |
| MO | Maintenance & Operation |
| MS | Mass Storage |
| Net | Net |
| NG | Natural gas |
| Opt | Optimal |
| Out | Outlet |
| P | Current node |
| part | Particle |
| PB | Power block |
| Pe | Péclet number |
| Pump | Pump/compressor |
| r | Reduced, radial direction |
| Ra | Radiation |
| Rec | Receiver |
| Rec | Recuperator |
| ref | Reference |
| rss | Radiative surface to surface |
| rvv | Radiative void to void |
| S | Solid |
| SF | Solar field |

| | |
|---|---|
| Site | Site |
| st | Steel |
| stag | Stagnated |
| Sto | Stored |
| T | Turbine |
| TES | Thermal energy storage |
| Total | Total |
| Trans | Transversal |
| W | West node |
| w | West interface |
| Wall | Wall |
| z | Axial interface |

**Miscellaneous**

| | |
|---|---|
| $\bar{}$ | Averaged value |
| $\langle\ \rangle$ | Time-averaged value |
| $\lceil\ \rceil$ | Ceiling value |
| $\lfloor\ \rceil$ | Rounded value |
| $\vec{}$ | Vector designator |
| $f$ | Function of |

**Non-dimensional numbers**

| | |
|---|---|
| $Bi$ | Biot number |
| $Nu$ | Nusselt number |
| $Pe$ | Péclet number |
| $Pr$ | Prandtl number |
| $Re$ | Reynolds number |

**CONTENTS**

# 1 INTRODUCTION

The importance of studying, developing, and optimizing power production systems, such as thermal power cycles, relies not only on economic and technical aspects but also on environmental concerns. Consequently, the study of advanced working fluids for such applications is gaining momentum. Supercritical carbon dioxide (s-$CO_2$) is increasingly standing out as a heat transfer fluid (HTF) mainly because of

- the variations of its thermophysical properties in the vicinity of its thermodynamic critical point, which occurs at low temperature and moderate pressure ($\sim$31 °C and $\sim$7.4 MPa) [1–4];
- its low environmental impact, which is comparable to water and lower than competitors, such as ethane – e.g., $CO_2$ may be considered to have low global warming and ozone depletion potentials [1];
- the high compactness levels it enables for thermal systems [5–7].

Motivated by the growing need for large-scale methods of electric power generation, numerous studies have drawn attention to s-$CO_2$-based power cycles while also focused on high-pressure and high-temperature equipment [8]. Though s-$CO_2$ has been initially proposed as a HTF to benefit nuclear reactors systems [5], in recent years, concentrated solar power (CSP) plants started considering such an HTF due to the possibility of they taking advantage of its inherent features, which include, for instance, high-efficiency values, one-phase flow, direct heating, dry cooling [9–13]. Moreover, this HTF presents sought-through characteristics, such as being non-toxic, thermally and chemically stable, having low cost and favorable heat transfer and pressure drop characteristics [14–17]. Furthermore, the operating temperature limit commonly assigned to commercial options of HTF for CSP – e.g., the degradation temperature of thermal oils – may be outweighed using s-$CO_2$ [18, 19].

Nevertheless, intrinsic technological challenges are still present when considering working fluids at supercritical conditions, which prevent the full commercial deployment

of s-$CO_2$-based cycles. For instance, leakages, which are accentuated by the expected large pressures differences in such systems, are a major concern to conventional parabolic trough collectors operating with s-$CO_2$ [19] and new tower receivers are only at design stage [36, 37]. Also, heat exchangers, turbo-alternator-compressors, and parabolic trough collectors designed for s-$CO_2$ have mostly been tested only at laboratory scale [19, 38].

Several thermal power systems using s-$CO_2$ have been investigated; researchers have considered different heat sources, cycle configurations and components [5, 6, 16, 20–25] aiming at the development of better and deployable on-demand power cycles, e.g., Refs. [14, 21]. Amongst the research lines considering s-$CO_2$, studies have focused on the optimization of power cycles [26, 27], comparisons with other working fluids [22], economic aspects [28], and exergetic analysis [14].

The precise design and evaluation of systems powered by intermittent renewable energy sources, such as CSP plants, require them to be modeled under transient conditions while considering the seasonal variability and availability uncertainty of such energy sources. Despite the clear requirement for time-dependent modeling, the literature shows that such systems are mostly modeled as quasi-steady-state or steady-state processes, e.g., Refs. [16, 29].

In general, quasi-steady-state modeling assumes that time-dependent variables are subjected to questionable time-equilibrium parameters [39]. Hence, it is assumed that during the heat source availability period (the hours comprehended between sunrise and sunset for solar-based plants, for instance), the system operates as a sequence of quasi-steady-state processes. A major advantage of this formulation is that the time-dependency may be simply included by varying the system boundary condition (the solar radiation flux with time) through a series of discrete steps. While the results generated under this formulation may provide indicatives of the system behavior over time, they may fail to account for important aspects, such as thermal inertia and time response of the different system components. Because of that, the evident alternative solution is modeling the system through fully transient processes. Obviously, for a solar-powered thermal cycle, this requires key components to be modeled as time-dependent, as well as the working fluid inventory to be accounted for at all times.

When dealing with solar-powered plants, thermal energy storage (TES) systems and hybridization with conventional heat sources are the favored approaches explored for increasing energy dispatchability. Both are used for dealing with the short-term variability of the solar resource due to atmospheric dynamics and long-lasting cloudy periods and nights while ensuring the stability of the producing processes and boosting the solar fraction of energy deployed. Focusing on the former, several alternatives are being studied, such as molten salts, thermal oils, concrete, phase-change materials, packed-bed.

Additional unknowns associated with the use of s-$CO_2$ in solar-powered plants concern specifically TES solutions. Amongst the available TES technologies, the current literature points towards packed-bed and two-tank systems as two promising alternatives. Specifically on packed-bed TES systems, they have been conventionally designed for working with compressed air, which allows for easier simulations and has well-documented thermal-hydraulic performance [30–32]. However, when dealing with high-pressure and high-temperature working conditions (possibly away from the Widom-line), it may be argued that the performance trends for s-$CO_2$-based TES systems may be expected to follow those for air-based ones, which are well known. Nonetheless, the lower viscosity and larger mass-specific heat at constant pressure and volume-specific mass that are familiar to s-$CO_2$ may substantially influence the TES performance through larger heat transfer coefficients and smaller pressure drops. Hence, particular aspects directly related to thermal storage for s-$CO_2$ are still mostly unavailable (e.g., design and operational parameters), which makes technical and economic predictions uncertain regarding the behavior of these systems. Besides, it is usual to only account for the dependence of the TES system on the power block indirectly. Although studies have indicated the compatibility of packed-bed TES solutions with s-$CO_2$, a number of authors have emphasized that such applications still face major technical barriers, especially because of the high pressures generally considered ($\gtrsim$ 25 MPa) [34].

Aware of the potential benefits associated with s-$CO_2$, this dissertation intends to further explore and study the transient performance of power cycles and TES systems using such an HTF while focusing on CSP applications through simulation, analysis, and optimization. Furthermore, the beginning of each of the studies composing this dissertation

presents details on its contributions and novelty aspects.

## 1.1 OBJECTIVES OF THE PRESENT WORK

### 1.1.1 Global objective

The global objective of this dissertation is the development of knowledge, from thermodynamic and numerical standpoints, on the transient performance of s-$CO_2$ Brayton power cycles coupled to TES systems focusing on CSP-powered plants.

### 1.1.2 Specific objectives

In order to accomplish the global objective of this work, the following specific objectives are considered:

- To provide a broad overview of the transient thermal-hydraulic performance of s-$CO_2$ CSP-based plants with TES systems;
- To contribute to the literature by exploring the yet incipient know-how regarding s-$CO_2$ TES solutions;
- To numerically study the transient performance of s-$CO_2$ Brayton cycle with TES system while including key aspects such as system control strategy and TES construction parameters;
- To address, from parametric and optimization standpoints, the technology gap regarding the thermal-hydraulic performance of s-$CO_2$-oriented packed-bed TES for CSP-powered plants;
- To economically and environmentally assess the feasibility of an integrated s-$CO_2$ CSP-plant with a packed-bed TES system through transient numerical simulation while considering actual time-dependent meteorological data.

## 1.2 STRUCTURE OF THE DISSERTATION

This dissertation comprehends three inter-complementary studies, which are presented in six chapters and one appendix. Apart from this introduction, the five remaining

chapters and the appendix are individually commented below.

Chap. 2 is dedicated to the literature review. Initially, special attention is given to $CO_2$ as working fluid for thermal cycles; then, a review of selected relevant works is presented. Chap. 3 is dedicated to present the methodology and the results of the first study, which deals with the transient analysis and optimization of a recuperative Brayton cycle assisted by solid TES and mass storage systems. Similarly, Chap. 4 presents the methodology and the results of the second study, which deals with the performance mapping of a packed-bed TES system for CSP plants using s-$CO_2$. Consequently, Chap. 5 presents the methodology and the results of the third study, which deals with the economic assessment of an integrated s-$CO_2$-based CSP plant composed of solar field, packed-bed TES system, and power block. Then, Chap. 6 is dedicated to the conclusions and suggestions for future works. Finally, Appx. A presents in detail the process for obtaining the energy equation general expression used throughout the three main studies of this dissertation.

# 2 LITERATURE REVIEW

This chapter is dedicated to the literature review. First, $CO_2$ as working fluid is presented from historical and technical standpoints, brief discussions on the critical point and supercritical state are presented, and, finally, a review of selected works is detailed.

## 2.1 HISTORICAL ASPECTS ON $CO_2$ APPLIED TO THERMAL CYCLES

By the end of the nineteenth century, $CO_2$ was used in commercial refrigeration; air conditioning systems in theaters, hospitals, and where toxic fluids were not acceptable [15]. Systems using $CO_2$ had low capacity and reduced efficiency at high ambient temperatures, they were susceptible to frequent leaks due to the high pressures required and poor sealing [40]. In the early twentieth century, $CO_2$ was gradually replaced by ammonia and halogenated fluids [41]. In the 1990s, with the rising of environmental concerns, the interest on $CO_2$ was renovated [42] and, since then, it has also been used in food and beverage refrigeration systems and heat pumps.

First proposed by Sulzer Bros in 1948, research on power cycles using $CO_2$ as working fluid was carried out in the former Soviet Union, Italy, United States [43]. After the intense years during the 1960s (e.g., Refs. [44–46]), the interest on such cycles declined until the 1990s, mainly due to heat source limitations and lacking of components for such cycles [5]. Nevertheless, many researchers have focused on supercritical Brayton cycles using high-temperature heat sources and high pressures for nuclear reactor applications [5, 47]. Currently, increased interest is observed for both low-temperature sources (mostly with Rankine cycles, e.g., waste heat, geothermal) and high-temperature sources (mostly with Brayton cycles, e.g., solar, nuclear).

## 2.2 CRITICAL POINT AND SUPERCRITICAL STATE

Through a series of experiments conducted in 1822 (e.g., Refs. [48, 49]) dealing with the discontinuity of the splashing sound of a ball in a rolling pressurized Papin's digester [1]

[1] A high-pressure steam cooker invented in 1679 by the French physicist Denis Papin, which is the forerunner of autoclaves and domestic pressure cookers.

partially filled with a fluid, Charles Cagniard de la Tour found that, at sufficiently high temperatures, as the solid ball penetrated the liquid-vapor interface, no splashing sound was generated because the fluid was at supercritical state [50].

Coined by Andrews in 1869 [51], the term "critical point" of a pure fluid refers to the point where saturated liquid and saturated vapor thermodynamic states coincide – at such a point in the $P$-$s$-$T$ manifold, $\left.\frac{\partial T}{\partial s}\right|_{\mathrm{P}} = \left.\frac{\partial^2 T}{\partial s^2}\right|_{\mathrm{P}} = 0$ [52]. The temperature and pressure at such a point are called "critical" and a fluid whose thermodynamic state presents temperature and pressure above of those of its critical point is called supercritical.

Supercritical fluids do not present a clear transition between the liquid-like and the gas-like phases, which leads to homogeneous thermophysical properties. According to Ref. [50], such fluids present liquid- and gas-like behaviors simultaneously: as gases, they can permeate solids; as liquids, they can dissolve materials. Even though the physical understanding of critical phenomena (and consequently of supercritical state) continues to be lacking [53, 54], there is a broad range of applications for fluids at supercritical conditions, which includes cooling, power generation, dry washing, extraction of substances, solvents.

## 2.3 $CO_2$ AS WORKING FLUID

From a technical standpoint, s-$CO_2$ has several advantages when compared with other working fluids: it is non-expensive, abundant, non-toxic, non-explosive, non-corrosive, chemically stable, it has a moderate critical pressure, its thermophysical properties are well known, it is environment-friendly, and related to high compactness of thermal systems [5–7, 14–17]. Specifically, in the vicinity of its thermodynamic critical point, $CO_2$ thermophysical properties are strongly affected by variations of temperature and pressure [55–60]. There are several studies dealing with properties variations of supercritical fluids, such as Refs. [55,56], and particularly focused on s-$CO_2$ as reported in Refs. [57–60].

Regarding the $CO_2$ thermophysical properties, throughout this dissertation, the CoolProp library [3, 4] is used, which relies on the Helmholtz free energy-based equation of state of Ref. [61], the thermal conductivity expression of Ref. [62], and the viscosity expression of Ref. [63]. Now, on the properties variations, Fig. 1 displays the mass-specific

heat at constant pressure as a function of the reduced temperature

$$T_{\mathrm{r}} = \frac{T}{T_{\mathrm{Crit}}} \tag{2.1}$$

for different values of reduced pressure

$$P_{\mathrm{r}} = \frac{P}{P_{\mathrm{Crit}}} \tag{2.2}$$

for $CO_2$ at supercritical state – with $P_{\mathrm{Crit}} = 7.3773$ MPa and $T_{\mathrm{Crit}} = 304.1282$ K [3, 4]. It is clear that the closer the thermodynamic state is to the critical point, the stronger the properties variations are. Moreover, it may be observed that, for each different value of reduced pressure, there is a clear peak at a specific different reduced temperature, which indicates the existence of a line of maxima that is a function of pressure and temperature (the gray dashed one in Fig. 1). The *locus* of such maxima in the $P - T$ manifold is commonly referred to as Widom line [64] and the specific temperatures to as pseudo-critical. Furthermore, as the thermodynamic state gets farther away from the critical point, even if on the Widom line, the property variation magnitude decreases up to a point where such a variation becomes unnoticeable.

Figure 1 – Mass-specific heat at constant pressure for $CO_2$ at supercritical state as function of the reduced temperature ($T_{\mathrm{r}}$) for five different values of reduced pressure ($P_{\mathrm{r}}$).

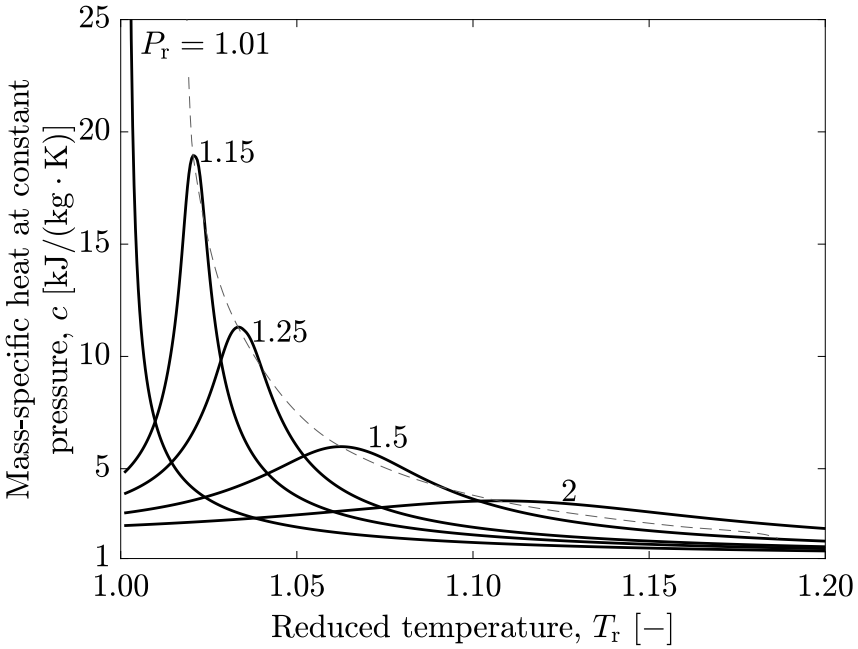


Note – Thermophysical property data obtained from CoolProp [3, 4].

To further illustrate the above-mentioned thermophysical properties variations, Fig. 2 presents $T_r - P_r$ color maps of mass-specific heat at constant pressure ($c$), volume-specific mass ($\rho$), dynamic viscosity ($\mu$), and thermal conductivity ($k$). Each property $\phi$ was normalized by the minimal and maximal values in the $P - T$ manifold considered, i.e.,

$$\phi^* = \frac{\phi - \min(\phi)}{\max(\phi) - \min(\phi)}. \tag{2.3}$$

Figure 2 – Normalized maps of selected $CO_2$ thermophysical properties as functions of reduced temperature and pressure.

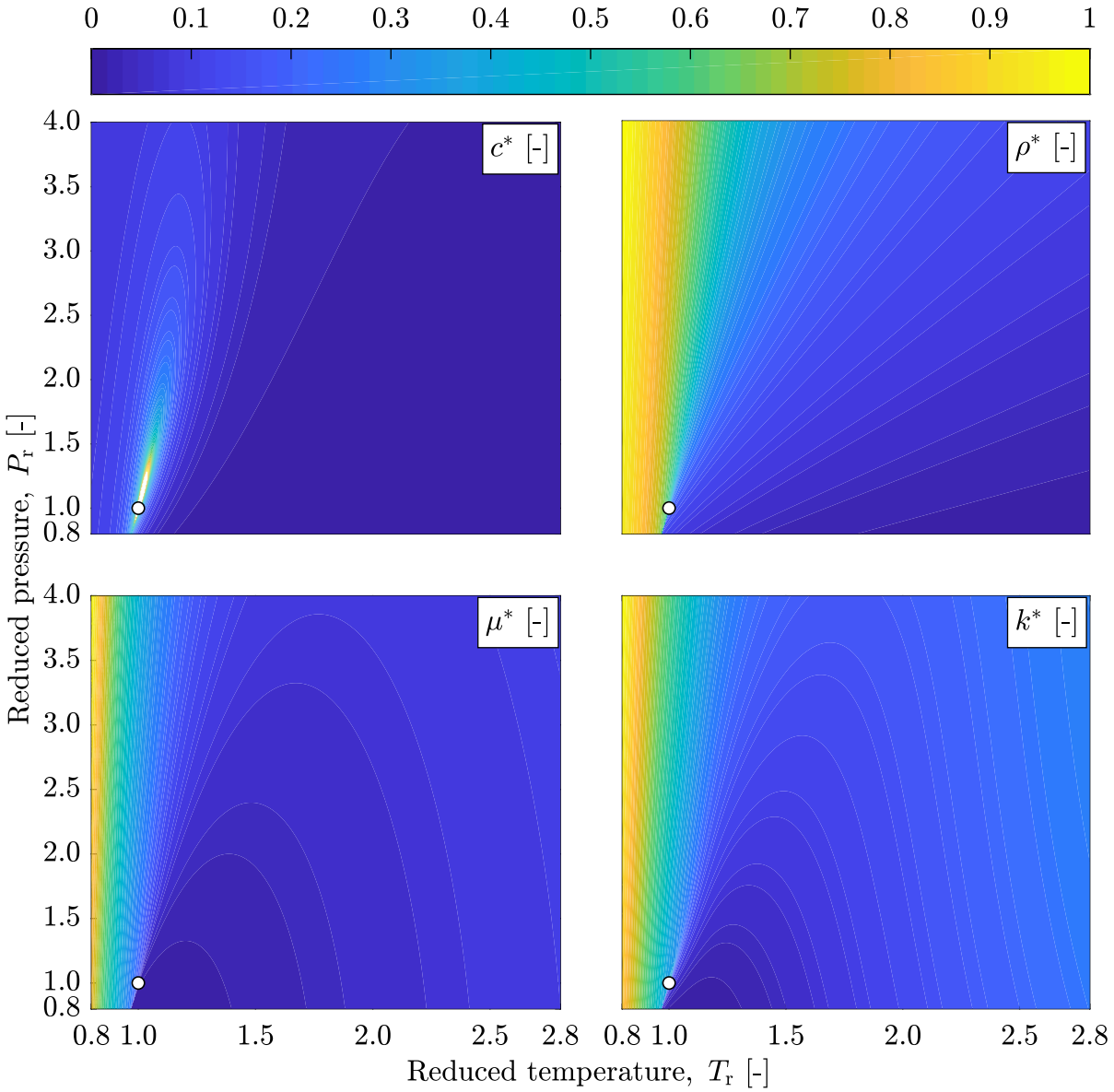


Note – Thermophysical properties data obtained from CoolProp [3, 4].

In Fig. 2, the color scale refers to the property normalized magnitude and the white circle indicates the location of the critical point. Also, the maximal $c$ used in Eq. 2.3

was obtained as an approximation due to the undefined value of such a thermophysical property at the fluid thermodynamic critical point – the mass-specific heat at constant pressure diverges as the fluid condition approaches such a point [52, 53].

Even though the physical understanding of these properties variations is lacking, they may be exploited to improve the performance of thermal applications. For instance, the size and efficiency of thermal devices may be significantly affected by variations of fluid properties, which influence heat transfer and fluid flow characteristics. Therefore, the performance of such devices should be evaluated and further optimized by taking these effects into account [17].

It must be mentioned that s-$CO_2$ also presents disadvantages, such as possible limitations within heat exchangers due to pinch point [17, 65], impaired heat rejection to the ambient due to its low critical temperature, high working pressures, high temperatures at turbine outlets, lacking of properly designed power generation equipment.

## 2.4 SELECTED WORKS

A comprehensive work regarding $CO_2$ Brayton cycles for nuclear applications was presented by Ref. [5]. Intending to select the best suitable cycle to meet established demands while keeping in mind global optimization, component design, economic analysis, and control scheme, the authors developed a not purely steady-state thermodynamic analysis. Numerical models for simulations of cycles and their components were presented and thermodynamic analyses of some advanced supercritical power cycles were carried out, which were followed by economic analysis, design, and selection of components.

Discussions about the use of recuperators for s-$CO_2$ power cycles in order to achieve larger 1$^{st}$ law efficiency values and about the use of mini/microchannel heat exchangers with high effectiveness were presented by Ref. [66]. Then, Ref. [67], continuing the earlier work, analyzed the $CO_2$ behavior in the pseudocritical region while focusing on possible heat exchange limitations related to pinch points within the recuperator and the effect of recompression. For taking advantage of the s-$CO_2$ decreased compressibility factor in the vicinity of its critical point, by selecting a low-end pressure of 7.55 MPa, the power required by the compressor was remarkably reduced. The cycle was parametrically optimized while

achieving a maximal 1st law efficiency of 45%, which is considerably higher than the ones achieved by typical Brayton cycles. It was emphasized that, for the proposed cycle, the 1st law efficiency is strongly affected by the pressure drop across the heat exchanger, hence indicating the importance of mini/microchannel heat exchangers.

Analyses on using $CO_2$ as working fluid for six Brayton cycles proposed by Ref. [44] – i.e., typical, pre-compression, recompression, split-expansion, partial cooling, and improved partial cooling with regeneration – were presented by Ref. [65]. The authors discussed the pinch point within the recuperators and how recompression may be used to prevent heat transfer limitations. Results showed that the operation in the vicinity of the critical point did not significantly improve the 1st law efficiency of the simple Brayton cycle, except for when high pressures were considered, i.e., ∼25 MPa. Also, the results clearly confirmed that there is not a global set of optimal parameters or configuration for the cycles, but different optima for different objective functions. The authors also mentioned some other aspects that could be investigated as future studies, such as the cycles dynamic behaviors, economic analyses, use of different materials.

Ref. [6] used solar energy collected through evacuated tubes to supply thermal power to a $CO_2$ transcritical Rankine cycle, intending to provide both electricity and heat. Due to the lack of a turbine that could operate with the supercritical fluid, a throttle valve was used; hence, the prototype could not actually provide electricity, with the power produced being thermodynamically estimated. Then, Refs. [68, 69] theoretically and experimentally investigated a $CO_2$ solar-powered transcritical Rankine cycle using evacuated tubes to supply both heat and electricity. In the theoretical study, the average temperature of 180 °C was adopted and a throttle valve with 90% efficiency was used instead of a turbine. In the experimental prototype, the same cycle configuration was used with the same components, reaching a maximal temperature of 187 °C and 70% of collector efficiency. Furthermore, through the theoretical study, the annual efficiency of electricity and heat supply reached 11.4% and 36.2%, respectively, and it was pointed out that, when compared to other working fluids, $CO_2$ presented the best performance. In the experimental study, the efficiency of power generation ranged from 8.78% to 9.45%.

Regarding the transient simulation of solar-powered plants operating with conven-

tional working fluids, the available literature is extensive, e.g., Ref. [70] for molten salts and Refs. [71, 72] for synthetic oils. However, limited studies are verified when considering s-$CO_2$ as working fluid. Hence, within the transient analysis of Brayton power cycles using such an HTF, Refs. [73, 74] conducted computational simulations with Dymola [75] while considering a cylinder-parabolic solar collector and disregarding TES systems. The authors studied the influence of volumetric ratios between the high-end and low-end pressure sides on the cycle transient performance to identify possible control strategies. Such volumetric ratios are associated with the heat source, demand to be met, cycle configuration, and components. The analyses provided a broad idea of the influence of the system dimensions and components on its transient behavior. Also, it was shown that larger volumetric ratios decrease the response time with respect to solar radiation fluctuations, which results in smaller changes to the variables affecting the performance and, consequentially, stabler power production. On the other hand, small volumetric ratios could lead to excessively high temperatures at the turbine inlet due to the low mass flow rates. It was found that the definition of a suitable control strategy for the $CO_2$ mass flow rate and a volumetric ratio larger than 1 can stabilize the turbine inlet temperature. Moreover, Ref. [76], continuing the previous studies, investigated a $CO_2$ mass flow rate control strategy, which maximizes the power produced by maintaining the turbine inlet temperature and pressure close to their design values, regardless of the ambient conditions. However, it is noteworthy that experimental validation for this control scheme was not provided. Moreover, Ref. [77] studied the transient behavior of a $CO_2$-based cycle powered with exhaust gases of internal combustion engines.

Concerning the influence of TES systems on the transient behavior of power cycles, Ref. [78] experimentally evaluated the behavior of a solar collector coupled to sensible and latent TES systems. Then, Ref. [79] focused on establishing design and coupling guidelines of concrete TES systems for solar-powered cycles. The number of works considering TES systems operating with supercritical fluids is somewhat limited. For instance, Ref. [80] fundamentally explored the potential of several supercritical fluids as thermal storage media, while investigating the effects of their properties variations near to their critical points, with no distinction for the TES technology to be applied. Specifically, focusing

on s-$CO_2$ as HTF, most of the studies are limited to investigate the power production effects, such as analyzing global control strategies [81], the transient behavior under specific operational conditions, e.g., Refs. [82, 83], and the performance of different power cycle configurations, e.g., Ref. [84]. Ref. [85] recommended using two-tank systems for solar plants operating with s-$CO_2$. Considering that more economical options are under development, the authors emphasized that the system costs are still high and that the temperature limit for the stability of the molten salts used (i.e., $\sim$ 600 °C) is the main weakness of this technology. Ref. [86] integrated a thermochemical energy storage to CSP plants having $CO_2$ as working fluid. Ref. [87] used different TES units considering $CO_2$ as HTF for storing either sensible or latent energy. Also, the short- and long-term behavior of a non-stratified two-tank molten salt TES for s-$CO_2$-based power plants was investigated in Ref. [88].

Still regarding TES devices working with s-$CO_2$, but now specifically considering the packed-bed technology, although only a couple of studies have actually focused on evaluating the efficiency of those devices, the current literature provides some insight into their use for solar-powered plants. Ref. [34] suggested that the packed-bed technology is technically feasible to store energy in a CSP plant running with s-$CO_2$. However, given that the cost is a major bottleneck of this technology due to the high operational pressures considered, the authors recommended the use of two-tank systems. Then, a simple thermodynamic and parametric investigation was conducted by Ref. [89] considering a solar-powered s-$CO_2$ Brayton cycle coupled to a TES device composed of granite spheres. The results obtained demonstrated the technical feasibility of s-$CO_2$ as working fluid as well as that the introduction of a TES device to the system may improve its efficiency by damping the effects of solar radiation fluctuations. According to the authors, the results established guidelines for experimental studies and system optimization.

Moreover, Ref. [90] reported an numerical analysis on the operation of a packed-bed TES device using s-$CO_2$ for CSP application – the simulations considered fixed parameters of design and operation. The study briefly discussed aspects related to size, thermal front within the bed, thermal losses, and cyclic behavior. Then, based on Ref. [90], Ref. [91] considered a higher operation temperature range for the packed-bed device, compared one-

and two-equation approaches for the porous medium modeling, discussed cyclic behavior and inefficiencies, all these under an exergetic standpoint. Once again, the design and operation parameters were held constant and a steady-state approach was used for dealing with the thermal losses to the environment. Recently, building upon Ref. [92], Ref. [93] explored a high-temperature and fixed-geometry hybrid TES device composed of packed-bed and phase change material (PCM) while operating with a fixed internal pressure of 25 MPa and either dry air or s-$CO_2$ as HTF. The study established a comparative analysis between the performance of the TES device using those HTFs in terms of the amounts of thermal energy stored/released, discharging time, thermal power transferred, and different amounts of PCM within the TES device. Furthermore, Ref. [94] performed two-fluid simulations with fluidized and a fixed-bed exergy recovery systems using alumina-based particles and s-$CO_2$ as HTF for analyzing their technical feasibility considering CSP plants. In summary, the available literature on packed-bed TES devices with s-$CO_2$ must be extended while including details about the influence of design and operational parameters on their efficiency.

Now, with respect to economic aspects, Ref. [95] considered CSP as the heat source for various s-$CO_2$ Brayton cycle configurations and studied both their cost and performance trade-offs. Also, for solar-powered plants using central receivers with s-$CO_2$ power blocks, Ref. [96] presented a techno-economic analysis for determining the cost and performance of the system components. Then, Ref. [97] coupled a packed-bed TES device with a CSP plant and used air within the solar field and TES while s-$CO_2$ within the power block – it was argued that the cost for using s-$CO_2$ within the TES would be prohibitive due to the thick pressure vessels required to contain the fluid at the high-pressures and temperatures required. The study presented a time-dependent methodology for the plant simulation and an economic model to evaluate its economic viability. The authors concluded that such a system may lead to improved thermo-economic performance regarding the molten salts-driven designs as well as that plant improvements may reduce the electricity cost. Moreover, Ref. [98] evaluated $CO_2$ mixtures for reducing the cost of the electricity produced by solar-powered plants using tower receivers. Recently, Ref. [99] presented a techno-economic assessment of a s-$CO_2$ CSP plant using a sodium-based receiver and a TES system.

# 3 TRANSIENT ANALYSIS AND OPTIMIZATION OF A RECUPERATIVE SUPERCRITICAL $CO_2$ BRAYTON CYCLE ASSISTED BY SOLID TES AND MASS STORAGE SYSTEMS

Based on the limited number of studies dealing with key aspects of transient power cycles [77], this chapter presents a transient model of a recuperative s-$CO_2$ Brayton cycle, which is indirectly heated by an HTF, whose temperature profile along the day mimics that of a hybrid power plant using an idealized solar radiation flux input on top of a constant baseline heat input. The cycle model includes TES and mass storage systems in addition to the five basic components of recuperative Brayton cycles, i.e., turbine, compressor, heater, cooler, and recuperator. The TES device is considered for extending the power delivered by the cycle beyond the idealized solar radiation availability hours. By varying its internal volume depending on the thermal energy input, the mass storage, which is modeled as a piston-cylinder apparatus, regulates the $CO_2$ mass flow rate through the cycle and, consequently, the pressure levels. In that way, this study adds to the purely parametrically-optimization-based literature, which is mostly composed of steady-state works, by focusing on the relevance of transient response analysis. The results show the importance of the TES device (including its charging and discharging processes), its influence on the system overall transient behavior, as well as the influence of its construction parameters (i.e., length, external diameter, and number of tubes) on its performance. Also, discussions on control strategy, thermophysical properties of the TES material, and the mass storage system are presented.

## 3.1 METHODOLOGY AND MODELING

This section comprehends seven subsections. First, Subs. 3.1.1 explores the system modeling and Subs. 3.1.2 its main routine. Then, Subs. 3.1.3, 3.1.4, and 3.1.5 present the specific modeling of the heat exchanger, the thermal energy storage (TES) system, and the mass storage device, respectively. Next, Subs. 3.1.6 shows the heat transfer correlations used and Subs. 3.1.7 discusses the modeling verification.

### 3.1.1 System modeling

The recuperative Brayton cycle considered is shown in Fig. 3, which is composed of: heater (He), recuperator (R), cooler (Co), turbine (T), compressor (C), plus mass storage (MS) and thermal energy storage (TES) systems. Note that, while the cycle uses $CO_2$ as working fluid, this is heated by Therminol VP1 (the HTF) and cooled with water.

Figure 3 – Recuperative Brayton cycle coupled to a solid TES system.

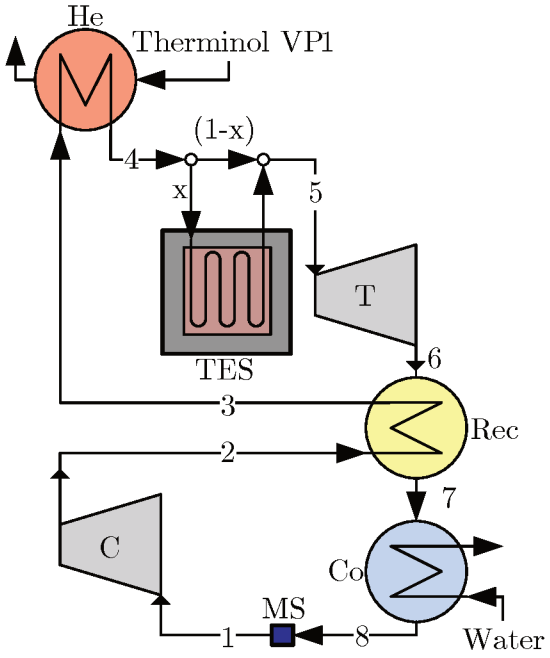


The hybrid aspect of the cycle is associated with the temperature profile imposed to the HTF at heater inlet, which is represented by the summation of two terms: a constant baseline and a time-dependent component – the latter represents an idealized solar input [100, 101] while the former may be seen as an auxiliary fossil heat source. During the 24 h of each day, the heat source provides a fixed mass flow rate of HTF of $\dot{m}^{\mathrm{In}}_{\mathrm{HSo}} = 0.0983$ kg/s, whose temperature baseline value is fixed at 200 °C. Following an idealized solar radiation heat flux-like profile, the heat source time-dependent component, then, increases such an inlet temperature from the baseline up to a maximum of 400 °C for 12 h each day while the inlet mass flow rate remains at its fixed value. Consequently, the $CO_2$ temperature is ramped up for a 6 h-period from baseline to maximum and ramped down for another 6 h-period from maximum back to baseline. The expression considered in this study for the aforementioned idealized Therminol VP1 temperature at the heater

inlet (i.e., $T_{\mathrm{HSo}}^{\mathrm{In}}$), for the 24 h-period, is

$$T_{\mathrm{HSo}}^{\mathrm{In}} = \begin{cases} 200\left[1+\sin\left(\frac{\pi\ t}{43200}\right)\right] \text{ for } 0 \leqslant t \leqslant 43200 \text{ s (i.e., 12 h)} \\ 200 \text{ for } 43200 \text{ s (i.e., 12 h)} < t < 86400 \text{ s (i.e., 24 h)} \end{cases}, \tag{3.1}$$

where $t$ is the time in seconds.

In the other end of the cycle, water is used as heat sink in the cooler with a fixed inlet temperature of $T_{\mathrm{HSi}}^{\mathrm{In}} = 20$ °C and a variable inlet mass flow rate, which is determined by energy and mass balances such that the $CO_2$ temperature entering the compressor is constantly maintained at $T_1 = 32$ °C – this is the $CO_2$ minimal temperature within the cycle and $\sim 1$ °C higher than its critical temperature ($T_{\mathrm{Crit}} \sim 31$ °C).

Because the model computes both the $CO_2$ time-dependent thermal inertia and mass variation, the $CO_2$ mass inventory must be accounted for all the cycle components – given that the actual plant layout is unknown, the modeling of the pipes connecting such components was disregarded. The cycle is assumed to operate between fixed high- and low-end pressures of $P_{\mathrm{High}} = 15$ MPa and $P_{\mathrm{Low}} = 8$ MPa, respectively, which agree, range wise, with values reported in the literature – note that the $CO_2$ pressure drop as it flows through/between the cycle components is not considered in the calculations. To stabilize the $CO_2$ pressure variations while the HTF temperature varies along the day, a mass storage device, located between the cooler and the compressor, is employed.

Defining the mass flow rate at the compressor inlet (i.e., at the mass storage outlet) as an operational parameter and considering it as having a fixed value of 0.1 kg/s, an initial inventory of $CO_2$ of $\sim 6.36$ kg in the mass storage was determined through a preliminary analysis for allowing the apparatus to absorb and/or release enough mass during the regular system operation, thus damping mass flow rate variations caused by thermodynamic changes within the cycle components. Then and also by controlling $T_1$, it is possible to maintain the compressor inlet condition stable and close to the $CO_2$ thermodynamic critical point, thus decreasing the required compression power by taking advantage of the $CO_2$ decreased compressibility factor [67]. Also, by controlling the compressor inlet mass flow rate, the mass storage is able to control the cycle pressure levels. Additionally, despite the transient nature of the study, zero-dimensional steady-state models are employed

for the turbomachinery due to their faster transient behavior in comparison to that of the heat exchangers. Also, both the turbine and compressor are modeled as having fixed isentropic efficiencies of $\eta_{\mathrm{T}} = \eta_{\mathrm{C}} = 0.8$. It is important to mention that, even though actual turbomachinery specifically designed for s-$CO_2$ applications are not available, the efficiency values chosen may be seen as representative averages of those employed in simulations available in the literature, e.g., Refs. [5, 14, 65, 89].

Therefore, considering the above-mentioned initial parameters, all simulations start with the cycle running with the 200 °C HTF baseline temperature while fully coupled to the TES system for allowing an initial steady-state regime to be reached. One should notice that the cycle only reaches the design net power output of 1 kW when the initial steady-state is reached – recall that the study only computes and reports net power outputs equal to or larger than 1 kW, which serves as a reference value, thus allowing results (e.g., TES contribution) to be interpreted as per kW unit [102]. An important aspect associated with this initial condition is that the temperature of the TES system is equal to the $CO_2$ temperature exiting the heater at the initial steady state for all simulations; hence, providing the same starting point for all analyses and, consequently, fair comparison conditions, independently of the TES system configuration. Next, with the time-dependent component of the heat source activated, but without relying on the TES device, the net power produced varies according to the heat source inlet temperature. Then, analyzing the response obtained after preliminary tests, a constant design net power demand of 2 kW was stipulated, which is the double of the reference baseline output and roughly 55% of the possible maximal net power produced. Therefore, with the coupling of a TES and an active control strategy, the routine sets the $CO_2$ mass flow rate fraction going through the TES device, i.e., $x$, aiming to minimize the difference between net power produced and the stipulated demand at each time step. This is possible because the fraction of the mass flow rate going through the TES device is then mixed with the remaining $CO_2$ flow, i.e, $1 - x$, thus controlling the turbine inlet temperature and, therefore, the net power produced.

Furthermore, as will be shown later in Sec. 3.2, the system transient response does not vary only throughout the day, but also from day to day, i.e., a several-days transient regime will be identified. Therefore, the analyses were performed on the tenth day for

allowing the cycle to reach a periodic representative operational pattern. To quantitatively evaluate the effect of the TES system on the cycle performance, an improvement index $\delta$ was taken as the figure of merit, which represents the surplus percentage of the cycle net power produced $\left(\dot{W}_{\mathrm{Net}}\right)$ throughout the tenth day with respect to the net power produced by the decoupled cycle $\left(\dot{W}_{\mathrm{Net}}^{\mathrm{Dec}}\right)$ (i.e., without TES device) throughout a day. Therefore, the improvement index can be defined as

$$\delta = 100\ \frac{\left(\dot{W}_{\mathrm{Net}} - \dot{W}_{\mathrm{Net}}^{\mathrm{Dec}}\right)}{\dot{W}_{\mathrm{Net}}^{\mathrm{Dec}}}, \tag{3.2}$$

with

$$\dot{W}_{\mathrm{Net}} = \begin{cases} \dot{W}_{\mathrm{T}} - \dot{W}_{\mathrm{C}} + \dot{W}_{\mathrm{MS}} \text{ if } \dot{W}_{\mathrm{T}} - \dot{W}_{\mathrm{C}} + \dot{W}_{\mathrm{MS}} \leqslant 2 \text{ kW} \\ 2 \text{ kW if } \dot{W}_{\mathrm{T}} - \dot{W}_{\mathrm{C}} + \dot{W}_{\mathrm{MS}} > 2 \text{ kW} \end{cases}, \tag{3.3}$$

where $\dot{W}_{\mathrm{T}}$ is the power produced by the turbine, $\dot{W}_{\mathrm{C}}$ is the power consumed by the compressor, and $\dot{W}_{\mathrm{MS}}$ is the power associated with the mass storage, which will be defined in Subs. 3.1.5. One should note that the 2 kW limitation presented in Eq. 3.3 refers to the specified constant demand value while any surplus is not accounted for. Additionally, a time step of $\Delta t = 600$ s was adopted as result of time-independence analyses regarding the percentage variation of the improvement index $\delta$.

Concerning the definition of $\delta$, it becomes clear that the ultimate goal of the present TES system is to explore the transient behavior of the modeled cycle, while attending the 2 kW demand for the widest time span possible, by optimally redistributing the exceeding thermal energy obtained from the 12 h per day transient heat source. With that in mind, three main parameters of the solid TES system were selected as optimization variables, as further discussed in Subs. 3.1.4.

Therefore, considering the complexity of the time-dependent thermal transport within the cycle due to the use of an unsteady heat source, home-made numerical transient finite volume-based models for the heat exchangers and for the TES device were specifically developed aiming to not only account for the $CO_2$ thermophysical properties variations [16, 103], but also for enabling transient and integrated responses of these key subsystems.

Furthermore, all numerical routines were written in MATLAB® [104] with thermophysical properties for $CO_2$ and water obtained from CoolProp [3, 4], and for Therminol VP1 from EES [105]. Moreover, the cycle itself was modeled by using the traditional formulation presented by references in thermodynamics, e.g., Ref. [106, 107]. Such a modeling includes mass and energy balances, observes the 2nd law of thermodynamics, and considers control volumes around each of the cycle components.

### 3.1.2 Main routine

Fig. 4 shows a general flowchart of the main numerical routine implemented for the entire cycle. The calculations begin by specifying the main inputs, e.g., geometries, materials, operational parameters, boundary conditions, thus allowing the cycle to run with the baseline value of the heat source inlet temperature until an initial steady state is reached (i.e., the TES system reaches thermal equilibrium with the $CO_2$ flow exiting the heater), which is common to all simulations.

Next, the routine advances a time step and each thermodynamic state evolves: State #1 (the compressor inlet) is defined in terms of $P$=$P_{\text{Low}}$ and $T_1 = 32$ °C; knowing that $\eta_{\text{C}} = 0.8$, State #2 (the compressor outlet) is defined in terms of $P = P_{\text{High}}$ and i=$f(P_{\text{High}}, \eta_{\text{C}}, s_1, i_1)$; running the transient model for the recuperator (Sub. 3.1.3), State #3 (the heater inlet) is defined based on the inputs of State #6 from the previous time step as an initial guess. The routine then enters the first loop, which is indicated with a light blue background and marked #1 in Fig. 4.

With the model for the heater (Sub. 3.1.3), State #4 (the heater outlet) is defined and State #5 (the turbine inlet) is set as equal to State #4 since the cycle is initially considered as decoupled from the TES system for the current time step. Using $\eta_{\text{T}} = 0.8$, State #6 (the turbine outlet) is defined in terms of $P = P_{\text{Low}}$ and $i = f(P_{\text{Low}}, \eta_{\text{T}}, s_5, i_5)$. With the updated State #6, the recuperator model runs again and an updated State #3 is achieved. Therefore, this process runs iteratively until the respective maximal variation of $T_3$, $T_4 = T_5$ and $T_6$ between each iteration is smaller than 0.01 °C. While this loop may seem unnecessary at first, its importance is associated with the reduction of the time required to run each time step, as better guesses are provided for the following steps of

Figure 4 – Main routine flowchart.

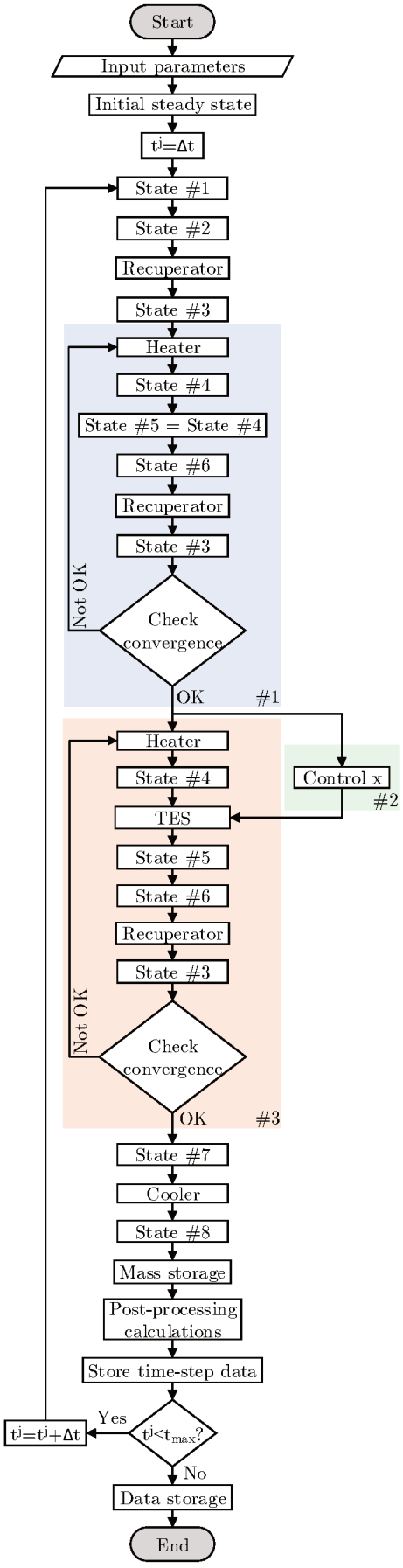

the transient simulation.

Next, the second loop, which is indicated with a light green background and marked #2 in Fig. 4, controls the mass fraction $x$, i.e., the $CO_2$ mass flow rate fraction directed towards the TES system after going through the heater – note that $0.001 < x \leq 1$, with $x$ always greater than zero because the model of the TES device cannot handle pure thermal diffusion. The $x$-fraction control is performed with a specific routine, which uses second-order Lagrange interpolating polynomials in a bisection-like minimization method. The process always starts by evaluating $x = 0.001$, $x = 0.5$, and $x = 1$, which serve as references for control decisions. For each given $x$, an inner routine is called to calculate the deviation between the net power produced and the demand. Because at the beginning of the first day the TES system is unable to supply sufficient energy to the fluid, the control indicates $x = 0.001$; however, when the demand is met, the control routine starts to increase $x$ (always limited to a maximal $x = 1$) so thermal power is directed to the TES system while the net power production equals the demand. As the day evolves and the heat source temperature decreases, the flow control continuously analyzes the opportunity of retrieving energy from the TES system so the demand is met as smoothly and constantly as possible. Within days, with the active control, a periodic representative operational pattern is achieved, as will be shown later on. The above-mentioned inner routine starts using State #3 and the heater model to define State #4, as previously stated; then, the model of the TES device is called and, for a given $x$, the model recalculates the $CO_2$ temperature and mass flow rate and the temperature distribution of the TES device. The $CO_2$ temperature and mass flow rate exiting the TES system are used to define State #5 based on $P = P_{\text{High}}$ and the mixture mass-specific enthalpy as

$$i_5 = \frac{\left[(1-x) i_4 \dot{m}_4 + i_{\text{TES}}^{\text{Out}} \dot{m}_{\text{TES}}^{\text{Out}}\right]}{\left[(1-x)\dot{m}_4 + \dot{m}_{\text{TES}}^{\text{Out}}\right]}, \tag{3.4}$$

which is readily obtained through mass and energy balances. Then, States #3 and #6 are defined as previously stated and this loop runs until the maximal respective variation of $T_3$, $T_4$, $T_5$, and $T_6$ between iterations becomes smaller than 0.01 °C. The bisection-like method dictates the new values of $x$ to be evaluated based on the second-order Lagrange interpolation until a deviation smaller than 1% of the demand is achieved between the net

power produced and the demand, for the given time step.

The third and last loop, which is indicated with a light red background and marked #3 in Fig. 4, follows the same steps of the inner routine of the second loop, but takes the controlled $x$ as input and defines States #3, #4, #5, and #6. State #7, the cooler inlet, is defined through the recuperator model. Next, the cooler model is coupled to the mass storage model to calculate the required water mass flow rate to maintain $T_1$ constant with the fixed $\dot{m}_1$. State #8, the cooler outlet, is defined by the cooler model and, then, the mass storage model is called.

The routine proceeds to post-processing calculations, e.g., thermal power transferred and power produced and consumed, and data storage. If the time at the current step $j$ (i.e., $t^{\mathrm{j}}$) is smaller than the maximal established time, it is updated as

$$t^{\mathrm{j}} = t^{\mathrm{j}} + \Delta t \tag{3.5}$$

and routine restarts at State #1; otherwise, the final data are stored and the routine ends.

Furthermore, it is worth mentioning that the procedure just described is executed to each set of optimization parameters. Therefore, for each set of parameters, the entire routine must run in order to enable the system optimization.

### 3.1.3 Heat exchanger

The heater, the recuperator, and the cooler were modeled as perfectly externally insulated counter-flow concentric circular tube-in-tube heat exchangers, which are comprised of an external annulus, an internal tube, and a thin solid wall separating both fluid streams. The homemade, one-dimensional, finite volume-based developed model disregards pressure drops for both streams (i.e., each fluid pressure is considered to be constant) and considers the fluids as always outside the saturation region – therefore $T = f(i)|_{\mathrm{P}} \leftrightarrow i = f^{-1}(T)|_{\mathrm{P}}$. Also, plug flow is assumed and axial discretization is employed aiming to consider the effects of thermophysical properties variations as well as to allow the average heat transfer coefficients ($\bar{h}$) to be calculated at each section individually. The geometric features, such as lengths, diameters (internal and external), and wall thickness are set and kept constant for each heat exchanger.

The numerical model, then, comprises three main domains, i.e., one for each fluid and another for the wall between them. For each fluid domain, the energy conservation is given by Eq. A.23 of Appx. A. Thus, for both fluid domains, by neglecting the influence of pressure variation ($DP/Dt$), the fluid energy equation yields

$$\int_t \int_V \frac{\partial (\rho i)}{\partial t} \, dV dt + \int_t \int_S (\rho \vec{u} i) \cdot \hat{n} \, dS dt = \int_t \int_S \left( k \vec{\nabla} T \right) \cdot \hat{n} \, dS dt. \tag{3.6}$$

At each axial section (node), the numerical domain considers three temperatures: a respective temperature for each stream (i.e., hot and cold) and an intermediate temperature for the wall. It is assumed that the hot stream flows from LHS to RHS and the cold stream from RHS to LHS. Then, using the node nomenclature presented by Ref. [108], UDS (Upwind Difference Scheme) for the advection within the fluid flows – so $i_{\mathrm{w}} = i_{\mathrm{W}}$ and $i_{\mathrm{e}} = i_{\mathrm{P}}$ for the hot fluid and $i_{\mathrm{w}} = i_{\mathrm{P}}$ and $i_{\mathrm{e}} = i_{\mathrm{E}}$ for the cold fluid –, implicitly evaluating the temporal term and thermophysical properties, and considering only the convective heat transfer between fluid flow and wall for the term on the RHS of Eq. 3.6 – axial diffusion is neglected due to the high $Pe$ –, it yields for the hot and cold streams, respectively,

$$\begin{aligned} V^{\mathrm{H}}_{\mathrm{F,P}} \left( \rho^{\mathrm{H}}_{\mathrm{F,P}} i^{\mathrm{H}}_{\mathrm{F,P}} - \rho^{\mathrm{H,0}}_{\mathrm{F,P}} i^{\mathrm{H,0}}_{\mathrm{F,P}} \right) + \left( \dot{m}^{\mathrm{H}}_{\mathrm{F,e}} i^{\mathrm{H}}_{\mathrm{F,e}} - \dot{m}^{\mathrm{H}}_{\mathrm{F,w}} i^{\mathrm{H}}_{\mathrm{F,w}} \right) \Delta t = \\ h^{\mathrm{H}}_{\mathrm{P}} A^{\mathrm{H}}_{\mathrm{F,P}} \left( T_{\mathrm{Wall,P}} - T^{\mathrm{H}}_{\mathrm{F,P}} \right) \Delta t, \end{aligned} \tag{3.7}$$

$$\begin{aligned} V^{\mathrm{C}}_{\mathrm{F,P}} \left( \rho^{\mathrm{C}}_{\mathrm{F,P}} i^{\mathrm{C}}_{\mathrm{F,P}} - \rho^{\mathrm{C,0}}_{\mathrm{F,P}} i^{\mathrm{C,0}}_{\mathrm{F,P}} \right) + \left( \dot{m}^{\mathrm{C}}_{\mathrm{F,w}} i^{\mathrm{C}}_{\mathrm{F,w}} - \dot{m}^{\mathrm{C}}_{\mathrm{F,e}} i^{\mathrm{C}}_{\mathrm{F,e}} \right) \Delta t = \\ h^{\mathrm{C}}_{\mathrm{P}} A^{\mathrm{C}}_{\mathrm{F,P}} \left( T_{\mathrm{Wall,P}} - T^{\mathrm{C}}_{\mathrm{F,P}} \right) \Delta t, \end{aligned} \tag{3.8}$$

where $V$ is the section volume, $\Delta t$ is the time step, $g$ is the coupling factor, $h$ is the convection heat transfer coefficient, $A$ is the section heat transfer area, and $\dot{m}$ is the mass flow rate. The the superscripts $H$ and $C$ refer to the hot and cold fluid streams, respectively; while, the subscripts $F$ and $Wall$ refer to fluid and wall, respectively.

From inspection of Eqs. 3.7 and 3.8, it is clear that they depend simultaneously on both the fluid mass-specific enthalpy and temperature. From a numerical standpoint, having such a simultaneous dependency increases the solution complexity due to the inter-dependency of these thermophysical properties during the solution. Hence, for obtaining

an easier-to-solve system of equations, the temperature-enthalpy coupling factor, for a node $P$ and an iteration $b$, which is given by

$$g_{\mathrm{P}}^{\mathrm{b}} = \frac{T_{\mathrm{F,P}}^{\mathrm{b\text{-}1}}}{i_{\mathrm{F,P}}^{\mathrm{b\text{-}1}}} \tag{3.9}$$

was employed so Eqs. 3.7 and 3.8 could be rewritten in terms of the fluid mass-specific enthalpy only. This approach may be seen as a somewhat linearization process, hence the temperature-enthalpy coupling factor must be updated at each iteration. Consequentially, using the coupling factor $g_{\mathrm{P}}$ to replace the fluids temperatures by their mass-specific enthlapies as $T_{\mathrm{F,P}} = g_{\mathrm{P}} i_{\mathrm{F,P}}$ and dividing Eqs. 3.7 and 3.8 by the time step $\Delta t$, they yield

$$V_{\mathrm{F,P}}^{\mathrm{H}} \frac{\left(\rho_{\mathrm{F,P}}^{\mathrm{H}} i_{\mathrm{F,P}}^{\mathrm{H}} - \rho_{\mathrm{F,P}}^{\mathrm{H,0}} i_{\mathrm{F,P}}^{\mathrm{H,0}}\right)}{\Delta t} + \dot{m}_{\mathrm{F,e}}^{\mathrm{H}} i_{\mathrm{F,P}}^{\mathrm{H}} - \dot{m}_{\mathrm{F,w}}^{\mathrm{H}} i_{\mathrm{F,W}}^{\mathrm{H}} = h_{\mathrm{P}}^{\mathrm{H}} A_{\mathrm{F,P}}^{\mathrm{H}} \left(T_{\mathrm{Wall,P}} - g_{\mathrm{P}}^{\mathrm{H}} i_{\mathrm{F,P}}^{\mathrm{H}}\right), \tag{3.10}$$

$$V_{\mathrm{F,P}}^{\mathrm{C}} \frac{\left(\rho_{\mathrm{F,P}}^{\mathrm{C}} i_{\mathrm{F,P}}^{\mathrm{C}} - \rho_{\mathrm{F,P}}^{\mathrm{C,0}} i_{\mathrm{F,P}}^{\mathrm{C,0}}\right)}{\Delta t} + \dot{m}_{\mathrm{F,w}}^{\mathrm{C}} i_{\mathrm{F,w}}^{\mathrm{C}} - \dot{m}_{\mathrm{F,e}}^{\mathrm{C}} i_{\mathrm{F,e}}^{\mathrm{C}} = h_{\mathrm{P}}^{\mathrm{C}} A_{\mathrm{F,P}}^{\mathrm{C}} \left(T_{\mathrm{Wall,P}} - g_{\mathrm{P}}^{\mathrm{C}} i_{\mathrm{F,P}}^{\mathrm{C}}\right). \tag{3.11}$$

And solving Eqs. 3.10 and 3.11 for $i_{\mathrm{F,P}}^{\mathrm{H}}$ and $i_{\mathrm{F,P}}^{\mathrm{C}}$, respectively, the equations used are finally obtained as

$$\begin{aligned} i_{\mathrm{F,P}}^{\mathrm{H}} \left(\frac{\rho_{\mathrm{F,P}}^{\mathrm{H}} V_{\mathrm{F,P}}^{\mathrm{H}}}{\Delta t} + g_{\mathrm{P}}^{\mathrm{H}} h_{\mathrm{P}}^{\mathrm{H}} A_{\mathrm{F,P}}^{\mathrm{H}} + \dot{m}_{\mathrm{F,e}}^{\mathrm{H}}\right) - i_{\mathrm{F,W}}^{\mathrm{H}} \dot{m}_{\mathrm{F,w}}^{\mathrm{H}} = \\ h_{\mathrm{P}}^{\mathrm{H}} A_{\mathrm{F,P}}^{\mathrm{H}} T_{\mathrm{Wall,P}} + \left(\frac{\rho_{\mathrm{F,P}}^{\mathrm{H,0}} V_{\mathrm{F,P}}^{\mathrm{H}} i_{\mathrm{F,P}}^{\mathrm{H,0}}}{\Delta t}\right), \end{aligned} \tag{3.12}$$

$$\begin{aligned} i_{\mathrm{F,P}}^{\mathrm{C}} \left(\frac{\rho_{\mathrm{F,P}}^{\mathrm{C}} V_{\mathrm{F,P}}^{\mathrm{C}}}{\Delta t} + g_{\mathrm{P}}^{\mathrm{C}} h_{\mathrm{P}}^{\mathrm{C}} A_{\mathrm{F,P}}^{\mathrm{C}} + \dot{m}_{\mathrm{F,w}}^{\mathrm{C}}\right) - i_{\mathrm{F,E}}^{\mathrm{C}} \dot{m}_{\mathrm{F,e}}^{\mathrm{C}} = \\ h_{\mathrm{P}}^{\mathrm{C}} A_{\mathrm{F,P}}^{\mathrm{C}} T_{\mathrm{Wall,P}} + \left(\frac{\rho_{\mathrm{F,P}}^{\mathrm{C,0}} V_{\mathrm{F,P}}^{\mathrm{C}} i_{\mathrm{F,P}}^{\mathrm{C,0}}}{\Delta t}\right). \end{aligned} \tag{3.13}$$

For both streams, the inlet mass flow rate and temperature are given as boundary conditions at each time step. Also, the hot fluid is considered always in the external annulus and the cold fluid always in the internal tube.

Moreover, for the incompressible and resting solid wall with constant thermophysical properties, Eq. A.1 from Appx. A simplifies to [109]

$$\frac{\partial\left(\rho e\right)}{\partial t}=\vec{\nabla}\cdot\left(k\vec{\nabla}T\right). \tag{3.14}$$

Using $\partial e_{\text{Wall}}=c_{\text{Wall}}\partial T_{\text{Wall}}$ and integrating Eq. 3.14 over the solid volume and the time

$$\int_t\int_V\rho c\frac{\partial T}{\partial t}\;dVdt=\int_t\int_V\vec{\nabla}\cdot\left(k\vec{\nabla}T\right)\;dVdt, \tag{3.15}$$

and, using the divergence theorem on the RHS term of Eq. 3.15,

$$\int_t\int_V\rho c\frac{\partial T}{\partial t}\;dVdt=\int_t\int_S\left(k\vec{\nabla}T\right)\cdot\hat{n}\;dSdt, \tag{3.16}$$

which yields

$$\begin{aligned}\rho_{\text{P,Wall}}c_{\text{P,Wall}}V_{\text{P,Wall}}\left(T_{\text{P,Wall}}-T^{0}_{\text{P,Wall}}\right)=h^{\text{H}}_{\text{P}}A^{\text{H}}_{\text{F,P}}\left(T^{\text{H}}_{\text{F,P}}-T_{\text{Wall,P}}\right)\Delta t+\\ h^{\text{C}}_{\text{P}}A^{\text{C}}_{\text{F,P}}\left(T^{\text{C}}_{\text{F,P}}-T_{\text{Wall,P}}\right)\Delta t.\end{aligned} \tag{3.17}$$

Dividing Eq. 3.17 by the time step $\Delta t$ and solving it for $T_{\text{P,Wall}}$, the equation used is finally obtained as

$$\begin{aligned}T_{\text{Wall,P}}\left(\frac{\rho_{\text{Wall,P}}V_{\text{Wall,P}}c_{\text{Wall,P}}}{\Delta t}+h^{\text{H}}_{\text{P}}A^{\text{H}}_{\text{F,P}}+h^{\text{C}}_{\text{P}}A^{\text{C}}_{\text{F,P}}\right)\\ -i^{\text{H}}_{\text{F,P}}\left(g^{\text{H}}_{\text{P}}h^{\text{H}}_{\text{P}}A^{\text{H}}_{\text{F,P}}\right)-i^{\text{C}}_{\text{F,P}}\left(g^{\text{C}}_{\text{P}}h^{\text{C}}_{\text{P}}A^{\text{C}}_{\text{F,P}}\right)=\frac{\rho_{\text{Wall,P}}V_{\text{Wall,P}}c_{\text{Wall,P}}T^{0}_{\text{Wall,P}}}{\Delta t}.\end{aligned} \tag{3.18}$$

Initial temperature and mass flow rate distributions are provided from the previous time step, thermophysical properties are obtained as functions of $T$ and $P$. Then, the coefficients of Eqs. 3.12, 3.13, and 3.18 are obtained for both streams (i.e., hot and cold) and wall. Next, the system of equations is solved and the mass flow rate of each node $P$ is updated as

$$\dot{m}_{\text{F,P}}=\dot{m}_{\text{F,1}}-\sum_{k=1}^{j-1}\left[\frac{V_{\text{P}}\left(\rho_{\text{F,P}}-\rho^{0}_{\text{F,P}}\right)}{\Delta t}\right]_{\text{k}}, \tag{3.19}$$

With the new $T$ and $\dot{m}$ distributions obtained, the process is repeated until convergence is achieved for all quantities $\phi$, at each time step, with respect to the previous iteration ($\phi^{\text{j-1}}$), i.e.,

$$\epsilon = \frac{\left|\phi^{\text{j}} - \phi^{\text{j-1}}\right|}{\phi^{\text{j-1}}} < \epsilon_{\max}. \tag{3.20}$$

For convergence, it is required that $\epsilon < \epsilon_{\text{Max}}$ for $T$, $\rho$, and $\dot{m}$, where $\epsilon_{\text{Max}} = 10^{-4}$. Also, the overall heat exchange at each device is checked to ensure that the model respects the 1$^{\text{st}}$ law of thermodynamics, i.e.,

$$\sum \left(\dot{E}_{\text{In}} + \dot{E}_{\text{Out}} + \dot{E}_{\text{Sto}}\right) \leq 10^{-4} \text{ W}. \tag{3.21}$$

Finally, internal diameters of $D_{\text{Int}} = 25.4$ mm and 1.5 $D_{\text{Int}}$ were assumed for the inner tube and the annulus (outer tube), respectively. The wall thickness of 1.5 mm was estimated for sustaining the high-end pressure at the given tube diameter, which also leads to an identical cross-sectional area for both streams in the heat exchangers. Moreover, the lengths of these three devices were selected as $L_{\text{He}} = 10$ m, $L_{\text{Rec}} = 5$ m, and $L_{\text{Co}} = 15$ m, which were axially discretized in 30 sections of equal length. Such a discretization was shown to be sufficient for properly capturing the effect of thermophysical properties variations while also satisfactory in terms of mesh density. The properties for the steel wall were set as $\rho_{\text{st}} = 8055$ kg/m$^3$, $c_{\text{st}} = 480$ J/(kg $\cdot$ K), and $k_{\text{st}} = 15.1$ W/(m $\cdot$ K), according to values reported in Ref. [110].

### 3.1.4 Thermal energy storage (TES) system

The TES system, which is shown in the leftmost portion of Fig. 5, was modeled as a perfectly externally insulated concrete annulus that surrounds a thin-walled circular tube through which the s-$CO_2$ flows – concrete is considered as having constant properties throughout the entire temperature range considered in the present study. Any pressure drop was neglected (local and distributed), CDS (Central Difference Scheme) was used for temperature gradients at the interfaces, plug flow was assumed, and the domain was considered as axisymmetric, which allowed the modeling of the TES device to be simplified so a two-dimensional formulation could be used. Furthermore, the three main parameters

of the solid TES system selected as optimization variables, i.e., external diameter ($D_{\text{Ext}}$), length ($L$), and number of tubes ($N$) are indicated in Fig. 5 and will be further discussed in this subsection.

Figure 5 – Sketch of the solid TES system.

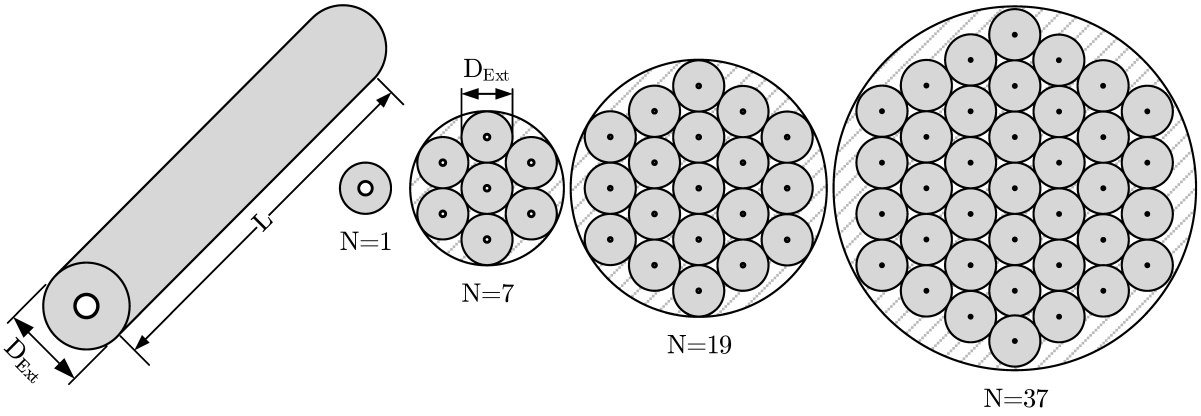


Considering the internal boundary condition due to convection, i.e.,

$$k_{\text{Wall}} \frac{\partial T_{\text{Wall}}}{\partial r}\bigg|_{r=D_{\text{Int}}/2} = h\left(T_{\text{Wall}} - T_{\text{F}}\right), \tag{3.22}$$

the energy equation for the internal volumes reads [108]

$$\begin{aligned} T_{\text{TES,P}}\left(\frac{\rho_{\text{TES,P}} V_{\text{TES,P}} c_{\text{TES,P}}}{\Delta t} + \psi_{\text{e}} + \psi_{\text{w}} + \psi_{\text{n}} + \psi_{\text{s}}\right) + \\ -\psi_{\text{e}} T_{\text{TES,E}} - \psi_{\text{w}} T_{\text{TES,W}} - \psi_{\text{n}} T_{\text{TES,N}} - \psi_{\text{s}} T_{\text{TES,S}} = \frac{\rho_{\text{TES,P}} V_{\text{TES,P}} c_{\text{TES,P}} T^{0}_{\text{TES,P}}}{\Delta t}, \end{aligned} \tag{3.23}$$

where $\psi$ represents coefficients whose generic expression is given by

$$\psi_{\alpha} = \frac{A_{TES,\alpha} k_{TES,\alpha}}{\Delta l_{TES,\alpha}}, \tag{3.24}$$

in which $\alpha$ refers to the nodes interfaces – i.e., $e$ for east, $w$ for west, $n$ for north, or $s$ for south –, $A$ to the interface area, $k$ to the interface thermal conductivity – which is calculated using a weighted harmonic mean –, and $\Delta l$ generically represents the distance between the subsequent nodes centers in a given direction.

Initial guesses for the wall temperature (the half-volume in contact with the fluid), the fluid mass flow rate, and temperature distribution are provided as well as the fluid inlet parameters (i.e., temperature and mass flow rate as boundary conditions). Then, the

coefficients of the equations are calculated and the system of equations for the fluid is solved so a new fluid temperature field is obtained and the fluid mass flow rate filed is updated, as shown in Eq. 3.19, for each section. The system of equations for the fluid is iteratively solved until convergence is achieved. With the temperature distribution of the TES device obtained, $T_{\text{Wall,P}}$ is recalculated and the process is repeated until convergence with respect to the previous iteration, as detailed in the Sub. 3.1.3.

Furthermore, the model requires input parameters for its construction materials and geometry. The properties for the steel wall were set like the ones used for the heat exchangers, and the properties for the concrete were set and kept constant as $\rho_{\text{TES}} = 2780$ kg/m$^3$, $c_{\text{TES}} = 700$ J/(kg $\cdot$ K), and $k_{\text{TES}} = 1.4$ W/(m $\cdot$ K), also according to values reported in Ref. [110] – the thermal conductivity of concrete will be relaxed later on in Fig. 18. The geometry parameters, as shown in Fig. 5, are intrinsically related to the optimization ones; therefore, four lengths of the TES device were evaluated, i.e., 1.0 m, 2.5 m, 5 m, and 10 m. Based on axial mesh analysis, for the axial length discretization, 40 elements were used. The wall thickness and the initial internal diameter of the tube were identical to the ones used in the heat exchangers. Next, by dividing the TES system into $N$ sub-TES devices (i.e., $N$ individual tubes surrounded by concrete) while maintaining the total flow cross-section area, as shown in Fig. 5, one is able to modify the total heat transfer area, the heat transfer coefficient, the type of flow (i.e., turbulent or laminar). For that, each TES tube internal diameter varies as

$$D_{\text{TES}} = \frac{D_{\text{Int}}}{\sqrt{N}}, \tag{3.25}$$

which ensures that the flow velocity is maintained constant. Four different values of $N$ were evaluated, i.e., 1, 7, 19, and 37 – being the three larger values obtained by dividing the initial tube into an equilateral triangle scheme. Also, note that the external diameter, which was varied from 10 mm to 400 mm, refers to the external diameter of the concrete annulus around every single tube and not the entire stack. Regardless of $N$, the wall thickness was always kept constant. As result of a mesh analysis, for the radial discretization, 3 elements were used for the steel wall and 10 elements were used for the concrete annulus.

### 3.1.5 Mass storage system

The mass storage was modeled as a perfectly externally insulated piston-cylinder apparatus. The device receives the s-$CO_2$ flow from the cooler and, by varying its volume while maintaining its moving face at $P = P_{\text{Low}}$ by using an active external device, it is capable of damping pressure variations. The mass and energy balances are given, respectively, by

$$\rho_{\text{F}} V_{\text{MS}} = \rho^{0}_{\text{F,P}} V^{0}_{\text{MS}} + \frac{\left(\dot{m}_{\text{F,In}} - \dot{m}_{\text{F,Out}}\right)}{\Delta t}, \tag{3.26}$$

$$\rho_{\text{F}} V_{\text{MS}} i_{\text{F}} = \rho^{0}_{\text{F}} V^{0}_{\text{MS}} i^{0}_{\text{F}} + \frac{\left(\dot{m}_{\text{F,In}} i_{\text{F,In}} - \dot{m}_{\text{F,Out}} i_{\text{F,Out}}\right)}{\Delta t}, \tag{3.27}$$

where the mass flow rate at the compressor inlet is fixed as $\dot{m}_{\text{F,P,Out}} = 0.1$ kg/s. Due to the mass storage volume variation, i.e., $\Delta V_{\text{MS}} = V_{\text{MS}} - V^{0}_{\text{MS}}$, there is an associated amount of power, i.e., $\dot{W}_{\text{MS}}$, which may be positive in case of expansion or negative otherwise. In this study, such a power is not accounted for in the net power produced in case of expansion, because it is not considered as useful for power generation; however, it is deducted from the net power produced in case of compression, because it is spent with the active external device. This relation is summarized by Eq. 3.28 as

$$\dot{W}_{\text{MS}} = \begin{cases} P_{\text{Low}}\ \Delta V_{\text{MS}}/\Delta t, \text{ if } \Delta V_{\text{MS}} \leqslant 0 \\ 0, \text{ if } \Delta V_{\text{MS}} > 0 \end{cases}, \tag{3.28}$$

### 3.1.6 Heat transfer correlations

For the convection heat transfer correlations, the mass flow rate at each section was considered as

$$\dot{m} = \rho_{\text{F}} u A_{\text{Trans}}, \tag{3.29}$$

and the fluid speed as

$$u \approx \overline{u} = \frac{0.5\left(\dot{m}_{\text{In}} + \dot{m}_{\text{Out}}\right)}{\rho A_{\text{Trans}}}. \tag{3.30}$$

The Reynolds number $Re_{\mathrm{D}}$ was evaluated based on the hydraulic diameter as

$$Re_{\mathrm{D}} \approx Re_{\mathrm{D_{Hyd}}} = \frac{\rho_{\mathrm{F}} u D_{\mathrm{Hyd}}}{\mu_{\mathrm{F}}} \approx \frac{\rho_{\mathrm{F}} \left[0.5\left(\dot{m}_{\mathrm{In}} + \dot{m}_{\mathrm{Out}}\right)\right] D_{\mathrm{Hyd}}}{\mu_{\mathrm{F}} A_{\mathrm{Trans}}}, \tag{3.31}$$

and the heat transfer coefficient was evaluated as

$$h = \frac{Nu_{\mathrm{D}} k}{D_{\mathrm{Hyd}}}. \tag{3.32}$$

Also, the hydraulic diameter is given as

$$D_{\mathrm{Hyd}} = \frac{4A_{\mathrm{Trans}}}{p}, \tag{3.33}$$

where $p$ is the wet perimeter.

Three convection heat transfer correlations were adopted for the s-$CO_2$ flows, i.e., two for turbulent flow and one for laminar flow. For the turbulent s-$CO_2$ heating process, the Jackson et al.'s correlation [111] was employed as

$$Nu_{\mathrm{D}} = 0.0183\ Re_{\mathrm{D}}^{0.82}\ \overline{Pr}^{0.5} \left(\frac{\rho_{\mathrm{Wall}}}{\rho_{\mathrm{F}}}\right)^{0.3}, \tag{3.34}$$

for which $\bar{Pr} = (\bar{c}\mu)/k$ is the average Prandtl number (considering the average $\bar{c}_{\mathrm{F}} = \Delta i_{\mathrm{F}}/\Delta T_{\mathrm{F}}$), and $\rho_{\mathrm{F}}$ and $\rho_{\mathrm{Wall}}$ are the s-$CO_2$ volume-specific masses evaluated at bulk and wall temperature, respectively.

Also for turbulent flow, but now considering the cooling of s-$CO_2$, the Petrov and Popov's correlation [112] was employed as

$$Nu_{\mathrm{D}} = \frac{\left(f\ Re_{\mathrm{D}}\ \overline{Pr}\right)/8}{1.07 + 12.7\sqrt{\frac{f}{8}}\left[Pr^{2/3}\sqrt{\frac{\rho_{\mathrm{Wall}}}{\rho}}\left(1 - 0.9\sqrt{\frac{|f_{\mathrm{ac}}|}{f}}\right)\left(1 - 1.0\sqrt{\frac{|f_{\mathrm{ac}}|}{f}}\right)\right]}, \tag{3.35}$$

for which

$$f = \left(\frac{\mu_{\mathrm{Wall}}}{\mu_{\mathrm{F}}}\right)^{1/4} e + 0.17\left(\frac{\rho_{\mathrm{Wall}}}{\rho_{\mathrm{F}}}\right)^{1/3} |f_{\mathrm{ac}}|, \tag{3.36}$$

and

$$f_{\mathrm{ac}} \approx 2D_{\mathrm{Hyd}}\rho_{\mathrm{F}}\ \frac{\partial}{\partial z}\left(\frac{1}{\rho_{\mathrm{F}}}\right), \tag{3.37}$$

with $\overline{Pr}$ and $\bar{c}$ as described for Equation 3.34. The friction factor $e$ is calculated using the Filonenko's correlation [112] for smooth tubes as

$$e = \left[0.79 \ln\left(Re_{\mathrm{D}}\right) - 1.64\right]^{-2}. \tag{3.38}$$

Moreover, for the laminar flow of s-$CO_2$, regardless of whether for heating or cooling process, it was simply employed that $Nu = 3.66$ [109].

Furthermore, for the HTF (i.e., Therminol VP1), the correlation presented in Ref. [113] was employed, which reads

$$Nu_{\mathrm{D}} = 0.025\ Re_{\mathrm{D}}^{0.79}\ Pr^{0.42} \left(\frac{\mu_{\mathrm{F}}}{\mu_{\mathrm{Wall}}}\right)^{0.11}, \tag{3.39}$$

where $Pr$ is the Prandtl number and $\mu$ and $\mu_{\mathrm{Wall}}$ are the dynamic viscosities evaluated at bulk and wall temperatures, respectively.

Finally, for the colling water, which goes to a heating process within the cooler, the Dittus-Boelter's correlation [114] was employed as

$$Nu_{\mathrm{D}} = 0.023\ {Re_{\mathrm{D}}}^{0.8}\ Pr^{0.4}. \tag{3.40}$$

### 3.1.7 Verification

Verifying a model against experimental data would be the best choice when regarding correctness itself. Now, if one considers the requirements for fully experimentally verifying the modeling presented, it becomes evident that it is not an easy task nor a plausible path to pursue for every thermodynamic modeling/analysis proposed. Furthermore, unfortunately, it was not possible to establish a direct comparison between the transient cycle modeling developed due to the lack of available applicable results in the literature – recall that one of the contributions of the present dissertation is associated with transient modeling of power cycles, which is a topic with a very limited literature, even more if considering s-$CO_2$ applications. However, it was possible to individually verify the modeling correctness of key components of the cycle through independent numerical solutions using Fluent® [115] – a widely recognized reliable software. For instance, the review on the state-of-the-art on heat transfer of s-$CO_2$ presented by Ref. [116] shows that

several studies have successfully compared experimental and numerical results considering the heat transfer process of s-$CO_2$ flowing through a tube – additionally, a dedicated subsection on simulation procedures using Fluent was presented, whose guidelines were followed in this verification procedure. Therefore, for verification purposes, both the heat exchanger and the TES models were individually compared to transient numerical simulations from Fluent while considering different pressures, temperatures, mass flow rates, and geometric parameters. It is worth mentioning that real fluid thermophysical properties for s-$CO_2$ were used. Also, because the entire study was conducted with $CO_2$ (i.e., the working fluid) always at supercritical state and both the Therminol VP1 and the water always at liquid state, no phase change processes were observed at any point of any simulation. Furthermore, the turbulence scheme chosen for the Fluent simulation was the $k-\varepsilon$, which is supported by the literature, e.g., Refs. [117, 118] – additionally, according to the review on the mechanisms responsible for the behavior of supercritical fluids in the pseudocritical temperature region performed by Ref. [119], roughly 50% of the papers reviewed by the authors, which were published between 1983 and 2008, employed such a turbulence model. Finally, because the present modeling disregards pressure drops, for the Fluent simulation, the working pressure selected is set as an outlet boundary.

To exemplify the comparisons performed, two representative cases were considered and whose results were obtained from Fluent simulations and from the present modeling after mesh independence analyses. First, for the heat exchanger, Fig. 6 presents the $CO_2$ temperature profile along the 5 m length of the hot side of a $CO_2$-$CO_2$ tube-in-tube heat exchanger with the internal diameters as those adopted throughout the study with a working pressure of 12 MPa and inlet mass flow rates of 1 kg/s for both streams. The inlet temperatures are considered constant at 500 K and 400 K for the hot and cold streams, respectively. Secondly, Fig. 7 shows the radial temperature profile at the axial position of 0.25 m from the stream inlet of a concrete TES device with $N = 1$, $L = 5$ m, and $D_{\text{Ext}} = 150$ mm at 15 s within the transient simulation considering an initial uniform temperature of 400 K for both the fluid and the solid domains. The $CO_2$ working pressure, the inlet temperature, and mass flow rate are set to 20 MPa, 500 K, and 1 kg/s, respectively.

Figure 6 – Hot stream axial temperature profile comparison between Fluent simulation and the developed model.

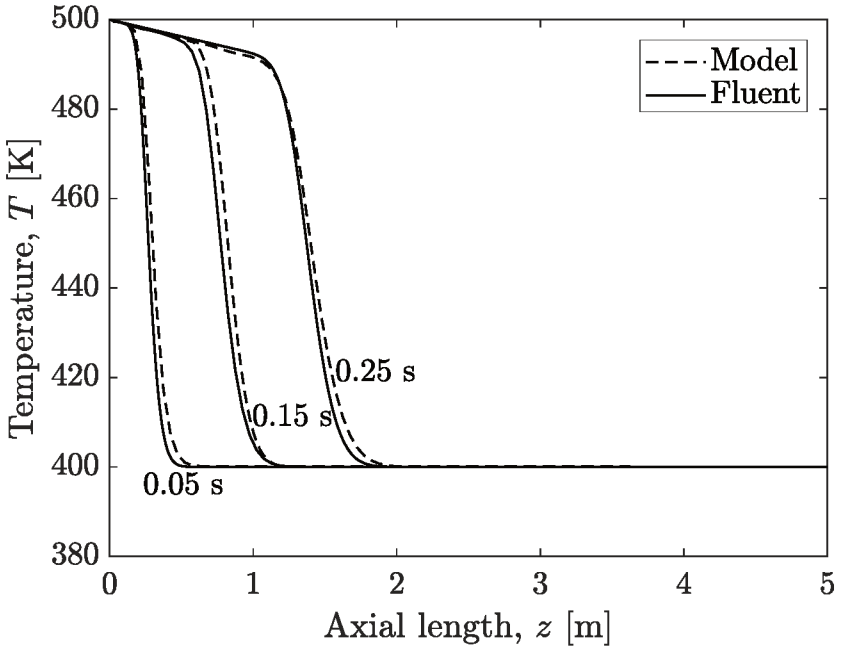


Figure 7 – Comparison between Fluent simulation and the developed model for the radial temperature profile of the TES device.

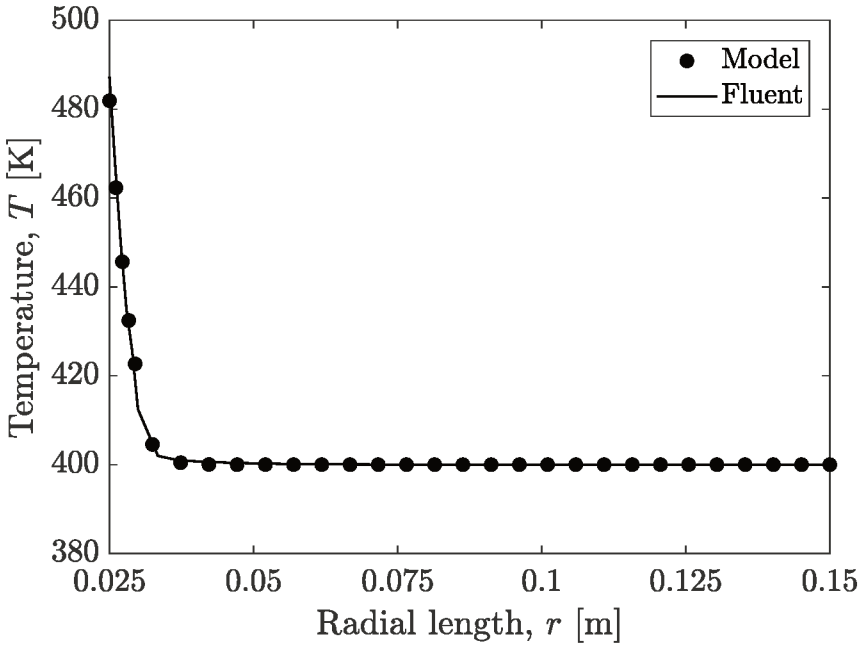

From a comparative analysis between the temperature profiles shown in Figs. 6 and 7, it was possible to infer the modeling correctness. Also, from the entire set of comparisons, it was possible to estimate a relative deviation of the developed modeling with respect to the Fluent simulations of $\sim 2\%$ or less. Finally, a series of checks were implemented throughout all models and components in terms of mass and energy balances as well as the 2$^{\text{nd}}$ law of thermodynamics to ensure the correct modeling implementation.

## 3.2 RESULTS

This section, which is divided into four subsections, explores the results obtained. First, Subs. 3.2.1 discusses the transient influence of the TES system on the power cycle. Then, Subs. 3.2.2 presents the results regarding the 1$^{\text{st}}$ law efficiency. Next, Subs. 3.2.3 explores the influence of the thermal conductivity of the TES medium. Finally, Subs. 3.2.4 discusses the influence on the overall system of the mass storage device and the complexity of the TES solution.

### 3.2.1 Transient influence of the TES system on the power cycle

Fig. 8 shows the ten-day behavior of the net power produced ($\dot{W}_{\text{Net}}$) for a TES configuration with $L = 5$ m and $N = 19$, and for three different values of the external diameter ($D_{\text{Ext}}$), i.e., 50 mm, 200 mm, and 300 mm – the gray shaded regions indicate the time periods in which the heat source temperature varies. Recalling that the inner diameter of the tubing going through the TES device is fixed, it may be realized that the larger $D_{\text{Ext}}$, the more TES material surrounds a given tube. As may be seen, for the 50 mm, $\dot{W}_{\text{Net}}$ seems to do not vary from day to day, which indicates a periodic pattern. Differently, the curves for 200 mm and 300 mm reveal a several-day transient, i.e., roughly 5 days for the former and 10 days for the latter. The behaviors presented are due to the different TES volumes and, therefore, time-scales related to the thermal response (or thermal inertia). For the 50 mm case, roughly all thermal energy stored during the initial 12 h period is withdrawn within the subsequent 12 h period, which may be verified since $\dot{W}_{\text{Net}} \rightarrow 1$ kW within the non-shaded regions, i.e., the power production consecutively returns to its baseline value. For the 200 mm case, the system is capable of storing all the excess thermal

energy during the first day (i.e., $\dot{W}_{\text{Net}} = 2$ kW), but it is not able to sustain the required thermal power delivery to meet the demand. The system response, then, evolves towards the second day when the TES device becomes saturated (i.e., $\dot{W}_{\text{Net}} > 2$ kW), so the power production surpasses the stipulated demand during the charge, but starts to meet the demand when operating in discharging mode. In comparison to the curve for 200 mm, for the 300 mm case, the behavior presented is somewhat similar during the charge, but with larger inertia (i.e., more time is required for the TES system to become saturated during charge), and also not being able to properly meet the demand during the discharge.

Figure 8 – Ten-day temporal behavior of $\dot{W}_{\text{Net}}$ for $L = 5$ m, $N = 19$, and three values of $D_{\text{Ext}}$.

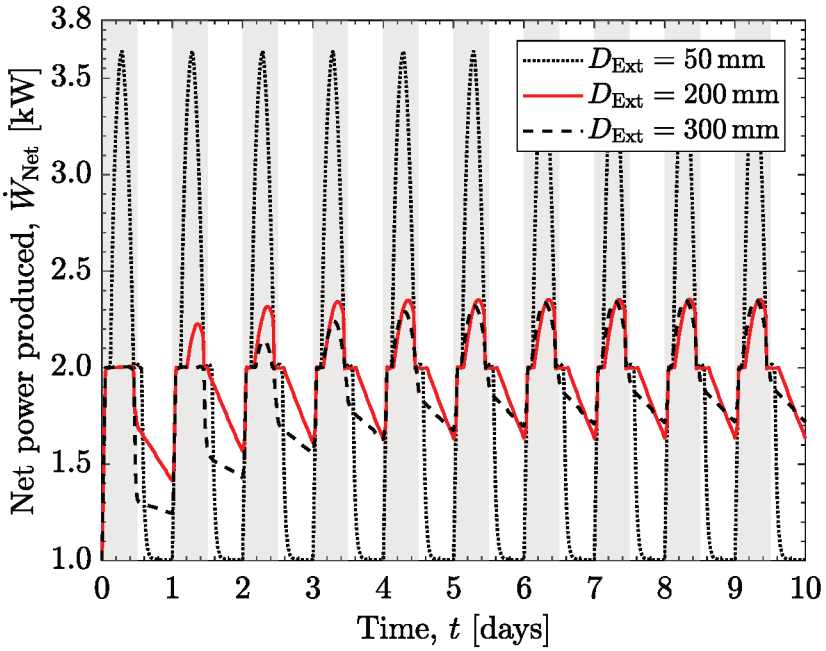


Now, focusing specifically on the 24 h of the tenth day, Fig. 9 shows in detail, on an hourly basis, the RHS of Fig. 8. As can be seen, the curve for 50 mm starts at 1 kW (circle), i.e., the baseline, then rapidly meets the demand (leftmost triangle), becomes thermally saturated (diamond) and achieves $\sim 3.6$ kW (star) while being able to control the net power produced for $\sim 1.5$ h during the charging process (i.e., between $\sim 1.3$ h and $\sim 2.8$ h on the x-axis). As the discharge begins (rightmost triangle) at $\sim 10.8$ h on the x-axis, the TES system is able to meet the demand for extra $\sim 2.5$ h (square), then returning to the baseline net power produced. Also, recalling the definition of $\delta$ from Eq. 3.2, though the curves for 200 mm and 300 mm present similar trends, a close analysis shows that the former achieves a higher $\delta$ because it controls the net power produced for

additional $\sim 1.3$ h during charge and $\sim 3.2$ h during discharge in comparison to the latter.

Figure 9 – Tenth day temporal behavior of $\dot{W}_{\text{Net}}$ for $L = 5$ m, $N = 19$, and three values of $D_{\text{Ext}}$.

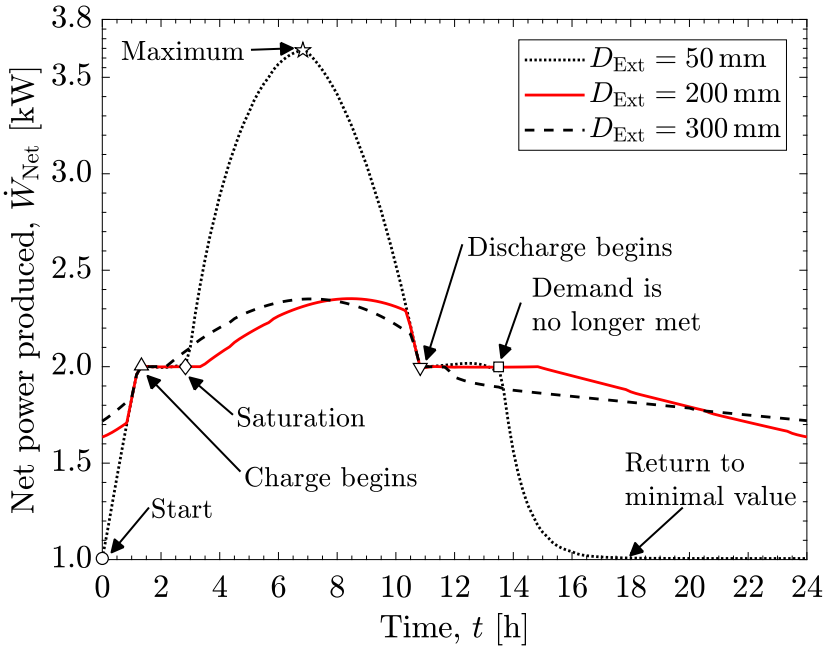


Next, Figs. 10 and 11 present a more detailed view of the TES system during the tenth day while considering $L = 10$ m, $N = 37$, and $D_{\text{Ext}} = 100$ mm. Fig. 10 shows the responses of the heater outlet temperature $\left(T_4\right)$, the TES outlet temperature $\left(T_{\text{TES}}^{\text{Out}}\right)$, and the turbine inlet temperature $\left(T_5\right)$. Then, Fig. 11 shows the respective response of $\dot{W}_{\text{Net}}$ and $x$. With these two figures, it is possible to analyze the s-$CO_2$ flow fraction control scheme employed. Because the curve for $T_4$ is mainly determined by the heat source, it is, shape-wise, analogous to the curve for $T_{\text{HSo}}^{\text{In}}$ shown in Eq. 3.1. However, by controlling $x$ so the constant 2 kW demand is met, it is possible to achieve a nearly constant $T_5$ and, consequently, a nearly constant $\dot{W}_{\text{Net}}$ since the mass flow rate presents small variations at the turbine inlet. That is because, recalling that the turbine inlet pressure is considered constant and, given the definition of $\dot{W}_{\text{Net}}$ in Eq. 3.3, the compressor power expenditure, which is defined as

$$\dot{W}_{\text{C}} = \dot{m}_1 \frac{\left[i\left(P_{\text{High}}, s_1\right) - i_1\right]}{\eta_{\text{C}}}, \tag{3.41}$$

does not depend on $x$. Also, since $|\dot{W}_{\text{MS}}| \ll \left(\dot{W}_{\text{T}} - \dot{W}_{\text{C}}\right)$ and

$$\dot{W}_{\text{T}} = \dot{m}_5 \eta_{\text{T}} \left[i_5 - i\left(P_{\text{Low}}, s_5\right)\right], \tag{3.42}$$

where $s_5 = s(i_5, P_{\text{High}})$, and $i_5$ depends on $x$ and $T_{\text{TES}}^{\text{Out}}$, as shown by Eq. 3.4, controlling $T_5$ allows $\dot{W}_{\text{Net}}$ to be controlled as well.

As can be seen in Fig.10, during the TES system charging process, $T_{\text{TES}}^{\text{Out}}$ decreases to a minimal, which roughly coincides, time-wise, with the maximal value of $T_4$, and then increases back to its initial value, as thermal power is being transferred to the TES system. Conversely, during the discharging process, $T_{\text{TES}}^{\text{Out}}$ presents the opposite behavior. Early in the day, $T_{\text{TES}}^{\text{Out}}$ is slightly higher than $T_5$ because there is still available thermal power being released by the TES system (see the left-most point of the curve for $T_{\text{TES}}^{\text{Out}}$). Now, analyzing $x$ in Fig. 11, early in the day, $x \to 1$ because the heat source does not supply enough thermal power to meet the demand. Then, as the demand is met by the heat source, $x$ decreases since no thermal power is needed to be withdrawn from the TES device. During the charging process, $x$ first increases then decreases following $T_4$, for ensuring that the demand is met. The abrupt variation between $\sim 10.8$ h and $\sim 12$ h refers to the transition process of thermal power being transferred to and from the TES, which is not immediate. So, at first, to ensure a constant $T_5$ while $T_4$ rapidly decreases, $x$ is abruptly increased, then it starts to decrease as the thermal power releasing process is initiated. After that, $x$ varies as the temperature distribution of the TES solution varies due to the thermal power transfer to the fluid. This process takes into account both the mass flow rate flowing through the TES system (which is represented by $x$) and its outlet temperature to control $T_5$ by mixing the $x$ and $(1-x)$ streams, which explains the opposite trend of $x$ and $T_{\text{TES}}^{\text{Out}}$ during the discharge.

For the same case analyzed in Figs. 10 and 11, Fig. 12 presents $\dot{E}_{\text{TES}}^{\text{Sto}}$, the thermal power transferred to and from of the TES device, which is calculated considering a control volume around it as

$$\dot{E}_{\text{TES}}^{\text{Sto}} \approx \left[ x\dot{m}_4 i_4 - N\dot{m}_{\text{TES}}^{\text{Out}} i_{\text{TES}}^{\text{Out}} \right], \tag{3.43}$$

where $\dot{m}_{\text{TES}}^{\text{Out}}$ is the mass flow rate exiting one of the $N$ tubes – a positive value of $\dot{E}_{\text{TES}}^{\text{Sto}}$ indicates that thermal power is being transferred to the TES device (i.e., charge), while a negative value indicates that thermal power is being transferred from the TES device (i.e., discharge). The curves shown in Fig. 12 represent the 10-day time period (solid line linked to the lower x-axis) and the tenth day period (dashed line linked to the upper

Figure 10 – Tenth day temporal behavior of $T_4$, $T_{\text{TES}}^{\text{Out}}$, and $T_5$ for the $L = 10$ m, $N = 37$, and $D_{\text{Ext}}$=100 mm TES configuration.

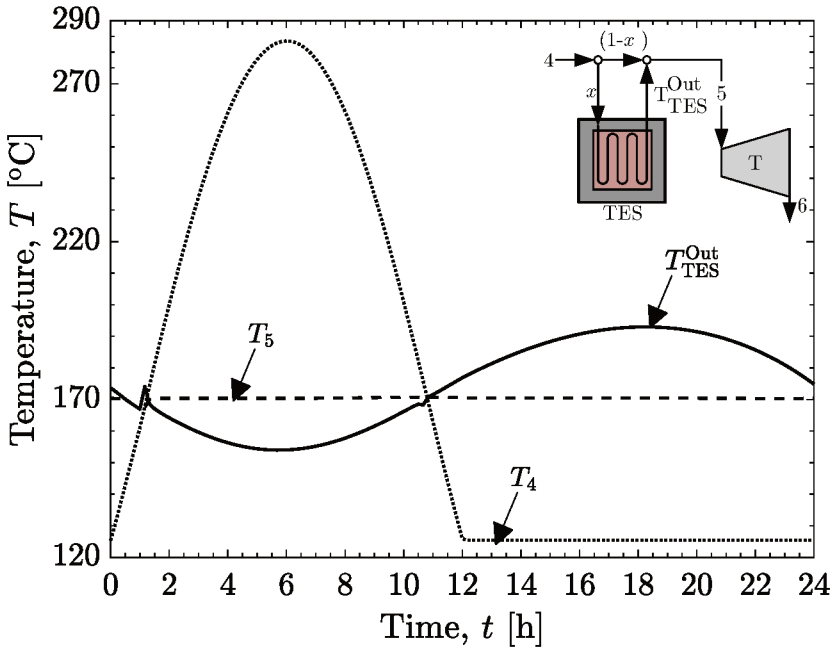


Figure 11 – Tenth day temporal behavior of $\dot{W}_{\text{Net}}$ and $x$ for the $L = 10$ m, $N = 37$, and $D_{\text{Ext}}$=100 mm TES configuration.

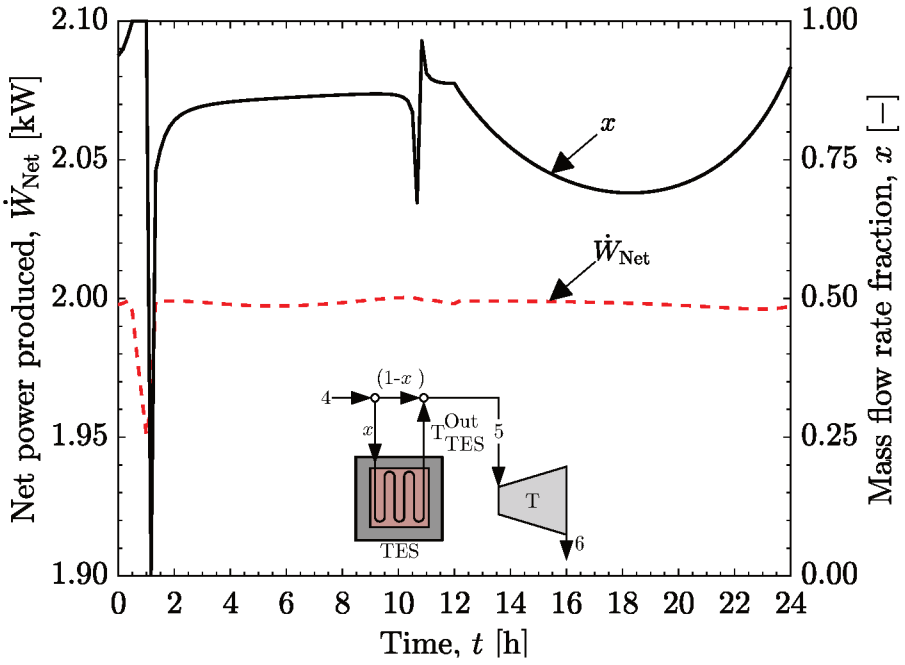

x-axis) – the vertical axis is common for both curves. According to the solid line, this TES configuration experiences energy flux variations during roughly the 4 first days as the thermal power transfer process evolves and shows the existence of maximal and minimal values of $\dot{E}_{\mathrm{TES}}^{\mathrm{Sto}}$. The maximal value of thermal power transferred to the TES device (i.e., $\sim 14.2$ kW) is intrinsically related to the maximal temperature of the working fluid and is approximately achieved at the sixth hour of each day. Differently, the maximal value of thermal power transferred from the TES device (i.e., $\sim -6.7$ kW) is related to the mass flow rate control strategy. Now focusing on the dashed curve, which represents $\dot{E}_{\mathrm{TES}}^{\mathrm{Sto}}$ in the tenth day, it becomes clear that the TES system must complement the energy input supplied by the heat source until the latter can provide enough thermal power to meet the demand, i.e., $\dot{E}_{\mathrm{TES}}^{\mathrm{Sto}} < 0$ for times smaller than $\sim 1.2$ h and, after that, the excess energy is stored until $\sim 10.8$ h. Starting at $\sim 10.8$ h, $T_4$ becomes lower than the required temperature for meeting the demand, thus additional thermal power becomes necessary, which forces $\dot{E}_{\mathrm{TES}}^{\mathrm{Sto}}$ to gradually increase (in absolute value) with time. Then, from 12 h to 24 h, as $T_4$ stabilizes at its minimal value, $\dot{E}_{\mathrm{TES}}^{\mathrm{Sto}}$ becomes seemingly constant because the control scheme maintain $T_5$ also constant.

Figure 12 – Ten-day and tenth day temporal behaviors of $\dot{E}_{\mathrm{TES}}^{\mathrm{Sto}}$ for the $L = 10$ m, $N = 37$, and $D_{\mathrm{Ext}} = 100$ mm TES configuration.

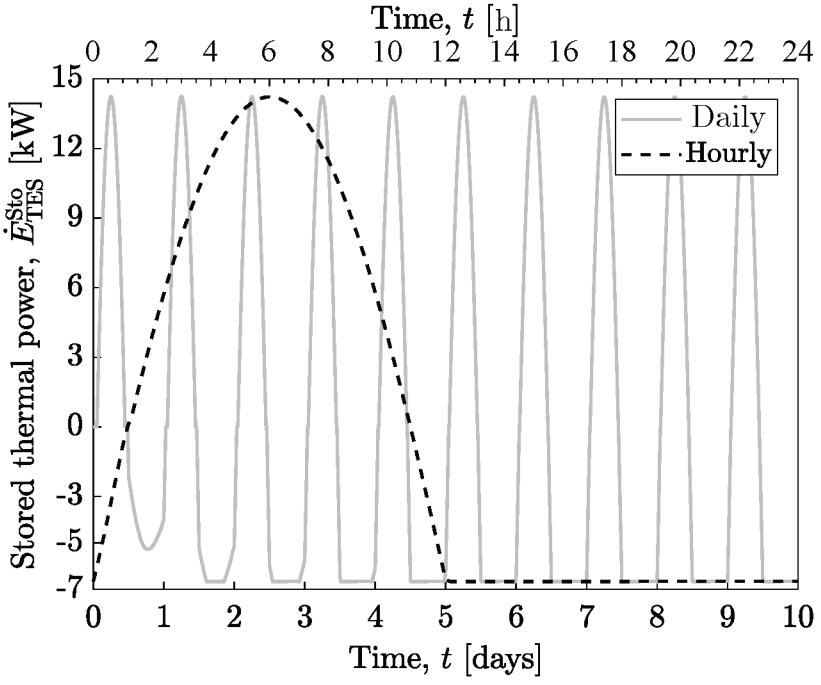


Still considering the TES system with $N = 37$, $L = 10$ m, and $D_{\mathrm{Ext}} = 100$ mm,

this next analysis discusses the reasonableness of the relative size of the TES device with respect to the power cycle is presented. First, one should realize that it is not an easy task to precisely determine the total size of power cycles when dealing with thermodynamic studies like the one presented within this dissertation. Actually, regarding the evaluation of power cycles sizes, authors have used the heat exchangers total heat transfer area (or global conductance) as a scale indicator, e.g., Refs. [29, 107, 120, 121]. Based on such a premise, and extending it to the TES system, it may be possible to indicate its relative scale to the cycle. Thus, considering the internal diameter of the TES device given by Eq. 3.25 (i.e., $D_{\text{TES}} = D_{\text{Int}}/\sqrt{N}$) and the heat exchangers lengths ($L_{\text{He}}$, $L_{\text{Rec}}$, and $L_{\text{Co}}$), the inner tubes wet area of the heat exchangers and TES device may be simply expressed as $\pi DL$. So, the relative area scale of the TES system to the heat exchangers (HX) is

$$\frac{A_{\text{TES}}}{A_{\text{HEx}}} = \frac{L_{\text{TES}}\ \sqrt{N}}{\left(L_{\text{He}} + L_{\text{Rec}} + L_{\text{Co}}\right)}. \tag{3.44}$$

Thus, for the aforementioned system, the analysis indicates an area ratio of $\sim 2$. Now, aiming to account for the TES external diameter ($D_{\text{Ext}}$), which was clearly disregarded in the $\left(A_{\text{TES}}/A_{\text{HEx}}\right)$ ratio, approximate volumes may be used for calculating the relative size. Hence, considering the heat exchangers outer tube internal diameter as 1.5 $D_{\text{Ext}}$ and the volumes of the heat exchangers and the TES system (each tube) as $\pi D^2 L$, the relative volume scale of the TES system to the heat exchangers becomes

$$\frac{V_{\text{TES}}}{V_{\text{HEx}}} = \frac{D_{\text{Ext}}^2\ L_{\text{TES}}\ N}{\left(1.5\ D_{\text{Int}}\right)^2 \left(L_{\text{He}} + L_{\text{Rec}} + L_{\text{Co}}\right)}. \tag{3.45}$$

Then, for the aforementioned system, this analysis indicates a volume ratio of $\sim 85$. Now, it is important to specifically point out that the relative size of the TES system used in this study with respect to the cycle or the power level should not be considered as an absolute value. In a real application, not only the system would most likely to be optimized, but also several changes would be made in terms of construction, operational parameters, technologies employed, which would possibly alter the system size and outputs. Therefore, because this study intends to analyze the transient response of the power cycle, comparisons regarding the system for a real application would not be suitable nor fare.

Up to this point, the analyses considered specific TES configurations while aiming to understand the transient influence of the TES system on the power cycle. Therefore, the

natural direction is to parametrically analyze the effect of the TES design parameters (i.e., $D_{\text{Ext}}$, $L$ and $N$) on $\delta$. Then, Fig. 13 shows the influence of the TES complexity, i.e., its number of tubes ($N$) on $\delta$, for the tenth day and a fixed $L = 5$ m, as function of $D_{\text{Ext}}$. The dashed horizontal red line represents the maximal possible value of $\delta$. Such a maximum would be achieved if the 2 kW demand was perfectly met during the entire 24 h period considered, which, given the operational conditions adopted, would indicate a maximal improvement index of $\delta \sim 37.5\%$ with respect to the cycle operating without TES device and under the same operational conditions. Moreover, this maximal value is intrinsically related to both the heat source and the stipulated demand, hence it may change with the operational conditions. Also, for the sake of clarity, the symbols indicate the simulated points, whereas the data-interpolated continuous gray line only facilitates the visualization

Figure 13 – $\delta$ as function of $D_{\text{Ext}}$ considering a TES system with $L = 5$ m and four different values of $N$.

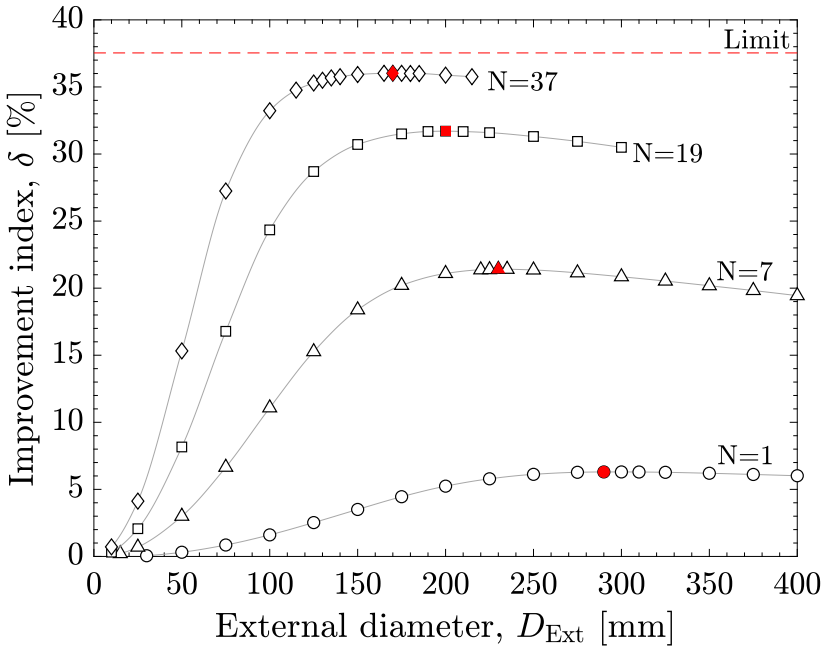


By first analyzing the LHS of Fig. 13, it is clear that, regardless of $N$, as $D_{\text{Ext}}$ tends to its minimal allowable value (which is determined by Eq. 3.25 and the wall thickness), $\delta$ tends to zero, which indicates that the TES system has a minor effect on the cycle performance due to the storage volume tending to zero. Now, for the RHS of Fig. 13, the curves decrease with a milder slope as $D_{\text{Ext}}$ increases, i.e., the increase of the TES volume leads to thermal power being constantly diverted outwards (away from the inner tube) through diffusion. Furthermore, the division of the TES system into $N > 1$ sub-devices

while keeping the transversal flow area constant increases the total heat transfer area by a factor of $\sqrt{N}$. Then, increasing the system complexity improves its ability to use larger storage volumes, which also increases its performance by enabling an optimal distribution of thermal energy through the transversal area for any given $D_{\text{Ext}}$. As may be observed, the increase of $N$ increases $\delta$; nevertheless, a diminishing return is observed. Noteworthy is that the maximal $\delta$ for $N = 37$ is roughly 6 times larger than the respective value for $N = 1$. Finally, Fig. 13 also indicates the existence of optimal $D_{\text{Ext}}$ values that maximize $\delta$ (one for each $N$ considered), which are indicated by the filled red symbols.

Next, Fig. 14 considers the effect of $D_{\text{Ext}}$ on the thermal performance of the TES system while keeping $N = 37$ for different values of $L$. Similar to the results shown in Fig. 13, larger $\delta$ values are obtained increasing the heat transfer area (i.e., larger values of $L$) – fixing $N$ also fixes the internal diameter, so the heat transfer area depends only on $L$. Also, for greater values of $L$, more TES material is located closer to the internal flow region, which ultimately eases the heat transfer to or from the TES device. Therefore, it is expected that $D_{\text{Ext,Opt}}$ decreases while $L$ increases, as shown by the filled symbols. Finally, for $L = 10$ m, $\delta$ approximately reaches its maximal value, eliminating the need to simulate cases with larger $L$ values.

Figure 14 – $\delta$ as function of $D_{\text{Ext}}$ considering a TES system with $N = 37$ and four different values of $L$.

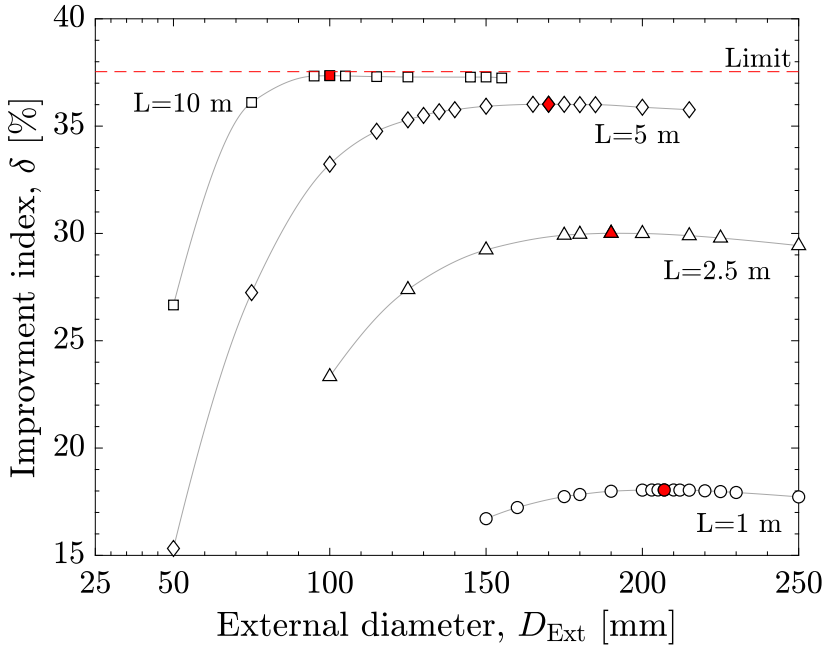

### 3.2.2 1st law efficiency

Recalling the efficiency definition regarding the 1st law of thermodynamics as

$$\eta_{\mathrm{I}} = \frac{\dot{W}_{\mathrm{Net}}}{\dot{E}_{\mathrm{In}}}, \tag{3.46}$$

Fig. 15 shows the transient behavior of $\eta_{\mathrm{I}}$ for two cycles: one with and another without a TES system. The TES design assumed $L = 10$ m, $N = 37$ and $D_{\mathrm{Ext}} = 100$ mm, which is the set of parameters that presented the highest value of $\delta$ in Fig. 14. The results show that the curve for $\eta_{\mathrm{I}}$ for the cycle without the TES device follows the trend of the curve for $T_4$ shown in Fig. 10, i.e., follows the variation of the heat source inlet temperature. Conversely, the curve for $\eta_{\mathrm{I}}$ for the cycle with the TES device presents an opposite behavior during charge and a higher constant value during discharge.

Figure 15 – Tenth day temporal behavior of $\eta_{\mathrm{I}}$ for the decoupled and coupled cycles considering a TES system with $L = 10$ m, $N = 37$, and $D_{\mathrm{Ext}} = 100$ mm.

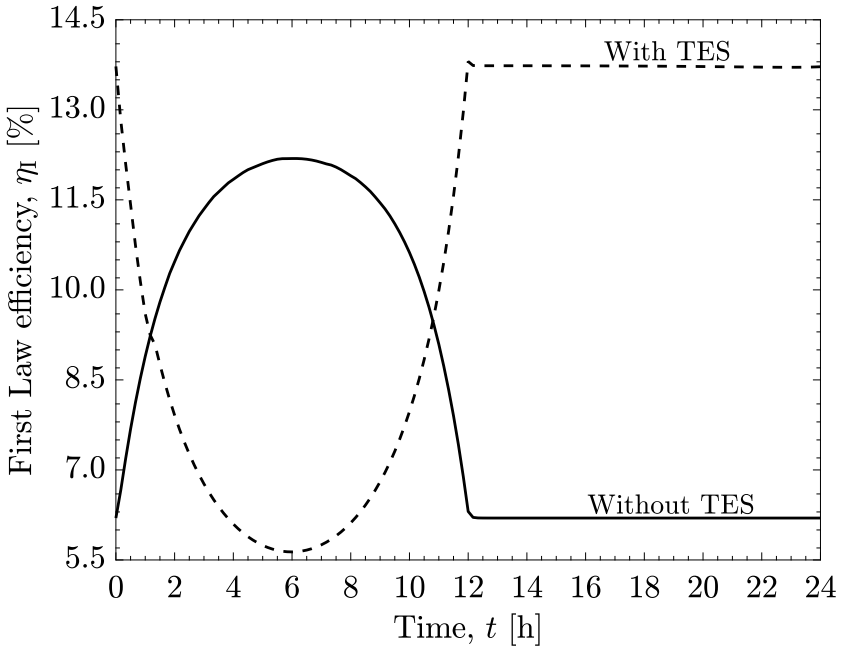


Focusing first on the charging process (i.e., $t < 12$ h), it can be realized that, since the control scheme provides an almost constant $\dot{W}_{\mathrm{Net}}$ (see the dashed line in Fig. 11) and that $\dot{E}_{\mathrm{In}}$ is directly proportional to the heat source inlet temperature, $\eta_{\mathrm{I}}$ decreases and reaches a minimum due to the charging of the TES device. During the discharge, the cycle with the TES device achieves an even higher value than the maximum of the cycle without the TES device. More specifically, between 12 h and 24 h, the coupled cycle achieves an

average 1st law efficiency value of $\sim 13.7\%$, which is $\sim 26\%$ higher than the one for the cycle without TES system. This difference is due to the extra thermal energy provided by the TES device, which is not included in the definition of $\eta_{\mathrm{I}}$. By analyzing the total effective energy supplied (i.e., integrating the net power produced over time), the coupled cycle produced $\sim 4.7\%$ more than the decoupled one. So, the use of a properly designed TES system allowed not only the demand to be better matched throughout the day, but also improved how the thermal power is transferred and converted into mechanical power (i.e., $\eta_{\mathrm{I}}$).

### 3.2.3 The influence of the thermal conductivity of the TES medium

The model implemented may also parametrically consider the effect of the thermophysical properties of the TES medium on $\delta$. In this sense, Figs. 16 and 17 vary the thermal conductivity ($k$) of the material, assuming three significantly distinct values, i.e., 1.4 W/(m · K), 14 W/(m · K), and 140 W/(m · K), for a TES configuration in which $L = 10$ m, $N = 37$, and $D_{\mathrm{Ext}}$ varies between 50 mm and 250 mm. First, in Fig. 16, for small values of $D_{\mathrm{Ext}}$, the effect of $k$ on $\delta$ is minor due to the small amount of storage material available. Differently, for large values of $D_{\mathrm{Ext}}$, lower thermal conductivities limit the radially outward thermal transport.

Figure 16 – Influence of the TES thermal conductivity on $\delta$ as function of $D_{\mathrm{Ext}}$ for a TES system with $L = 10$ m and $N = 37$.

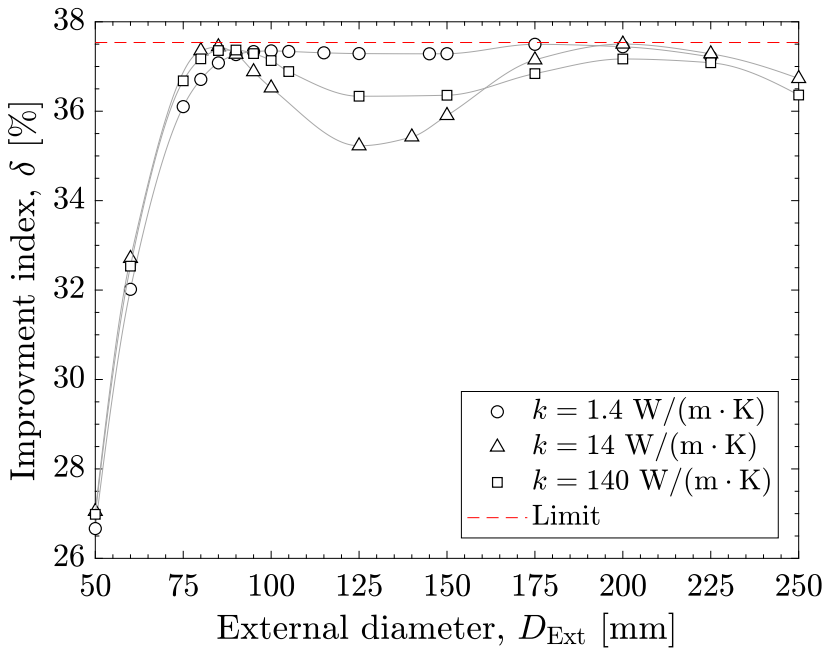

To further verify this analysis, Fig. 17 shows the time and space-averaged TES thermal conductance, which considers conduction and convection, as the inverse of the equivalent thermal resistance, i.e., $\bar{R}_{\mathrm{eq}}^{-1} = \left(\bar{R}_{\mathrm{CD}} + \bar{R}_{\mathrm{CV}}\right)^{-1}$. For $k = 1.4$ W/(m · K), the thermal conductance is fairly constant, but, for the other two values considered, it presents two well identifiable peaks, i.e., at $D_{\mathrm{Ext}} \sim 90$ mm and $D_{\mathrm{Ext}} \sim 200$ mm, which are related to different sources: the working fluid thermophysical properties variations throughout the TES system, the control scheme adopted, the different effect of $D_{\mathrm{Ext}}$ on $\bar{R}_{\mathrm{CD}}$ and $\bar{R}_{\mathrm{CV}}$.

Figure 17 – Thermal conductance of the TES system as function of $D_{\mathrm{Ext}}$ for three values of thermal conductivity considering a TES system with $L = 10$ m and $N = 37$.

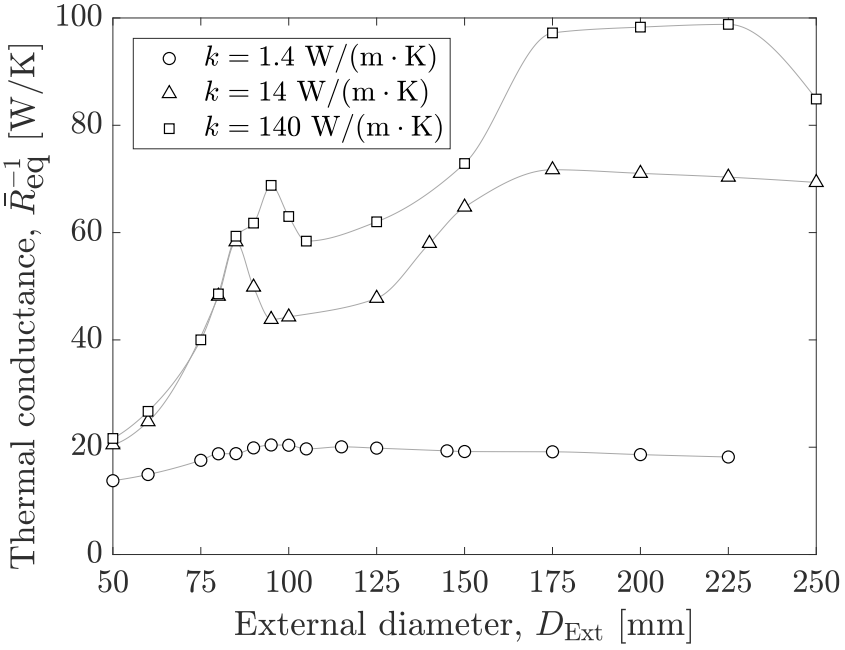


### 3.2.4 Mass storage device and the complexity of the TES system

Now, on the mass storage device, it is worth recalling that its control is responsible for enabling the cycle to maintain stable pressure levels throughout the day as well as that the initial mass inventory of $\sim 6.36$ kg mentioned in Sec. 3.1 is only specified as an initial condition at day one. Then, Fig. 18 presents the variation of the mass storage inventory for the tenth day considering a TES configuration of $L = 10$ m, $D_{\mathrm{Ext}} = 150$ mm, and four values of $N$. The general trend presented by all four curves is related to the transient behavior of the cycle and, more specifically, to the mass flow rate variations in the heat exchangers and TES system. When the s-$CO_2$ is being heated, the decrease of

volume-specific mass forces mass out of the components while the opposite occurs for the cooling process. Therefore, the general trend presented for all curves follows the heat source temperature variation and, consequently, the charging and discharging sequences. More interesting is the different response obtained with the increase in the number of tubes ($N$). As the complexity of the TES system increases, so does the device ability to better store energy, which, ultimately, diminishes mass flow rate variations on the low-pressure end, as the turbine inlet conditions are kept almost constant, which leads to less accumulated mass in the mass storage.

Figure 18 – Tenth day temporal variation of $m_{\mathrm{MS}}$ for a TES system with $L = 5$ m, $D_{\mathrm{Ext}} = 150$ mm, and four different values of $N$.

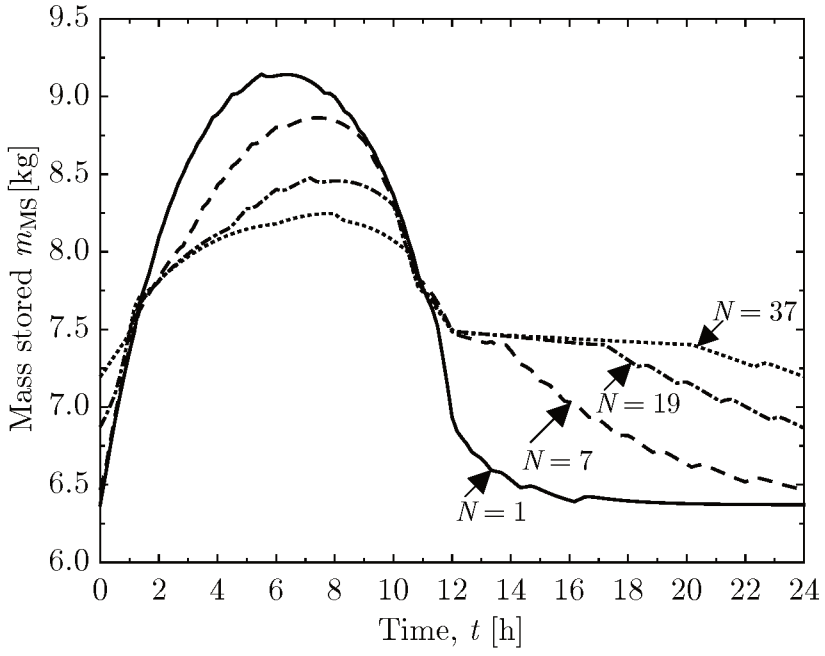

# 4 PERFORMANCE MAPPING OF PACKED-BED TES SYSTEMS FOR CONCENTRATED SOLAR-POWERED PLANTS USING SUPERCRITICAL $CO_2$

Following the analyses of Chap. 3 and having in mind the current increased interest in using s-$CO_2$ as HTF for solar-powered plants, this chapter builds upon the existing literature by assessing the performance of s-$CO_2$ packed-bed TES applications, which remains as a gap within the TES technology. Hence, this study explores the thermal-hydraulic performance of a packed-bed TES system directly coupled to a concentrated solar-powered s-$CO_2$ recompression Brayton cycle, while considering a comprehensive set of operational and design parameters — e.g., storage tank size and its arrangement (aspect ratio), porous medium particle diameter, mass flow rates, charging temperature. A thoroughly detailed transient and discretized numerical model is presented, discussed, and verified, which is based on well-developed packed-bed TES methodology and, in addition, encompasses several adaptations for dealing with a supercritical HTF. Such adaptations are necessary for including the effects of thermophysical properties variations on the energy and mass balances, something generally neglected for air-based applications. By considering the integration between the solar field, TES system, and power block, the analyses assess, from parametric and optimization standpoints, the operation of the TES system through its charging-discharging combined efficiency, also carefully discussing the system performance and indicating or clarifying trends of such a solution using s-$CO_2$. The outcomes provided clearly point out novel optimal directions to be followed in terms of the packed-bed TES concept while matching demands from the CSP industry regarding the use of s-$CO_2$ as HTF [34]. Therefore, this dissertation not only contributes to the literature by exploring the yet incipient know-how regarding technical aspects on s-$CO_2$-based packed-bed TES systems, but also facilitates the development of several further follow-up analyses, which, for instance, may include scaling influence, economic feasibility, and exergetic assessments.

## 4.1 METHODOLOGIES FOR MODELING AND EVALUATION

The following subsections present the methodology employed for modeling and evaluation: (i) Subs. 4.1.1 explores the system layout and Subs. 4.1.2 the modeling of the packed-bed TES device; (ii) Subs. 4.1.3 and 4.1.4 show the fluid and solid energy equations, respectively; (iii) Subs. 4.1.5 presents the linearization of the solid mass-specific internal energy and Subs. 4.1.6 the solid effective thermal conductivity; (iv) Subs. 4.1.7 introduces the volumetric heat transfer coefficient and Subs. 4.1.8 presents the pressure drop correlation; (v) Subs. 4.1.9 and 4.1.10 present the energy conservation equations and heat transfer coefficient of the lids and wall, respectively; (vi) Subs. 4.1.11 and 4.1.12 explore the numerical routines and the power balance of the TES system, respectively; (vii) Subs. 4.1.13 discusses the spatial and temporal discretization independence; (viii) Subs. 4.1.14 presents the modeling verification; and (ix) Subs. 4.1.15 discusses the charging and discharging processes of the TES system and their efficiencies.

### 4.1.1 System modeling

Fig. 19 depicts the conventional layout of a solar field coupled to a power block with a parallel TES system. The solar field provides thermal power during the day, which may be used by the power block for producing electricity or be stored within the TES system. Also, there are two auxiliary compression systems, A1 and A2, at the TES system outlet (one for charging and one for discharging). These auxiliary systems are responsible for compressing the mass flow rate at the TES system outlet to the solar field or power block inlet pressures (thus compensating the pressure drop due to the flow through the porous medium). A control system is responsible for dictating the mass flow rate circulating between the solar field and the TES system, such that the s-$CO_2$ arrives at the design condition at the power block. Next, the fluid mass flow rate is returned by the power block already pressurized, but at low temperature (i.e., at discharging temperature) and may be directed to the solar field or to the TES system depending on the control strategy employed. At this point, it is important to mention that the use of a compressor in the TES discharging outlet is associated with a numerical convenience and that, in a real

application, the compressor would most likely be placed in a more favorable position (i.e., at the TES discharging inlet). However, given that prior to the development of the study, the actual pressure drop behavior for the HTF-TES association is not known, this simplification eases the numerical solution. Also, by knowing the system behavior regarding the pressure drop, one may use the trends obtained as baseline for further developments. This is because the pumping power values obtained with this arrangement are greater than those that would be required for a compressor positioned in the alternative position due to the greater volume-specific mass at the discharging outlet.

Figure 19 – Integrated overall layout.

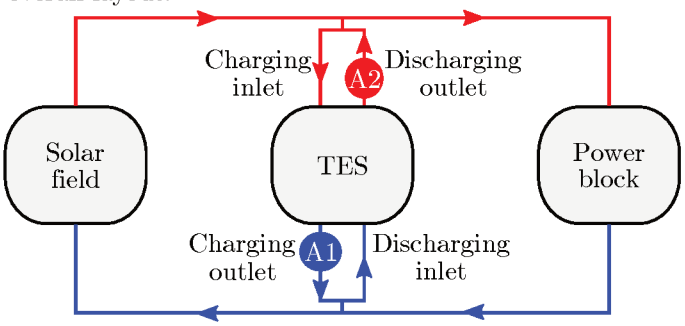


The power block, whose layout is shown in Fig. 20, is a conventional recompression s-$CO_2$ Brayton cycle, which is composed of turbine (T), main (MC) and recompression (RC) compressors, cooler (CO), and low and high-temperature recuperators (LTR and HTR, respectively). Additionally, the solar field is considered as the system heat source.

Figure 20 – Recompression power block layout.

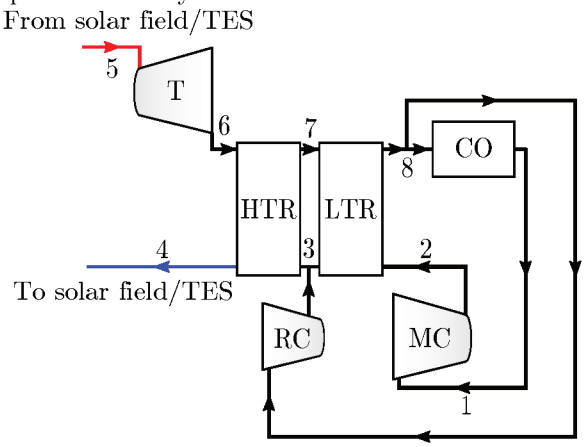


Though this study mainly focuses on the packed-bed TES itself instead of the control of the solar field-TES-power block system, the integration between the TES and the power block is not disregarded since changes in the turbine inlet temperature directly

impact the fluid pressure and temperature upstream the TES system. In order to deal with this off-design power block dynamic, the modeling suggested by Ref. [122] is utilized to assign the thermodynamic states in the power block. Ref. [123] employed such an approach for a transient analysis of an s-$CO_2$ recompression Brayton cycle coupled to a solar field without TES system. Therefore, based on and using the modeling of Ref. [123], the minimal s-$CO_2$ temperature and pressure values within the cycle (point 1 in Fig. 20) were determined as $T_1 = 32$ °C and $P_1 = 8$ MPa, respectively, with a fixed recompression mass flow rate fraction (from point 8 to point 3 in Fig. 20) of 38.3%. Also, for the power block design mass flow rate, a downscale value of roughly 1% of that used in Refs. [122,123] was chosen, i.e., 1 kg/s. Then, by defining a set of power block inlet temperatures ($T_{\mathrm{PB,In}}$), which are taken as TES charging temperatures ($T_{\mathrm{C}}$), the respective optimal power block outlet temperatures ($T_{\mathrm{PB,Out}}$) and high-end pressure ($P_{\mathrm{PB,High}}$) are calculated and taken as TES discharging temperatures ($T_{\mathrm{D}}$) and inlet working pressures ($P_{\mathrm{In}}$), respectively. The optimal values obtained using the modeling of Refs. [122, 123] as well as the respective power block thermal efficiencies are shown in Tab. 1.

Table 1 – Discharging temperature and working pressures from the optimal power block design and its respective thermal efficiencies for different inlet temperatures.

| $T_{\mathrm{PB,In}} = T_{\mathrm{C}}$[°C] | $T_{\mathrm{PB,Out}} = T_{\mathrm{D}}$[°C] | $P_{\mathrm{PB,High}} = P$[MPa] | $\eta_{\mathrm{PB}}$[–] |
|---|---|---|---|
| 400 | 263 | 24.30 | 0.3632 |
| 425 | 281 | 24.46 | 0.3890 |
| 450 | 300 | 24.60 | 0.4109 |
| 475 | 318 | 24.75 | 0.4298 |
| 500 | 338 | 24.87 | 0.4463 |
| 525 | 357 | 24.99 | 0.4608 |
| 550 | 378 | 25.10 | 0.4738 |
| 575 | 398 | 25.19 | 0.4855 |
| 600 | 420 | 25.29 | 0.4960 |
| 625 | 440 | 25.36 | 0.5055 |
| 650 | 462 | 25.44 | 0.5141 |

Moreover, to clarify the s-$CO_2$ recompression Brayton cycle, Fig. 21 shows its $T$-$s$ diagram while considering $T_{\mathrm{PB,In}} = 550$ °C – all the thermodynamic states 1 to 8 of Fig. 20 are indicated with their relative position with respect to the critical isobaric.

It is relevant to mention that the fixed input operation parameters shown in Tab. 1

Figure 21 – $T$-$s$ diagram for the s-$CO_2$ recompression Brayton cycle considering $T_{PB,In} = 550$ °C.

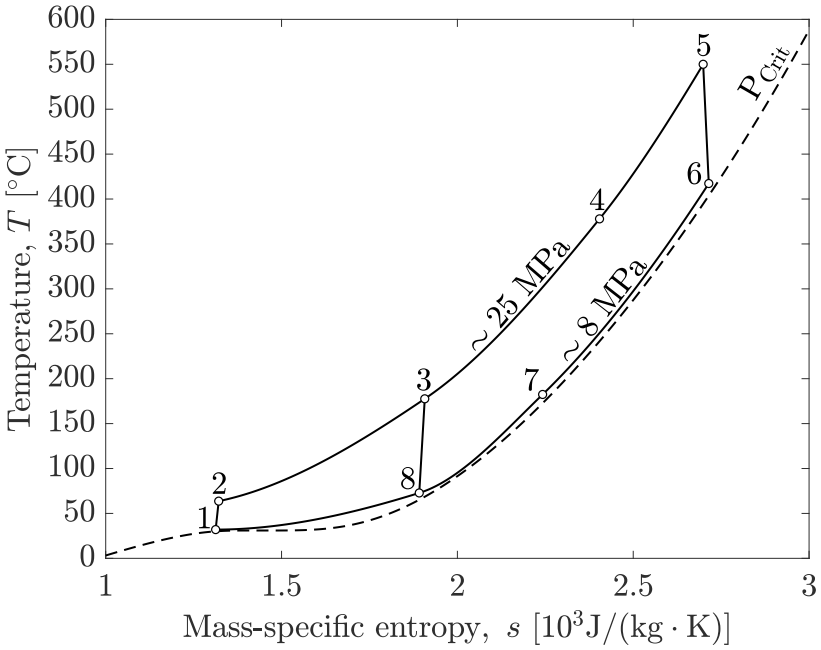


might seem unjustified if one only considers that TES systems are likely to be subjected to time-dependent inputs (i.e., variable inlet mass flow rate and/or temperature), which depend on the energy source availability and the control strategy employed. However, the choice for such a fixed-values set of parameters intends to not overly specify the analyses according to a given set of time-dependent inputs. Then, fixed inputs may arguably be seen as the less overly restricting possibility. Finally, the results presented in the following section would be modified if a different set of input values was used; however, it is expected that the main trends will not.

### 4.1.2 Modeling of the packed-bed TES device

In order to deal with the s-$CO_2$ thermophysical properties variations as well as the time-dependent behavior to which the TES system will be subjected, a specific transient model was developed and implemented as a numerical routine, which was then verified against independent data. The model is primarily based on Ref. [30], with several adaptations included due to the change of the HTF from air to s-$CO_2$. The core of the TES device is modeled as an in-ground horizontal cylindrical tank, which is characterized by the bed diameter $D$ and bed length $L$ and whose cut view along the axial direction is shown in Fig. 22. To compose the packed-bed, the cylindrical cavity is filled with solid

spheres of diameter $d$ and then, subsequently, surrounded by thermal insulation (innermost white layer) of thickness $t_{\mathrm{i}}$, steel wall (central gray layer) of thickness $t_{\mathrm{st}}$, and ground (outermost brown layer) of thickness $t_{\mathrm{g}}$ – the multilayer sequence follows that of Ref. [91]. Furthermore, following the study on packed-bed TES with s-$CO_2$ of Ref. [91], the material chosen for the solid spheres is alumina.

Figure 22 – Packed-bed TES system model.

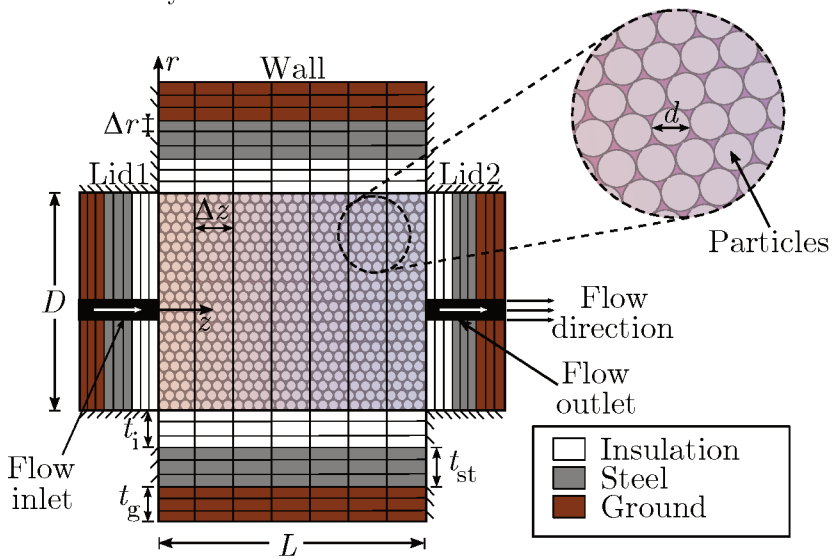


As can be observed in Fig. 22, the geometry of the TES device was considered as having flat instead of domed ends as usually employed for pressure vessels, which may affect both structural and thermohydraulic aspects. Also, the modeling disregards the inlet and outlet manifolds and, consequently, two-dimensional flows at the packed-bed inlet and outlet as well as local pressure drops. While these simplifications may deviate the simulations from real applications, they substantially simplify the numerical domain, allowing the use of the plug flow assumption and further enabling the development of a time-efficient numerical routine for dealing with the s-$CO_2$ packed-bed.

The packed-bed core numerical model is implemented as a one-dimensional ($z$-wise) axisymmetric and axially-uniformly-discretized horizontal cylinder, which comprises solid (porous medium) and fluid (s-$CO_2$) domains. A two-temperature formulation is adopted, which implies that the fluid and the solid within each axial discretized volume are characterized by a uniform temperature (hence, a uniform set of properties) each – the need for a two-equation formulation instead of an one-equation formulation is associated to both the s-$CO_2$ properties variations along the TES device and the optimization nature of this

analysis, which requires a more robust formulation. For the fluid domain, the discretized numerical expression for the conservation of energy [124], using the finite-volumes method, is detailed in Sub. 4.1.3. On the other hand, for the incompressible and resting solid domain, the expression is detailed in Sub. 4.1.4. The solid internal energy is linearized as depicted in Sub. 4.1.5 and its effective thermal conductivity, which accounts for diffusion and radiation, is obtained through the Kunii and Smith's correlation [125, 126], as depicted by Ref. [30] and detailed in Sub. 4.1.6. The numerical model considers heat exchange not only between the fluid and the solid phases due to convection but also between subsequent axial solid nodes due to diffusion while all heat losses to the environment are accounted for in the fluid expression.

The axially and temporally variable volumetric convective heat transfer coefficient used in the energy conservation expressions is obtained through the Pfeffer's correlation for spherical particles [127], which is detailed in Sub. 4.1.7. Moreover, due to the HTF variable thermophysical properties and the transient nature of the study, the HTF acceleration and pressure drop, which are important for the system performance, are considered. For the pressure drop, the modified Ergun's correlation [128] is used, which is detailed in Sub. 4.1.8, and, for the mass flow rate update, the approach used is presented in Sub. 4.1.11.

Now, focusing on the TES container, as shown in Fig. 22, the wall comprises three concentric annuli, whereas each lid comprises three concentric circular slabs, i.e., the wall and each lid are composed of insulation, steel, and ground layers. The ground temperature at the external face of the ground layer, i.e., as far as 0.2 m from the steel external surface, is assumed to be constant at $T_{\mathrm{g}} = 25$ °C. In order to properly accounts for the time-dependent variation of the heat losses to the surrounding ground, for the wall and lids domains, dedicated finite-volumes numerical routines were developed for solving the temperature fields. Information on the wall and lids as well as the equations used in these routines are detailed in Sub. 4.1.9. Furthermore, the convective heat transfer coefficient between fluid and the inner walls of the TES device is given, following Refs. [30, 129, 130], as the summation of a convective-based coefficient and a conductive-radiative-based coefficient, as detailed in Sub. 4.1.10.

In a brief description, the main numerical routine is fed with input and initial

parameters and, for each time step, the fluid mass-specific enthalpy and the porous medium temperature fields are obtained by solving a linear system of equations. Then, variables are updated, temperature fields for the wall and lids are obtained, and the system is rerun until convergence is achieved iteratively. Further details on the numerical routines are provided in Sub. 4.1.11. Furthermore, for the convergence at each time step, the TES overall power balance is observed, which is detailed in Sub. 4.1.12. Additionally, from the time and space discretization independence study detailed in Sub. 4.1.13, the time step $\Delta t$ and number of axial elements $N_z$ are obtained through bilinear interpolation based on the bed length and diameter.

Even though the heat transfer and pressure drop correlations adopted were not specifically developed for s-$CO_2$ flowing through a porous-medium, they were chosen due to the lack of better and reliable options to date – regarding the heat transfer, for instance, there are even experimental studies on this matter, e.g., Ref. [131], but they do not provide an employable numerical expression. As will be shown in Sub. 4.1.14, results obtained using these correlations were compared to those from an independent work and displayed good agreement. Moreover, based on characteristics inherent to s-$CO_2$, which are widely reported in the literature (e.g., Refs. [5, 15, 132]), it is expected that the TES thermo-hydraulic performance benefits from the use of such an HTF. For instance, the sharp increase of its volume-specific mass and the decrease of its dynamic viscosity with the increase of the temperature may lead to improvements in terms of heat transfer increase and the pressure drop reduction. Hence, it is arguably acceptable to conceive the usage of the above-mentioned correlations for establishing baseline trends.

Finally, it is important mentioning that all analyses (except for those of Sub. 4.2.5) are performed for a single charging-discharging cycle, i.e., a single charge immediately followed by a discharge, without any idle time in between. Since a single charging-discharging cycle is considered, the system performance evaluations might lack the effect of achieving a periodic representative operational pattern, as discussed in Chap. 3. This approach was chosen aiming to considerably decrease the simulation time required for the analyses without undermining the focus on the TES overall performance trends regarding design and operational parameters because the specific values obtained are not the main goal by

themselves. Also, the validity of such an approach will be further discussed in Sub. 4.2.5.

### 4.1.3 Fluid energy equation

Using Eq. A.23 (from Appx. A) for a fluid central node of the packed-bed (i.e., not in contact with a lid), recognizing that the node volume occupied by the fluid phase is $\varepsilon V$ and that the total mass flow rate is actually given by $\dot{m} = \varepsilon \rho u A$, neglecting thermal dispersion within the fluid, implicitly evaluating the temporal terms, and assuming plug flow, the fluid energy conservation equation yields

$$\begin{aligned} \varepsilon V_{\mathrm{P}} \left( \rho_{\mathrm{F,P}} i_{\mathrm{F,P}} - \rho^{0}_{\mathrm{F,P}} i^{0}_{\mathrm{F,P}} \right) + \left( \dot{m}_{\mathrm{F,e}} i_{\mathrm{F,e}} - \dot{m}_{\mathrm{F,w}} i_{\mathrm{F,w}} \right) \Delta t = \\ h_{\mathrm{part,P}} A_{\mathrm{HT,P}} \left( T_{\mathrm{S,P}} - T_{\mathrm{F,P}} \right) \Delta t + \varepsilon V_{\mathrm{P}} \left( P_{\mathrm{F,P}} - P^{0}_{\mathrm{F,P}} \right) + \\ \left( \frac{\dot{m}_{\mathrm{F,e}}}{\rho_{\mathrm{F,e}}} \right) \left( P_{\mathrm{F,e}} - P_{\mathrm{F,P}} \right) \Delta t + \left( \frac{\dot{m}_{\mathrm{F,w}}}{\rho_{\mathrm{F,w}}} \right) \left( P_{\mathrm{F,P}} - P_{\mathrm{F,w}} \right) \Delta t + \\ h_{Wall,P} A_{Wall,P} \left( T_{Wall,P} - T_{F,P} \right) \Delta t, \end{aligned} \tag{4.1}$$

for which $\dot{m}$ is the total mass flow rate through the packed-bed, $\varepsilon$ the packed-bed porosity, $V$ the node total volume, $\rho$ the volume-specific mass, $t$ the time, $T$ the temperature, $P$ the thermodynamic pressure, $h$ the convective heat transfer coefficient.

Using UDS for the advective terms while considering the flow from LHS to RHS, recognizing that $h_{\mathrm{part}} A_{\mathrm{HT}} = \hbar V$ (as will be shown in Sub. 4.1.7), using the enthalpy-temperature coupling factor $g_{\mathrm{P}}$ to replace the fluid temperature by its mass-specific enthalpy as $T_{\mathrm{F,P}} = g_{\mathrm{P}} i_{\mathrm{F,P}}$, and dividing Eq. 4.1 by the time step $\Delta t$, it yields

$$\begin{aligned} \varepsilon V_{\mathrm{P}} \frac{\left( \rho_{\mathrm{F,P}} i_{\mathrm{F,P}} - \rho^{0}_{\mathrm{F,P}} i^{0}_{\mathrm{F,P}} \right)}{\Delta t} + \left( \dot{m}_{\mathrm{F,e}} i_{\mathrm{F,P}} - \dot{m}_{\mathrm{F,w}} i_{\mathrm{F,W}} \right) = \\ \hbar_{\mathrm{P}} V_{\mathrm{P}} \left( T_{\mathrm{S,P}} - g_{\mathrm{P}} i_{\mathrm{F,P}} \right) + \varepsilon V_{\mathrm{P}} \frac{\left( P_{\mathrm{F,P}} - P^{0}_{\mathrm{F,P}} \right)}{\Delta t} + \\ \left( \frac{\dot{m}_{\mathrm{F,e}}}{\rho_{\mathrm{F,e}}} \right) \left( P_{\mathrm{F,e}} - P_{\mathrm{F,P}} \right) + \left( \frac{\dot{m}_{\mathrm{F,w}}}{\rho_{\mathrm{F,w}}} \right) \left( P_{\mathrm{F,P}} - P_{\mathrm{F,w}} \right) + \\ h_{Wall,P} A_{Wall,P} \left( T_{Wall,P} - g_{\mathrm{P}} i_{\mathrm{F,P}} \right). \end{aligned} \tag{4.2}$$

Thus, solving Eq. 4.2 for $i_{\mathrm{F,P}}$, it yields

$$\begin{aligned}\left(-\dot{m}_{\mathrm{F,w}}\right) i_{\mathrm{F,w}} + \left[\frac{\varepsilon V_{\mathrm{P}} \rho_{\mathrm{F,P}}}{\Delta t} + \dot{m}_{\mathrm{F,e}} + g_{\mathrm{P}} \hbar_{\mathrm{P}} V_{\mathrm{P}} + g_{\mathrm{P}} h_{Wall,P} A_{Wall,P}\right] i_{\mathrm{F,P}} + \\ \left(-\hbar_{\mathrm{P}} V_{\mathrm{P}}\right) T_{\mathrm{S,P}} = \left(\frac{\varepsilon V_{\mathrm{P}} \rho^{0}_{\mathrm{F,P}} i^{0}_{\mathrm{F,P}}}{\Delta t}\right) + h_{Wall,P} A_{Wall,P} T_{Wall,P} + \\ \varepsilon V_{\mathrm{P}} \left(\frac{P_{\mathrm{F,P}} - P^{0}_{\mathrm{F,P}}}{\Delta t}\right) + \left(\frac{\dot{m}_{\mathrm{F,e}}}{\rho_{\mathrm{F,e}}}\right)\left(P_{\mathrm{F,e}} - P_{\mathrm{F,P}}\right) + \left(\frac{\dot{m}_{\mathrm{F,w}}}{\rho_{\mathrm{F,w}}}\right)\left(P_{\mathrm{F,P}} - P_{\mathrm{F,w}}\right).\end{aligned} \tag{4.3}$$

Then, Eq. 4.3 may be rewritten in a generic form for encompassing all heat losses as

$$\begin{aligned}\left(-\dot{m}_{\mathrm{F,w}}\right) i_{\mathrm{F,w}} + \left[\frac{\varepsilon V_{\mathrm{P}} \rho_{\mathrm{F,P}}}{\Delta t} + \dot{m}_{\mathrm{F,e}} + g_{\mathrm{P}} \hbar_{\mathrm{P}} V_{\mathrm{P}} + g_{\mathrm{P}} \sum_{loss} h_{\alpha} A_{\alpha}\right] i_{\mathrm{F,P}} + \\ \left(-\hbar_{\mathrm{P}} V_{\mathrm{P}}\right) T_{\mathrm{S,P}} = \left(\frac{\varepsilon V_{\mathrm{P}} \rho^{0}_{\mathrm{F,P}} i^{0}_{\mathrm{F,P}}}{\Delta t}\right) + \varepsilon V_{\mathrm{P}} \left(\frac{P_{\mathrm{F,P}} - P^{0}_{\mathrm{F,P}}}{\Delta t}\right) + \\ \left(\frac{\dot{m}_{\mathrm{F,e}}}{\rho_{\mathrm{F,e}}}\right)\left(P_{\mathrm{F,e}} - P_{\mathrm{F,P}}\right) + \left(\frac{\dot{m}_{\mathrm{F,w}}}{\rho_{\mathrm{F,w}}}\right)\left(P_{\mathrm{F,P}} - P_{\mathrm{F,w}}\right) + \sum_{loss} h_{\alpha} A_{\alpha} T_{\alpha},\end{aligned} \tag{4.4}$$

for which the subscripts $F$ and $S$ refer to the fluid (s-$CO_2$) and solid (porous medium material) phases, respectively; the superscript 0 refers to the previous time step while no superscript indicates the current time step. The summation indicated by the subscript $loss$ is used for compactness and refers to all thermal losses, so the subscript $\alpha$ encompasses both the storage wall and lids. For the wall,

$$h_{\alpha} A_{\alpha} = h_{\mathrm{Wall}} \pi D \Delta z, \tag{4.5}$$

whereas for either lid,

$$h_{\alpha} A_{\alpha} = h_{\mathrm{Lid}} \frac{\pi D^2}{4}. \tag{4.6}$$

The node total volume, which is given by

$$V_{\mathrm{P}} = \frac{\pi D^2}{4} \Delta z \tag{4.7}$$

is multiplied by $\varepsilon$ to account for the fluid-filled volume only. The axially discretized length is given by

$$\Delta z = \frac{L}{N_z} \tag{4.8}$$

and further detailed in Sub. 4.1.13. Once again, the temperature-enthalpy coupling factor $g$, which was already discussed along with Eq. 3.9, linearizes the mass-specific enthalpy, thus allowing the fluid energy equation to be written in terms of the fluid mass-specific enthalpy only, which eases the numerical solution. Furthermore, for obtaining Eq. 4.4, plug flow was assumed throughout the porous medium, which allows the fluid mass flow rate, temperature, and pressure (and, thus, its thermophysical properties) to be considered uniform at each section and, consequently, also allows the calculation of a heat transfer coefficient for each section based on a specific correlation.

### 4.1.4 Solid energy equation

For the incompressible and resting solid phase with constant volume-specific mass, as shown in Ref. [109], Eq. A.1 (from Appx. A) simplifies to

$$\frac{\partial\left(\rho_{\mathrm{S}} e_{\mathrm{S}}\right)}{\partial t} = \vec{\nabla} \cdot \left(k_{\mathrm{S}} \vec{\nabla} T_{\mathrm{S}}\right). \tag{4.9}$$

So, integrating Eq. 4.9 over the solid volume and the time, it yields

$$\int_t \int_V \frac{\partial\left(\rho_{\mathrm{S}} e_{\mathrm{S}}\right)}{\partial t}\, dV dt = \int_t \int_V \vec{\nabla} \cdot \left(k_{\mathrm{S}} \vec{\nabla} T_{\mathrm{S}}\right)\, dV dt, \tag{4.10}$$

and, applying the divergence theorem to the term on the RHS of Eq. 4.10, it yields

$$\int_t \int_V \frac{\partial\left(\rho_{\mathrm{S}} e_{\mathrm{S}}\right)}{\partial t}\, dV dt = \int_t \int_S \left(k_{\mathrm{S}} \vec{\nabla} T_{\mathrm{S}}\right) \cdot \hat{n}\, dS dt. \tag{4.11}$$

Thus, for the solid phase of a central node of the packed-bed (i.e., not in contact with a lid) and implicitly evaluating of the temporal terms, the solid energy conservation equation

yields

$$\begin{aligned}(1-\varepsilon)\,V_{\mathrm{P}}\left(\rho_{\mathrm{S,P}}e_{\mathrm{S,P}}-\overset{0}{\rho}_{\mathrm{S,P}}\overset{0}{e}_{\mathrm{S,P}}\right)=h_{\mathrm{P}}A_{\mathrm{HT,P}}\left(T_{\mathrm{F,P}}-T_{\mathrm{S,P}}\right)\Delta t+\\ \left(k_{\mathrm{S,eff}}A_{\mathrm{Trans}}\frac{\partial T_{\mathrm{S}}}{\partial z}\right)_{\mathrm{e}}\Delta t-\left(k_{\mathrm{S,eff}}A_{\mathrm{Trans}}\frac{\partial T_{\mathrm{S}}}{\partial z}\right)_{\mathrm{w}}\Delta t,\end{aligned} \tag{4.12}$$

for which

$$A_{\mathrm{Trans}}=\frac{\pi D^{2}}{4}. \tag{4.13}$$

As already mentioned, the solid material chosen is alumina, which is considered as having a constant volume-specific mass of $\rho_{\mathrm{S}}=3950\ \mathrm{kg/m^{3}}$. The node total volume is multiplied by the $(1-\varepsilon)$ to account for the solid volume only. Once again, the effective thermal conductivity is detailed in Sub. 4.1.6. Using CDS for the derivatives on the RHS of Eq. 4.12, recognizing, once again, that $h_{\mathrm{part}}A_{\mathrm{HT}}=\hbar V$, and dividing Eq. 4.12 by the time step $\Delta t$, it yields

$$\begin{aligned}(1-\varepsilon)\,V_{\mathrm{P}}\rho_{\mathrm{S,P}}\frac{\left(e_{\mathrm{S,P}}-\overset{0}{e}_{\mathrm{S,P}}\right)}{\Delta t}=\hbar_{\mathrm{P}}V_{\mathrm{P}}\left(T_{\mathrm{F,P}}-T_{\mathrm{S,P}}\right)+\\ \left[k_{\mathrm{S,eff,e}}A_{\mathrm{Trans,e}}\frac{\left(T_{\mathrm{S,E}}-T_{\mathrm{S,P}}\right)}{\Delta z}\right]-\left[k_{\mathrm{S,eff,w}}A_{\mathrm{Trans,w}}\frac{\left(T_{\mathrm{S,P}}-T_{\mathrm{S,W}}\right)}{\Delta z}\right].\end{aligned} \tag{4.14}$$

To ease the numerical solution, as will be discussed in Sub. 4.1.5, the solid mass-specific internal energy is linearized as

$$e_{\mathrm{S}}\left(T_{\mathrm{S}}\right)=\alpha_{1}T_{\mathrm{S}}+\alpha_{2}. \tag{4.15}$$

Also, using, once again, the coupling factor $g_{\mathrm{P}}$ from Eq. 3.9 to replace the fluid temperature by its mass-specific enthlapy as $T_{\mathrm{F,P}}=g_{\mathrm{P}}i_{\mathrm{F,P}}$, Eq. 4.15 yields

$$\begin{aligned}(1-\varepsilon)\,V_{\mathrm{P}}\rho_{\mathrm{S}}\frac{\left[\left(\alpha_{1,\mathrm{P}}T_{\mathrm{S,P}}+\alpha_{2,\mathrm{P}}\right)-\overset{0}{e}_{\mathrm{S,P}}\right]}{\Delta t}=\hbar_{\mathrm{P}}V_{\mathrm{P}}\left(g_{\mathrm{P}}i_{\mathrm{F,P}}-T_{\mathrm{S,P}}\right)+\\ \left[k_{\mathrm{S,eff,e}}A_{\mathrm{e}}\frac{\left(T_{\mathrm{S,E}}-T_{\mathrm{S,P}}\right)}{\Delta z}\right]-\left[k_{\mathrm{S,eff,w}}A_{\mathrm{w}}\frac{\left(T_{\mathrm{S,P}}-T_{\mathrm{S,W}}\right)}{\Delta z}\right].\end{aligned} \tag{4.16}$$

Then, solving Eq. 4.16 for $T_{\mathrm{S}}$, it yields

$$\begin{gathered}\left(-\frac{k_{\mathrm{S,eff,w}}A_{\mathrm{w}}}{\Delta z}\right)T_{\mathrm{S,W}}+\left[\frac{(1-\varepsilon)\,V_{\mathrm{P}}\rho_{\mathrm{S}}\alpha_{1,\mathrm{P}}}{\Delta t}+\hbar_{\mathrm{P}}V_{\mathrm{P}}+\frac{k_{\mathrm{S,eff,w}}A_{\mathrm{w}}}{\Delta z}\right]T_{\mathrm{S,P}}+\\ \left(-\frac{k_{\mathrm{S,eff,e}}A_{\mathrm{e}}}{\Delta z}\right)T_{\mathrm{S,E}}+\left(-\hbar_{\mathrm{P}}V_{\mathrm{P}}g_{\mathrm{P}}\right)i_{\mathrm{F,P}}=\frac{(1-\varepsilon)\,V_{\mathrm{P}}\rho_{\mathrm{S}}\left(e^{0}_{\mathrm{S,P}}-\alpha_{2,\mathrm{P}}\right)}{\Delta t}\end{gathered} \tag{4.17}$$

Finally, the effective thermal conductivities at the volume interfaces are evaluated through harmonic means as

$$\begin{aligned}k_{\mathrm{S,eff,w}}&=\frac{2k_{\mathrm{S,eff,W}}k_{\mathrm{S,eff,P}}}{k_{\mathrm{S,eff,W}}+k_{\mathrm{S,eff,P}}}\\ k_{\mathrm{S,eff,e}}&=\frac{2k_{\mathrm{S,eff,P}}k_{\mathrm{S,eff,E}}}{k_{\mathrm{S,eff,P}}+k_{\mathrm{S,eff,E}}}\end{aligned}\,. \tag{4.18}$$

### 4.1.5 Linearization of the solid mass-specific internal energy

Following Ref. [30], the solid internal energy is expressed as

$$e_{\mathrm{S}}\left(T_{\mathrm{S}}\right)=\int_{T_{ref}}^{T_{\mathrm{S}}}\left(c_{\mathrm{S}}\right)dT_{\mathrm{S}}, \tag{4.19}$$

for which the solid temperature-dependent mass-specific heat $c_{\mathrm{S}}$ is expressed as

$$c_{\mathrm{S}}=\varphi_1\left[\varphi_2+\varphi_3T_{\mathrm{S}}+\varphi_4\left(\frac{1}{T_{\mathrm{S}}^2}\right)\right], \tag{4.20}$$

with the $\varphi_{\mathrm{j}}$ coefficients being obtained for alumina by fitting the data of Ref. [133] in Eq. 4.20 and whose values are shown in Tab. 2 – the values obtained through Eq. 4.20 and the $\varphi_{\mathrm{j}}$ coefficients of Tab. 2 agree with those of Refs. [110, 134].

Table 2 – Coefficients of Eq. 4.20 for alumina obtained through data fitting.

| Coefficient | $\varphi_1$ | $\varphi_2$ | $\varphi_3$ | $\varphi_4$ |
|---|---|---|---|---|
| Value | $1.712\ 10^{3}$ | 0.658 | $6.750\ 10^{-5}$ | $-2.010\ 10^{4}$ |

Then, assuming $e_{\mathrm{S,ref}}=e_{\mathrm{S}}\left(T_{\mathrm{ref}}\right)=0$, for which the reference temperature was selected as $T_{\mathrm{ref}}=25$ °C, the solid mass-specific internal energy is obtained through integration as

$$e_{\mathrm{S}}\left(T_{\mathrm{S}}\right)=\varphi_1\left[\varphi_2\left(T_{\mathrm{S}}-T_{\mathrm{ref}}\right)+\varphi_3\left(\frac{T_{\mathrm{S}}^2-T_{\mathrm{ref}}^2}{2}\right)-\varphi_4\left(\frac{1}{T_{\mathrm{S}}}-\frac{1}{T_{\mathrm{ref}}}\right)\right]. \tag{4.21}$$

Moreover, the well-known expression

$$f\left(T_{\mathrm{S}}\right) \approx f\left(T_{\mathrm{S}} = T_{\mathrm{S,a}}\right) + \left(T_{\mathrm{S}} - T_{\mathrm{S,a}}\right) f'\left(T_{\mathrm{S}} = T_{\mathrm{S,a}}\right), \tag{4.22}$$

is used for linearizing a given function of the solid temperature $T_{\mathrm{S}}$, with $T_{\mathrm{S,a}}$ as an approximation (i.e., a guess) of $T_{\mathrm{S}}$. Then, applying Eq. 4.22 for the nonlinear terms of Eq. 4.21, they yield

$$\begin{aligned} T_{\mathrm{S}}^2 &\approx T_{\mathrm{S,a}}^2 + 2T_{\mathrm{S,a}}(T_{\mathrm{S}} - T_{\mathrm{S,a}}), \\ \tfrac{1}{T_{\mathrm{S}}} &\approx \left(\tfrac{1}{T_{\mathrm{S,a}}}\right) - \left(\tfrac{T_{\mathrm{S}} - T_{\mathrm{S,a}}}{T_{\mathrm{S,a}}^2}\right). \end{aligned} \tag{4.23}$$

Hence, using Eq. 4.23, the linearized expression for the solid mass-specific internal energy becomes

$$e_{\mathrm{S}}\left(T_{\mathrm{S}}\right) = \alpha_1 T_{\mathrm{S}} + \alpha_2, \tag{4.24}$$

for which

$$\begin{aligned} \alpha_1 &= \varphi_1 \left[\varphi_2 + \varphi_3 T_{\mathrm{S,a}} + \varphi_4 \left(\tfrac{1}{T_{\mathrm{S,a}}^2}\right)\right], \\ \alpha_2 &= \left(-\varphi_1\right) \left[\varphi_2 T_{\mathrm{ref}} + \varphi_3 \left(\tfrac{T_{\mathrm{S,a}}^2 + T_{\mathrm{ref}}^2}{2}\right) + \varphi_4 \left(\tfrac{2}{T_{\mathrm{S,a}}} - \tfrac{1}{T_{\mathrm{ref}}}\right)\right]. \end{aligned} \tag{4.25}$$

Finally, the numerical model starts each time step using the temperature distribution from the previous time step as $T_{\mathrm{S,a}}$ for the first iteration and then continuously updates $T_{\mathrm{S,a}}$.

### 4.1.6 Solid effective thermal conductivity

As depicted by Ref. [30], the solid effective thermal conductivity $k_{\mathrm{eff}}$ is obtained through the Kunii and Smith's correlation [125], which is given by

$$k_{\mathrm{eff}} = k_{\mathrm{F}} \left[\varepsilon \left(1 + \beta_1 \frac{h_{rvv} d}{k_{\mathrm{F}}}\right) + \frac{\beta_1 \left(1 - \varepsilon\right)}{\left(\frac{1}{\omega} + \frac{h_{\mathrm{rss}} d}{k_{\mathrm{F}}}\right)^{-1} + \frac{\beta_2}{\kappa}}\right]. \tag{4.26}$$

The parameter $\beta_1$ is the ratio between the effective length between centers of two neighboring solid particles in the heat flow direction and the particle diameter, which ranges from 0.9 (close packing) to 1 (loose packing) for almost all actual packed-beds. Throughout

this study, it was adopted $\beta_1 = 0.9$. Also, the parameter $\beta_2$ is the ratio between the solid particle effective heat transfer length and the particle diameter and whose value is 2/3. Moreover, the parameter $\kappa$ is the ratio between solid and fluid thermal conductivities, which is given by

$$\kappa = \frac{k_S}{k_F}. \tag{4.27}$$

Then, the void to void radiative heat transfer coefficient given by [126]

$$h_{rvv} = \frac{0.1952\left(T_F/100\right)^3}{1 + \left\{\left[\varepsilon\left(1-\epsilon_S\right)\right] / \left[2\epsilon_S\left(1-\varepsilon\right)\right]\right\}}, \tag{4.28}$$

whereas the surface-to-surface radiative heat transfer coefficient given by [126]

$$h_{rss} = 0.1952\left(\frac{\epsilon_S}{2-\epsilon_S}\right)\left(\frac{T_F}{100}\right)^3, \tag{4.29}$$

for which $T_F$ is used in Kelvin and $\epsilon_S$ is the alumina emissivity, which, following the indicative and using the total normal emissivity data of Ref. [135], is obtained through interpolation. The cubic polynomial obtained is given by

$$\epsilon_S\left(T_S\right) = 0.5201 - 0.1794T_S^* + 0.01343T_S^{*2} + 0.01861T_S^{*3}, \tag{4.30}$$

for which

$$T_S^* = \frac{T_S - 953.8151}{432.1046} \tag{4.31}$$

is used for centering and scaling the solid temperature – the data fitting of Eq. 4.30 presented $R^2 \approx 0.7$ – and $T_S$ is also used in Kelvin. With Eqs. 4.30 and 4.31 for evaluating the alumina emissivity at the lowest and highest temperatures considered for the packed-bed operation (which are shown in Tab. 1), it is possible to observe that the material emissivity varies from $\sim 0.7$ at 230 °C to $\sim 0.5$ at 700 °C, which justifies the use of a temperature-depended approach for the alumina emissivity.

Also, the alumina temperature-dependent thermal conductivity is given by [136]

$$k_S = 85.868 - 0.22972T_S + 2.607 \cdot 10^{-4}T_S^2 - 1.3607 \cdot 10^{-7}T_S^3 + 2.7092 \cdot 10^{-11}T_S^4, \tag{4.32}$$

whose values agree with those of Refs. [110, 137] ($T_{\mathrm{S}}$ is used in Kelvin).

Moreover, the parameter $\omega$ in Eq. 4.26 is the ratio between the effective thickness of the fluid film adjacent to the surface of two solid particles and the particle diameter obtained through interpolation as [125]

$$\omega = \omega_1 + (\omega_2 - \omega_1)\left(\frac{\varepsilon - \varepsilon_1}{\varepsilon_2 - \varepsilon_1}\right), \tag{4.33}$$

for which $\varepsilon_1 = 0.26$ and $\varepsilon_2 = 0.476$ [125] are the minimal and maximal allowable porosities, respectively. Moreover, $\omega_{1,\mathrm{p}}$ and $\omega_{2,\mathrm{P}}$ are obtained from Ref. [125] as

$$\omega_{\mathrm{j}} = \left(\frac{1}{2}\right)\frac{\left[(\kappa-1)/\kappa\right]^2 \sin^2\left(\Theta_{\mathrm{j}}\right)}{\ln\left[\kappa - (\kappa-1)\cos\left(\Theta_{\mathrm{j}}\right)\right] - \left[(\kappa-1)/\kappa\right]\left(1-\cos\left(\Theta_{\mathrm{j}}\right)\right)} - \frac{2}{3\kappa}, \tag{4.34}$$

with $j = 1$ and $j = 2$, respectively. Furthermore, $\Theta$ is the heat flow area boundary angle for one contact point [125], then $\sin^2\left(\Theta_1\right) = 1/1.5$, $\sin^2\left(\Theta_2\right) = 1/\left(4\sqrt{3}\right)$ [125], and $\cos\left(\Theta_{\mathrm{j}}\right) = \sqrt{1 - \sin^2\left(\Theta_{\mathrm{j}}\right)}$ [129].

### 4.1.7 Volumetric heat transfer coefficient

The volumetric convection heat transfer coefficient $\hbar$ is obtained by multiplying the convection heat transfer coefficient for a spherical particle $h_{\mathrm{part}}$ by a coefficient that represents the ratio between the particles total heat transfer area and the bed total volume [138], i.e.,

$$h_{\mathrm{part}} A_{\mathrm{HT}} = \hbar V \rightarrow \hbar = h_{\mathrm{part}} \frac{A_{\mathrm{HT}}}{V}. \tag{4.35}$$

Considering that the number of spherical particles in the porous medium may be expressed as

$$n = \frac{V_{\mathrm{S}}}{V_{\mathrm{part}}} = \frac{(1-\varepsilon)V}{\left(\pi d^3/6\right)}, \tag{4.36}$$

the total heat transfer area follows as

$$A_{\mathrm{HT}} = nA_{\mathrm{part}} = n\pi d^2 = \frac{6(1-\varepsilon)V}{d}, \tag{4.37}$$

and, as shown by Refs. [138, 139],

$$\hbar = h_{\text{part}} \frac{6\,(1-\varepsilon)}{d}, \tag{4.38}$$

for which $d$ is the particle diameter. The Pfeffer's correlation [127] was adapted and used for the particle convection heat transfer coefficient as

$$h_{\text{part}} = \max \left[ \; 1.26 \left( \tfrac{1-(1-\varepsilon)^{5/3}}{W} \right)^{1/3} (cG)^{1/3} \left( \tfrac{k}{d} \right)^{2/3} \quad , \quad 2 \left( \tfrac{k}{d} \right) \; \right], \tag{4.39}$$

where

$$\gamma = 2 - 3(1-\varepsilon)^{1/3} + 3(1-\varepsilon)^{5/3} - 2(1-\varepsilon)^2, \tag{4.40}$$

$c$ and $k$ are the fluid mass-specific heat at constant pressure and thermal conductivity, respectively, and

$$G_{\text{P}} = \frac{\dot{m}_{\text{P}}}{\varepsilon A_{\text{Trans}}} = \frac{\left( \dot{m}_{\text{P,In}} + \dot{m}_{\text{P,Out}} \right)/2}{\varepsilon\,(\pi D^2/4)} \tag{4.41}$$

is the effective mass flow rate per cross-section area [30]. Furthermore, the adaptation of Eq. 4.39 is due to the limiting case of a stagnated fluid in the packed-bed, for which the Pfeffer's correlation would predict no heat transfer between fluid and solid even if a finite temperature difference existed between them (i.e., $u \to 0$, $G \to 0$, $h_{\text{part}} \to 0$). Therefore, in order to prevent this model limitation, because the analytical heat transfer lower limit for a heated isothermal sphere in a quiescent fluid medium is [110]

$$h_{\text{part}}\,(u \to 0) = \frac{2k}{d}, \tag{4.42}$$

the heat transfer coefficient given by Eq. 4.39 is taken as the maximal between that of the Pfeffer's correlation and the lower limiting value.

### 4.1.8 Pressure drop correlation

The pressure drop for a node $P$ is obtained through the modified Ergun's correlation [128] as

$$(\Delta P)_{\mathrm{P}} = \frac{\Delta z \; G_{\mathrm{P}}^2}{\rho_{\mathrm{F,P}} \; d} \left[ \xi_1 \frac{(1-\varepsilon)^2}{\varepsilon^3 \; \Psi^2} \frac{\mu_{\mathrm{F,P}}}{G_{\mathrm{P}} \; d} + \xi_2 \frac{(1-\varepsilon)}{\varepsilon^3 \Psi} \right], \tag{4.43}$$

in the same manner used by and with the same values of parameters used in Refs. [30, 91]. The first summand within the brackets is associated with the frictional loss, whereas the second summand is associated with the inertial loss. For all studies and assuming that the particles have smooth surfaces, the values of the parameters $\xi_1$ and $\xi_2$ were assumed as 180 and 1.8, respectively, as indicated by Ref. [140] – these values agree, range-wise, with those used by Refs. [30, 91]. Although the hypothesis of spherical particles was assumed, aiming for more realistic results, the sphericiy $\Psi = 0.9$ was used.

### 4.1.9 Wall and lids energy equations

The domain for the composed wall is axially and radially discretized, whereas the domains for the composed lids are only axially discretized. The insulation and the ground thicknesses are defined as $t_{\mathrm{i}} = t_{\mathrm{g}} = 0.2$ m. The steel wall thickness is calculated to bear the internal high working pressure as [141]

$$t_{\mathrm{st}} = \frac{P\left(D + 2t_{\mathrm{i}}\right)}{2\left(\sigma_{\mathrm{st}} - 0.6P\right)}, \tag{4.44}$$

where $P$ is the fluid maximal working pressure and $\sigma_{\mathrm{st}} = 140$ MPa is the material yield strength, whose value of already accounts for the material tensile strength reduction due to the high working temperature and a safety factor.

For the composed wall and lids domains, dedicated diffusion-based finite-volumes numerical routines are employed for solving their temperature fields. Both numerical routines are based on the discretization of the energy equation for a solid [109], which is similar to Eq. 4.9 and given by

$$\frac{\partial\left(\rho_{\mathrm{Wall}} c_{\mathrm{Wall}} T_{\mathrm{Wall}}\right)}{\partial t} = \vec{\nabla} \cdot \left(k_{\mathrm{Wall}} \vec{\nabla} T_{\mathrm{Wall}}\right), \tag{4.45}$$

for which the subscript $Wall$ is loosely used for indicating all layers of both the wall and the lids. The thermophysical properties of the three composing materials are considered constant throughout all studies. Following the same steps between Eqs. 4.9 and 4.12 for the composed lateral wall, using a two-dimension model in cylindrical coordinates ($z$ and $r$), and implicitly evaluating the temporal terms, the energy conservation equation for a central node of the wall yields

$$\begin{aligned} V_{\mathrm{Wall,P}}\rho_{\mathrm{Wall,P}}c_{\mathrm{Wall,P}}\left(T_{\mathrm{Wall,P}}-T^{0}_{\mathrm{Wall,P}}\right)= \\ \left(k_{\mathrm{Wall}}A_{\mathrm{Wall}}\frac{\partial T_{\mathrm{Wall}}}{\partial z}\right)_{\mathrm{e}}\Delta t+\left(k_{\mathrm{Wall}}A_{\mathrm{Wall}}\frac{\partial T_{\mathrm{Wall}}}{\partial z}\right)_{\mathrm{w}}\Delta t+ \\ \left(k_{\mathrm{Wall}}A_{\mathrm{Wall}}\frac{\partial T_{\mathrm{Wall}}}{\partial r}\right)_{\mathrm{re}}\Delta t+\left(k_{\mathrm{Wall}}A_{\mathrm{Wall}}\frac{\partial T_{\mathrm{Wall}}}{\partial r}\right)_{\mathrm{ri}}\Delta t, \end{aligned} \tag{4.46}$$

for which the subscripts $re$ and $ri$ indicate outward and inward radial interfaces, respectively. Also, the wall areas and volume are given by

$$\begin{aligned} A_{\mathrm{Wall,e}}=A_{\mathrm{Wall,w}}&=\frac{\pi\left(r^{2}_{\mathrm{re}}-r^{2}_{\mathrm{ri}}\right)}{4}, \\ A_{\mathrm{Wall,ri}}&=2\pi r_{\mathrm{ri}}\Delta z, \\ A_{\mathrm{Wall,re}}&=2\pi r_{\mathrm{re}}\Delta z, \\ V_{\mathrm{Wall}}&=\frac{\pi\left(r^{2}_{\mathrm{re}}-r^{2}_{\mathrm{ri}}\right)}{4}\Delta z. \end{aligned} \tag{4.47}$$

Using CDS for the derivatives on the RHS of Eq. 4.46 and dividing it by the time step $\Delta t$, it yields

$$\begin{aligned} V_{\mathrm{Wall,P}}\rho_{\mathrm{Wall,P}}c_{\mathrm{Wall,P}}\frac{\left(T_{\mathrm{Wall,P}}-T^{0}_{\mathrm{Wall,P}}\right)}{\Delta t}= \\ k_{\mathrm{Wall,e}}A_{\mathrm{Wall,e}}\frac{\left(T_{\mathrm{Wall,E}}-T_{\mathrm{Wall,P}}\right)}{\Delta z}+k_{\mathrm{Wall,w}}A_{\mathrm{Wall,w}}\frac{\left(T_{\mathrm{Wall,W}}-T_{\mathrm{Wall,P}}\right)}{\Delta z}+ \\ k_{\mathrm{Wall,re}}A_{\mathrm{Wall,re}}\frac{\left(T_{\mathrm{Wall,RE}}-T_{\mathrm{Wall,P}}\right)}{r_{\mathrm{RE}}-r_{\mathrm{P}}}+k_{\mathrm{Wall,ri}}A_{\mathrm{Wall,ri}}\frac{\left(T_{\mathrm{Wall,RI}}-T_{\mathrm{Wall,P}}\right)}{r_{\mathrm{RI}}-r_{\mathrm{P}}}, \end{aligned} \tag{4.48}$$

for which $\Delta r_{\mathrm{re}}=\left(r_{\mathrm{RE}}-r_{\mathrm{P}}\right)$ and $\Delta r_{\mathrm{ri}}=\left(r_{\mathrm{RI}}-r_{\mathrm{P}}\right)$ are, respectively, the distances in the radial direction between the volume centers of the $RE$ (radial outward) and $P$ and $RI$

(radial inward) and $P$ nodes. Even though for the present study each material layer is uniformly discretized in $N_{\mathrm{z}}$ elements of length $\Delta z$ in the axial direction and $N_{\mathrm{r}}$ elements in the radial direction, their thicknesses are variable, so the distance between centers in the radial direction is not necessarily uniform. Then, solving Eq. 4.48 for $T_{\mathrm{Wall,P}}$, it yields

$$\begin{aligned} T_{\mathrm{Wall,P}}\Bigg[\frac{\left(V_{\mathrm{Wall,P}}\rho_{\mathrm{Wall,P}}c_{\mathrm{Wall,P}}\right)}{\Delta t}+\frac{\left(k_{\mathrm{Wall,e}}A_{\mathrm{Wall,e}}\right)}{\Delta z}+\frac{\left(k_{\mathrm{Wall,w}}A_{\mathrm{Wall,w}}\right)}{\Delta z}+ \\ \frac{\left(k_{\mathrm{Wall,re}}A_{\mathrm{Wall,re}}\right)}{(\Delta r)_{\mathrm{re}}}+\frac{\left(k_{\mathrm{Wall,ri}}A_{\mathrm{Wall,ri}}\right)}{(\Delta r)_{\mathrm{ri}}}\Bigg]=\frac{\left(V_{\mathrm{Wall,P}}\rho_{\mathrm{Wall,P}}c_{\mathrm{Wall,P}}\right)}{\Delta t}T^{0}_{\mathrm{Wall,P}}+ \\ \frac{\left(k_{\mathrm{Wall,e}}A_{\mathrm{Wall,e}}\right)}{\Delta z}T_{\mathrm{Wall,E}}+\frac{\left(k_{\mathrm{Wall,w}}A_{\mathrm{Wall,w}}\right)}{\Delta z}T_{\mathrm{Wall,W}}+ \\ \frac{\left(k_{\mathrm{Wall,re}}A_{\mathrm{Wall,re}}\right)}{(\Delta r)_{\mathrm{re}}}T_{\mathrm{Wall,RE}}+\frac{\left(k_{\mathrm{Wall,ri}}A_{\mathrm{Wall,ri}}\right)}{(\Delta r)_{\mathrm{ri}}}T_{\mathrm{Wall,RI}}. \end{aligned} \tag{4.49}$$

Furthermore, the thermal conductivities at the volume interfaces are evaluated as

$$\begin{aligned} k_{\mathrm{Wall,w}}&=\frac{2k_{\mathrm{Wall,W}}k_{\mathrm{Wall,P}}}{k_{\mathrm{Wall,W}}+k_{\mathrm{Wall,P}}}, \\ k_{\mathrm{Wall,e}}&=\frac{2k_{\mathrm{Wall,P}}k_{\mathrm{Wall,E}}}{k_{\mathrm{Wall,P}}+k_{\mathrm{Wall,E}}}, \\ k_{\mathrm{Wall,re}}&=\frac{(\Delta r)_{\mathrm{P}}+(\Delta r)_{\mathrm{RE}}}{\frac{(\Delta r)_{\mathrm{P}}}{k_{\mathrm{Wall,P}}}+\frac{(\Delta r)_{\mathrm{RE}}}{k_{\mathrm{Wall,E}}}}, \\ k_{\mathrm{Wall,ri}}&=\frac{(\Delta r)_{\mathrm{RI}}+(\Delta r)_{\mathrm{P}}}{\frac{(\Delta r)_{\mathrm{RI}}}{k_{\mathrm{Wall,RI}}}+\frac{(\Delta r)_{\mathrm{P}}}{k_{\mathrm{Wall,P}}}}, \end{aligned} \tag{4.50}$$

i.e., harmonic means as those of Eq. 4.18 are used for the axial direction, whereas length-weighted harmonic means are used for the radial direction. In Eq. 4.50, $(\Delta r)_{\mathrm{RE}}$ and $(\Delta r)_{\mathrm{RI}}$ are, respectively, the radial outward and inward nodes radial lengths. For each layer, i.e., insulation, steel, and ground, the node radial length varies as

$$(\Delta r)_{\mathrm{i}}=\frac{t_{\mathrm{i}}}{N_{\mathrm{i}}},(\Delta r)_{\mathrm{st}}=\frac{t_{\mathrm{st}}}{N_{\mathrm{st}}},(\Delta r)_{\mathrm{g}}=\frac{t_{\mathrm{g}}}{N_{\mathrm{g}}}. \tag{4.51}$$

At the wall inner radial surface, there is heat transfer due to convection between fluid and the insulation layer; whereas, at the wall outer radial surface there is heat transfer

due to conduction to the ground. Thus, for wall volumes at the inner radial surface, the fourth term on the RHS of Eq. 4.46 should be replaced by

$$\left(k_{\mathrm{Wall}}A_{\mathrm{Wall}}\frac{\partial T_{\mathrm{Wall}}}{\partial r}\right)_{\mathrm{ri}}\Delta t \rightarrow h_{\mathrm{Wall,P}}A_{\mathrm{Wall,P}}\left(T_{\mathrm{F,P}}-T_{\mathrm{Wall,P}}\right)\Delta t, \tag{4.52}$$

and, for wall volumes at the outer radial surface, the third term on the RHS of Eq. 4.46 should be replaced by

$$\left(k_{\mathrm{Wall}}A_{\mathrm{Wall}}\frac{\partial T_{\mathrm{Wall}}}{\partial r}\right)_{\mathrm{re}}\Delta t \rightarrow k_{\mathrm{g}}A_{\mathrm{Wall,P}}\frac{\left(T_{\mathrm{g}}-T_{\mathrm{Wall,P}}\right)}{\left(\Delta r\right)_{\mathrm{P}}/2}\Delta t. \tag{4.53}$$

The wall outer axial surfaces are considered to be perfectly thermally insulated, thus, for wall volumes at the outer axial right surface, the first term on the RHS of Eq. 4.46 should be replaced by

$$\left(k_{\mathrm{Wall}}A_{\mathrm{Wall}}\frac{\partial T_{\mathrm{Wall}}}{\partial z}\right)_{\mathrm{e}}\Delta t \rightarrow 0, \tag{4.54}$$

and, for wall volumes at the outer axial left surface, the second term on the RHS of Eq. 4.46 should be replaced by

$$\left(k_{\mathrm{Wall}}A_{\mathrm{Wall}}\frac{\partial T_{\mathrm{Wall}}}{\partial z}\right)_{\mathrm{w}}\Delta t \rightarrow 0. \tag{4.55}$$

Then, with Eqs. 4.52, 4.53, 4.54, and 4.55 for modifying Eq. 4.46 as necessary, a set of equations for all wall volumes is obtained.

For both lids, the numerical expression is simpler than that for the wall because the heat transfer is one-dimensional, hence

$$\begin{aligned} V_{\mathrm{Lid,P}}\rho_{\mathrm{Lid,P}}c_{\mathrm{Lid,P}}\left(T_{\mathrm{Lid,P}}-T^{0}_{\mathrm{Lid,P}}\right) = \\ \left(k_{\mathrm{Lid}}A_{\mathrm{Lid}}\frac{\partial T_{\mathrm{Lid}}}{\partial z}\right)_{\mathrm{e}}\Delta t+\left(k_{\mathrm{Lid}}A_{\mathrm{Lid}}\frac{\partial T_{\mathrm{Lid}}}{\partial z}\right)_{\mathrm{w}}\Delta t, \end{aligned} \tag{4.56}$$

Following similar steps to those for the wall, the equivalent of Eq. 4.49 for a central node

of one lid is

$$T_{\mathrm{Lid,P}}\left[\frac{\left(V_{\mathrm{Lid,P}}\rho_{\mathrm{Lid,P}}c_{\mathrm{Lid,P}}\right)}{\Delta t}+\frac{\left(k_{\mathrm{Lid,e}}A_{\mathrm{Lid,e}}\right)}{\Delta z}+\frac{\left(k_{\mathrm{Lid,w}}A_{\mathrm{Lid,w}}\right)}{\Delta z}\right]= \frac{\left(V_{\mathrm{Lid,P}}\rho_{\mathrm{Lid,P}}c_{\mathrm{Lid,P}}\right)}{\Delta t}T^{0}_{\mathrm{Lid,P}}+\frac{\left(k_{\mathrm{Lid,e}}A_{\mathrm{Lid,e}}\right)}{\Delta z}T_{\mathrm{Lid,E}}+\frac{\left(k_{\mathrm{Lid,w}}A_{\mathrm{Lid,w}}\right)}{\Delta z}T_{\mathrm{Lid,W}}, \tag{4.57}$$

with interface thermal conductivities following Eq. 4.50.

The lids outer radial surfaces are also considered to be perfectly thermally insulated. Moreover, at the inner axial surfaces of each lid, there is heat transfer due to convection between fluid and the insulation layer; whereas, at the outer axial surface of each lid, there is heat transfer due to conduction to the ground. Thus, for a lid volume in the inner axial surface of the left lid, the first term on the RHS of Eq. 4.49 should be replaced by

$$\left(k_{\mathrm{Lid}}A_{\mathrm{Lid}}\frac{\partial T_{\mathrm{Lid}}}{\partial z}\right)_{\mathrm{e}}\Delta t\rightarrow h_{\mathrm{Wall,P}}A_{\mathrm{Lid,P}}\left(T_{\mathrm{F,P}}-T_{\mathrm{Lid,P}}\right)\Delta t, \tag{4.58}$$

and, for a lid volume at the outer axial surface of the left lid, the second term on the RHS of Eq. 4.49 should be replaced by

$$\left(k_{\mathrm{Lid}}A_{\mathrm{Lid}}\frac{\partial T_{\mathrm{Lid}}}{\partial z}\right)_{\mathrm{w}}\Delta t\rightarrow k_{\mathrm{g}}A_{\mathrm{Lid,P}}\frac{\left(T_{\mathrm{g}}-T_{\mathrm{Lid,P}}\right)}{\left(\Delta z\right)_{\mathrm{P}}/2}\Delta t. \tag{4.59}$$

For the right lid, equivalent expressions to Eqs. 4.58 and 4.59 may be obtained according to the shifted volume position. Furthermore, the convective heat transfer coefficient used for the lids is assumed as that of the closest wall element.

The values of the thermophysical properties considered for the materials composing the lateral wall and the lids are shown in Tab. 3.

Table 3 – Thermophysical properties for insulation, steel, and ground.

| | $k$ [W/(m · K)] | $\rho$ [kg/m$^3$] | $c$ [J/(kg · K)] |
|---|---|---|---|
| Insulation (i) [91] | 0.25 | 250 | 1190 |
| Steel (st) [91] | 11.7 | 8050 | 483.1 |
| Ground (g) [142] | 2.9 | 2650 | 732.2 |

### 4.1.10 Wall heat transfer coefficient

The convection heat transfer coefficient between the fluid and the inner walls of the TES device is given, following the indicatives of Refs. [30, 129, 130], by

$$h_{\text{Wall}} = h_{\text{Wall}}^{\text{Cv}} + h_{\text{Wall}}^{\text{Cd,Ra}}, \tag{4.60}$$

i.e., the summation of a convective effect due to the fluid (Cv) and a conductive-radiative effect due to the solid (Cd,Ra). For the convective term, the correlation of Ref. [139] is employed as

$$h_{\text{Wall}}^{\text{Cv}} = \left(2.58 Re_{\text{d}}^{1/3} Pr^{1/3} + 0.094 Re_{\text{d}}^{4/5} Pr^{2/5}\right) \left(\frac{k_{\text{F}}}{d}\right). \tag{4.61}$$

Then, for the conductive-radiative term, according to Ref. [130], the expression is given by

$$h_{\text{Wall}}^{\text{Cd,Ra}} = \frac{k_{\text{Wall}}^{\text{stag}} k_{\text{eff}}^{\text{stag}}}{\left(k_{\text{eff}}^{\text{stag}} - k_{\text{Wall}}^{\text{stag}}/2\right)}, \tag{4.62}$$

for which

$$k_{\text{eff}}^{\text{stag}} = k_{\text{F}} \left[ \varepsilon \left(1 + \frac{h_{rvv} d}{k_{\text{F}}}\right) + \frac{(1-\varepsilon)}{\left(\frac{1}{\omega} + \frac{h_{\text{rss}} d}{k_{\text{F}}}\right)^{-1} + \left(\frac{2k_{\text{F}}}{3k_{\text{S}}}\right)} \right] \tag{4.63}$$

and

$$k_{\text{Wall}}^{\text{stag}} = k_{\text{F}} \left[ \varepsilon_{\text{Wall}} \left(2 + \frac{h_{rvv} d}{k_{\text{F}}}\right) + \frac{\left(1-\varepsilon_{\text{Wall}}\right)}{\left(\frac{1}{\omega_{\text{Wall}}} + \frac{h_{\text{rss}} d}{k_{\text{F}}}\right)^{-1} + \left(\frac{1k_{\text{F}}}{3k_{\text{S}}}\right)} \right], \tag{4.64}$$

with $\kappa$, $h_{\text{rvv}}$, $h_{\text{rss}}$, and $\omega$ being given by Eqs. 4.27, 4.28, 4.29, and 4.33, respectively. Because of the large expected $D/d$ ratio, the wall porosity is assumed constant as $\varepsilon_{\text{Wall}} = 0.4$ [130, 143] (the closest packing of spheres on a flat plate), whereas $\omega_{\text{Wall}}$ is given by [144, 145]

$$\omega_{\text{Wall}} = \left(\frac{1}{4}\right) \frac{\left[(\kappa-1)/\kappa\right]^2}{\ln(\kappa) - \left[(\kappa-1)/\kappa\right]} - \frac{1}{3\kappa}. \tag{4.65}$$

### 4.1.11 Numerical routines for the TES system

All numerical routines were implemented in MATLAB® [104] with fluids thermophysical properties obtained from CoolProp [3, 4]. Following the main flowchart shown in Fig. 23, the main numerical routine is fed with input parameters (and the admissible deviations, which are detailed further on). Then, values for the variables considered are assigned and the spatial and temporal discretization parameters are obtained as functions of $L$ and $D$, as detailed in Sub. 4.1.13. After that, fields for all variables $\phi$ (i.e., $i_{\mathrm{F}}$, $T_{\mathrm{F}}$, $P_{\mathrm{F}}$, $\rho_{\mathrm{F}}$, $c_{\mathrm{F}}$, $k_{\mathrm{F}}$, $\mu_{\mathrm{F}}$, $\dot{m}_{\mathrm{F}}$, $T_{\mathrm{S}}$, $k_{\mathrm{S}}$, $h_{\mathrm{v}}$, $h_{\mathrm{Wall}}$, etc) are obtained for the steady-state, considering the TES system filled and pressurized with stationary fluid at discharging temperature and steady-state temperature distributions at lids and wall (insulation, steel, and ground layers) – because the fluid is stationary with length-wise uniform temperature, the wall and lids initial temperature distributions are easily obtained through equivalent resistances from undergraduate heat transfer literature.

For each time step of the system charging process, which is shown by the light blue shade and indicated as "Charging" in Fig. 23, a specific numerical routine, which is indicated by the dashed line rectangle and named "Packed-bed inner routine", is called for solving the new fields. Such a routine, which is shown in Fig. 24 and detailed further on, takes data from the previous time step and iteratively obtains the new fields. Then, the $Bi \leq 0.1$ assumption (which is also discussed further on) is checked: if OK, the algorithm continues; if otherwise, the simulation stops with an error flag. If the $Bi$ assumption is satisfied, the algorithm checks the charging stopping criterion $\Delta T_{\mathrm{F,Out,C}}$ through the fluid outlet temperature. If $T_{\mathrm{F,Out,C}} \leq T_{\mathrm{D}} + \Delta T_{\mathrm{F,Out,C}}$, the algorithm checks if the current time is less than the maximal charging time $t_{\mathrm{C,Max}}$: if it is not, the charging is stopped and the charging time is defined as $t = t_{\mathrm{C,Max}}$; if otherwise, the current fields are used as inputs for the inner routine for the next time, i.e., $t = t + \Delta t$. Now, if $T_{\mathrm{F,Out,C}} > T_{\mathrm{D}} + \Delta T_{\mathrm{F,Out,C}}$, the charging is stopped and the charging time is defined as that of the previous time step (i.e., as $t_{\mathrm{C}} = t - \Delta t$). Then the pumping power is calculated and the charging data is stored.

When the charging process ends, the flow stops, thus the mass flow rate field becomes null and the pressure field uniform at the inlet value. Then, for starting the

Figure 23 – Main numerical routine flowchart for the packed-bed TES system.

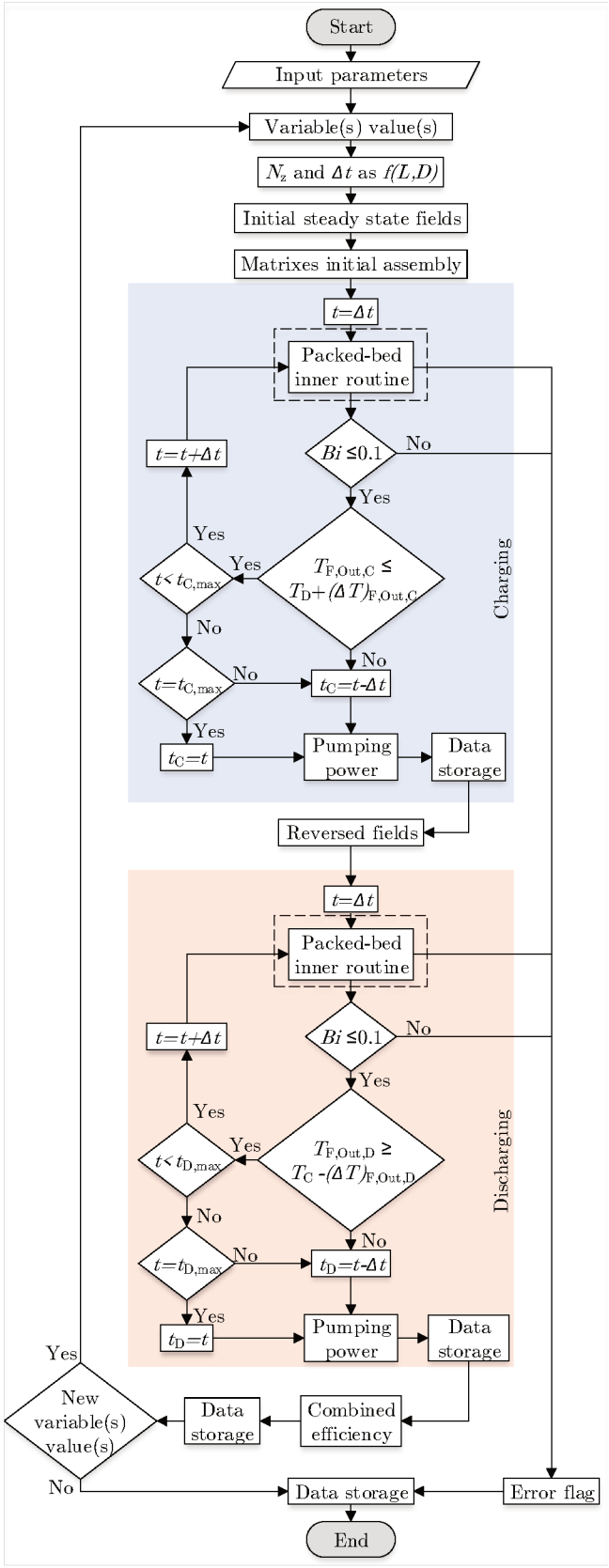

Figure 24 – Inner numerical routine flowchart for the packed-bed TES system.

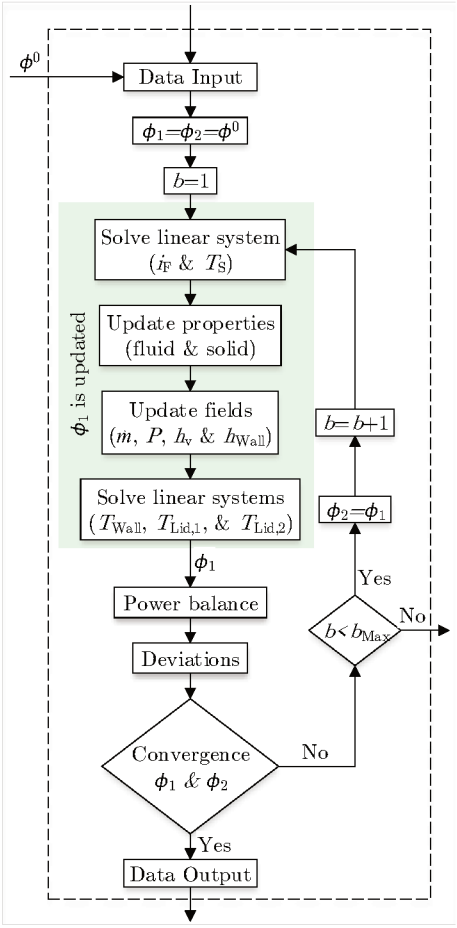


discharging process, the fields of $i_F$ and $T_S$ (and, consequently, all property fields) are axially reversed, which is indicated in Fig. 23 as "Reversed fields". This step is useful for enabling the same inner routine to be used for the discharge, which occurs in the opposite direction to the charge, without any major modifications.

Then, the algorithm for the discharging process, which is shown by the light red shade and indicated as "Discharging" in Fig. 23, follows similar steps to those of the charging process and, therefore, further discussions are omitted.

Following the discharge end, the combined efficiency is calculated and all relevant data are stored. Then, the algorithm checks if there are any other variable values to be considered: if there is any, the whole process thus far described is repeated; if otherwise, all relevant data are stored and the algorithm ends. It is worth mentioning that a similar algorithm structure is utilized for optimizing variables, i.e., instead of a loop for evaluating the system performance for a given set of variable values, an optimization algorithm is called.

Now, for the packed-bed inner routine, Fig. 24 shows its routine flowchart. The numerical algorithm receives input data and the previous time step fields, which are generically represented by $\phi^0$. The routine starts based on $\phi^0$, i.e., it initially assumes the new fields as $\phi_1 = \phi^0$. The algorithm is based on successive substitutions, then an auxiliary set of fields is also initialized as $\phi_2 = \phi^0$. The iteration counter $b$ is set to 1. For obtaining the new fields, the algorithm performs the tasks encompassed by the light green shade in Fig. 24. A sparse linear system of equations is assembled using Eqs. 4.4 and 4.17 for solving the fluid mass-specific enthalpy and the porous medium temperature fields simultaneously. With the new values of $T_{\mathrm{S}}$, the solid properties are updated. Also, with the new values of $i_{\mathrm{F}}$ for the iteration $b$, fluid properties (i.e., $T_{\mathrm{F}}$, $\rho_{\mathrm{F}}$, $c_{\mathrm{F}}$, $k_{\mathrm{F}}$, and $\mu_{\mathrm{F}}$) are updated as $f\left(i_{\mathrm{F,P}}, P_{\mathrm{F,P}}^{\text{b-1}}\right)$, where $P_{\mathrm{F,P}}^{\text{b-1}}$ is the fluid pressure interpolated at the node $P$ center using the pressures at the node interfaces from the previous iteration, i.e., $P_{\mathrm{F,w}}^{\text{b-1}}$ and $P_{\mathrm{F,e}}^{\text{b-1}}$. Similarly, the volume-specific mass at the nodes interfaces required for Eq. 4.4 is obtained through interpolation/extrapolation using the values at the center nodes. Then, the mass flow rate field is updated at each node $P$ interface(except for the inlet mass flow rate, which is a boundary condition) through a cumulative summation as

$$\dot{m}_{\mathrm{F,j}} = \dot{m}_{\mathrm{F,1}} - \sum_{k=1}^{j-1} \left[ \frac{\varepsilon V_{\mathrm{P}} \left( \rho_{\mathrm{F,P}} - \rho_{\mathrm{F,P}}^{0} \right)}{\Delta t} \right]_{\mathrm{k}}, \tag{4.66}$$

with $\dot{m}_{\mathrm{F,1}}$ as the inlet mass flow rate, which is constant for a given time step and iteration. So, Eq. 4.66 may be regarded as the conservation of mass equation, for which the term within the brackets indicates the net mass variation within a discretized node and a time step, which is related to the fluid acceleration. Similarly to for the mass flow rate, the pressure field is updated as

$$P_{\mathrm{F,j}} = P_{\mathrm{F,1}} - \sum_{k=1}^{j-1} \left[ (\Delta P)_{\mathrm{P}} \right]_{\mathrm{k}}, \tag{4.67}$$

with $P_{\mathrm{F,1}}$ as the inlet pressure, which is also constant for a given time step and iteration, and $(\Delta P)_{\mathrm{P}}$ as the pressure drop obtained with the Modified Ergun's correlation of Ref. [128], which was detailed in Sub. 4.1.8. Furthermore, the volumetric and the wall heat transfer convective coefficients are updated using the expressions already detailed in Subs. 4.1.7

and 4.1.10, respectively. Then, with the updated wall heat transfer convective coefficient field, the new wall and lids temperature fields are obtained by solving a specific sparse linear system of equations for each, which are based on the expressions already detailed in Sub. 4.1.9. Thus, the new fields $\phi_1$ are obtained.

The routine, then, verifies the power balance, as will be detailed in Sub. 4.1.12, and calculates the deviations of $\phi_1$ with respect to $\phi_2$. Because not only properties, but also pressure drop and heat transfer coefficients are temperature-dependent, at each time step, the iterative solution requires the convergence of fluid mass-specific enthalpy, temperature, volume-specific mass, pressure, and mass flow rate; porous medium, wall and lids temperatures; heat transfer coefficients (to the porous medium, the wall, and the lids). The convergence criteria between subsequent iterations are divided into two categories, i.e., absolute and relative, whose values are shown in Tab. 4.

Table 4 – Convergence criteria values.

| Variable | $T_{\mathrm{F}}$ | $P$ | $T_{\mathrm{S}}$ | $i_{\mathrm{F}}$ | $\rho_{\mathrm{F}}$ | $\dot{m}$ | $\hbar, h_{\mathrm{Wall}}$ | $T_{\mathrm{Wall}}, T_{\mathrm{Lid}}$ |
|---|---|---|---|---|---|---|---|---|
| Absolute | 0.05 °C | 0.1 Pa | 0.05 °C | – | – | – | – | – |
| Relative [%] | – | – | – | 0.01 | 0.1 | 0.1 | 0.1 | 0.05 |

If the convergence between $\phi_1$ and $\phi_2$ for all parameters including the power balance is achieved, the routine outputs the $\phi_1$ fields to the main routine (i.e., that of Fig. 23); if otherwise, the routine checks if the iteration counter is smaller than the maximal iteration number $b_{\mathrm{Max}}$. If $b \geq b_{\mathrm{Max}}$, the inner routine stops and outputs an error flag to the main routine; if otherwise, the routine updates the fields $\phi_2 = \phi_1$ and the iteration counter $b = b + 1$ and proceeds to resolve the sparse linear system of equations for $i_{\mathrm{F}}$ and $T_{\mathrm{S}}$, so the iterative loop is set up.

Additionally, it is worth mentioning that the formulation presented thus far assumes that, for each axial section, the solid spheres comprising the porous medium are isothermal and the lumped capacitance method may be applied. Hence, it is required such an assumption to be verified once convergence within a time step is achieved. That was performed through checking if the condition of $Bi \leq 0.1$ [110] is not violated at each node.

Then, for the $n$ spherical particles within an axial section, it means

$$Bi = \frac{h_{\text{part}}\left(\frac{nV_{\text{part}}}{nA_{\text{HT,part}}}\right)}{k_{\text{S}}} = \frac{h_{\text{part}}\left(\frac{V_{\text{part}}}{A_{\text{HT,part}}}\right)}{k_{\text{S}}} = \frac{\left[\hbar\frac{d}{6(1-\varepsilon)}\right]\left[\frac{\left(\pi d^3/6\right)}{\pi d^2}\right]}{k_{\text{S}}} = \frac{\left[\hbar\frac{d^2}{36(1-\varepsilon)}\right]}{k_{\text{S}}} = \frac{\hbar d^2}{36\left(1-\varepsilon\right)k_{\text{S}}} \leq 0.1. \tag{4.68}$$

### 4.1.12 TES power balance equations

The TES overall power balance is obtained by the summation of the net thermal power delivered/retrieved by the HTF ($\dot{E}^{\text{Net}}$), the overall thermal power stored ($\dot{E}^{\text{Sto}}$), the power related to pressure variation ($\dot{E}^{\Delta\text{P}}$), and the overall thermal power associated to losses to the surrounding environment ($\dot{E}^{\text{Loss}}$) as

$$\lambda = \dot{E}^{\text{Net}} - \dot{E}^{\text{Sto}} + \dot{E}^{\Delta\text{P}} - \dot{E}^{\text{Loss}}, \tag{4.69}$$

where $\lambda$ is the overall power deviation, which tends to zero as the convergence is reached. Considering the terms on the RHS of Eq. 4.69, first, the net thermal power delivered/retrieved by the HTF is given by

$$\dot{E}^{\text{Net}} = \dot{m}_{\text{In}} i_{\text{In}} - \dot{m}_{\text{Out}} i_{\text{Out}}. \tag{4.70}$$

Secondly, the overall thermal power stored is given by

$$\dot{E}^{\text{Sto}} = \dot{E}^{\text{Sto}}_{\text{S}} + \dot{E}^{\text{Sto}}_{\text{F}} + \dot{E}^{\text{Sto}}_{\text{Lid,1}} + \dot{E}^{\text{Sto}}_{\text{Lid,2}} + \dot{E}^{\text{Sto}}_{\text{Wall}}, \tag{4.71}$$

which accounts for the temporal variation of the thermal energy stored in the solid porous medium (S), in the fluid within the porous medium (F), in both lids (Lid), and in the composed lateral wall (Wall). Thirdly, the power related to the pressure variation is given by

$$\dot{E}^{\Delta\text{P}} = \sum_{j=1}^{N_{\text{z}}} \left[ \varepsilon V \frac{\left(P_{\text{F,P}} - P^{0}_{\text{F,P}}\right)}{\Delta t} + \frac{\dot{m}_{\text{F,e}}}{\rho_{\text{F,e}}}\left(P_{\text{F,e}} - P_{\text{F,P}}\right) + \frac{\dot{m}_{\text{F,w}}}{\rho_{\text{F,w}}}\left(P_{\text{F,P}} - P_{\text{F,w}}\right) \right]_j. \tag{4.72}$$

Finally, the thermal loss is given by

$$\dot{E}^{\mathrm{Loss}} = \dot{E}^{\mathrm{Loss}}_{\mathrm{Lid,1}} + \dot{E}^{\mathrm{Loss}}_{\mathrm{Lid,2}} + \dot{E}^{\mathrm{Loss}}_{\mathrm{Wall}}, \tag{4.73}$$

which includes the thermal losses to the surrounding ground through both lids and the composed lateral wall.

Moreover, the thermal power stored in the solid porous medium is given by

$$\dot{E}^{\mathrm{Sto}}_{\mathrm{S}} = (1-\varepsilon)\,\rho_{\mathrm{S}} \sum_{j=1}^{N_{\mathrm{z}}} \left[ V \frac{\left(e_{\mathrm{S,P}} - e^{0}_{\mathrm{S,P}}\right)}{\Delta t} \right]_j . \tag{4.74}$$

Similarly, for the fluid within the porous medium, the thermal power stored is given by

$$\dot{E}^{\mathrm{Sto}}_{\mathrm{F}} = \varepsilon \sum_{j=1}^{N_{\mathrm{z}}} \left[ V \frac{\left(\rho_{\mathrm{F}} i_{\mathrm{F,P}} - \rho^{0}_{\mathrm{F}} \overset{.0}{i}_{\mathrm{F,P}}\right)}{\Delta t} \right]_j . \tag{4.75}$$

Also, the thermal power stored in the lids is given by

$$\dot{E}^{\mathrm{Sto}}_{\mathrm{Lid}} = \rho_{\mathrm{Lid}} c_{\mathrm{Lid}} \sum_{j=1}^{N_{\mathrm{i}}+N_{\mathrm{st}}+N_{\mathrm{g}}} \left[ V_{\mathrm{Lid}} \frac{\left(T_{\mathrm{Lid}} - T^{0}_{\mathrm{Lid}}\right)}{\Delta t} \right]_j , \tag{4.76}$$

and in the composed wall by

$$\dot{E}^{\mathrm{Sto}}_{\mathrm{Wall}} = \rho_{\mathrm{Wall}} c_{\mathrm{Wall}} \sum_{j=1}^{N_{\mathrm{z}}(N_{\mathrm{i}}+N_{\mathrm{st}}+N_{\mathrm{g}})} \left[ V_{\mathrm{Wall}} \frac{\left(T_{\mathrm{Wall}} - T^{0}_{\mathrm{Wall}}\right)}{\Delta t} \right]_j . \tag{4.77}$$

Furthermore, the thermal losses through conduction to the surrounding ground through each lid is given by

$$\dot{E}^{\mathrm{Loss}}_{\mathrm{Lid}} = k_{\mathrm{g}} \frac{\pi D^2}{4} \frac{\left(T^{\mathrm{Lid}}_{\mathrm{Ext}} - T_{\mathrm{g}}\right)}{0.5(\Delta z)_g}, \tag{4.78}$$

and through the composed lateral wall by

$$\dot{E}^{\mathrm{Loss}}_{\mathrm{Wall}} = k_{\mathrm{g}} \pi \left[ D + 2\left(t_{\mathrm{i}} + t_{\mathrm{st}} + t_{\mathrm{g}}\right) \right] \Delta z \sum_{j=1}^{N_{\mathrm{z}}} \left\{ \frac{\left(T^{\mathrm{Lid}}_{\mathrm{Ext}} - T_{\mathrm{g}}\right)}{0.5(\Delta r)_{\mathrm{g}}} \right\}. \tag{4.79}$$

Finally, for the overall thermal power balance, the convergence is assumed satisfied when

$$\frac{100\,|\lambda|}{\max\left(\begin{array}{c}\left|\dot{E}^{\mathrm{Net}}\right|,\left|\dot{E}^{\mathrm{Sto}}_{\mathrm{S}}\right|,\left|\dot{E}^{\mathrm{Sto}}_{\mathrm{F}}\right|,\left|\dot{E}^{\mathrm{Sto}}_{\mathrm{Lid,1}}\right|,\left|\dot{E}^{\mathrm{Sto}}_{\mathrm{Lid,2}}\right|,\\ \left|\dot{E}^{\mathrm{Sto}}_{\mathrm{Wall}}\right|,\left|\dot{E}^{\Delta\mathrm{P}}\right|,\left|\dot{E}^{\mathrm{Loss}}_{\mathrm{Lid,1}}\right|,\left|\dot{E}^{\mathrm{Loss}}_{\mathrm{Lid,2}}\right|,\left|\dot{E}^{\mathrm{Loss}}_{\mathrm{Wall}}\right|,\end{array}\right)} < 0.5, \tag{4.80}$$

which represents a percentage ratio between the overall power balance deviation and the maximal TES power exchange within a time step, smaller than 0.5.

### 4.1.13 Spatial and temporal discretization independences

The mesh independence studies comprise both the spatial ($N_{\mathrm{z}}$) and the temporal ($\Delta t$) discretization. Because the main figure of merit of this work is the TES thermal-hydraulic charging-discharging combined efficiency, the analyses are held regarding $\eta_{\mathrm{Comb}}$. Thus, the discretization independence is considered to be achieved when the absolute percentage variation of $\eta_{\mathrm{Comb}}$ obtained for a finer $(j+1)$ set of parameters $N_{\mathrm{z,j+1}}$ and $(\Delta t)_{\mathrm{j+1}}$ with respect to $N_{\mathrm{z,j}}$ and $(\Delta t)_{\mathrm{j}}$ set of parameters is smaller than or equal to 1%, i.e.,

$$100\frac{\left|\eta_{\mathrm{Comb}}\left(N_{\mathrm{z,j+1}},(\Delta t)_{\mathrm{j+1}}\right)-\eta_{\mathrm{Comb}}\left(N_{\mathrm{z,j}},(\Delta t)_{\mathrm{j}}\right)\right|}{\eta_{\mathrm{Comb}}\left(N_{\mathrm{z,j}},(\Delta t)_{\mathrm{j}}\right)} \leq 1. \tag{4.81}$$

Then, the parameters $N_{\mathrm{z,j}}$ and $(\Delta t)_{\mathrm{j}}$ are selected for the converged meshes.

Nine pairs of length and internal diameter of the TES system were considered, which are obtained from combining $L = 1$ m, $L = 5.5$ m, and $L = 10$ m and $D = 0.5$ m, $D = 1.75$ m, and $D = 3$ m, i.e., both extreme and the middle values for each dimension. The independence studies first access the temporal converge for each spatial mesh, then, starting with $N_{\mathrm{z}} = 150$, for each combination of $L$ and $D$, $\eta_{\mathrm{Comb}}$ is evaluated for different values of $\Delta t$, which start as 30 s and are subsequently cut by half. When the temporal independence is achieved for each pair of $L$ and $D$, the number of axial elements is doubled to $N_{\mathrm{z}} = 300$ and the process for the temporal independence is repeated. After the temporal independence is achieved once again for each pair of $L$ and $D$, the spatial independence is accessed

between the respective $L$-$D$-temporal-independent results for $N_z = 150$ and $N_z = 300$. This doubled-layer process is repeated until both spatial and temporal independences are achieved simultaneously.The results obtained for $Nz$ and $\Delta t$ through this process while considering $T_C = 550$ °C, $d = 3$ mm, $\varepsilon = 0.35$, $\dot{m}_C = \dot{m}_D = 1$ kg/s, $\Delta T_{F,Out,C} = 15$ °C, and $\Delta T_{F,Out,D} = 100$ °C are shown in Tab. 5.

Table 5 – Values of $N_z$ and $\Delta t$ obtained with the discretization independence study.

| $N_z$ [–] | | | | $\Delta t$ [s] | | | |
|---|---|---|---|---|---|---|---|
| $L$ [m]\$D$ [m] | 0.5 | 1.75 | 3 | $L$ [m]\$D$ [m] | 0.5 | 1.75 | 3 |
| 1 | 300 | 150 | 300 | 1 | 3.75 | 7.5 | 15 |
| 5.5 | 150 | 300 | 600 | 5.5 | 7.5 | 15 | 30 |
| 10 | 300 | 600 | 1200 | 10 | 15 | 30 | 30 |

Therefore, the values of $N_z$ and $\Delta t$ for each pair of $L$ and $D$ considered throughout all studies are obtained through bilinear interpolation using the data of Tab. 5 and both $L$ and $D$ as entries. Also, for the wall and lids, the axial discretization was assumed as the one obtained for the bed and, from a similar mesh analysis, it was concluded that $N_r = 10$ radially-discretized elements were enough for each layer, i.e., $N_i = N_{st} = N_g = N_r$.

### 4.1.14 Verification

Once the model was implemented, the numerical routine employed was verified for correctness and outputs consistency. Such a verification was carried out with respect to Ref. [91]. With the input parameters of Ref. [91] and the numerical routine developed, the analysis was conducted by evaluating the spatial and temporal temperature profiles during the charging and discharging of a packed-bed TES device filled with alumina particles with $d = 3$ mm, $\varepsilon = 0.35$ porosity, and bed diameter and length of $D = 3.5$ m and $L = 9.1$ m, respectively. The bed was surrounded by an insulation layer with $t_{ins} = 102$ mm and an Inconel 740 metallic vessel with $t_{st} = 127$ mm – Ref. [91] provides for insulation and storage vessel properties. The comparison between results from the modeling developed and those of Ref. [91] is shown in Figs. 25 and 26, which consider a mass flow rate of 8.17 kg/s, an inlet pressure of $P = 27.5$ MPa, and inlet temperatures of $T_C = 750$ °C for charging (Fig. 25) and $T_D = 500$ °C for discharging (Fig. 26). For considering a similar heat loss condition to that of Ref. [91], in the present in-ground model, heat loss is considered through the lateral

wall only, the ground temperature was set to $T_g = 10$ °C (the external air temperature of Ref. [91]), and the thickness of the ground layer was set such that its thermal resistance equates that of the considered $h_{Air} = 5$ W/(m$^2 \cdot$ K) heat transfer coefficient to air of Ref. [91], i.e., $t_g = R_{st}\left\{\exp\left[k_g/(h_{Air}R_{st})\right] - 1\right\}$ with $R_{st} = (D/2) + t_{ins} + t_{st}$ as the external radius of the steel layer.

Figure 25 – Model validation for the charging process.

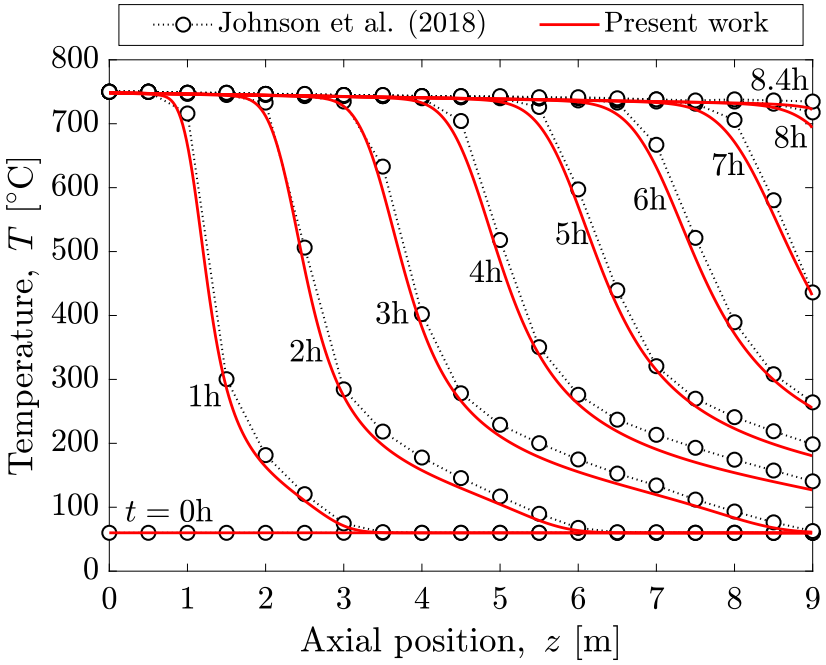


Figure 26 – Model validation for the discharging process.

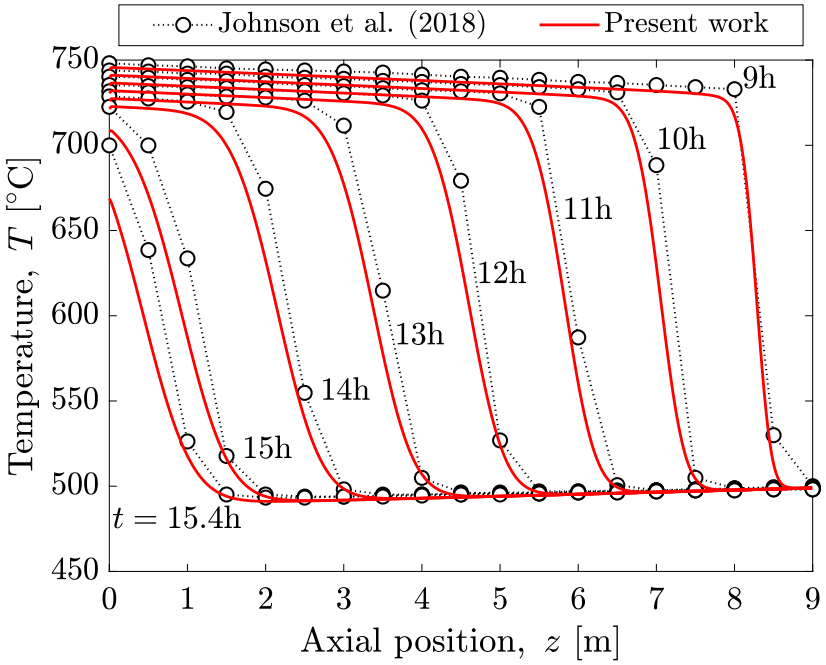

As shown in both Figs. 25 and 26, there is a good agreement between the two sets of results for the temperature profiles obtained during the charging process while the discharging profiles displayed minor discrepancies, although closely resembling their respective references in terms of temporal behavior. The occurrence of small differences in the temperature profiles between the models is reasonable due to the diverse approaches considered between the present modeling and that of Ref. [91] regarding the energy storage in the wall and heat loss. Therefore, the key point of these two figures is to demonstrate the consistency of the results and that the numerical routine was properly implemented.

#### 4.1.15 Charging and discharging processes of the TES system and their efficiencies

As previously discussed, s-$CO_2$-based packed-bed TES devices could take advantage of using characteristics of a supercritical fluid in order to develop more efficient systems. Based on that, a parametric analysis on key design and operational parameters of the charging and discharging efficiencies is presented. The efficiencies were calculated based on the definition presented by Ref. [31]. For the charging process, the efficiency is defined as the ratio between the total thermal power stored by the TES system ($\dot{E}_{\mathrm{C}}^{\mathrm{Sto}}$) and the summation of the net thermal power delivered by the HTF to the TES system ($\dot{E}_{\mathrm{C}}^{\mathrm{Net}}$) and the compressor power required to overcoming the pressure drop ($\dot{W}_{\mathrm{C}}^{\mathrm{Pump}}$) as

$$\eta_{\mathrm{C}} = \frac{\dot{E}_{\mathrm{C}}^{\mathrm{Sto}}}{\dot{E}_{\mathrm{C}}^{\mathrm{Net}} + \dot{W}_{\mathrm{C}}^{\mathrm{Pump}}}. \tag{4.82}$$

For the discharging process, the efficiency is defined as the ratio between the net thermal power recovered by the HTF ($\dot{E}_{\mathrm{D}}^{\mathrm{Net}}$) and the summation of the total thermal power delivered by the TES system ($\dot{E}_{\mathrm{D}}^{\mathrm{Sto}}$) and the compressor power required to overcoming the pressure drop ($\dot{W}_{\mathrm{D}}^{\mathrm{Pump}}$) as

$$\eta_{\mathrm{D}} = \frac{\dot{E}_{\mathrm{D}}^{\mathrm{Net}}}{\dot{E}_{\mathrm{D}}^{\mathrm{Sto}} + \dot{W}_{\mathrm{D}}^{\mathrm{Pump}}}. \tag{4.83}$$

Both definitions indicate instantaneous efficiencies contrary to as typically presented in the literature, e.g., Ref. [31]. Obviously, one may obtain average efficiency values from Eqs. 4.82 and 4.83 by further integrating their numerators and denominators over specific time intervals; however, the analysis proposed initially considers instantaneous values in

order to explore the time-dependent behavior of the heat exchanges between s-$CO_2$ and TES system.

For both Eqs. 4.82 and 4.83, the net thermal power delivered/recovered by the HTF is defined as shown in Eq. 4.70, while the total thermal power stored/delivered by the TES system is defined as shown in Eq. 4.71. Furthermore, the pumping power [146], in its discretized form, is determined as

$$\dot{W}^{\mathrm{Pump}} = \left(\frac{1}{\eta_{\mathrm{Comp}}}\right) \sum_{\mathrm{j}=1}^{N_{\mathrm{z}}} \left[ \left( \frac{\dot{m}_{\mathrm{F,w}} + \dot{m}_{\mathrm{F,e}}}{2} \right) \left( \frac{P_{\mathrm{F,w}} - P_{\mathrm{F,e}}}{\rho_{\mathrm{F,P}}} \right) \right], \tag{4.84}$$

i.e., the evaluation, for the node $P$ and a time step, is performed at each discrete volume $j$ in the axial ($z$) direction (from $j = 1$ to $N_{\mathrm{z}}$), and the total value is obtained from the overall summation assuming a constant compressor efficiency of $\eta_{\mathrm{Comp}} = 0.89$ [5].

Having said that, Fig. 27 shows the net (black continuous curves) and stored (dashed curves) thermal powers (left axes) and the pumping power (right axes) along the time for charging (top plot) and discharging (middle plot) processes, respectively, while considering the charging temperature $T_{\mathrm{C}} = 550$ °C, bed length $L = 3$ m, bed diameter $D = 2$ m, particle diameter $d = 3$ mm, porosity $\varepsilon = 0.35$, and charging and discharging mass flow rates $\dot{m}_{\mathrm{C}} = \dot{m}_{\mathrm{D}} = 1$ kg/s. For charging, both thermal powers slightly increase at first (pressure drop and thermal losses pull down the fluid mass-specific enthalpy downstream the TES device), which is followed by a sharp drop (approximation to saturation) and a nearly steady end (saturation). The difference between the net and the stored thermal powers is directly related to the degree of irreversibility generated along the process, i.e., heat losses and fluid friction. In other words, the behavior shown by the thermal power curves is associated with the larger thermal power values promoted by the large temperature difference between fluid and bed at the beginning of the process. This temperature difference is reduced as the bed becomes thermally saturated and the HTF temperature downstream the TES device starts to increase, which drops the values of both curves. Moreover, such curves seem closer during this decay, which occurs because, in this region, the heat losses from the HTF to the surroundings also decrease and stabilize. Lastly, as the curves draw near to the end of the processes (i.e., $t > 8$ h), the thermal power stored tends to zero as the TES device becomes saturated and the net thermal power delivered to

the system equals the loss to the environment. Over the discharge, the behavior is similar to that just discussed, except for the pressure drop profile, which decays along the time contrary to what is observed for the charging. Regarding the compressing power required for both processes, it is important to note that the absolute values presented are almost negligible, which, once again, demonstrates the small pressure drops of systems operating with s-$CO_2$.

Figure 27 – Temporal behavior of the thermal and pumping powers for charging (top plot) and discharging (middle plot) processes and the instantaneous charging and discharging efficiencies (bottom plot) along the time.

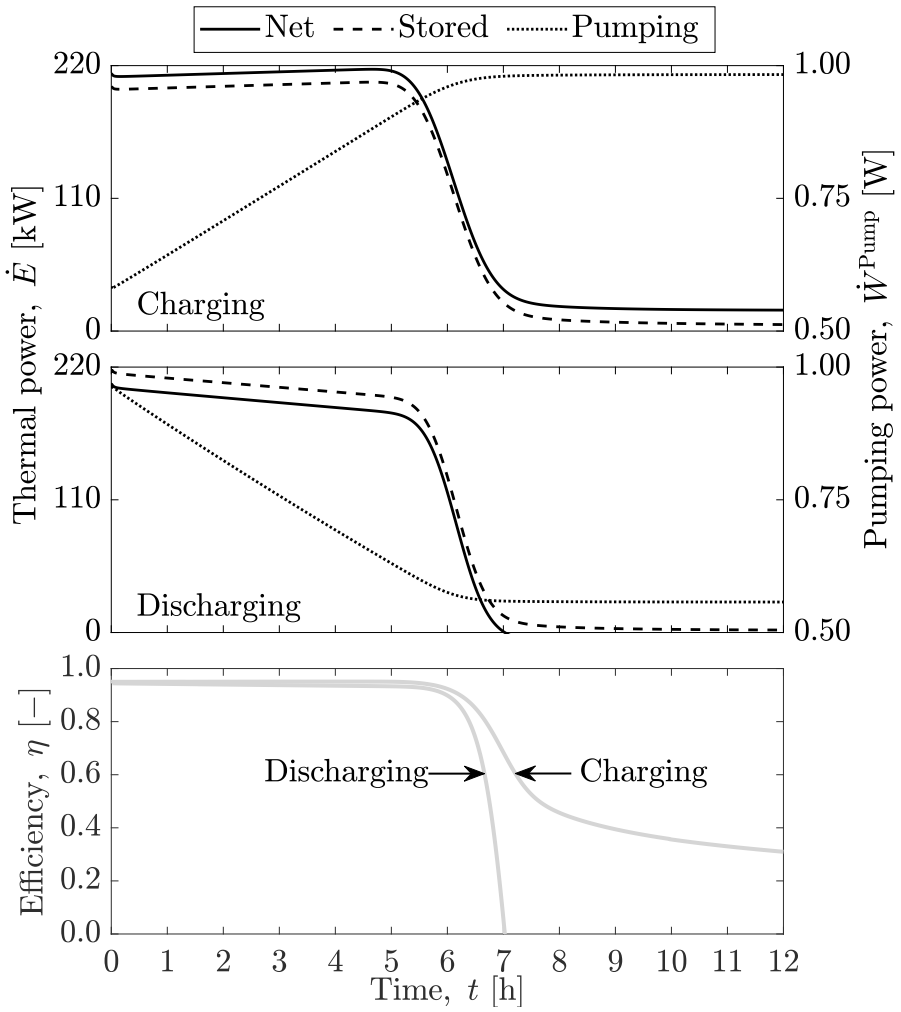


Furthermore, the bottom plot of Fig. 27 shows the above-mentioned charging and discharging efficiencies (gray continuous curves) – i.e., Eqs. 4.82 and 4.83, respectively – in which each set of three curves of the top and middle plots becomes a single curve. Looking at both efficiency curves, it becomes clear that there are time intervals in which the efficiencies are nearly constant, which, for this specific case, extend themselves up to

the time $t \sim 5.8$ h (each with its maximal value), then being followed by a sudden drop. After that, the charging efficiency presents a less steep rate of change due to heat losses to the surroundings, making it harder to thermally saturate the TES device. The discharging efficiency, on the other hand, does not present the same behavior because the heat losses favor the TES discharge. Obviously, the transition point from nearly constant to steep drop values depends on design and operation parameters, such as the amount and the arrangement of the storage material and the mass flow rates.

Based on this discussion, clearly defining both the charging and discharging time extents is, arguably, of uttermost importance in order that they meet the established operational requirements while considering the figures of merit chosen. For instance, taking either the charging or the discharging efficiency, the influence of the process time span on it is evident, regardless of whether an instantaneous or an average evaluation is considered. For the case discussed in the bottom plot of Fig. 27, the prolongation of either process beyond $t \sim$ 5.5 h leads to a progressively diminished efficiency return. This naturally depends on the set of design and operational parameters of the TES system examined. Then, due to the amplitude of such features to which the TES device may be exposed in a parametric study as the one proposed, a fixed set of time periods for the processes may be appropriated to some particular systems, but also too short or extensive to others. Hence, for the sake of fairness, objective criteria for stopping the charging and discharging processes should be established based on TES outputs, instead of time spans to be arbitrarily fixed. Such criteria may allow comparisons between distinct systems to be carried while observing equivalent chosen outputs. Therefore, considering the HTF outlet temperature as the main TES output for the power cycle to which it is coupled, HTF outlet temperature differences with respect to references for charging (i.e., $\Delta T_{\mathrm{F,Out,C}}$) and discharging (i.e., $\Delta T_{\mathrm{F,Out,D}}$) are established for equally limiting the processes. Similar to the approach employed by Ref. [147], for the charging, the criterion is defined as the difference between the HTF outlet temperature and its respective discharging temperature, i.e.,

$$\Delta T_{\mathrm{F,Out,C}} = T_{\mathrm{F,Out,C}} - T_{\mathrm{ref,C}}; \tag{4.85}$$

whereas, for the discharging, the criterion is defined as the difference between its respective

charging temperature and the HTF discharging outlet temperature, i.e.,

$$\Delta T_{\mathrm{F,Out,D}} = T_{\mathrm{ref,D}} - T_{\mathrm{F,Out,D}}. \tag{4.86}$$

These criteria were chosen not only because they are easy to introduce on the design but also because they indicate deviations from the desirable operational conditions, i.e., the increase of the HTF outlet temperature for the charging process and the decrease of such a temperature for the discharging process are associated with drops in efficiency. To better illustrate such criteria and to complement Fig. 27, Fig. 28 shows the TES outlet temperature along charging and discharging processes. For all the next analyses, it will be considered that $\Delta T_{\mathrm{F,Out,C}} = 15$ °C and $\Delta T_{\mathrm{F,Out,D}} = 100$ °C, which, for the present case, lead to the charging and discharging times $t_{\mathrm{C}} \approx 5.5$ h and $t_{\mathrm{D}} \approx 6.1$ h, respectively, as indicated as the time instant when the respective $T_{\mathrm{TES}}^{\mathrm{Out}}$ satisfies the corresponding chosen values of $\Delta T_{\mathrm{F,Out,C}}$ and $\Delta T_{\mathrm{F,Out,D}}$. Although arguably arbitrary, these values represent a design decision aiming to prevent further delay in stopping the processes and consequently, efficiency falls – one may verify that after the indicated times, the respective efficiencies begin to drastically diminish in the bottom plot of Fig. 27. Finally, as will be shown later, the TES system sensitivity to these parameters will be further examined.

Figure 28 – TES outlet temperature along charging and discharging processes.

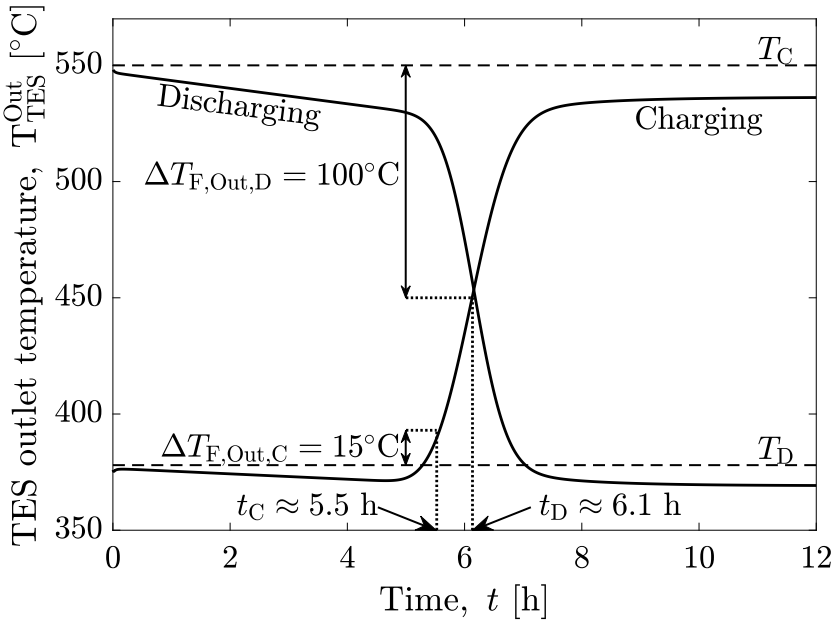


Now, for analyzing the combined charging-discharging efficiency of the TES system

while accounting for the aforementioned temperature difference parameters, the combined efficiency figure of merit is defined, according to Ref. [148], as

$$\eta_{\mathrm{Comb}} = \frac{\int_{\mathrm{D}} \dot{E}_{\mathrm{D}}^{\mathrm{Net}} dt}{\int_{\mathrm{C}} \dot{E}_{\mathrm{C}}^{\mathrm{Net}} dt + \int_{\mathrm{C}} \dot{W}_{\mathrm{C}}^{\mathrm{Pump}} dt + \int_{\mathrm{D}} \dot{W}_{\mathrm{D}}^{\mathrm{Pump}} dt}, \tag{4.87}$$

for which the integral subscripts C and D indicate integration over the charging and discharging times, respectively. One should note that Eq. 4.87 differs from Eqs. 4.82 and 4.83 because it combines the charging and discharging processes instead of dealing with each one individually. Also, because such an expression is an integrated-over-time evaluation rather than an instantaneous one – i.e., both the thermal and the compressing powers are integrated over time. Therefore, a particularly striking interpretation of this figure of merit is that it is an over-the-cycle (i.e., charging followed by discharging) evaluation of the fraction of the overall energy supplied by the HTF to the TES system that is effectively recovered from it by the HTF during the discharge. Taking the verification case for instance, the combined efficiency for the first charging-discharging cycle (with a cold start) is $\eta_{\mathrm{Comb}} \sim 0.34$. It is worth mentioning that this figure of merit accounts for the three main inefficiency sources concerning stratified TES applications (which is the case of a packed-bed), i.e., thermal loss to the surroundings, thermal dispersion, and pumping power required for the operation. For clarification, the first two sources are indirectly accounted for through the ability of the HTF to deliver thermal energy to the packed-bed during the charging and retrieve it back from the TES system during the discharging, i.e., through $\dot{E}_C^{Net}$ and $\dot{E}_D^{Net}$. Additionally, for all analyses presented beyond this point, the charging and discharging times are limited to 12 h (maximal solar availability time extent considered) and 24 h (day time extent), respectively. Thus, if the temperature limits $\Delta T_{\mathrm{F,Out,C}}$ and $\Delta T_{\mathrm{F,Out,D}}$ are not achieved within these time periods, the results are indicated as non-saturated.

## 4.2 RESULTS

This section explores the results obtained in five subsections. First, Subs. 4.2.1 discusses the influence of the HTF, and then parametric analyses are developed in Subs. 4.2.2. Next, a discussion on thermal loss and insulation thickness is presented in Subs. 4.2.3.

Regarding the system optimization, Subs. 4.2.4 discusses the effects of the charging temperature and overall dimensions of the TES system. Finally, the influence of the TES charging-discharging cycling is explored in Subs. 4.2.5.

### 4.2.1 The influence of the HTF on the performance of the TES device

The analysis presented in this section explores the main differences between s-$CO_2$ and air as HTF with respect to heat transfer and pumping power within a packed-bed TES device. The literature on the use of s-$CO_2$ as HTF for such an application is still limited, hence thorough analyses are required because such a fluid may present particularities regarding its thermophysical properties as well as heat transfer and pressure drop characteristics. Also, air is used as a baseline HTF because it is recognized as a well-behaved fluid and its performance is well known within the scope of packed-bed TES devices.

Moreover, the choice of the HTF severely influences the system outputs since figures of merit for assessing the system thermal-hydraulic performance are most likely directly related not only to design and operational conditions but also to the HTF properties and its flow characteristics.

Then, for this analysis, the same TES configuration used for obtaining Figs. 27 and 27 is considered, i.e., $L = 3$ m, $D = 2$ m, $d = 3$ mm, and $\varepsilon = 0.35$. The charging and discharging processes are held with constant inlet temperatures of $T_{\mathrm{C}} = 550$ °C and $T_{\mathrm{D}} = 378$ °C, inlet pressure of $P = 25$ MPa (which are values commonly adopted for s-$CO_2$ CSP plants [9, 10, 122]), and mass flow rates of $\dot{m}_{\mathrm{C}} = \dot{m}_{\mathrm{D}} = 1$ kg/s for obtaining results per unit of mass flow rate. So, by fixing design and operation parameters, the influence of the HTF selection on the system performance may be singly explored. Additionally, $\Delta T_{\mathrm{F,Out,C}}$ and $\Delta T_{\mathrm{F,Out,D}}$ were not fixed for allowing the system to reach saturation during the charging and discharging processes.

The charging and discharging results are shown in the top and bottom plots of Fig. 29, respectively, which display the temporal behavior of the thermal power stored (left y-axis) and the pumping power (right y-axis) for s-$CO_2$ (continuous curve) and air (dashed curve). For both charging and discharging processes, the air pumping power is $\sim 2.5$ times

that of the s-$CO_2$, which can be justified by the higher volume-specific mass and lower viscosity of the latter fluid. Thus, as the s-$CO_2$ allows smaller pressure drops, which is an especially advantageous and sought-after characteristic for decreasing the pumping power expenditure of thermal systems, it follows that s-$CO_2$-based packed-bed systems may operate with different aspect ratios ($\zeta = L/D$) and particle diameters than those commonly employed with air. Now, for the thermal power stored (i.e., the heat transferred from the fluid and stored by the TES system), it is shown that the s-$CO_2$ allows a $\sim 10\%$ greater heat transfer rate per unit of mass flow rate than air for roughly 5.5 h for both charging and discharging processes, which then decreases as the system approaches the saturation. Regarding specifically the thermal power delivered, the larger per mass flow rate values obtained using s-$CO_2$ are related not only to the greater average specific heat at constant pressure ($\sim 10\%$ larger than for air at the conditions considered), but also to the smaller thermal resistance of its flow, which derives from the larger convective heat transfer coefficient achieved with such a fluid flow.

Figure 29 – Net and stored thermal powers and pumping power along the time for air and s-$CO_2$ during the charging and discharging processes.

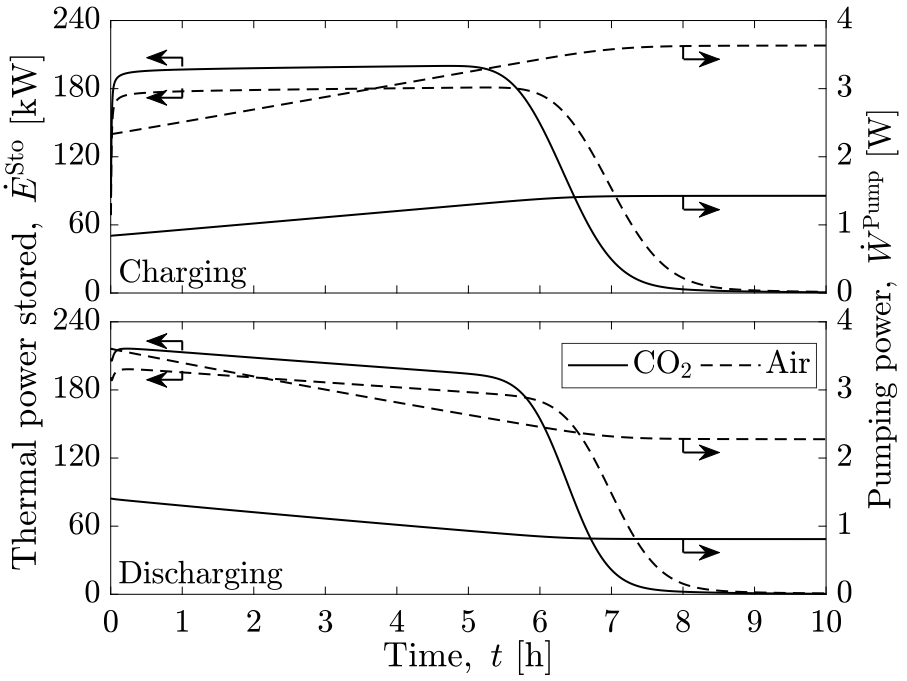


So, complementing Fig. 29, Fig. 30 displays the temporal behavior of the length-averaged Nusselt number based on the particle diameter along with both charging and discharging processes for both fluids. For the conditions considered, the Nusselt curves

show that the s-$CO_2$ enables larger convective heat transfer coefficients than the air, which allow faster processes. Therefore, this analysis points towards the importance of dedicated studies for further analyzing s-$CO_2$ as HTF in packed-bed TES applications while comparing its performance to that of air.

Figure 30 – Length-averaged particle Nusselt for the charging and discharging processes considering air and s-$CO_2$.

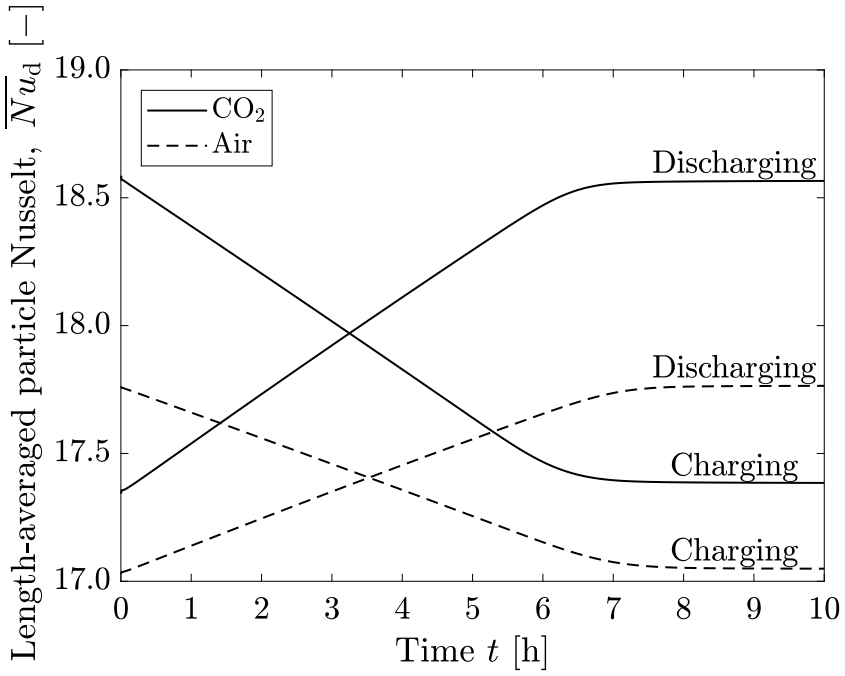


### 4.2.2 Parametric analyses

Initially focusing on design parameters, specifically on the storage tank size (internal volume) and aspect ratio ($\zeta = L/D$), Fig. 31 displays a mapping of the combined efficiency (color scale) with respect to $D$ and $L$, ranging from 0.5 m to 3 m and from 1 m to 10 m, respectively, for $T_C = 550$ °C, $d = 3$ mm, $\varepsilon = 0.35$, $\dot{m}_C = \dot{m}_D = 1$ kg/s, $\Delta T_{F,OutC} = 15$ °C, and $\Delta T_{F,OutD} = 100$ °C. As can be seen from the color map, higher combined efficiencies are not achieved for limiting values, but rather for specific combinations of parameters. The combination of $L$ and $D$ that maximizes the combined efficiency with the value of $\eta_{Comb} \approx 0.92$, which is represented by the black circle marker, is $D \approx 0.83$ m and $L \approx 1.11$ m. This maximum arises from the competing effects of thermal power transfer – within the TES device (thermal dispersion) and to the surroundings (losses) – and pressure drop during the charging and discharging processes, which are strongly affected not only

by the proper matching of the inlet energy input and the overall size of the storage unit, but also by its aspect ratio. More importantly, however, is that this mapping provides a broad assessment from a design standpoint because it includes several combinations of storage volume and aspect ratios, which allows an easy analysis on the influence of these two main design parameters. Each one of the dashed black lines, which are obtained for different aspect ratios, refers to a different storage volume. As may be seen from the constant-volume curves, the combined efficiency is strongly influenced by the storage volume, with larger efficiency values for smaller storage vessels. Also, the non-saturated region (NSR) above the continuous black line refers to combinations of $L$ and $D$ that have not reached at least one of the temperature difference limits established within the time limits – the NSR is related to TES designs with large volumes. Furthermore, these results may be put forth as one of the key elements involved in the manufacturing costs, which are recognized in the literature (e.g., Ref. [34]) as a bottleneck for implementing such TES systems.

Figure 31 – Combined efficiency mapping as function of bed length $L$ and diameter $D$ considering: $T_{\mathrm{C}} = 550$ °C, $d = 3$ mm, $\varepsilon = 0.35$, $\dot{m}_{\mathrm{C}} = \dot{m}_{\mathrm{D}} = 1$ kg/s, $\Delta T_{\mathrm{F,OutC}} = 15$ °C, and $\Delta T_{\mathrm{F,OutD}} = 100$ °C.

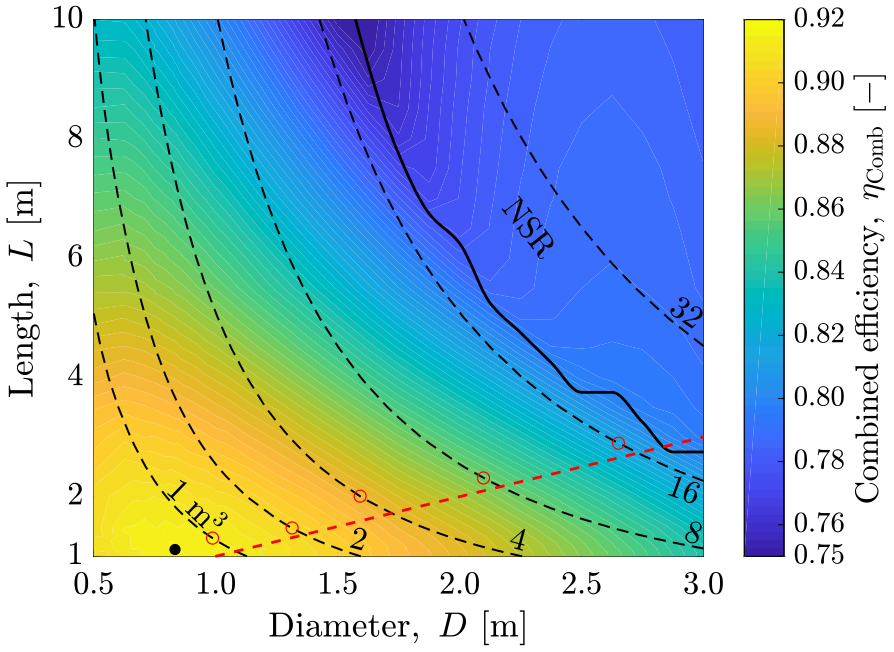


Furthering the discussion on Fig. 31 and using basic expressions for the total internal volume $V = (\pi D^2/4)\, L$ of the cylindrical packed-bed core, it is possible to express its correspondent total combined wall and lids area $A_{\mathrm{Total}} = \pi DL + 2\,(\pi D^2/4)$ as $A_{\mathrm{Total}} =$

$(4V/D) + (\pi D^2/2)$. With such an expression, it is possible to show that, for a given $V$, there is a bed diameter that minimizes the total device area, which is given by $D = (4V/\pi)^{1/3}$. The red dashed line in Fig. 31 indicates the locus of such minima. Then, using data interpolation, the maximal $\eta_{\text{Comb}}$ along with each of the fixed-volume curves already shown is indicated by the red circle markers. Comparing the relative location of such markers to the red dashed line, the relationship between them becomes clear.

Following Fig. 31, Fig. 32 displays the corresponding mapping of discharging time. Once again, the dashed black lines correspond to fixed-volume storage configurations. It becomes clear, for volumes up to roughly 16 $m^3$, the already expected tight correlation between the storage volume and its discharging time, i.e., the larger the volume, the greater the discharging time. For larger volumes, the discharging time reaches a plateau close to 12 h, which derives from the non-saturation during the charging process (which is limited to a 12 h period) due to the excessively large amount of storage material. Clearly, the values shown are substantially affected by the other design and operational parameters, nevertheless, the analysis indicates the importance of well-matching the vessel size to the intended process characteristics. Taking Figs. 31 and 32, for instance, even though there is an optimal combination of $L$ and $D$ for achieving the maximal combined efficiency, this same combination leads to a severely impaired discharging time due to the respective reduced storage volume. Then, this trade-off between combined efficiency and discharging time indicates the importance of optimization-based design while considering multiple parameters and performance indicators. Also, the charging mapping is omitted not only for the sake of brevity, but also because the overall behavior and trends are almost identical to those of the discharging process.

For the sake of better understanding the influence of the aspect ratio on the system performance, the top plot of Fig. 33 displays the combined efficiency (left y-axis) and the discharging time (right y-axis) versus the storage aspect ratio for a fixed volume, i.e., as if one considers the analysis while on one of the black dashed lines of Figs. 31 and 32. For now, the design considers $T_{\text{C}} = 550$ °C, $d = 3$ mm, $\varepsilon = 0.35$, $\dot{m}_{\text{C}} = \dot{m}_{\text{D}} = 1$ kg/s, $\Delta T_{\text{F,Out,C}} = 15$ °C, $\Delta T_{\text{F,Out,D}} = 100$ °C, and a storage volume of $V = 7.5$ $m^3$. The circle markers indicate the simulated points, whereas the data-interpolated continuous gray

Figure 32 – Respective discharging time mapping to Fig. 31.

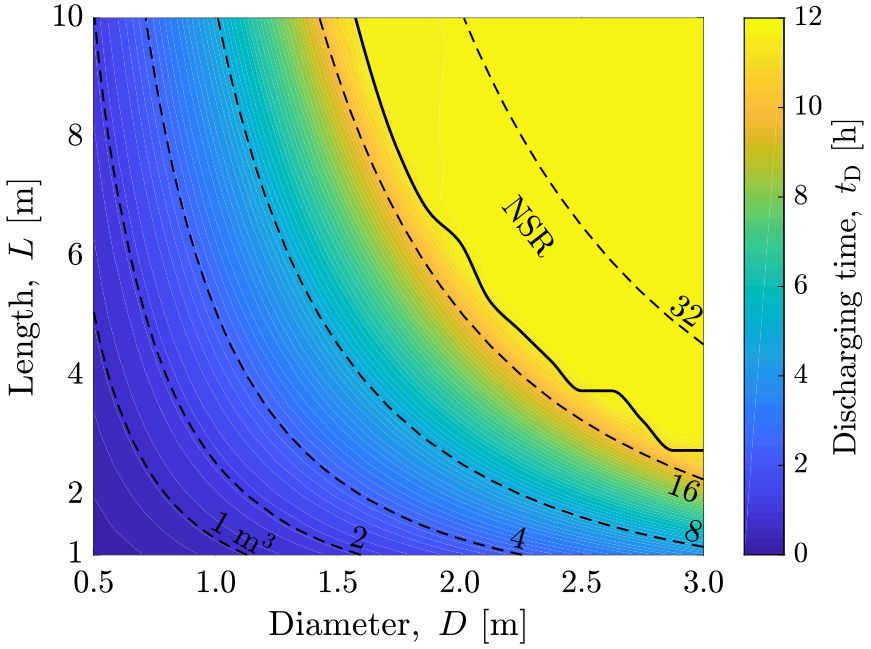


line only facilitates the visualization. The existence of a maximal value for $\eta_{\text{Comb}}$ clearly indicates that there is an optimal aspect ratio, which reinforces the analysis presented in Fig. 31 and indicates that not only the storage volume must be considered but also its arrangement. The optimal value obtained points to an aspect ratio of $\zeta \sim 1.0$, i.e., a roughly equally longer and wider TES device. This tendency is arguably related to the thermal losses and to the trade-off between heat transfer (which includes effects of thermal dispersion) and pressure drop. Moreover, the discharging time may be considered roughly constant from an operational standpoint because it presents a roughly negligible variation between $\sim$ 4.5 h and $\sim$ 4.6 h over the range of $L/D$ considered, which indicates that the discharge time is mostly driven by the storage volume, with little influence of the aspect ratio. Now, the bottom plot of Fig. 33 shows the respective time-averaged thermal power released by the porous medium (Solid) and absorbed by the fluid (Fluid) during the discharge phase – the difference between the curves may be interpreted as the heat loss to the ground. It is possible to verify that a commonly used approximation for the discharging time may be obtained from [149]

$$V = \frac{\left\langle \dot{E}_{\text{S}}^{\text{Sto}} \right\rangle t_{\text{D}}}{(1-\varepsilon)\,\rho_{\text{S}}\bar{c}_{\text{S}}\Delta\bar{T}_{\text{S}}} \rightarrow t_{\text{D}} = \frac{V\,(1-\varepsilon)\,\rho_{\text{S}}\bar{c}_{\text{S}}\Delta\bar{T}_{\text{S}}}{\left\langle \dot{E}_{\text{S}}^{\text{Sto}} \right\rangle}. \tag{4.88}$$

For the optimal aspect ratio $\zeta \approx 1.0$, the time-averaged thermal power released by the solid

$\langle \dot{E} \rangle \approx 195$ kW (obtained from inspection of the bottom plot of Fig. 33). Also, considering $\bar{c}_{\mathrm{S}} \approx 1150$ J/(kg $\cdot$ K) and $\Delta \bar{T}_{\mathrm{S}} = 144$ °C, and using $\rho_{\mathrm{S}} \approx 3950$ kg/m$^3$ (from Sub. 4.1.4), $V = 7.5$ m$^3$, and $\varepsilon = 0.35$, it is possible to obtain an approximated discharging time of $t_{\mathrm{D}} \approx 4.54$ h, which agrees with the data shown in Fig. 33 – $\bar{c}_{\mathrm{S}}$ was obtained through the expression shown in Sub. 4.1.5 as an average value for the temperature range while $\Delta \bar{T}_{\mathrm{S}}$ was obtained as the solid axially-averaged temperature difference between the beginning and the end of the discharging.

Based on the analysis presented in Fig. 33 on the existence of a maximal $\eta_{\mathrm{Comb}}$ value, i.e., $\eta_{\mathrm{Comb,Max}}$, with respect to the storage aspect ratio given a fixed storage volume, Fig. 34 explores the effect of varying the storage volume itself. Therefore, for the same parameters of Fig. 33, Fig. 34 brings $\eta_{\mathrm{Comb,Max}}$ (left y-axis) as a function of the storage volume (x-axis) and the respective optimal aspect ratio (right y-axis), i.e., $(L/D)_{\mathrm{Opt}}$. For each storage volume value, a dedicated optimization was performed with the aspect ratio range observing the ranges for storage length and diameter of Fig. 31. Hence, each point obtained in Fig. 34 may be understood as the highest $\eta_{\mathrm{Comb}}$ within a given constant-volume line of Figs. 31 and 32. For the range of 2 m$^3$ to 20 m$^3$, $\eta_{\mathrm{Comb,Max}}$ decreases almost quadratically with the increase of the storage volume, which indicates a diminishing return with respect to the storage volume, something arguably related to the increase of thermal losses. With the increase of the storage volume, the optimal aspect ratio oscillates between roughly 1.0 and 1.4, which reveals that such values of $\zeta$ are the most desirable as effective geometries. This trend corroborates the discussion for Fig. 31, because the minimal total combined wall and lids area occurs for $\zeta = 1$.The error bars indicate the range of $\zeta = L/D$ values within which $\eta_{\mathrm{Comb}}$ is at least 99.9% of the maximum for that storage volume. Although the system performance depends on its aspect ratio given the evident overall trend, the large amplitudes of the error bars indicate an arguably weak sensitivity to this parameter in the vicinity of $\zeta \sim 1$.

Another relevant aspect concerning design parameters is the particle (spheres) diameter ($d$). Because there is an inverse dependence on the particle diameter of both the particle convective heat transfer coefficient and the heat transfer area – hence, of the overall volumetric heat transfer coefficient (see Sub. 4.1.7) –, it is plausible to infer that,

Figure 33 – Combined efficiency and discharging time (top plot), and time-averaged thermal power released by the porous medium (Solid) and absorbed by the fluid (Fluid) during the discharging process (bottom plot) versus the storage aspect ratio for a fixed storage volume of $V = 7.5$ m$^3$ considering: $T_{\mathrm{C}} = 550$ °C, $d = 3$ mm, $\varepsilon = 0.35$, $\dot{m}_{\mathrm{C}} = \dot{m}_{\mathrm{D}} = 1$ kg/s, $\Delta T_{\mathrm{F,Out,C}} = 15$ °C, and $\Delta T_{\mathrm{F,Out,D}} = 100$ °C.

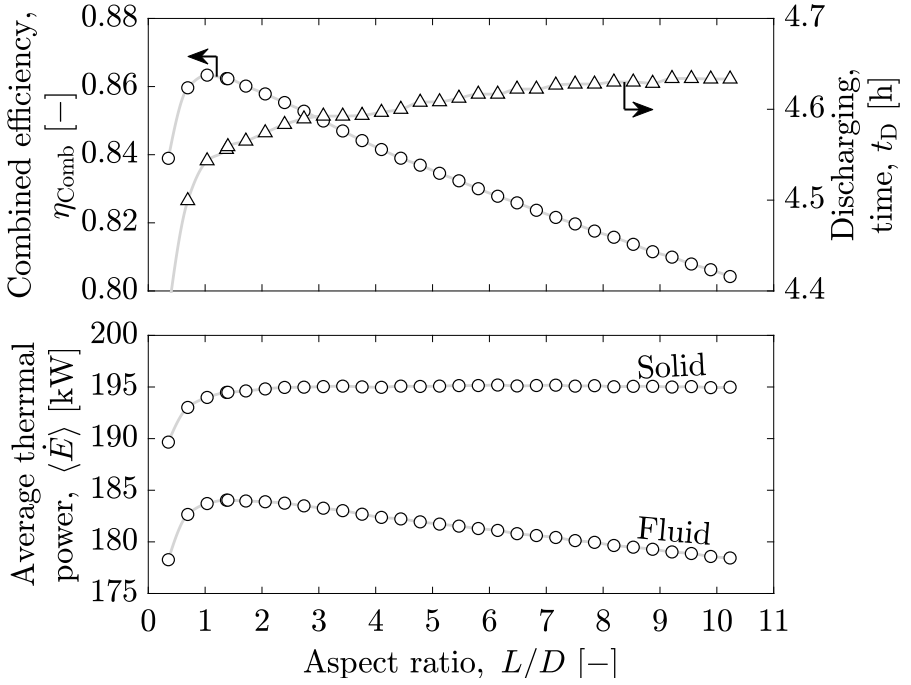


Figure 34 – Maximal combined efficiency and the respective optimal storage aspect ratio versus the storage volume.

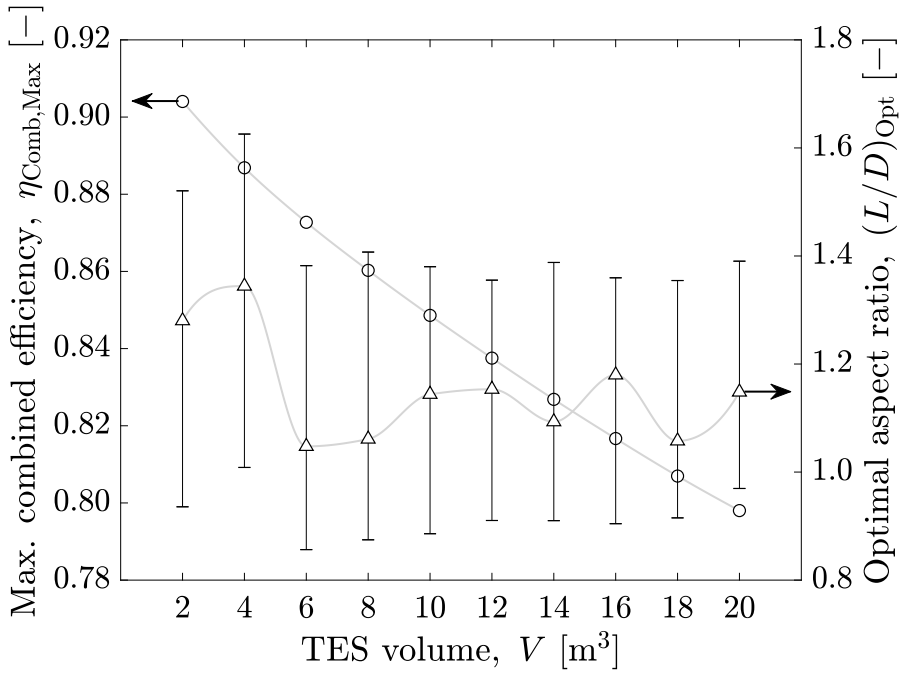

for a fixed bed volume (fixed $L$ and $D$), the smaller the particle diameter, the larger the heat transfer gain. However, there is also and inverse dependence on the particle diameter of the pressure drop in packed-beds (see Sub. 4.1.8). Then, it is reasonable to expect a trade-off relation between heat transfer and pressure drop while considering heat losses to the surroundings and thermal dispersion, with the particle diameter selection affecting the system efficiency. In this sense, air-based systems usually employ $d \sim 30$ mm [30], while smaller values as $d \sim 3$ mm have been reported when dealing with s-$CO_2$ [91]. Therefore, the mapping shown in Fig. 35 seeks to establish the simultaneous influence of the bed and particle diameters on the combined efficiency by plotting $\eta_{\text{Comb}}$ as a function of $D$ ranging from 0.5 m to 3 m and $d$ ranging from 0.5 mm to 35 mm for $T_{\text{C}} = 550$ °C, $L = 3$ m, $\varepsilon = 0.35$, $\dot{m}_{\text{C}} = \dot{m}_{\text{D}} = 1$ kg/s, $\Delta T_{\text{F,Out,C}} = 15$ °C, and $\Delta T_{\text{F,Out,D}} = 100$ °C. Considering the limits established for both diameters, it is possible to determine a specific pair of $D$ and $d$ that maximizes the combined efficiency, which is indicated by the black circle marker at $D \approx 0.625$ m and $d \approx 1.25$ mm. Actually, the gray dotted line roughly indicates the optimal region, i.e., the locus of $\eta_{\text{Comb}}$ maxima for each particle diameter. This behavior may be explained by the aforementioned competition of the pressure drop and the heat transfer rates. Furthermore, the black dashed lines indicate fixed discharging-time lines. As shown in Fig. 32, for a fixed $L$, the larger the bed diameter, the larger the discharging time, which is clear in Fig. 35 because the correspondent $t_{\text{D}}$ values for the dashed lines increase with $D$. Also from the dashed lines, their mild leaning tendency reveals that the discharging process is actually not only affected by the bed diameter, but also by the particle diameter, as larger spheres lead to slightly shorter discharging processes. Moreover, it is important to recall that all the previous analyses held the bed porosity fixed at $\varepsilon = 0.35$, which is a value commonly found in the literature, e.g., Refs. [30, 91].

While the results from Fig. 35 rely on a fixed value for the medium porosity, Fig. 36 now explores the effect of simultaneously varying this parameter and the particle diameter. The bed porosity is a result of the arrangement of same-diameter spheres inside the cylindrical vessel, thus, for jammed structures, extreme values are unachievable. The literature presents $\varepsilon \sim 0.36$ [150] as a common value for the close-packing arrangement of same-size spheres in a cylindrical container without wall effect (i.e., $d << D$ and

Figure 35 – Effect of the particle and the TES diameters ($d$ and $D$, respectively) on the combined efficiency considering: $T_{C} = 550$ °C, $L = 3$ m, $\varepsilon = 0.35$, $\dot{m}_{C} = \dot{m}_{D} = 1$ kg/s, $\Delta T_{F,Out,C} = 15$ °C, and $\Delta T_{F,Out,D} = 100$ °C.

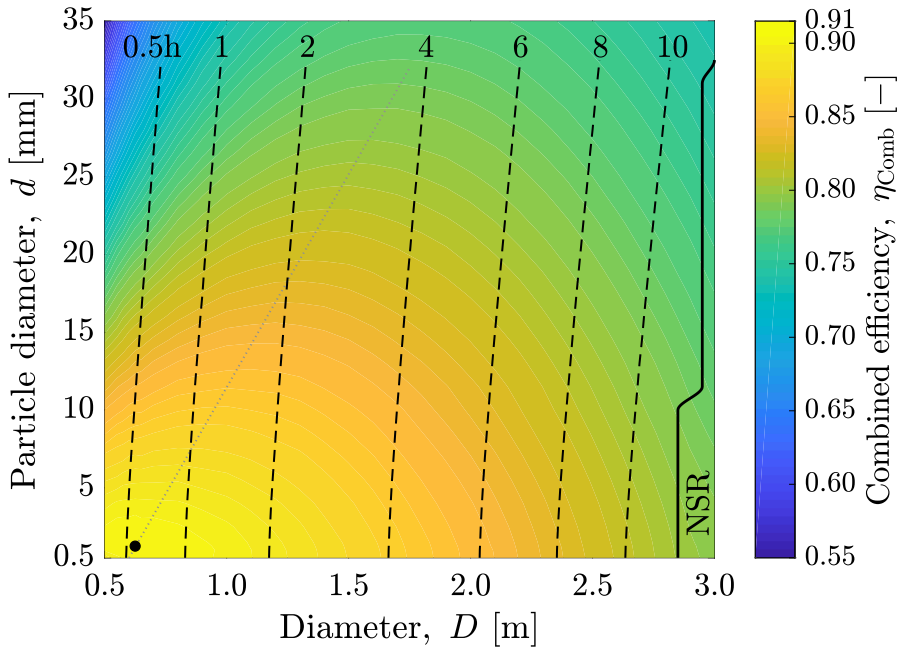


$d << L$) – the minimal theoretical achievable value is $\sim 0.22$ [151] and the maximal $\sim 0.6$ [152] for a jammed-packed configuration. Although it may be argued that the bed porosity is not an easily-controlled parameter per itself, or that it is actually a function of the particle/bed diameters ratio (e.g., Refs. [153, 154]), for further understanding the influence of this parameter on the system performance, it was chosen to map $\eta_{Comb}$ while independently varying $d$ and $\varepsilon$ within acceptable ranges. Therefore, the range for the bed porosity was chosen from 0.26 to 0.476, which are the limiting values for the Kunii and Smith's solid effective thermal conductivity correlation [125] employed and are deemed acceptable according to the discussion reported in Ref. [150]. As may be seen in Fig. 36, which is obtained for $T_{C} = 550$ °C, $L = 3$ m, $D = 2$ m, $\dot{m}_{C} = \dot{m}_{D} = 1$ kg/s, $\Delta T_{F,Out,C} = 15$ °C, and $\Delta T_{F,Out,D} = 100$ °C, the overall behavior seems to be that, for a fixed particle diameter, increasing the porosity decreases the combined efficiency. Such a tendency is more noticeable for larger particles, i.e., the $\eta_{Comb}$ variation regarding the porosity is greater for larger particle diameters. For $d \lessapprox 15$ mm, there is an optimal relation between the particle diameter and the porosity, i.e., for each $d$, there is an optimal $\varepsilon$ that maximizes $\eta_{Comb}$. This optimal region is roughly depicted by the gray dotted line ending at the black circle marker, which indicates the optimal parameter combination

$\varepsilon \approx 0.33$ and $d \approx 0.5$ mm that maximizes the combined efficiency. As already discussed, the larger the sphere diameter, the smaller the heat transfer area for a fixed porosity, which impairs the heat transfer and, ultimately, reduces the combined efficiency. Furthermore, it is noticeable that the effect of the particle diameter on the combined efficiency is more pronounced for large porosity values, which, once again, is related to the reduction of the heat transfer area and also to the reduction of the storage material availability. It is, thus, concluded that the impact of the porosity for small particle diameters is limited because the large heat transfer areas ensure the efficiency gain. Additionally, the inclined fixed discharging-time lines (black dashed lines) indicate that the process is well influenced by both parameters considered. Within the parameters values limits considered, the largest $t_{\mathrm{D}}$ values correspond to small sphere diameters and low porosities. While the inverse trend between $t_{\mathrm{D}}$ and $\varepsilon$ is easily understood using Eq. 4.88, the also inverse relation between $t_{\mathrm{D}}$ and $d$ may not be as evident. First, from Eq. 4.37, for a fixed bed volume, decreasing the particle diameter while maintaining $\varepsilon$ fixed increases the available heat transfer area, which, arguably, increases the heat transfer rate and, consequently, decreases $t_{\mathrm{D}}$. Nonetheless, such an effect of increasing the heat transfer area not only affects the discharging but also the charging process, whose time is likewise increased. Therefore, the increase of $t_{\mathrm{D}}$ observed as $d$ decreases for a fixed $\varepsilon$ is due to the additional energy store during the charging process available for being retrieved during the discharge.

Moving away from design parameters, the study now focuses on the effect of the operation conditions on the combined efficiency of the TES system. Concentrating first on the charging and discharging mass flow rates, Fig. 37 depicts $\eta_{\mathrm{Comb}}$ for $T_{\mathrm{C}} = 550$ °C, $L = 3$ m, $D = 2$ m, $d = 3$ mm, $\varepsilon = 0.35$, $\Delta T_{\mathrm{F,Out,C}} = 15$ °C, and $\Delta T_{\mathrm{F,Out,D}} = 100$ °C. Although it is somewhat obvious that the larger the mass flow rates involved in the TES charging and discharging processes, the higher its efficiency, one primary purpose of this analysis is to precisely show how both mass flow rates (i.e., $\dot{m}_{\mathrm{C}}$ and $\dot{m}_{\mathrm{C}}$) interact with each other. At this point, it is important to note that the charging mass flow rate directly depends on the available solar field area ($A_{\mathrm{SF}}$), i.e., $\dot{m}_{\mathrm{C}} \sim A_{\mathrm{SF}}$, while the discharging is associated with the fraction of power production supplied by the stored energy. The color map shows that, for large discharging mass flow rates, take for instance $\dot{m}_{\mathrm{C}} = 1$ kg/s, i.e.,

Figure 36 – Mapping of the TES combined efficiency as a function of the particle diameter $d$ and the porous medium porosity $\varepsilon$ as independent variables for $T_{C} = 550$ °C, $L = 3$ m, $D = 2$ m, $\dot{m}_{C} = \dot{m}_{D} = 1$ kg/s, $\Delta T_{F,Out,C} = 15$ °C, and $\Delta T_{F,Out,D} = 100$ °C.

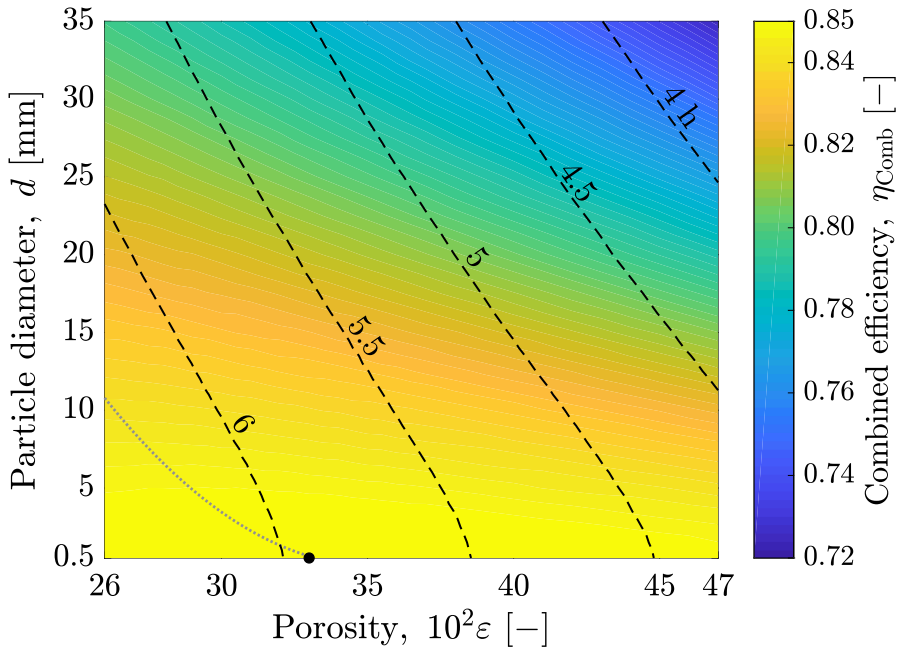


the case in which the discharging process is capable of fully satisfying the power block design point mass flow rate, the efficiency is sensitive to increases of the charging mass flow rate, which indicates a desirable impact on the TES performance of increasing the solar field area. On the other hand, for small discharging mass flow rates, the impact of the solar field area is not equally relevant. Moreover, it is also evident that increasing the solar field area to attend larger charging mass flow rates (i.e., $\dot{m}_{C} >> 1$ kg/s) seems not to affect to the same extent the TES performance, which possibly supports the concept of an economic trade-off. Hence, it becomes clear the relevance of choosing a suitable solar multiple (the ratio between the actual and the design solar field areas) that can be economically acceptable regarding the operation strategy established. Furthermore, the black dashed constant discharging-time lines clearly show that the discharging process is essentially governed by $\dot{m}_{D}$, as expected. Additionally, the non-saturated region over the edges of Fig. 37 corresponds to charging and discharging mass flow rates that are too small for the storage operation, i.e., which prohibit the processes from meeting $\Delta T_{F,Out,C}$ and/or $\Delta T_{F,Out,D}$ within the time limits established.

Recalling the discussion regarding Fig. 28, by regulating the HTF temperature downstream the TES system during the charge and discharge, one is able of controlling

Figure 37 – Effect of the charging and discharging mass flow rates ($\dot{m}_{\mathrm{C}}$ and $\dot{m}_{\mathrm{D}}$, respectively) on the TES combined efficiency assuming $T_{\mathrm{C}} = 550$ °C, $L = 3$ m, $D = 2$ m, $d = 3$ mm, $\varepsilon = 0.35$, $\Delta T_{\mathrm{F,Out,C}} = 15$ °C, and $\Delta T_{\mathrm{F,Out,D}} = 100$ °C.

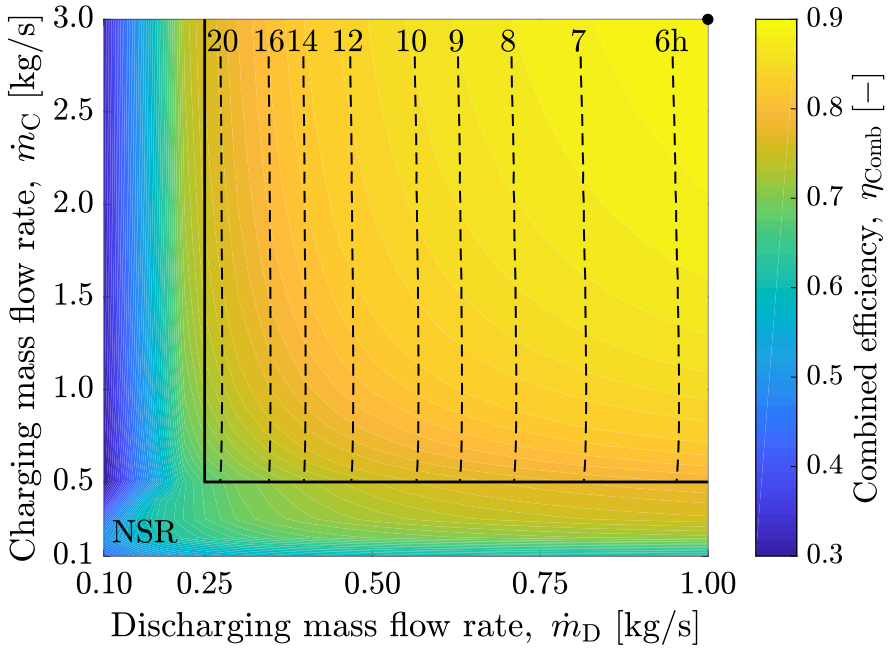


the time spans of such processes. Thus, also considering the definition of $\eta_{\mathrm{Comb}}$ from Eq. 4.87, it is possible to infer that one is also capable of largely affecting the combined efficiency. As previously discussed, such time spans control may be achieved through the temperature differences with respect to the processes references, i.e., $\Delta T_{\mathrm{F,Out,C}}$ and $\Delta T_{\mathrm{F,Out,D}}$. Also, as mentioned before, the effects of varying such parameters have not been directly assessed yet because the values assumed in the previous analyses were kept fixed (i.e., $\Delta T_{\mathrm{F,Out,C}} = 15$ °C and $\Delta T_{\mathrm{F,Out,D}} = 100$ °C). Therefore, Fig. 38 considers $T_{\mathrm{C}} = 550$ °C, $L = 3$ m, $D = 2$ m, $d = 3$ mm, $\varepsilon = 0.35$, and $\dot{m}_{\mathrm{C}} = \dot{m}_{\mathrm{D}} = 1$ kg/s while both $\Delta T_{\mathrm{F,Out,C}}$ and $\Delta T_{\mathrm{F,Out,D}}$ are varied simultaneously from 1 °C for charging and 15 °C for discharging to 170 °C – roughly the maximal possible temperature difference between charging at 550 °C and its respective discharging at 378 °C (see Tab. 1). Between both temperature differences, $\Delta T_{\mathrm{F,Out,D}}$ clearly presents the stronger effect on $\eta_{\mathrm{Comb}}$ because it is directly related to the fluid outlet temperature when it is recovering energy from the TES device, which indicates that the dynamics of the system performance is mainly governed by the discharge. The sharp decrease of the combined efficiency for the low limit of $\Delta T_{\mathrm{F,Out,D}}$ is related to the unattainability of thermal power recovery from the porous medium during extremely short discharging time spans (due to the small values of $\Delta T_{\mathrm{F,Out,D}}$ allowed).

Although outside the non-saturated region the impact of $\Delta T_{\mathrm{F,Out,C}}$ is barely noticeable, for $\Delta T_{\mathrm{F,Out,D}}$ between $\sim 20$ °C and $\sim 110$ °C, for each $\Delta T_{\mathrm{F,Out,D}}$, there actually is an optimal $\Delta T_{\mathrm{F,Out,C}}$, whose value decreases roughly linearly from $\sim 155$ °C to $\sim 60$ °C; then, for $\Delta T_{\mathrm{F,Out,D}} > 110$ °C, the optimal $\Delta T_{\mathrm{F,Out,C}}$ suddenly drops from $\sim 60$ °C to $\sim 1$ °C. The gray dotted line roughly indicates the locus of such an optimal relation, whose behavior underlines the occurrence of a variable optimal charging time given a discharging time (or outlet temperature difference).

Figure 38 – Combined efficiency mapping for different charging and discharging temperature difference limits ($\Delta T_{\mathrm{F,Out,C}}$ and $\Delta T_{\mathrm{F,Out,D}}$, respectively) assuming $T_{\mathrm{C}} = 550$ °C, $L = 3$ m, $D = 2$ m, $d = 3$ mm, $\varepsilon = 0.35$, and $\dot{m}_{\mathrm{C}} = \dot{m}_{\mathrm{D}} = 1$ kg/s.

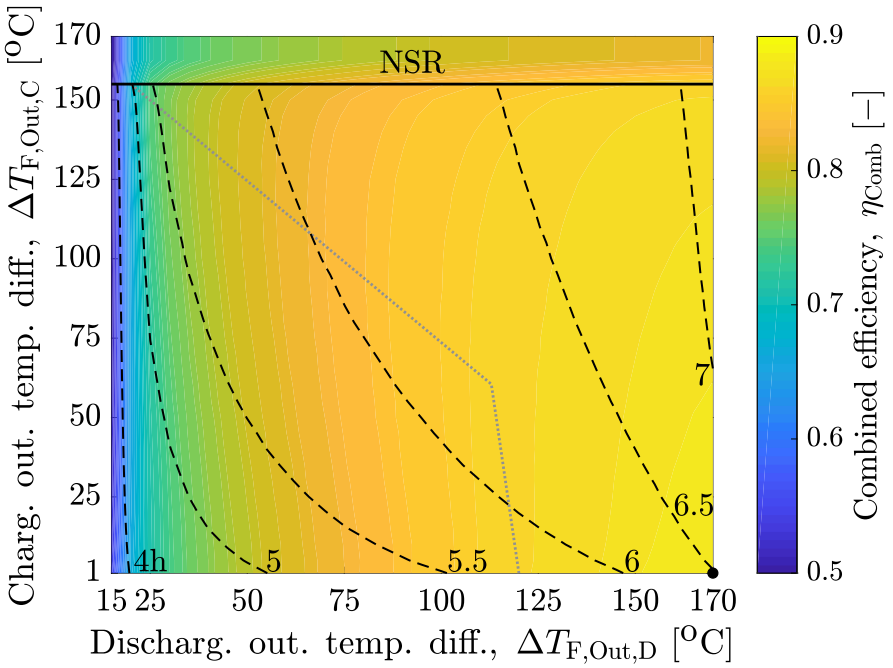


Still on Fig. 38, an extreme value of $\Delta T_{\mathrm{F,Out,C}}$ is associated with a long charging process, possibly even larger than the 12 h limit established, thus explaining the existence of the non-saturated area for $\Delta T_{\mathrm{F,Out,C}} \gtrsim 155$ °C. In contrast, ever-larger values of $\Delta T_{\mathrm{F,Out,D}}$ lead to higher efficiencies since the energy stored remains continuously being retrieved, which suggests that there is no optimal time to stop the discharging process from an efficiency standpoint. Yet on the discharging time, the trends displayed by the black dashed lines of constant $t_{\mathrm{D}}$ show that not only $\eta_{\mathrm{Comb}}$ increases with $\Delta T_{\mathrm{F,Out,D}}$ but also does $t_{\mathrm{D}}$ itself. Also, for achieving a given discharging time, a short charging time (i.e., a smaller $\Delta T_{\mathrm{F,Out,C}}$) requires a larger $\Delta T_{\mathrm{F,Out,D}}$. Finally, it is worth mentioning that, when considering the coupled solar field, TES device and power block, both $\Delta T_{\mathrm{F,Out,C}}$

and $\Delta T_{\mathrm{F,Out,D}}$, may influence the overall system efficiency, thus indicating optimization potential. For instance, while for some cases larger $\Delta T_{\mathrm{F,Out,C}}$ values may lead to larger TES combined efficiencies, they also decrease the solar field efficiency by increasing its inlet temperature.

### 4.2.3 Thermal losses: insulation thickness and thermal dispersion

Examining the influence of the TES thermal insulation thickness and the temperature of the device installation ground, it is possible to verify the relevance of the TES heat losses to the environment. Then, considering $T_{\mathrm{C}} = 550$ °C, $L = 3$ m, $D = 2$ m, $d = 3$ mm, $\varepsilon = 0.35$, $\dot{m}_{\mathrm{C}} = \dot{m}_{\mathrm{D}} = 1$ kg/s, $\Delta T_{\mathrm{F,Out,C}} = 15$ °C, and $\Delta T_{\mathrm{F,Out,D}} = 100$ °C, Fig. 39 shows the influence of the insulation thickness, which varies between 5 mm and 500 mm, on the combined efficiency. The circle markers indicate the simulated points, whereas the data-interpolated continuous gray line only facilitates the visualization.

Figure 39 – Impact of the insulation thickness $t_{\mathrm{i}}$ on $\eta_{\mathrm{Comb}}$ for $T_{\mathrm{C}} = 550$ °C, $L = 3$ m, $D = 2$ m, $d = 3$ mm, $\varepsilon = 0.35$, $\dot{m}_{\mathrm{C}} = \dot{m}_{\mathrm{D}} = 1$ kg/s, $\Delta T_{\mathrm{F,Out,C}} = 15$ °C, and $\Delta T_{\mathrm{F,Out,D}} = 100$ °C.

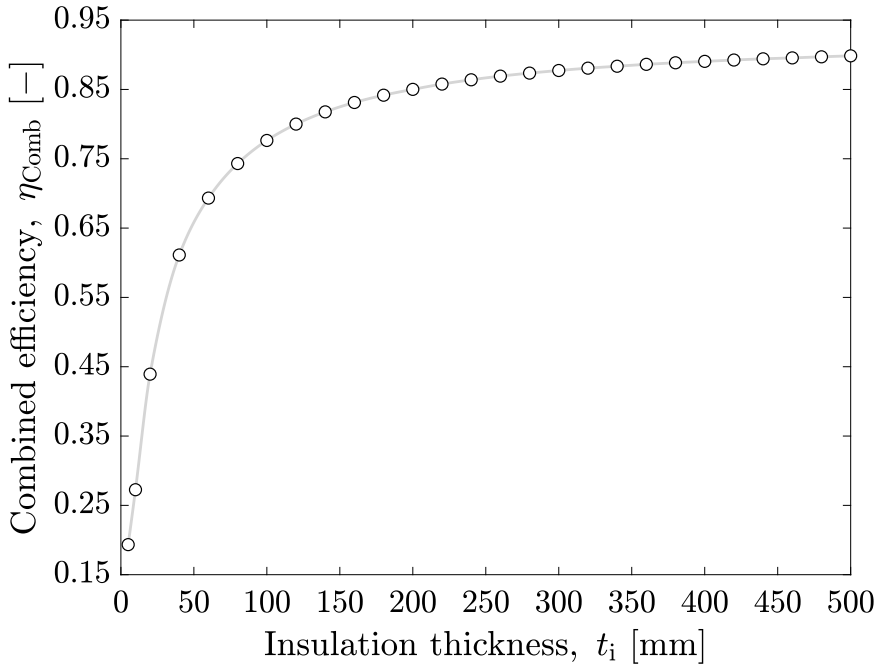


The well-expected trend that the thicker the insulation, the smaller the heat loss is easily observed while $\eta_{\mathrm{Comb}}$ varies from $\sim 0.2$ to $\sim 0.9$ within the $t_{\mathrm{i}}$ range considered. Moreover, considering the low rate of increase of $\eta_{\mathrm{Comb}}$ with the insulation thickness at $t_{\mathrm{i}} = 200$ mm, it is possible to note the reasonableness of the value used thus far.

Furthermore, still based on such $t_{\mathrm{i}}$ value, the effects of the ground temperature may be considered almost negligible since the figure of merit varied linearly between $\sim 0.84$ and $\sim 0.85$ for ground temperatures ranging from $-30$ °C to $+40$ °C. Finally, further studies may explore the possible economic optimal relationship between $\eta_{\mathrm{Comb}}$ and $t_{\mathrm{i}}$.

Next, it is also important to examine another key source of inefficiency of packed-bed TES devices, i.e., the thermal dispersion. For that, following the analysis presented by Ref. [91], the performance of the TES device was evaluated for all cases reported in Fig. 31 while considering it as being perfectly thermally insulated from the surroundings – i.e., no heat losses through the lids and/or wall (and their transient temperature fields were not solved).

Because the maximal possible combined efficiency is $\eta_{\mathrm{Comb}} = 1$, the amounts $(1 - \eta_{\mathrm{Comb}})$ and $(1 - \eta_{\mathrm{Comb}}^{\mathrm{Adiab}})$ refer to the inefficiencies for the non-adiabatic and adiabatic cases, respectively. Hence, by dividing the latter by the former, it is possible to quantitatively evaluate the effect of all other factors apart from the heat losses in the combined inefficiency through the inefficiency ratio given by

$$\Gamma \;=\; \frac{1 - \eta_{\mathrm{Comb}}^{\mathrm{Adiab}}}{1 - \eta_{\mathrm{Comb}}}. \tag{4.89}$$

First, one should recall that the sources of inefficiency of the packed-bed TES device are related to (i) pumping power, (ii) thermal losses to the surroundings, and (iii) thermal dispersion. Secondly, considering the small pressure drops shown, their effect is arguably much smaller than the effects of thermal losses to the combined inefficiency. So, it is possible to interpret $\Gamma$ as a quantitative indicator of the thermal dispersion effect on the total inefficiency of the TES device.

From the discussion above, Fig. 40 shows the mapping of $\Gamma$ for the same $L$ and $D$ ranges of Fig. 31 while also using $T_{\mathrm{C}} = 550$ °C, $d = 3$ mm, $\varepsilon = 0.35$, $\dot{m}_{\mathrm{C}} = \dot{m}_{\mathrm{D}} = 1$ kg/s, $\Delta T_{\mathrm{F,OutC}} = 15$ °C, and $\Delta T_{\mathrm{F,OutD}} = 100$ °C. Examining the values indicated in Fig. 40, it is easy to realize that the main inefficiency factor is highly dependent on the combination of $L$ and $D$ considered, with $\Gamma$ varying substantially from $\sim 5\%$ to $\sim 70\%$ – similar analyses may be extended for evaluating the effects of not only other design parameters but also operational ones on $\Gamma$. Moreover, because $\Gamma$ may be used to indicate whether the main

inefficiency effect is due to thermal losses or thermal dispersion, to ease the analysis, a continuous red line was included, which indicates a constant value of $\Gamma = 0.5$. Given that the region to the left of and below such a line indicates $\Gamma > 0.5$, it becomes clear that only a small area of the mapping has its inefficiency dominated by thermal dispersion. This result may be seen as an expansion of the limited discussion of Ref. [91], which concluded that thermal dispersion was the main source of exergetic inefficiency for the design considered. Such a difference between conclusions may be mostly related to the different approaches used to deal with the thermal losses between studies and to that Ref. [91] based its analysis on only a fixed set of design and operation parameters, instead of a parametric evaluation.

Figure 40 – Mapping of the inefficiency ratio of the TES device for the same conditions of Fig. 31.

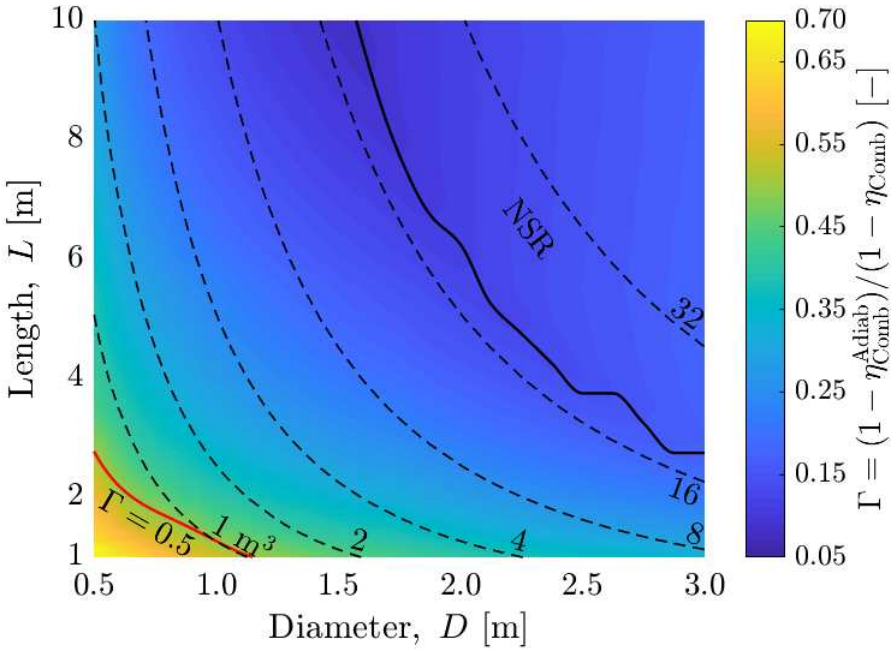


### 4.2.4 Optimization of the TES device with regard to its charging temperature and overall dimensions

Different power block operations imply different working pressures and charging (from the solar field) and discharging (from the power block) temperatures – one should remember that Tab. 1 provides both $T_{\mathrm{D}}$ and $P$ for each $T_{\mathrm{C}}$. Then, exploring the effects of changing the power block operation design point are certainly relevant under the TES point of view. Such an analysis is shown in the top plot of Fig. 41 for which two approaches

are followed: (a) fixed values of $L = 3$ m and $D = 2$ m are set, and (b) these two parameters are simultaneously optimized for each charging temperature considered. Fig. 41 considers a TES device using $d = 3$ mm, $\varepsilon = 0.35$, $\dot{m}_{\mathrm{C}} = \dot{m}_{\mathrm{D}} = 1$ kg/s, $\Delta T_{\mathrm{F,Out,C}} = 15$ °C, and $\Delta T_{\mathrm{F,Out,D}} = 100$ °C while being driven exclusively by the solar field during the charge and by the power block during the discharge. Also, the markers represent the simulated points, whereas the data-interpolated continuous gray lines only facilitate the visualization. Regarding the combined efficiency, the two main points to be observed in the top plot of Fig. 41 are that it decreases with the increase of $T_{\mathrm{C}}$ (with a subtle quadratic dependence) and that it may actually be maximized for each $T_{\mathrm{C}}$ by optimizing the $L$ and $D$ parameters. For the first point, the higher the charging temperature, the lower the combined efficiency due to the increase of thermal losses – a similar behavior is often observed in solar collectors [36]. On the other hand, power blocks benefit from increasing their high-end temperature [106], which, for instance, may be observed by the roughly quadratically increase of $\eta_{\mathrm{PB}}$ with $T_{\mathrm{PB,In}} = T_{\mathrm{C}}$ in Tab. 1. Hence, there may be a trade-off relationship, which, consequently, may indicate a possible optimal working temperature for the integrated system, i.e., solar field, TES device, and power block.

Figure 41 – Combined efficiency (top plot) versus charging temperature for a bed with $L = 3$ m and $D = 2$ m and with optimized $L$ and $D$ considering $d = 3$ mm, $\varepsilon = 0.35$, $\dot{m}_{\mathrm{C}} = \dot{m}_{\mathrm{D}} = 1$ kg/s, $\Delta T_{\mathrm{F,Out,C}} = 15$ °C, and $\Delta T_{\mathrm{F,Out,D}} = 100$ °C as well as the respective optimal values of $L$ and $D$(bottom plot).

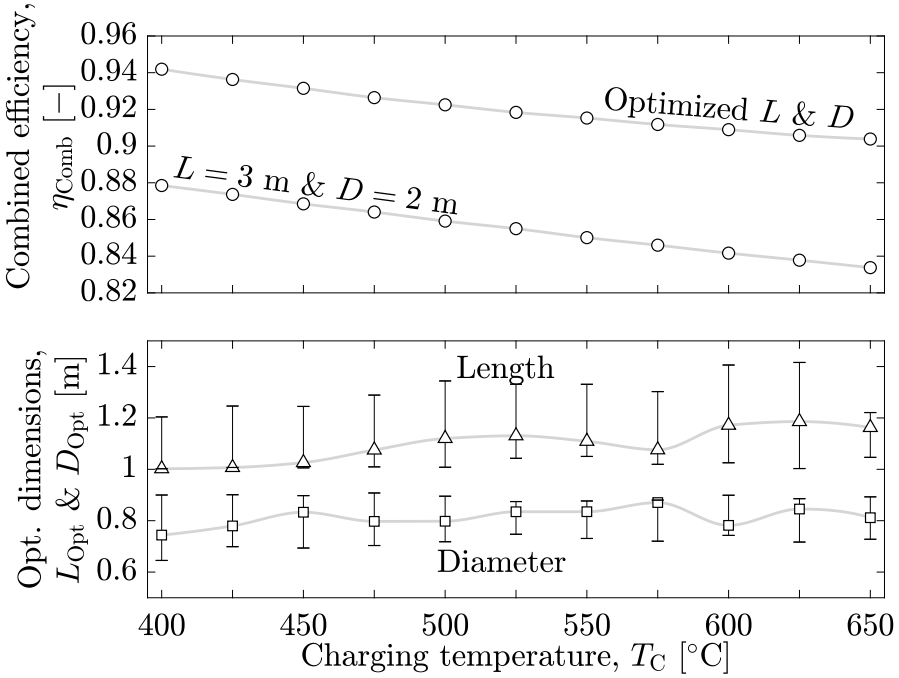

Moreover, for the second point, optimizing the geometry may substantially increase the combined efficiency because an optimal storage volume may be employed with an optimal aspect ratio. Thus, complementing the top plot of Fig. 41, its bottom plot shows the optimal values for $L$ (circle markers) and $D$ (triangle markers) versus the charging temperature. The error bars indicate, for each $T_{\mathrm{C}}$, the range of $L$ and $D$ for the specific combinations evaluated whose $\eta_{\mathrm{Comb}}$ values are at least 99.9% of the respective maximum. The data obtained suggest an overall mild increasing trend with the charging temperature for $L_{\mathrm{Opt}}$, while $D_{\mathrm{Opt}}$ tends to remain roughly constant. Furthermore, because of these overall trends with $T_{\mathrm{C}}$ for the optimal dimensions, both the optimal storage volume ($V_{\mathrm{Opt}} = \pi D_{\mathrm{Opt}}^2 L_{\mathrm{Opt}}/4$) and the optimal aspect ratio arguably follow the $L_{\mathrm{Opt}}$ behavior with $T_{\mathrm{C}}$, i.e., as the charging temperature increases, the total volume increases and its arrangement tends to be more elongated. This trend is arguably related to the increasing charging-discharging temperature difference ($T_{\mathrm{C}} - T_{\mathrm{D}}$) with $T_{\mathrm{C}}$. According to Tab. 1, as the charging temperature increases, so does the temperature amplitude to which the TES system is subjected during the charging-discharging process. Hence, a higher temperature difference implies larger available energy to be stored; consequently, larger storage volumes are required and longer geometries are more effective.

### 4.2.5 Charging-discharging cycling of the TES device

An also important analysis on the performance of the TES system concerns its operation under repeated charging-discharging cycling. For that, based on Fig. 31, six combinations of bed length and diameter were chosen: (a) $L = 1$ m & $D = 0.5$ m, (b) $L = 1$ m & $D = 3$ m, (c) $L = 10$ m & $D = 0.5$ m, (d) $L = 6$ m & $D = 2$ m, (e) $L = 1.41$ m & $D = 0.76$ m, (f) $L = 3$ m & $D = 2$ m. Combinations (a), (b), and (c) refer to the limiting cases outside the NSR; combination (d) refers to a large-volume case outside the NSR; combination (e) refers to the maximum of Fig. 31; and combination (f) refers to the baseline case used throughout the previous analyses. For all cases, the baseline parameters were adopted, i.e., $T_{\mathrm{C}} = 550$ °C, $d = 3$ mm, $\varepsilon = 0.35$, $\dot{m}_{\mathrm{C}} = \dot{m}_{\mathrm{D}} = 1$ kg/s, $\Delta T_{\mathrm{F,Out,C}} = 15$ °C, and $\Delta T_{\mathrm{F,Out,D}} = 100$ °C. Then, Fig. 42 displays the combined efficiency of all six configurations for five consecutive charging-discharging cycles (top plot) and the

respective combined efficiency percentage deviation with respect to the previous cycle (bottom plot). Because all analyses for the packed-bed TES system considered an initial uniform temperature distribution at discharging condition (and steady-state temperature distributions for wall and lids), the combined efficiency periodic representative pattern value is achieved within few cycles. Actually, this may be observed since the combined efficiency percentage deviation is smaller than 1% for all combinations beyond the second cycle. Furthermore, small-volume configurations are the most sensitive to cycling, which indicates that Fig. 31 might vary if cycling is considered. For instance, at the second cycle, combination (a) (that with the smallest volume) achieves a higher $\eta_{\text{Comb}}$ than combination (e) (that of the maximum for one cycle). Also, for the combination (f), the combined efficiency percentage deviation is $\sim 1.4\%$ already at the second cycle, which arguably suggests that trends for a single cycle may be acceptable for representing the periodic representative pattern. Such an analysis corroborates the validity of performing the previous parametric/optimization analyses considering a single charging-discharging cycle.

Figure 42 – Combined efficiency (and its deviation) versus charging-discharging cycles for various $L$ and $D$ combinations considering $T_{\text{C}} = 550$ °C, $d = 3$ mm, $\varepsilon = 0.35$, $\dot{m}_{\text{C}} = \dot{m}_{\text{D}} = 1$ kg/s, $\Delta T_{\text{F,Out,C}} = 15$ °C, and $\Delta T_{\text{F,Out,D}} = 100$ °C.

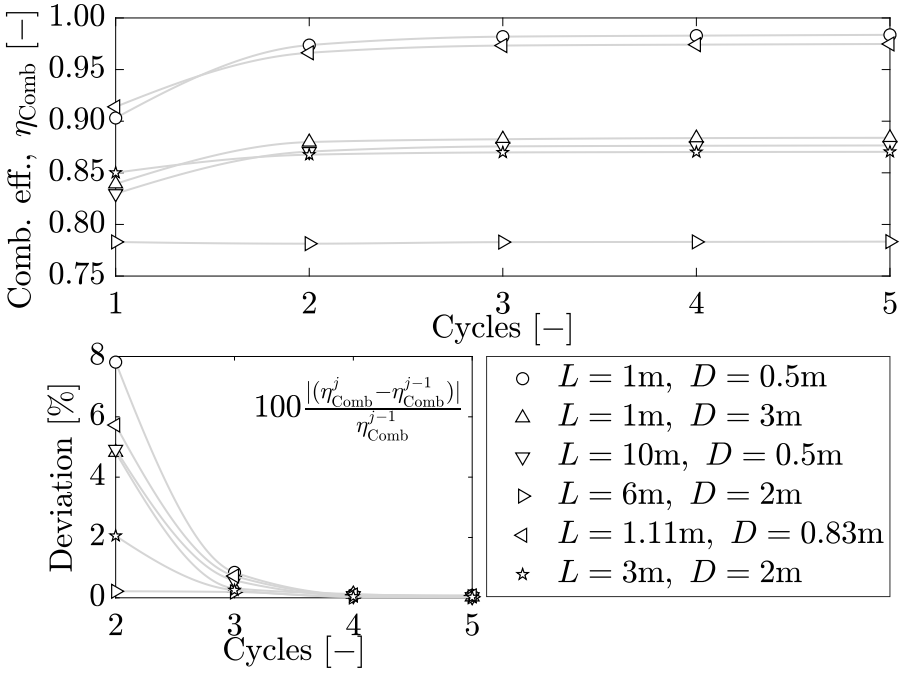


Following on the cycling influence over the performance of the TES device, it is relevant to evaluate the system operation over cycles comprised of a full day each.

Then, assuming once again $T_{C} = 550$ °C, $d = 3$ mm, $\varepsilon = 0.35$, $\Delta T_{F,Out,C} = 15$ °C, and $\Delta T_{F,Out,D} = 100$ °C, also considering that the solar field could charge the TES system for $t_{C} \sim 10$ h (considering the solar availability during the day), a discharging time of $t_{D} \sim 14$ h would then be required while providing the power block with a discharging mass flow rate of $\dot{m}_{D} = 1$ kg/s. From the discussion of Figs. 32 and 33, it is possible to infer that the discharging time is dominated by the TES volume. Then, considering a similar solid axially-averaged temperature difference between the beginning and the end of the discharging, scaling the TES volume for $t_{D} \sim 14$ h leads to $V \approx 23.03$ m$^3$. For determining the actual dimensions of the packed-bed, the aspect ratio is also required. From Fig. 34, for TES systems slightly larger than 20 m, it may be extrapolated an optimal aspect ratio of $\zeta = 1.2$, which leads to $L = 3.49$ m and $D = 2.90$ m for $V \approx 23.03$ m$^3$. Now, for the charging process subjected to $t_{C} \sim 10$ h, with Fig. 37 it is clear that the charging mass flow rate could be varied independently of the discharging one roughly without influencing the discharging time. Then, as may be also inferred that the charging time is inversely related to the charging mass flow rate, a charging mass flow rate of $\dot{m}_{C} = 1.4$ kg/s is adopted. Fig. 43 shows in its top plot the combined efficiency for 5 consecutive charging-discharging cycles for the TES configuration described without idle time, i.e., $t_{I} = 0$ h. As expected due to the large volume, the system performance variation with cycling is negligible (the deviation is less than $\sim 0.4\%$ for all cycles). The charging and discharging times for all cycles are close to the specified ones, which corroborates the design choices. For instance, with this configuration and operating with $T_{C} = 550$ °C, the TES system is capable of providing heat for the power block operating with 1 kg/s during the $\sim 14$ h time span, which allows a net power production of $\sim 0.1$ MW using the respective power block thermal efficiency of 0.4738 from Tab. 1.

Furthermore, another suitable discussion on the TES cycling refers to the influence of an idle period between the end of the charge and the beginning of the discharge. Such an analysis is relevant due to the importance of the system capability of not only storing and releasing thermal energy as required but also of retaining it until necessary. Then, still considering the same system configuration and discharging time of $t_{D} \sim 14$ h, the charging process is shorted from $t_{C} \sim 10$ h to $\sim 9$ h, $\sim 8$ h, and $\sim 7$ h, for allowing idle

Figure 43 – Combined efficiency (and its deviation) versus charging-discharging cycles for various $L$ and $D$ combinations considering $T_{\mathrm{C}} = 550$ °C, $d = 3$ mm, $\varepsilon = 0.35$, $\dot{m}_{\mathrm{C}} = \dot{m}_{\mathrm{D}} = 1$ kg/s, $\Delta T_{\mathrm{F,Out,C}} = 15$ °C, and $\Delta T_{\mathrm{F,Out,D}} = 100$ °C.

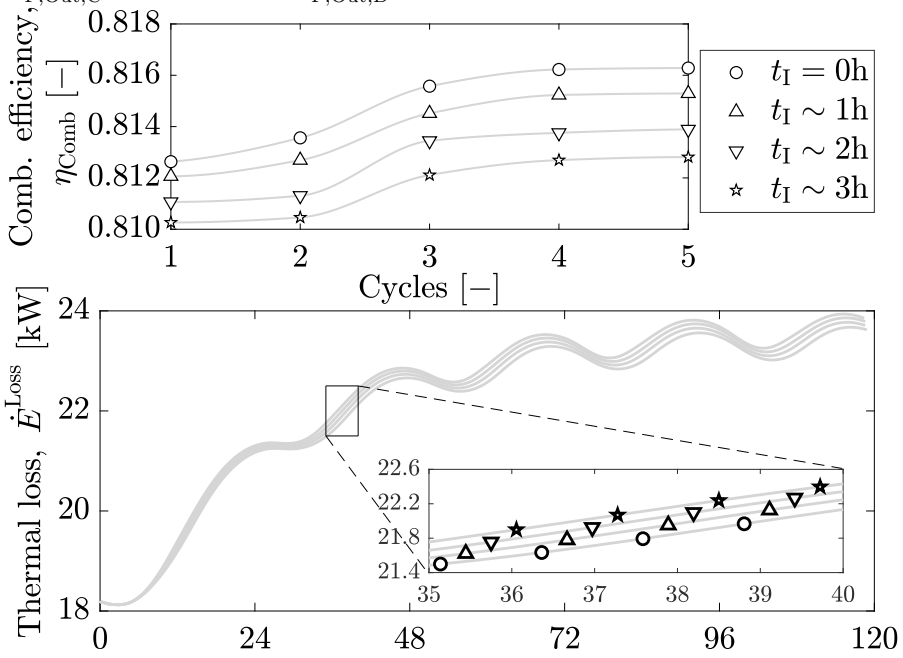


times of $t_{\mathrm{I}} \sim 1$ h, $\sim 2$ h, and $\sim 3$ h, respectively. For achieving that, it is considered that the charging mass flow rate is set for each case as $\dot{m}_{\mathrm{C}} = 1.56$ kg/s, 1.75 kg/s, and 2 kg/s, respectively. When the charging process ends, the idle period begins; the mass flow stops and the pressure field becomes uniform at the inlet value. During the idle time span, the heat transfer, within a node, occurs between the fluid and solid phases; whereas, between neighbor nodes, the heat transfer occurs only between the solid phases considering the solid effective thermal conductivity – the heat transfer between the fluid phases due to diffusion is arguably much smaller. Also, during the idle time, the fluid mass contained within the packed-bed at the charge end remains inside the TES vessel, which has a fixed volume. Hence, because the TES device loses thermal power to the surroundings, the uniform pressure field must be adjusted so the total fluid mass remains constant. For that, the pressure update step described in Sub. 4.1.11 uses the fluid equation of state instead of the Modified Ergun's correlation (because there is no fluid flow). The fluid mass within each node is calculated using the fluid volume-specific mass, which depends on the updated temperature field and on the pressure value, and the summation of all fluid nodes masses must equal the total mass from the charge end. The pressure value for each time step is easily obtained using the FSOLVE function from MATLAB®. So,

also in the top plot of Fig. 43, the combine efficiency values for five consecutive cycles for each idle time considered are shown. The variation of the combined efficiency is roughly negligible both between cycles and between idle times, which indicates that the system performance may already be considered as if in periodic representative operational pattern and that idle times (within the range considered) have little influence over the system performance for the configuration considered. Finally, complementing the analysis, the bottom plot of Fig. 43 displays the temporal behavior of the total thermal power loss (i.e., the summation of losses through the wall and both lids) during the five cycles. It is quite clear that the thermal loss rapidly achieves the expected sinusoidal behavior over the time, as discussed by Ref. [91]. Moreover, the steep thermal loss increase from the initial steady-state condition at the beginning of the first charging processes arguably indicates that the analyses presented considering only one charging-discharging cycle may overestimate the charging efficiency. Nonetheless, because the system performance is mostly influenced by the discharging process and the thermal loss over the discharge for the first cycle is somewhat similar to that over the remaining cycles, it may actually be conceived that the system performance may indeed vary little between cycles, as discussed.

# 5 ECONOMIC-ENVIRONMENTAL ASSESSMENT AND OPTIMIZATION OF A $CO_2$ SOLAR-POWERED PLANT WITH PACKED-BED THERMAL ENERGY STORAGE

When dealing with solar-powered plants, the use of TES technologies is undoubtedly one of the key approaches explored for increasing energy dispatchability while boosting the solar fraction of energy deployed. In spite the fact that a few theoretical studies addressed the use of TES solutions for s-$CO_2$ -based plants, these do not provide sufficient and reliable information on designing and minimizing inherent costs for such systems, e.g., highlighting optimal design and operation parameters and the system integration.

Therefore, following the technical analysis of Chap. 4 and because packed-bed TES is a technology demanding an assessment on its economic feasibility for s-$CO_2$ applications, this study aims to analyze overall economic trends of an integrated system composed of such a TES system, a solar field, and a power block while considering s-$CO_2$ as HTF and using auxiliary conventional heating. The analysis is carried out through numerical simulations for exploring several operational conditions while regarding typical meteorological year (TMY) data for a reference city on CSP applications, i.e., Daggett/USA. Additionally, not only both the size of the TES system and the required auxiliary heating depend on the operational conditions, but also do the related costs, which are considered in detail.

Furthermore, endorsing the idea of an integrated power plant running solely with s-$CO_2$ as HTF, the packed-bed TES system thoroughly discussed in Chap. 4 was chosen for storing the surplus of energy from the solar field. Then, by drawing upon parametric analyses, the study stresses combinations of solar field and TES sizes and considers the levelized cost of energy (LCOE) as the main figure of merit. In addition, the analysis accounts for the system environmental sustainability through a penalization cost regarding $CO_2$ emissions due to the auxiliary heating.

## 5.1 METHODOLOGY FOR THE SYSTEM MODELING AND EVALUATION

The following subsections present the methodology employed for the system modeling and evaluation. Sub. 5.1.1 describes the integrated system and its numerical routine,

whereas Subs. 5.1.2, 5.1.3, and 5.1.4 present the models considered for simulating the power block, the solar field, and the packed-bed TES system, respectively. Additionally, Sub. 5.1.5 presents the approach for the system economics assessment. Moreover, all numerical routines were implemented in MATLAB® [104] using fluids properties from CoolProp [3, 4].

### 5.1.1 Integrated system and its numerical routine

Fig. 44 presents the overall layout of the integrated system considered in this study. The s-$CO_2$ recompression Brayton cycle, which is a highly-ranked configuration for solar-powered plants, was chosen for the power block, as detailed in Sub. 5.1.2. The solar thermal power input, as detailed in Sub. 5.1.3, is accounted for through a parabolic trough collector field, which has been tested with s-$CO_2$ and has valuable experimental data for theoretical modeling and verification [19]. A packed-bed TES system, as detailed in Sub. 5.1.4, is responsible for storing (charging) and releasing (discharging) the surplus of thermal power from the solar field aiming to extend the power production beyond the solar availability. At this point, it is worth to recall that specific optimization of packed-bed TES devices for s-$CO_2$-based CSP generation is a major feature to be investigated since, although they may be more efficient than two-tank devices, the working pressures required by the s-$CO_2$ might impair their economic feasibility [34]. Also, following the discussion on Fig. 19 in Sub. 4.1.1 , the packed-bed TES device considered includes auxiliary compressors at each end for recirculating the HTF, which were omitted in this graphic representation of Fig. 44. Moreover, the power block is designed regarding a nominal net power production of $\sim 10$ MW while being assisted by a conventional auxiliary heater using natural gas as fuel, which assures that the power block inlet design conditions are met at all time. Hence, the power block may be considered as always in steady state regardless of the solar gains.

As shown in Fig. 44, the parallel disposition between solar field, TES system, and power block (with the auxiliary heater between the TES system and the power block) allows different dynamic operation strategies. The simplest strategy disregards both the solar field and the TES system, i.e., the system runs through the recirculation bypass with the auxiliary heater as the energy source for the power block. However, other system

Figure 44 – Overall layout of the integrated system.

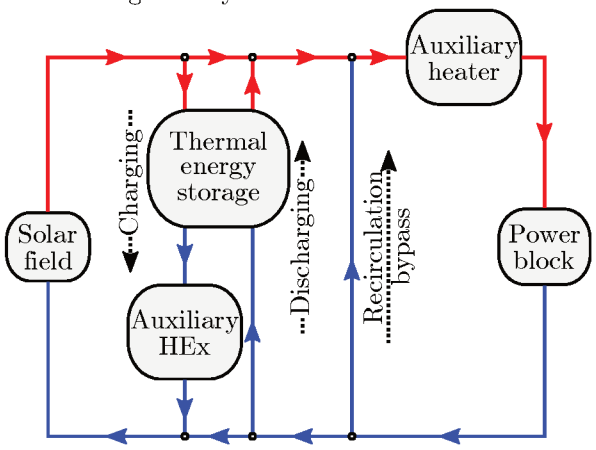


strategies emerge with the solar field being able to act as heat source. If the solar field provides a mass flow rate equal to the power block design value, the system disregards the TES device and the HTF flows through the auxiliary heater to the power block. If the solar field provides a mass flow rate greater than the power block design value, the system splits the HTF flow so the power block receives the design value and the remaining fraction is directed to the TES for charging the surplus thermal energy. Now, if the solar field provides less mass flow rate than the power block design value, the system first asses the possibility of discharging the TES with a mass flow rate equal to the missing fraction to retrieve energy for meeting the required power block inlet design and, if possible, the TES system is discharged; on the other hand, if the discharge is not possible, the system uses the recirculation bypass and, then, the auxiliary heater. The final strategy comes from the impossibility of the solar field acting as heat source at all, in which the system follows the strategy just discussed, but now considering the entire mass flow rate instead of just a fraction of it. Moreover, if for a given system time step the CSP could provide a mass flow rate greater than the power block design value, but the TES device is unable to be charged, the system control points to defocus the solar field so the mass flow rate provided equals the power block design value. Additionally, for all time steps when the TES system idles, i.e., when it is not being charged or discharged, it follows the procedure described in Sub. 4.2.5.

Furthermore, when the heat gain from the solar field is excessive to be used by the power block and stored by the TES system, it is common to reject its surplus (e.g., defocus of the solar field). For facilitating the numerical simulations, in current modeling,

an auxiliary heat exchanger was included at the TES charging outlet (see "Auxiliary HEx" in Fig. 44) for heating or cooling the mass flow rate exiting the TES system during the charging, in order to maintain its temperature always equal to that of the mass flow rate exiting the power block. The inclusion of this component may seem somewhat unpractical, but it was necessary for assuring the inlet condition to the solar field, which was considered to remain constantly at design condition throughout all time steps of all simulations as further discussed in Sub. 5.1.3. This boundary condition was included to avoid the numerical iteration between the solar field and the TES solution within a system time step, thus allowing the annual economic assessment to be performed in a time-efficient manner. Such a component should be considered artificial, because it would not be used in an actual system, and its inclusion is only acceptable due to it significantly lowering the simulation ruining time. For the actual system, an active overall controller would be used considering the solar field-TES system interaction. Finally, considering the auxiliary heat exchanger, for heating the HTF, all the energy is computed and included as portion of the total auxiliary heating; for cooling the HTF, on the other hand, the energy is simply considered lost – something similar to what would happen with the solar gain with the decrease of the solar field efficiency with the increase of its HTF inlet temperature.

The numerical routine was implemented to run the integrated system on an annual basis, following the discussion above. For helping the understanding, the overall system control strategy is summarized by the flowchart shown in Fig. 45.

For all the simulations performed, the system time step is $\Delta t_{\mathrm{Sys}} = 1$ h, the TES time step is $\Delta t_{\mathrm{TES}} = 60$ s, and the TES axial discretization is $N_{\mathrm{z}} = 160$. For a given set of input parameters (which follow those of Chap. 4 for the TES device) and variables values (i.e., see Sub. 5.1.4), the routine starts at $t_{\mathrm{Sys}} = \Delta t_{\mathrm{Sys}} = 1$ h by evaluating the solar field availability. Then, the control scheme decides for TES charging (light blue background), TES discharging (light red background), or straight auxiliary heating based on the outlet temperature for a TES time step of $\Delta t_{\mathrm{TES}} = 60$ s.

Figure 45 – Main numerical routine flowchart.

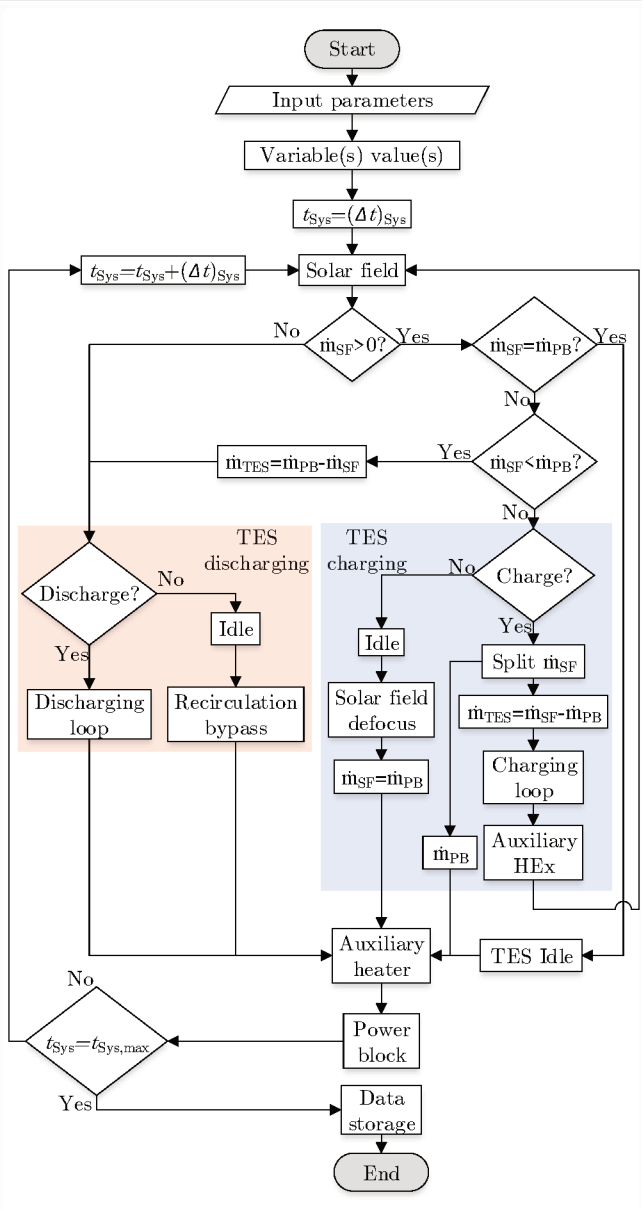


### 5.1.2 Power block

Several Brayton cycle configurations have been tested for high-temperature s-$CO_2$ solar-powered plants, which include re-heating, recompression, and intercooling designs for increasing overall efficiency [8]. Nevertheless, recuperative and recompression cycles may be considered satisfactory in terms performance-relative costs since further increasing the configuration complexity seems not to directly translate into a relative performance upgrade. Therefore, because the cycle enhancement is not the main focus of analysis, in the present study, the recompression Brayton cycle is considered.

The power block is modeled using the methodology of Ref. [122] for s-$CO_2$ recom-

pression cycles, which includes off-design effects on assessing the cycle thermal performance while regarding a nominal net power production of $\sim 10$ MW. More specifically, in this modeling, the turbomachinery efficiencies rely on performance maps experimentally validated, which relate such values to the corresponding s-$CO_2$ mass flow rates. Also, the inefficiencies of the heat exchangers, such as thermal resistance and pressure drop, are predicted and scalable in terms of their mass flow rates. Such a modeling approach has been considered by different authors, e.g., Refs. [73, 123, 155]. In addition, further details are available in the complete formulation of Ref. [122]. Having said that, in order to avoid eventual overlapping, this subsection focus on the particular selected input parameters.

In this sense, for the $\sim 10$ MW net power production set as the design target, the power block input data set requires an inlet temperature (i.e., the power cycle high-temperature-end or the turbine upstream temperature), which was assumed as $T_{\mathrm{PB,In}} = 550$ °C. Also, for the power cycle low-temperature-end, the main compressor upstream temperature and pressure of 50 °C and $P_{\mathrm{PB}}^{\mathrm{Low}} = 10$ MPa, respectively, were set. For the recompression stage, a fixed mass flow rate fraction of 25.8% was employed. With such parameters, the power cycle model outputs a high-temperature-end pressure of $P_{\mathrm{PB}}^{\mathrm{High}} \approx 25$ MPa, a mass flow rate of $\dot{m}_{\mathrm{PB}} = 133.2$ kg/s, a power block outlet temperature of $T_{\mathrm{PB,Out}} = 407.42$ °C and a net power output of $\dot{W}_{\mathrm{PB}}^{\mathrm{Net}} = 9.93$ MW $\approx 10$ MW.

### 5.1.3 Solar field

For the solar field, the already validated modeling of Refs. [123, 156] is employed. The solar heat gain in the solar collector field is calculated using the thermal performance reported for a parabolic trough field, whose efficiency depends on the average temperature of the absorber. For the time-dependent collector outlet temperature, the efficiency is calculated based on the LS-2 geometry and heat transfer mechanics reported in Ref. [157]. Thus, for the energy balance in the absorber, the heat gain is expressed as [123, 156]

$$m_{\mathrm{Coll}} c_{\mathrm{Coll}} \frac{dT_{\mathrm{Coll}}}{dt} = \eta_{\mathrm{Coll}} I_{\mathrm{b}} \left( \frac{A_{\mathrm{Aper}}}{N_{\mathrm{Coll}}} \right) + 2\dot{m}_{\mathrm{F}} c_{\mathrm{F}} \left( T_{\mathrm{F,In}} - T_{\mathrm{F}} \right), \tag{5.1}$$

where $I_{\mathrm{b}}$ is the beam radiation, $A_{\mathrm{Aper}}$ the total solar field aperture area of mirrors, and $N_{\mathrm{Coll}}$ the number of independent parallel collector rows into which the solar field is split, which was set as 100 for this study. The beam radiation is obtained as

$$I_{\mathrm{b}} = DNI \cdot \cos\theta_{\mathrm{b}}, \tag{5.2}$$

where $DNI$ is the direct normal irradiation, $\theta_{\mathrm{b}}$ is the angle of incidence (details regarding its calculation are shown in Ref. [157]). The total solar field aperture area of mirrors is given as

$$A_{\mathrm{Aper}} = SM \cdot A_{\mathrm{SF,ref}}, \tag{5.3}$$

where $SM$ is the solar multiple and $A_{\mathrm{SF,ref}}$ the reference solar field aperture area. The $A_{\mathrm{SF,ref}}$ value was determined such that the solar field would provide a total mass flow rate equal to that required by the power block, i.e., $\dot{m}_{\mathrm{PB}} = 133.2$ kg/s, while observing the HTF outlet temperature to be equal to $T_{\mathrm{PB}}^{\mathrm{In}} = 550$ °C. Then, assuming the reference conditions of solar normal radiation of 900 W/m$^2$, air temperature of 20 °C, no wind, and HTF inlet temperature of $T_{\mathrm{PB}}^{\mathrm{Out}} = 407.42$ °C, the value of $A_{\mathrm{SF,ref}} = 435.5$ m$^2$ was determined.

Similar to previously stated for the power block, because the specifics on the solar collector are not within the main scope of this dissertation, these are omitted for the sake of brevity – Refs. [88, 123, 156] provide detailed information on the modeling employed.

For all the analyses, the $DNI$, air temperature ($T_{\mathrm{Air}}$), and wind speed ($u_{\mathrm{Air}}$) data for Daggett/USA were used as inputs, which were obtained from the TMY basis of Ref. [35]. Fig. 46 graphically shows such data, in which each of the 8760 black dots represents one hour of the year.

Furthermore, the solar field modeling and the TMY data were used for obtaining the solar field HTF outlet temperature and mass flow rate for each hour of the year considering that the HTF always entered the solar field at $T_{\mathrm{PB}}^{\mathrm{Out}} = 407.42$ °C and $P_{\mathrm{PB}}^{\mathrm{High}} \approx 25$ MPa, as previously mentioned. Then, for each $SM$ value investigated, the solar field annual

Figure 46 – Typical Meteorological Year (TMY) direct normal irradiation, air temperature, and wind speed data for Daggett/USA from Ref. [35].

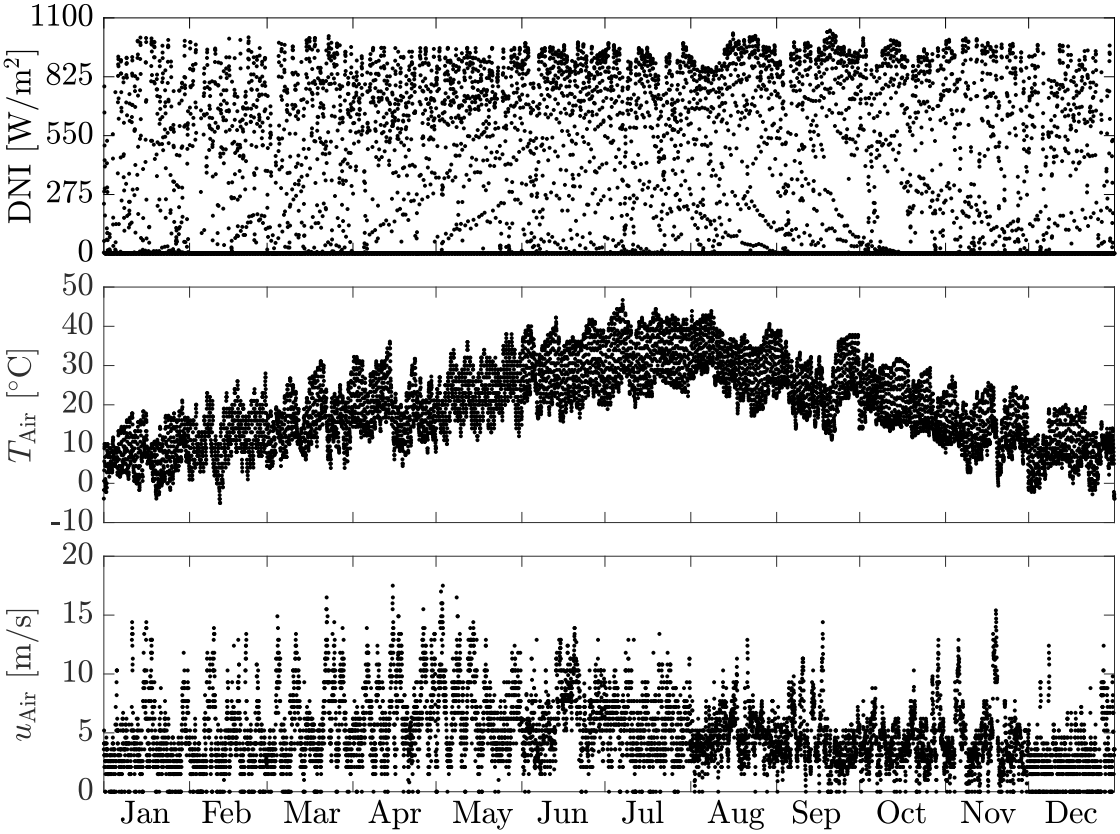


outputs were obtained by optimizing the mass flow rate so that $T_{\mathrm{SF}}^{\mathrm{Out}}$ would be as close as possible to $T_{\mathrm{PB}}^{\mathrm{In}} = 550$ °C. Therefore, intending to investigate a broad range of inputs, this procedure was observed for $SM$ values of 1.5, 2.0, 2.5, 3.0, 3.5, and 4.0.

### 5.1.4 Packed-bed TES

The numerical modeling utilized for evaluating the performance of the packed-bed TES system in this study follows that thoroughly presented and discussed in Chap. 4, except for the temperature-enthalpy coupling factor $g$, for which, aiming to substantially improve the numerical routine stability, a new approach was considered. Similarly to shown in Eq. 4.22, one may approximate the fluid mass-specific enthalpy through a linearization process as

$$i_{\mathrm{F}}\left(T_{\mathrm{F}}\right) \approx i_{\mathrm{F}}\left(T_{\mathrm{F}} = T_{\mathrm{F,a}}\right) + \left(T_{\mathrm{F}} - T_{\mathrm{F,a}}\right) \left.\frac{\partial i_{\mathrm{F}}}{\partial T_{\mathrm{F}}}\right|_{T_{\mathrm{F}}=T_{\mathrm{F,a}}}, \tag{5.4}$$

and using $\partial i_{\mathrm{F}}/\partial T_{\mathrm{F}} \approx c_{\mathrm{F}}$, it follows that

$$T_{\mathrm{F}} \approx T_{\mathrm{F,a}} + \left[\frac{i_{\mathrm{F}}\left(T_{\mathrm{F}}\right) - i_{\mathrm{F}}\left(T_{\mathrm{F,a}}\right)}{c_{\mathrm{F}}\left(T_{\mathrm{F,a}}\right)}\right]. \tag{5.5}$$

Then, using Eq. 5.5, it is possible to obtain the updated expressions for the fluid, solid, and wall/lids similarly to the development presented in Subs. 4.1.3, 4.1.4, and 4.1.9 – these developments will by omitted for the sake of brevity. With this simple approach, by using the previous iteration value as approximation for the fluid temperature, the numerical stability is improved because the updated value is obtained by adding to the approximation value a somewhat correction factor, which is based on the mass-specific heat. Also, it was observed that this approach not only improves the numerical routine stability but also its convergence, mostly because the linearization provides better guesses for the subsequent iteration.

Following Eq. 4.88, the sizing of the total TES volume is obtained as a function of the selected number of design discharging hours ($t_{\mathrm{TES}}$) as

$$V_{\mathrm{TES,Total}} = \frac{\dot{m}_{\mathrm{PB}}\left[i_{\mathrm{F}}\left(T_{\mathrm{PB,In}}, P_{\mathrm{PB}}\right) - i_{\mathrm{F}}\left(T_{\mathrm{PB,out}}, P_{\mathrm{PB}}\right)\right] t_{\mathrm{TES}}}{\left(1-\varepsilon\right)\rho_{\mathrm{S}}\bar{c}_{\mathrm{S}} 0.8\left(T_{\mathrm{PB,In}} - T_{\mathrm{PB,Out}}\right)}, \tag{5.6}$$

for which $i_{\mathrm{F}}$ is fluid mass-specific enthalpy as a function of temperature an pressure, $\varepsilon = 0.35$ the porosity, $\rho_{\mathrm{S}} \approx 3950$ kg/m$^3$ and $\bar{c}_{\mathrm{S}} \approx 1150$ J/(kg $\cdot$ K) the particles volume-specific mass and average mass-specific heat at constant pressure, respectively. For design, the solid axially-averaged temperature difference was considered as 80% of the inlet and outlet power block temperature difference, and it was assumed that the time-averaged thermal power released by the solid equals the power required for taking the power block mass flow rate $\dot{m}_{\mathrm{PB}}$ from the outlet to the inlet power block conditions. Moreover, using Eq. 5.6, the length for each TES device is given by

$$L_{\mathrm{TES}} = \frac{4V_{\mathrm{TES,Total}}}{\pi D_{\mathrm{TES}}^2 N_{\mathrm{TES}}}, \tag{5.7}$$

with which the $L_{\mathrm{TES}}$ values shown in Tab. 6 are obtained for various $N_{\mathrm{TES}}$, $t_{\mathrm{TES}}$, and $D_{\mathrm{TES}}$.

Table 6 – TES length ($L_{\mathrm{TES}}$, [m]) based on the discharging time ($t_{\mathrm{TES}}$), TES diameter ($D_{\mathrm{TES}}$), and number of TES ($N_{\mathrm{TES}}$)

| $N_{\mathrm{TES}} = 5$ | | | | | | | |
|---|---|---|---|---|---|---|---|
| $D_{\mathrm{TES}}$ | $t_{\mathrm{TES}} = 0.25$ h | 0.5 h | 1 h | 2 h | 4 h | 6 h | 8 h |
| 2.0 | 4.0131 | 8.0262 | 16.0524 | 32.1047 | 64.2095 | 96.3142 | – |
| 3.0 | 1.7836 | 3.5672 | 7.1344 | 14.2688 | 28.5375 | 42.8063 | 57.0751 |
| 4.0 | 1.0033 | 2.0065 | 4.0131 | 8.0262 | 16.0524 | 24.0786 | 32.1047 |
| 5.0 | 0.6421 | 1.2842 | 2.5684 | 5.1368 | 10.2735 | 15.4103 | 20.5470 |
| $N_{\mathrm{TES}} = 10$ | | | | | | | |
| $D_{\mathrm{TES}}$ | $t_{\mathrm{TES}} = 0.25$ h | 0.5 h | 1 h | 2 h | 4 h | 6 h | 8 h |
| 1.5 | 3.5672 | 7.1344 | 14.2688 | 28.5375 | 57.0751 | 85.6126 | 114.1502 |
| 2.0 | 2.0065 | 4.0131 | 8.02620 | 16.0524 | 32.1047 | 48.1571 | 64.2095 |
| 3.0 | 0.8918 | 1.7836 | 3.56720 | 7.13440 | 14.2688 | 21.4032 | 28.5375 |
| 4.0 | 0.5016 | 1.0033 | 2.00650 | 4.01310 | 8.02620 | 12.0393 | 16.0524 |
| $N_{\mathrm{TES}} = 15$ | | | | | | | |
| $D_{\mathrm{TES}}$ | $t_{\mathrm{TES}} = 0.25$ h | 0.5 h | 1 h | 2 h | 4 h | 6 h | 8 h |
| 1.5 | 2.3781 | 4.7563 | 9.5125 | 19.025 | 38.0501 | 57.0751 | 76.1001 |
| 2.0 | 1.3377 | 2.6754 | 5.3508 | 10.7016 | 21.4032 | 32.1047 | 42.8063 |
| 3.0 | 0.5945 | 1.1891 | 2.3781 | 4.7563 | 9.5125 | 14.2688 | 19.025 |
| 4.0 | 0.3344 | 0.6688 | 1.3377 | 2.6754 | 5.3508 | 8.0262 | 10.7016 |

The $N_{\mathrm{TES}}$ variable was included in the study due to possibly large pressure drops related to larger mass flow rates flowing through the porous medium structure of the packed-bed. Hence, the charging or discharging mass flow rate is equally divided between the $N_{\mathrm{TES}}$ packed-bed TES devices considered. Also, because all TES are equal and subjected to the same inputs and boundary conditions, just one is simulated and its response used for all the remaining. Also, given that the TES simulation is performed with a much smaller time step than that of the integrated system, for easing the further calculations, the TES outlet fluid mass flow rate and mass-specific enthalpy are obtained as temporal averages for each system time step as

$$\left\langle \dot{m}_{\mathrm{TES}} \right\rangle = \frac{1}{\Delta t_{\mathrm{Sys}}} \int_{\Delta t_{\mathrm{Sys}}} \dot{m}_{\mathrm{TES}}^{\mathrm{Out}} dt \tag{5.8}$$

and

$$\langle i_{\mathrm{F,TES}} \rangle = \frac{\int_{\Delta t_{\mathrm{Sys}}} \dot{m}_{\mathrm{TES}}^{\mathrm{Out}} i_{\mathrm{F,TES}}^{\mathrm{Out}} dt}{\int_{\Delta t_{\mathrm{Sys}}} \dot{m}_{\mathrm{TES}}^{\mathrm{Out}} dt}. \tag{5.9}$$

And the power spent with the auxiliary compressors is added to the outlet fluid flow through energy balances for obtaining the actual outlet mass-specific enthalpy.

Furthermore, aiming to better account for the thermal losses, following indicatives of Ref. [158], instead of a fixed value for the ground temperature it was considered to be 3 °C above the air temperature at each system time step.

### 5.1.5 System economics

The economic assessment of the integrated CSP plant evaluates the costs of the main equipment composing of the three major subsystems, i.e., solar field, TES system, and power block. Based on the literature (e.g., Refs. [159, 160]), the widely-regarded approach of using scalable functions was chosen. This method indicates that the costs for different sizes of components are related to reference cases previously determined following a similar expression to

$$\frac{C}{C_{\mathrm{ref}}} = \left( \frac{S}{S_{\mathrm{ref}}} \right)^{n}, \tag{5.10}$$

where $C$ is the cost, $S$ a metric for the equipment size, $n$ the scaling exponent, and the subscript ref refers to the reference case. Therefore, the costs of manufacturing the subsystems within the power block may be estimated relying on reference data for s-$CO_2$ [95]. Additionally, Eq. 5.10 may also be used for estimating the costs for the solar field and the auxiliary heating process. Tab. 7 presents the expressions used for determining the equipment costs for the power block and the solar field.

Therefore, for the recompression power block (whose layout is shown in Fig. 20) composed of a turbine, a main compressor, a recompressor, two recuperators (high and low temperature), an air cooler, and an electric generator, using the expressions from Tab. 7,

Table 7 – Equipment cost expressions for solar field and power block.

| Equipment | Cost expression* [US$] |
|---|---|
| Turbine [95] | $9923.7\dot{W}^{0.5886}$ |
| Compressor [95] | $643.15\dot{W}^{0.9142}$ |
| Recuperator [95] | $5.2\,(UA)^{0.8933}$ |
| Air cooler [98] | $1100\left[177.03\dot{E}_{\mathrm{Co}} - \left(2\dot{E}_{\mathrm{Co}}^{2}/10^{3}\right) + \left(1.32\dot{E}_{\mathrm{Co}}^{3}/10^{8}\right)\right]$ |
| Electric generator [98] | $6\cdot 10^{6}\left(\dot{W}_{\mathrm{Ele}}/160\right)^{0.7}$ |
| Site preparation [98] | $20A_{\mathrm{Aper}}$ |
| Mirrors [98] | $120A_{\mathrm{Aper}}$ |
| Receivers [98] | $140\cdot 10^{6}\left(A_{\mathrm{Rec}}/1571\right)^{0.7}$ |

*$[\dot{W}]$ = kW, $[UA]$ = W/K, $[\dot{E}_{\mathrm{Co}}] = [\dot{W}_{\mathrm{Ele}}]$ = MW, $[A_{\mathrm{Aper}}] = [A_{\mathrm{Rec}}]$ = m$^2$

the cost is estimated as

$$C_{\mathrm{PB}} = C_{\mathrm{T}} + C_{\mathrm{MC}} + C_{\mathrm{RC}} + C_{\mathrm{HTR}} + C_{\mathrm{LTR}} + C_{\mathrm{Co}} + C_{\mathrm{EG}}. \tag{5.11}$$

The turbine and compressors costs are estimated based on the power produced/consumed per each, which are determined by the mass flow rate through and the inlet-outlet mass-specific enthalpy difference of each one. For the recuperators, the costs are estimated based on the global conductance, which is obtained using discretization (into $N$ sub-heat exchangers), considering the total thermal power transferred within each heat exchanger and its logarithmic mean temperature difference (LMTD) as [103]

$$(UA) = \sum_{j=1}^{N} \frac{\left(\dot{E}/N\right)}{\Delta T_{\mathrm{LMTD,j}}}. \tag{5.12}$$

The air cooler cost is estimated based on the thermal power exchanged $\left(\dot{E}_{\mathrm{Co}}\right)$, which is also determined by the mass flow rate through and the inlet-outlet mass-specific enthalpy difference of the heat exchanger. The electric generator cost is estimated based on the electric power generated, which was set as $\sim 10$ MW.

Regarding the main heat supplying device, similar to Eq. 5.11, the solar field cost is obtained as

$$C_{\mathrm{SF}} = C_{\mathrm{Site}} + C_{\mathrm{Mirror}} + C_{\mathrm{Rec}}. \tag{5.13}$$

Both the site preparation and the mirrors costs are estimated based on the aperture area, which is simply obtained from the reference area and the solar multiple – as indicated in Eq. 5.3 – whereas the receivers cost is estimated based on their tubes external area, which is obtained from

$$A_{\mathrm{Rec}} = \pi D_{\mathrm{Rec,Ext}} L_{\mathrm{Aper}}, \tag{5.14}$$

with each receiver length as $L_{\mathrm{Aper}} = A_{\mathrm{Aper}}/5.45$ from the area-to-length relation for the chosen collector geometry (i.e., 545 $\mathrm{m}^2$ of collector area to each 100 m of collector length).

On the other hand, for the packed-bed TES device, the cost estimate relies on a different approach since parameters for scaling this component are still somewhat unknown. Such an approach relies on assuming the major costs of the packed-be TES device to be related to the pressure vessel [34] and to the alumina particles. In this sense, the steel cost may be estimated as

$$C_{\mathrm{TES,st}} = b_{\mathrm{st}} \rho_{\mathrm{st}} \left( V_{\mathrm{TES,Wall,st}} + 2V_{\mathrm{TES,Lid,st}} \right), \tag{5.15}$$

for which the TES steel wall and lid volumes are defined as

$$\begin{gathered} V_{\mathrm{TES,Wall,st}} = \tfrac{\pi}{4} \left[ \left( D_{\mathrm{TES}} + 2t_{\mathrm{i}} + 2t_{\mathrm{st}} \right)^2 - \left( D_{\mathrm{TES}} + 2t_{\mathrm{i}} \right)^2 \right] L_{\mathrm{TES}} \\ V_{\mathrm{TES,Lid,st}} = \tfrac{\pi}{4} D_{\mathrm{TES}}^2 t_{\mathrm{st}} \end{gathered}, \tag{5.16}$$

and $b_{\mathrm{st}} = 1.553$ US$/kg is the steel specific cost, which was obtained as the average of the global composite prices for carbon steel and stainless steel 304 from Ref. [161], from January to August of 2019. For the alumina, similar to for the steel, the cost is estimated as

$$C_{\mathrm{TES,S}} = b_{\mathrm{S}} \rho_{\mathrm{S}} \left(1 - \varepsilon\right) V_{\mathrm{TES}}, \tag{5.17}$$

where $V_{\mathrm{TES}}$ is the TES total internal volume and $b_{\mathrm{S}} = 1.15$ US$/kg is the alumina specific cost, which was obtained based on the range of 1.0 US$/kg and 1.3 US$/kg for ceramic

particles indicated by Ref. [95]. Therefore, the total cost for the TES system is obtained as

$$C_{\mathrm{TES}} = N_{\mathrm{TES}} \left( C_{\mathrm{TES,st}} + C_{\mathrm{TES,S}} \right), \tag{5.18}$$

where $N_{\mathrm{TES}}$ accounts for the number of TES devices employed.

Thus, from Eqs. 5.11, 5.13, and 5.18, the overall equipment investment cost is estimated as

$$C_{\mathrm{Equip}} = C_{\mathrm{PB}} + C_{\mathrm{SF}} + C_{\mathrm{TES}}, \tag{5.19}$$

which disregards any equipment cost related to the auxiliary heat exchanger discussed in Sub. 5.1.1.

For the auxiliary conventional heating, which was adopted as using natural gas as fuel, the cost is estimated based on the specific fuel cost as

$$C_{\mathrm{Aux}} = b_{\mathrm{Aux}} E_{\mathrm{Aux}}, \tag{5.20}$$

where $b_{\mathrm{Aux}} = b_{\mathrm{NG}} = 3.5 \cdot 10^{-9}$ US\$/J is the auxiliary heating fuel specific cost, which was obtained as the average value for California/USA considering the available data for the last 10 years from Ref. [162] – it was considered that the energy of $1\mathrm{ft}^3_{\mathrm{NG}} \approx 1030$ Btu = 1.0867 MJ [163]. Also, $E_{\mathrm{Aux}}$ accounts for the annual overall summation of energy obtained from the auxiliary heating, which is determined as

$$E_{\mathrm{Aux}} = E^{\mathrm{PB}}_{\mathrm{Aux}} + E^{\mathrm{TES}}_{\mathrm{Aux}}, \tag{5.21}$$

where $E^{\mathrm{PB}}_{\mathrm{Aux}}$ is the auxiliary heating energy spent for the power block inlet and $E^{\mathrm{TES}}_{\mathrm{Aux}}$ for the TES outlet, which are obtained, respectively, from summations throughout the 8760 h of the year as

$$E^{\mathrm{PB}}_{\mathrm{Aux}} = \sum_{j=1}^{8760} \dot{m}_{\mathrm{PB}} \left( i^{\mathrm{In}}_{\mathrm{F,PB}} - i^{\mathrm{In}}_{\mathrm{F,Aux,j}} \right) \Delta t_{\mathrm{Sys}} \tag{5.22}$$

and

$$E_{\text{Aux}}^{\text{TES}} = N_{\text{TES}} \sum_{j=1}^{8760} \begin{cases} \left\langle \dot{m}_{\text{TES,C}} \right\rangle_{\text{j}} \left( i_{\text{F,PB}}^{\text{Out}} - \left\langle i_{\text{F,TES,C}}^{\text{Out}} \right\rangle_{\text{j}} \right) \Delta t_{\text{Sys}}, \; T_{\text{TES,C}}^{\text{Out}} < T_{\text{PB}}^{\text{Out}} \\ 0, \; T_{\text{TES,C}}^{\text{Out}} \geq T_{\text{PB}}^{Out} \end{cases} . \quad (5.23)$$

Also, the auxiliary heater inlet mass-specific enthalpy $i_{\text{F,Aux}}^{\text{In}}$ is obtained, for each system time step $j$, from the thermal balance from the solar field and TES outlets and the bypass as

$$\dot{m}_{\text{SF}} i_{\text{F,SF}}^{\text{Out}} + N_{\text{TES}} \left\langle \dot{m}_{\text{TES}} \right\rangle \left\langle i_{\text{F,TES}}^{\text{Out}} \right\rangle + \dot{m}_{\text{Bypass}} i_{\text{F,PB}}^{\text{Out}} = \dot{m}_{\text{PB}} i_{\text{F,Aux}}^{\text{In}}. \quad (5.24)$$

The environmental cost associated with the emission of $CO_2$ due to the use of auxiliary heating is also accounted for. Considering a lower heating value (LHV) of $LHV_{\text{NG}} = 45.5895$ MJ/kg [164] for the natural gas and that, from stoichiometry, the complete combustion of 1 kg of natural gas produces 2.75 kg of $CO_2$, the environmental cost is estimated as

$$C_{\text{Env}} = b_{\text{Env}} \frac{2.75 E_{\text{Aux}}}{LHV}, \quad (5.25)$$

where $b_{\text{Env}} = 90 \cdot 10^{-3}$ US$/kg [165] is the environmental specific cost for the $CO_2$ emitted, i.e., a taxation regarding the reduction of greenhouse emissions. It is worth mentioning that a future sensibility analysis regarding such a value is recommended.

Furthermore, considering the difficulty of estimating the maintenance and operation costs, following Ref. [98], these were estimated as

$$C_{\text{MO}} = b_{\text{MO}} W_{\text{PB,Net}}, \quad (5.26)$$

where $W_{\text{PB,Net}}$, the net energy produced by the power block, is obtained from

$$W_{\text{PB,Net}} = \sum_{j=1}^{8760} \dot{W}_{\text{PB,j}}^{\text{Net}} \Delta t_{\text{Sys}}, \quad (5.27)$$

and $b_{\mathrm{MO}} = 0.9722$ US\$/J $= 3.5$ US\$/MWh [98].

Therefore, as figure of merit to evaluate the costs of energy production over the system lifetime, the analysis uses the levelized cost of energy (LCOE) approach [166], for which the $LCOE$, in US\$/MWh, is given by

$$LCOE = 3.6 \cdot 10^9 \left[ C_{\mathrm{Equip}} + \sum_{j=1}^{LT} \frac{\left( C_{\mathrm{Aux,j}} + C_{\mathrm{Env,j}} + C_{\mathrm{MO,j}} \right)}{(1+dr)^j} \right] / \left[ \sum_{j=1}^{LT} \frac{W_{\mathrm{Sys,Net,j}}}{(1+dr)^j} \right], \quad (5.28)$$

considering, for a given year $j$ within the system $LT$ years lifetime, all costs described above to produce the annual system net energy $W_{\mathrm{Sys,Net}}$, which is obtained as

$$W_{\mathrm{Sys,Net}} = W_{\mathrm{PB,Net}} - \sum_{j=1}^{8760} \dot{W}_{\mathrm{TES,j}}^{\mathrm{Pump}} \Delta t_{\mathrm{Sys}}, \quad (5.29)$$

i.e., by subtracting from the annual net energy produced by the power block – considering that $\dot{W}_{\mathrm{PB}}^{\mathrm{Net}} = 9.93$ MW $\approx 10$ MW is constant throughout the year – the annual energy expenditure with the TES auxiliary compressors – which are described in Sec. 5.1 and whose power consumption is expressed in and Sub. 4.1.15. Also, for all analyses, following Ref. [167], a lifetime of $LT = 20$ years and an annual discount rate of $dr = 5\%$ were considered.

Finally, it is important to mention that the adopted cost estimation methodology and reference values are not specific for the HTF considered. Therefore, it is expected, based on the available literature, results accuracy to be roughly limited to a $\pm 30\%$ range [98,167].

## 5.2 RESULTS

For the economic assessment, first, the influence of the size of the TES system is examined in Fig. 47. Such a figure shows the integrated system $LCOE$ variation with the design discharging time $t_{\mathrm{TES}}$ while considering three TES diameters, a solar multiple of $SM = 2$ and $N_{\mathrm{TES}} = 5$ TES packed-bed devices. Additionally, the dash-dotted line indicates the $LCOE$ value if no TES system is considered, which is referred to as reference $LCOE$ value. Regarding the configurations with an embedded TES system (solid lines), one may notice that none achieved a lower $LCOE$ than the reference. Furthermore, the

rightmost portion of Fig. 47 reveals that smaller $D_{\mathrm{TES}}$ are preferable for larger $t_{\mathrm{TES}}$ values, whereas the leftmost portion, which is zoomed in the detail plot, shows that there is a swap between the preferable $D_{\mathrm{TES}}$ as $t_{\mathrm{TES}}$ decreases.

Figure 47 – $LCOE$ variation with $t_{\mathrm{TES}}$ for three TES diameters considering $SM = 2$ and $N_{\mathrm{TES}} = 5$.

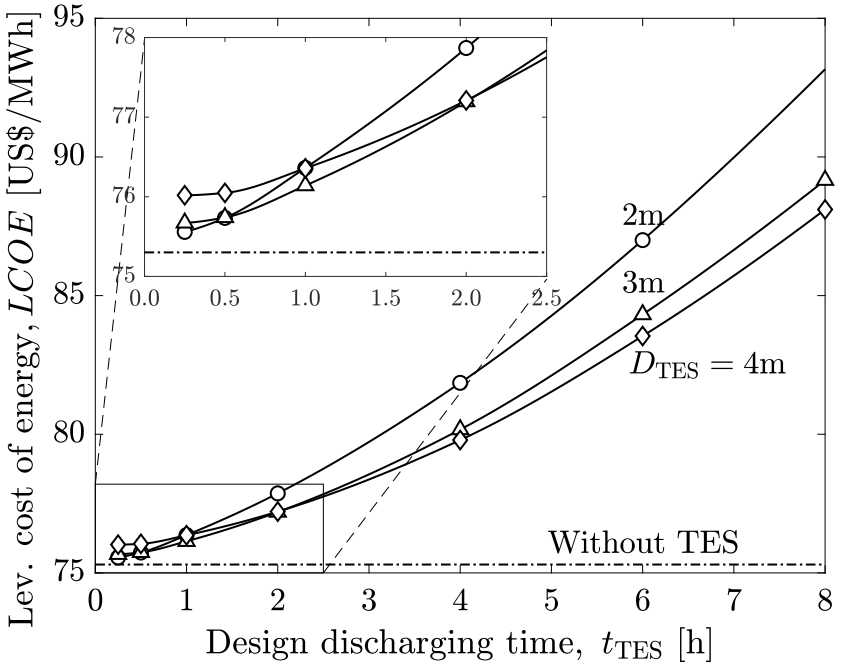


It should be mentioned that the convergence for the reference $LCOE$ value as $t_{\mathrm{TES}} \to 0$ is not observed. This convergence may be expected because the system response for ever-decreasing TES sizes increasingly approaches that of the system without any TES device and also because the associated TES cost should approach zero. Nevertheless, although for a given $D_{\mathrm{TES}}$, $L_{\mathrm{TES}} \to 0$ as $t_{\mathrm{TES}} \to 0$ (see Eqs. 5.6 and 5.7), the associated steel cost for the TES lids does not depend on $L_{\mathrm{TES}}$ (as is the case for the associated steel cost for the TES wall), but only on $D_{\mathrm{TES}}$. Thus, this discussion clarifies the non-convergence of the $LCOE$ curves for different $D_{\mathrm{TES}}$ as $t_{\mathrm{TES}} \to 0$.

In order to account for the effects of the solar field size, which is expressed in terms of the solar multiple $SM$, on the levelized cost of energy, Fig. 48 shows the $LCOE$ variation for five design discharging times $t_{\mathrm{TES}}$ considering a TES diameter of $D_{\mathrm{TES}} = 2$ m and $N_{\mathrm{TES}} = 5$ TES packed-bed devices. Once again the dash-dotted line indicates the reference $LCOE$ values for each $SM$ if no TES system is considered. The main point to be observed is the existence of local minima, i.e., for each $t_{\mathrm{TES}}$, there is a $SM$ minimizing the $LCOE$. Moreover, the optimal $SM$ values decrease from roughly 3.5 to 2.0 as $t_{\mathrm{TES}}$

decreases from 8 h to the reference line (i.e., 0 h). This optimal trend is arguably related to matching the solar field and TES systems sizes. Furthermore, as shown in Fig. 47, the greater the TES size (i.e., its storage capacity), the greater the $LCOE$.

Figure 48 – $LCOE$ variation with $SM$ for five $t_{\mathrm{TES}}$ considering $N_{\mathrm{TES}} = 5$ and $D_{\mathrm{TES}} = 2$ m.

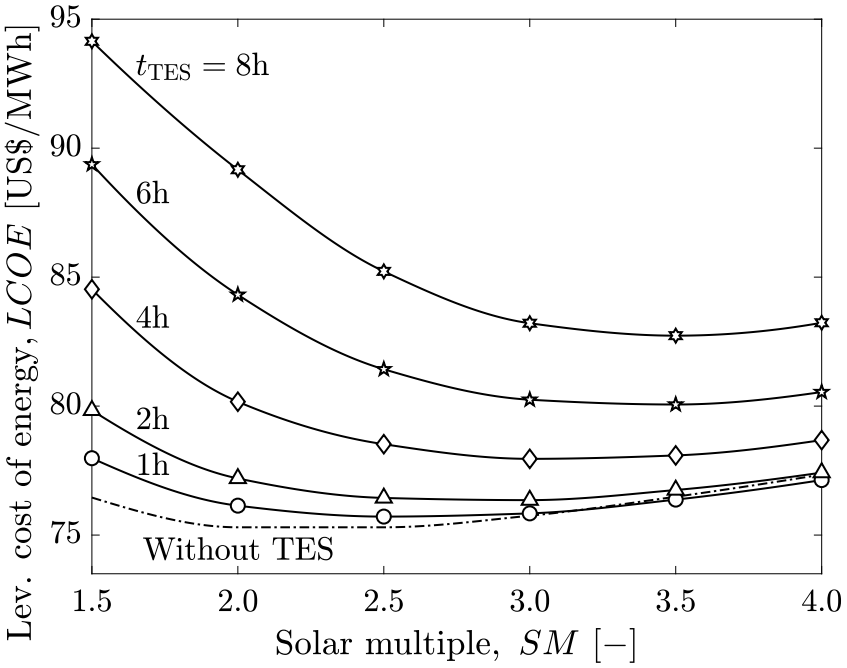


The influence of the number of TES devices on the $LCOE$ may be observed Fig. 49, which was obtained considering $SM = 2$ and a TES diameter of $D_{\mathrm{TES}} = 3$ m. Although a discreet variation may be observed at $N_{\mathrm{TES}} = 10$, the $LCOE$ variation within the range of $N_{\mathrm{TES}} = 5$ and $N_{\mathrm{TES}} = 15$ may be considered as actually insignificant.

Even though the environmental-related economic cost of the $CO_2$ emissions is already accounted for in the $LCOE$ itself, it is arguably reasonable to search for a compromise solution that not only minimizes the $LCOE$ but also that regards the environmental sustainability. Hence, considering the annual $CO_2$ mass emitted by the auxiliary heating ($m_{\mathrm{CO2}}$) as a second independent figure of merit, Fig. 50 shows with black markers the values of $LCOE$ (y-axis) and $m_{\mathrm{CO2}}$ (x-axis) for 137 combinations of $SM$, $N_{\mathrm{TES}}$, $t_{\mathrm{TES}}$, and $D_{\mathrm{TES}}$ – whose ranges are, respectively, 1.5 and 4.0, 0 and 15, 0 h and 8 h, and 1.5 m and 5 m. Both figures of merit, i.e., $LCOE$ and $m_{\mathrm{CO2}}$, were normalized by the maximal and minimal values of each (see Eq. 2.3) for the set of combinations considered – for the $LCOE$, the limit values are 75.30 US$/MWh and 94.64 US$/MWh; whereas, for the $m_{\mathrm{CO2}}$, the limit values are $19.36 \cdot 10^6$ kg and $32.15 \cdot 10^6$ kg.

Figure 49 – $LCOE$ variation with $N_{\text{TES}} = 5$ for five $t_{\text{TES}}$ considering $SM = 2$ and $D_{\text{TES}} = 3$ m.

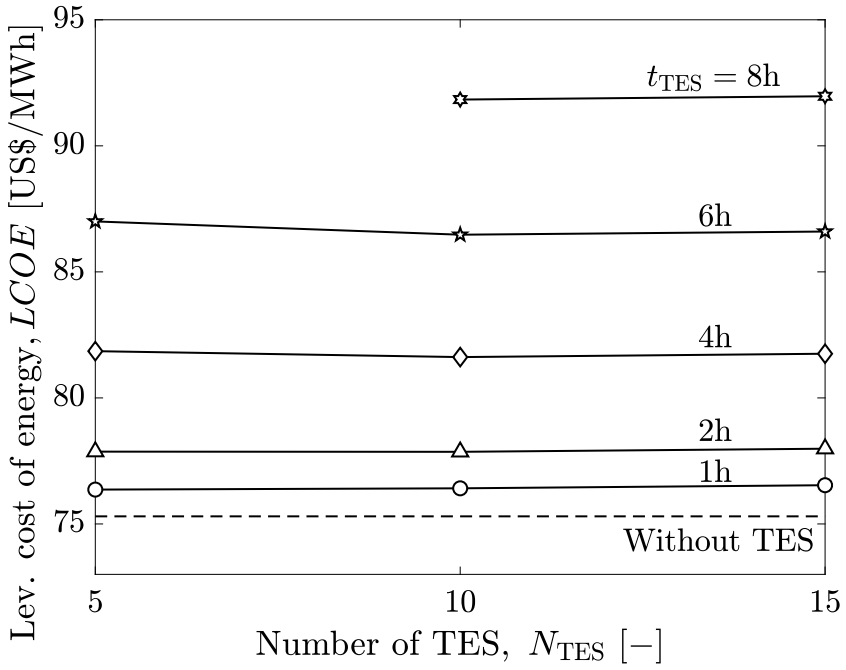


It is somewhat expected a competing effect between $LCOE$ and $m_{\text{CO2}}$, i.e., the cleaner the solution, the greater the associated cost. Such a trend is visible in Fig. 50, especially in its left lower quadrant, which may suggest the possibility of using an optimization-based approach for finding the Pareto front. Then, considering even weights to both figures of merit, the distance $\Lambda$ of each point to the origin was simply evaluated as

$$\Lambda = \sqrt{(LCOE^*)^2 + \left(m^*_{\text{CO2}}\right)^2}. \tag{5.30}$$

Thus, the 20 best out of the 137 evaluated combinations (i.e., those with smaller $\Lambda$) are indicated in Fig. 50 by the x markers and named alphabetically according to the increasing distance to the origin while the remaining combinations are indicated by the dot markers. The best compromise solution found, which is indicated by point A, was obtained with the combination $SM = 4$, $N_{\text{TES}} = 10$, $t_{\text{TES}} = 6$ h, and $D_{\text{TES}} = 3$ m and achieved $LCOE = 79.59$ US$/MWh and $m_{\text{CO2}} = 21.02 \cdot 10^6$ kg.

Focusing on the aforementioned 20 best combinations and aiming to clarify the components of each one, Fig. 51 shows the values of $SM$, $N_{\text{TES}}$, $t_{\text{TES}}$, and $D_{\text{TES}}$ for each of those cases. It is possible to verify that, for these combinations, none was obtained with a $SM$ value smaller than 3.0, which indicates that an arguably larger solar field is

Figure 50 – Normalized $LCOE$ versus normalized annual $m_{\mathrm{CO2}}$ considering 137 combinations of $SM$, $N_{\mathrm{TES}}$, $t_{\mathrm{TES}}$, and $D_{\mathrm{TES}}$.

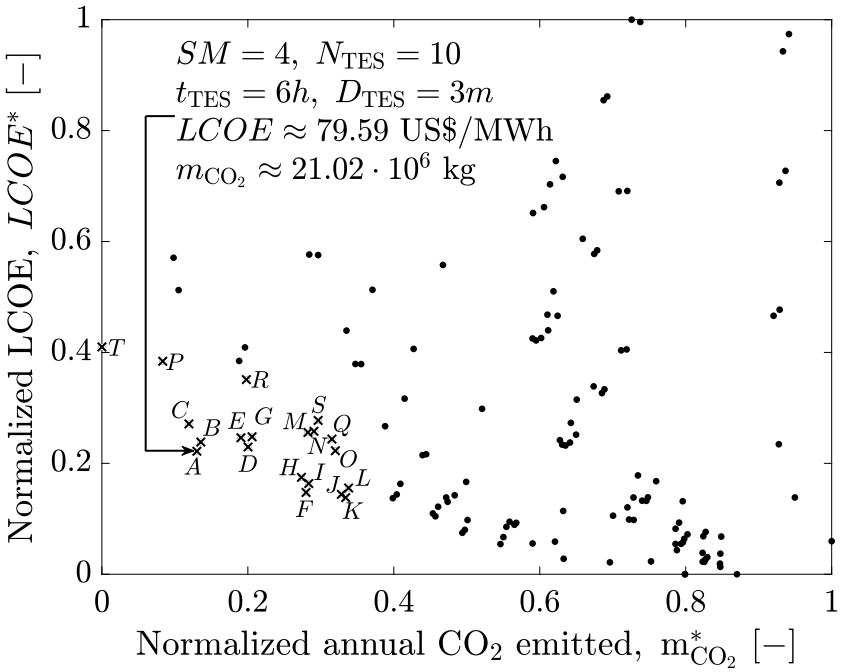


preferred. Also, regarding the TES system, it is not possibly to infer any clear tendency regarding the number of devices, which agrees with the analysis presented in Fig. 49. Moreover, on the design discharging time (which is directly related to the TES volume), the best combinations were obtained with at least 4 h, which is roughly half of the range considered; then, it is conceivable that small TES systems do not play a significant role. And, finally, except for three, all the best combinations considered $D_{\mathrm{TES}} = 3$ m, which may indicate an optimal value for the diameter of the TES device.

Now, Fig. 52 brings the breakdown into percentage component of the $LCOE$ of the aforementioned 20 best combinations, while also using the $LCOE$ to sort them. First, with regard of the percentage costs, one may check that there is a somewhat direct correlation between $LCOE$ and the percentage $C_{\mathrm{Equip}}$ – a specific discussion on the equipment cost will be presented next. Then, it is also possible to verify a fairly inverse correlation between $LCOE$ and the combined percentage $C_{\mathrm{Aux}} + C_{\mathrm{Env}}$. Following, the percentage $C_{\mathrm{MO}}$ remained nearly constant for all the 20 best combinations. Moreover, the last column on the RHS of Fig. 52 brings the total emitted $CO_2$, whose tendency follows that of the combined $C_{\mathrm{Aux}} + C_{\mathrm{Env}}$, which is something expected because $m_{\mathrm{CO2}}$, $C_{\mathrm{Aux}}$, and $C_{\mathrm{Env}}$ are all directly dependent on $E_{\mathrm{Aux}}$ (one may see that from Eqs. 5.20 and 5.25). Also, yet on the combined

Figure 51 – Values of $SM$, $N_{TES}$, $t_{TES}$, and $D_{TES}$ for the 20 best combinations of Fig. 50.

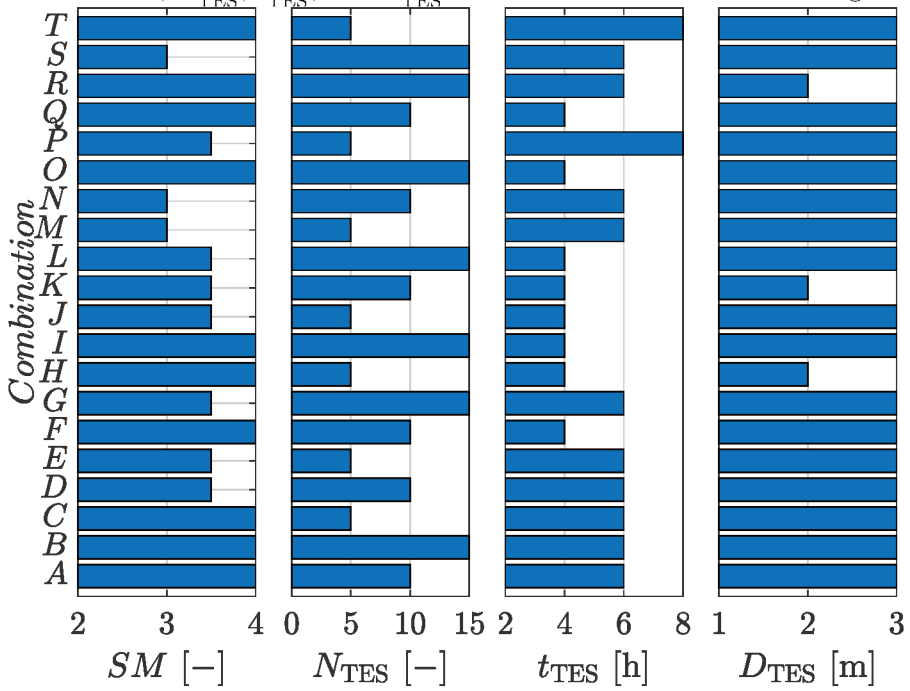


$C_{Aux} + C_{Env}$, given the values adopted for $b_{Aux}$, $b_{Env}$, and $LHV$, it is possible to infer that this summation is dominated by the environmental taxation, which represents roughly 60% of the total amount, against the remaining roughly 40% due to the fuel cost. Furthermore, the competing effect between $LCOE$ and $m_{CO2}$ discussed in Fig. 50 becomes even clearer when comparing the first and last columns of Fig. 52.

Figure 52 – $LCOE$, its percentage breakdown into components, and $m_{CO2}$ for the 20 best combinations of Fig. 50 (combinations are sorted according to their $LCOE$ values).

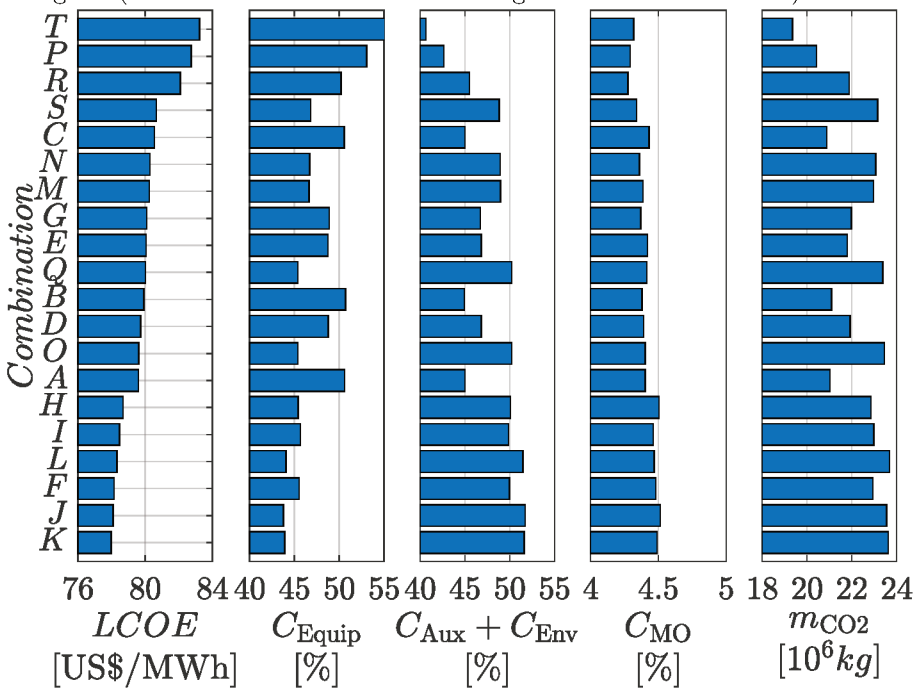

Considering the equipment cost, Fig. 53 shows, once again, the 20 best combinations sorted according to their $LCOE$, but now it brings the total equipment cost and its percentage breakdown into solar field ($C_{SF}$), TES system ($C_{TES}$), and power block ($C_{PB}$). It is possible to observe that the increase of the total equipment cost for the 20 best combinations is mostly driven by the TES cost, given that both the percentage $C_{SF}$ and $C_{PB}$ decrease as the $LCOE$ increases. This analysis indicates the importance of investigating better and cost-effective materials for the TES construction.

Figure 53 – $LCOE$, total equipment cost and its breakdown into components for the 20 best combinations of Fig. 50 (combinations are sorted according to their $LCOE$ values).

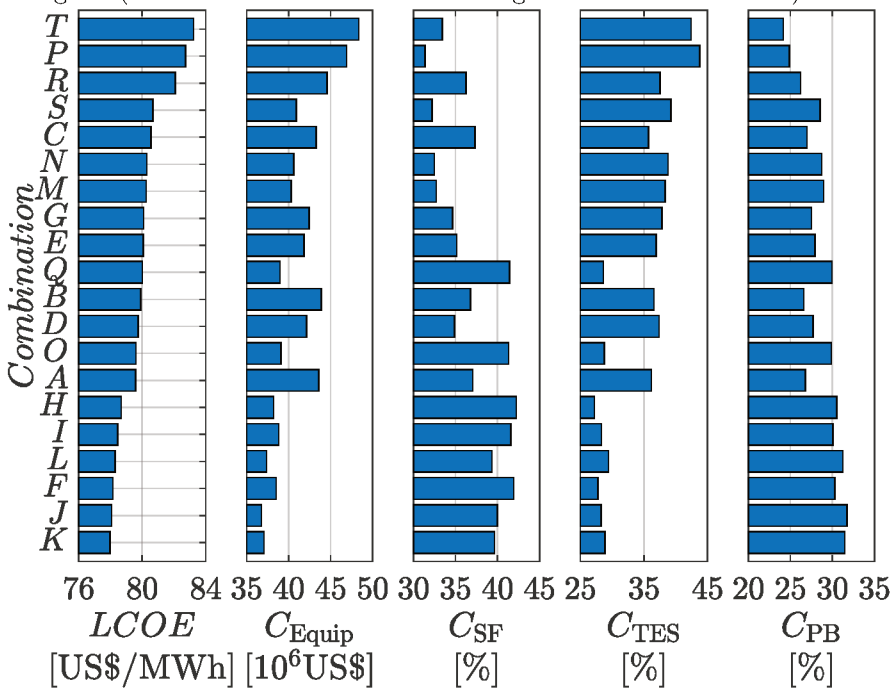


Finally, it is worth mentioning that, because this economic and environmental assessment is substantially influenced by several parameters, follow-up sensibility analyses are highly-recommended for analyzing the influence of, for instance, thermodynamic efficiencies and specific costs, such as the environmental taxation on the figures of merit considered. Therefore, this set of analyses and discussions should be regarded as a preliminary assessment for facilitating and encouraging further related developments.

# 6 CONCLUSIONS

Aiming at the development of thermodynamic and numerical approaches regarding the use of s-$CO_2$ as working fluid/HTF for CSP-powered plants, transient models for Brayton cycles with TES systems were presented and simulations results thoroughly discussed.

The first part of this dissertation deals with the homemade finite-volume-based routine developed to simulate and analyze the transient behavior of a hybrid recuperative s-$CO_2$ Brayton cycle with solid TES and mass storage systems. The study focused on exploring the effects of a concrete TES system on the cycle power delivery output. Also, to deal with the s-$CO_2$ mass flow rate fluctuations caused by thermal transfer processes within the cycle and, consequently, pressure variations, a mass storage system with a variable volume was included. The figure of merit used to evaluate the performance of the thermal system, i.e., the improvement index ($\delta$), represents, for the tenth day of operation, the percentage difference between the net work delivered by the cycle with and without a TES device, which is normalized by the net work delivered by the cycle without the TES device.

As expected, the results showed that the use of a TES system enables improvement index values much higher than zero. For instance, for some of the cases simulated, $\delta \rightarrow 36\%$, which is close to the highest improvement possible given the operational constraints imposed. Also, as expected, it was possible to notice the strong dependence of $\delta$ on the construction parameters and thermophysical properties of the TES system. As a general trend, it was observed that there is a combination of ideal dimensions for a given set of thermophysical properties. More specifically, it was shown that the ability of the TES device to store/deliver power, which is related to its thermal conductivity, limits the amount of storage medium that should thermally interact with the working fluid – other studies have specifically dealt with this issue, e.g., Refs. [79, 168]. Furthermore, the analysis indicated that the commonly adopted hypotheses of steady-state and quasi-steady-state processes must be used with care when a power plant is assisted by a TES system. This is mainly because the thermal

inertia of the coupled system (i.e., cycle main components and TES devices) may require several days to reach a periodic representative operational pattern. Therefore, imposing an ill-conceived initial thermal condition to the assembled cycle may lead to unrealistic scenarios. This is especially critical for applications such as solar-powered plants because the radiation fluxes continuously vary within the day and from day to day, which suggests that, for certain cases, the aforementioned operational pattern may never be reached.

The second part of this dissertation relied on the modeling of a packed-bed TES system operating with s-$CO_2$ as HTF in order to map the influence of several design and operational parameters on its charging-discharging combined efficiency. The modeling was specifically implemented with the purpose of accounting for the unique behavior assigned to the HTF used, such as low viscosity, variations of thermophysical properties, and operation at elevated pressure. While initially proposed to operate with air, only few details have been reported in the literature about packed-bed TES devices operating with s-$CO_2$ and, more specifically, about the effects of crucial parameters on its performance, which reinforces the originality and relevance of the study presented.

Regarding the charging-discharging combined efficiency, the findings of this work stressed a broad range of trends that may assist the design of packed-bed TES systems for CSP applications with s-$CO_2$. Design parameters, such as the bed length and diameter, revealed the possibility for optimization, and the ideal particle diameter was shown to be much smaller than that for air-based applications. Moreover, the existence of optimal aspect ratios for fixed bed volumes indicated the most efficient setup for these systems. When dealing with operational parameters, the results indicated advantages in charging mass flow rates up to twice that of the design value for the power block, which may be translated to solar multiples up to 3, thus preventing the solar field oversize while reducing unnecessary investment costs. Still on operational parameters, controlling the temperature downstream of the TES system during both charging and discharging processes has also demonstrated to be relevant due to its influence over defining the time spans of the processes. Over the former, the optimal temperature limit decreases with increasing the discharging temperature limits; contrarily, on the latter, the lower the outlet temperature, the higher the combined efficiency. Additionally, choosing the proper insulation thickness

has proved to be highly recommended since a significant amount of thermal energy may be lost in case of mismatching. Discussions on the main inefficiency factors of the packed-bed TES device, i.e., thermal losses to the surroundings and thermal dispersion, were presented, which indicated that their relevance on the performance of the device depends on the design and operational parameters considered. Also, even though increasing the high-end temperature increases the power cycle efficiency, it compromises the TES efficiency, which may indicate a possible overall optimal efficiency for the coupled solar field, TES device, and power block system. Last of all, the charging-discharging cycling effect over the system thermal-hydraulic performance was discussed.

The third part of this dissertation assessed the economics of an integrated plant composed of solar field, packed-bed TES system, and power block, while operating with s-$CO_2$ as HTF. The preliminary study presented may be considered as an exploratory effort on assessing the economic feasibility of such an integrated solution. Although the solutions with the packed-bed TES systems investigated did not present substantial improvements in terms of $LCOE$ by itself when compared to the respective references, the results revealed not only the possible feasibility of the integrated system using such a TES technology for s-$CO_2$, but also evidenced several venues for further examination.

The studies discussed in this dissertation showed that while s-$CO_2$ is a suitable working fluid for CSP applications, additional work in several directions is still needed for the development of this rapidly expanding field of increasing interest, which may contribute to the further development of efficient power generation.

## 6.1 FUTURE WORKS

Following the line of research of this dissertation, efforts should be devoted to further developing models that are capable of representing transient conditions of power plants (solar-powered cycles, for instance) while considering realistic solar radiation and demand profiles as well as improved turbomachinery models. Also, the TES systems (i.e., technology, configuration), their coupling and control strategies as well as their transient thermal response/inertia should be further studied. These models should also include the transient behavior of solar receivers (e.g., solar trough collectors) since their efficiencies

vary largely with the ambient conditions (e.g., air temperature, wind speed). Ultimately, such transient models could replace steady-state formulations and be used to precisely determine the real behavior of solar-powered plants for a wide range of climates, while accounting for geographical and environmental conditions.

Also, future works, such as exploring economic aspects related to optimal parameters and exergetic augmentation, need attention. Based on this, a multi-objective optimization may be the natural continuation of this work, concerning the simultaneous integration of all the relevant parameters mentioned as well as the costs involved in system manufacturing, operation and maintenance, and its environmental impact. Such an analysis is indeed required for further assessing in detail the feasibility of s-$CO_2$ packed-bed TES systems for real scale power plants. Hence, further studies on the integration of solar field, TES device, and power block with the controlling system are required, while the annual assessments relying on the actual solar and power demand data still seems to be an interesting study venue.

Amongst several points still requiring a further examination for improving the results obtained, one may indicate: (i) the necessity of a proper and improved active and possibly predictive controlling system – e.g., including the stopping charging and/or discharging parameters following the $\Delta T_{\mathrm{F,Out,C}}$ and $\Delta T_{\mathrm{F,Out,D}}$ discussed in Chap. 4, (ii) investigation on better and cost-effective materials for the packed-bed TES construction – i.e., for the wall and lids, and for the spherical particles –, and (iii) sensibility analyses for assessing the influence of parameters such as thermodynamic efficiencies, design specifications (e.g., insulation, wall, and ground thicknesses), and specific costs (e.g., the environmental taxation) on the figures of merit considered.

# REFERENCES

1 NIU, X.-D.; YAMAGUCHI, H.; ZHANG, X.-R.; IWAMOTO, Y.; HASHITANI, N. Experimental study of heat transfer characteristics of supercritical $CO_2$ fluid in collectors of solar rankine cycle system. **Applied Thermal Engineering**, v. 31, n. 6–7, p. 1279 – 1285, 2011.

2 LIPA, J.; EDWARDS, C.; BUCKINGHAM, M. Specific heat of $CO_2$ near the critical point. **Physical Review A**, 1977.

3 BELL, I.; WRONSKI, J.; QUOILIN, S.; LEMORT, V. Pure and pseudo-pure fluid thermophysical property evaluation and the open-source thermophysical property library coolprop. **Industrial & Engineering Chemistry Research**, 2014.

4 BELL, I. **Coolprop website**. Available at: <<http://coolprop.org>>. Accessed in: March 25$^{th}$, 2019.

5 DOSTAL, V.; DRISCOLL, M.; HEJZLAR, P. A supercritical carbon dioxide cycle for next generation nuclear reactors. **MIT-ANP-TR-100**, 2004. Available at: <<http://hdl.handle.net/1721.1/17746>>.

6 YAMAGUCHI, H.; ZHANG, X.; FUJIMA, K.; ENOMOTO, M.; SAWADA, N. A solar energy powered rankine cycle using supercritical carbon dioxide. **Applied Thermal Engineering**, v. 26, n. 17–18, p. 2345 – 2354, 2006.

7 LUDINGTON, A. **Tools for supercritical carbon dioxide cycle analysis and the cycle's applicability to fast reactors**. Dissertação (Mestrado) — MIT, 2009.

8 CRESPI, F.; GAVAGNIN, G.; SÁNCHEZ, D.; MARTÍNEZ, G. S. Supercritical carbon dioxide cycles for power generation: A review. **Applied energy**, Elsevier, v. 195, p. 152–183, 2017.

9 STEIN, W.; BUCK, R. Advanced power cycles for concentrated solar power. **Solar energy**, Elsevier, v. 152, p. 91–105, 2017.

10 TURCHI, C. S.; MA, Z.; NEISES, T. W.; WAGNER, M. J. Thermodynamic study of advanced supercritical carbon dioxide power cycles for concentrating solar power systems. **Journal of Solar Energy Engineering**, American Society of Mechanical Engineers, v. 135, n. 4, p. 041007, 2013.

11 NEISES, T.; TURCHI, C. A comparison of supercritical carbon dioxide power cycle configurations with an emphasis on csp applications. **Energy Procedia**, Elsevier, v. 49, p. 1187–1196, 2014.

12 DUNHAM, M. T.; IVERSON, B. D. High-efficiency thermodynamic power cycles for concentrated solar power systems. **Renewable and Sustainable Energy Reviews**, Elsevier, v. 30, p. 758–770, 2014.

13 SARMIENTO, C.; CARDEMIL, J. M.; DÍAZ, A. J.; BARRAZA, R. Parametrized analysis of a carbon dioxide transcritical rankine cycle driven by solar energy. **Applied Thermal Engineering**, Elsevier, v. 140, p. 580–592, 2018.

14 WANG, J.; SUN, Z.; DAI, Y.; MA, S. Parametric optimization design for supercritical $CO_2$ power cycle using genetic algorithm and artificial neural network. **Applied Energy**, v. 87, n. 4, p. 1317 – 1324, 2010.

15 KIM, M.-H.; PETTERSEN, J.; BULLARD, C. W. Fundamental process and system design issues in $CO_2$ vapor compression systems. **Progress in Energy and Combustion Science**, v. 30, n. 2, p. 119 – 174, 2004.

16 CAYER, E.; GALANIS, N.; DESILETS, M.; NESREDDINE, H.; ROY, P. Analysis of a carbon dioxide transcritical power cycle using a low temperature source. **Applied Energy**, v. 86, n. 7–8, p. 1055 – 1063, 2009.

17 CHEN, Y.; LUNDQVIST, P. Analysis of supercritical carbon dioxide heat exchangers in cooling process. **International Refrigeration and Air Conditioning Conference at Purdue**, 2006.

18 MUÑOZ-ANTÓN, J.; RUBBIA, C.; ROVIRA, A.; MARTÍNEZ-VAL, J. M. Performance study of solar power plants with $CO_2$ as working fluid. a promising design window. **Energy conversion and management**, Elsevier, v. 92, p. 36–46, 2015.

19 MUÑOZ-ANTON, J.; BIENCINTO, M.; ZARZA, E.; DÍEZ, L. E. Theoretical basis and experimental facility for parabolic trough collectors at high temperature using gas as heat transfer fluid. **Applied energy**, Elsevier, v. 135, p. 373–381, 2014.

20 CHENNOUF, N.; NEGROU, B.; DOKKAR, B.; SETTOU, N. Valuation and estimation of geothermal electricity production using carbon dioxide as working fluid in the south of algeria. **Energy Procedia**, v. 36, n. 0, p. 967 – 976, 2013.

21 CHEN, H.; GOSWAMI, D. Y.; STEFANAKOS, E. K. A review of thermodynamic cycles and working fluids for the conversion of low-grade heat. **Renewable and Sustainable Energy Reviews**, v. 14, n. 9, p. 3059 – 3067, 2010.

22 BAIK, Y.-J.; KIM, M.; CHANG, K. C.; KIM, S. J. Power-based performance comparison between carbon dioxide and R125 transcritical cycles for a low-grade heat source. **Applied Energy**, v. 88, n. 3, p. 892 – 898, 2011.

23 CHEN, Y.; LUNDQVIST, P.; JOHANSSON, A.; PLATELL, P. A comparative study of the carbon dioxide transcritical power cycle compared with an organic rankine cycle with R123 as working fluid in waste heat recovery. **Applied Thermal Engineering**, v. 26, n. 17–18, p. 2142 – 2147, 2006.

24 TUO, H. Analysis of a reheat carbon dioxide transcritical power cycle using a low temperature heat source. ASME, p. 219–225, 2011.

25 YANG, J. L.; MA, Y. T.; LIU, S. C. Performance investigation of transcritical carbon dioxide two-stage compression cycle with expander. **Energy**, v. 32, n. 3, p. 237 – 245, 2007.

26 SARKAR, J. Second law analysis of supercritical $CO_2$ recompression brayton cycle. **Energy**, v. 34, n. 9, p. 1172 – 1178, 2009.

27 SARKAR, J.; BHATTACHARYYA, S. Optimization of recompression S-$CO_2$ power cycle with reheating. **Energy Conversion and Management**, v. 50, n. 8, p. 1939 – 1945, 2009.

28 AKBARI, A. D.; MAHMOUDI, S. M. Thermoeconomic analysis & optimization of the combined supercritical $CO_2$ (carbon dioxide) recompression brayton/organic rankine cycle. **Energy**, v. 78, n. 0, p. 501 – 512, 2014.

29 BATTISTI, F. G.; CARDEMIL, J. M.; da SILVA, A. K. A multivariable optimization of a brayton power cycle operating with $CO_2$ as working fluid. **Energy**, Elsevier, v. 112, p. 908–916, 2016.

30 ZANGANEH, G.; PEDRETTI, A.; ZAVATTONI, S.; BARBATO, M.; STEINFELD, A. Packed-bed thermal storage for concentrated solar power–pilot-scale demonstration and industrial-scale design. **Solar Energy**, Elsevier, v. 86, n. 10, p. 3084–3098, 2012.

31 ZANGANEH, G.; PEDRETTI, A.; ZAVATTONI, S.; BARBATO, M.; HASELBACHER, A.; STEINFELD, A. Design of a 100 MWhth packed-bed thermal energy storage. **Energy Procedia**, Elsevier, v. 49, p. 1071–1077, 2014.

32 CÁRDENAS, B.; DAVENNE, T.; WANG, J.; DING, Y.; JIN, Y.; CHEN, H.; WU, Y.; GARVEY, S. Techno-economic optimization of a packed-bed for utility-scale energy storage. **Applied Thermal Engineering**, Elsevier, 2019.

33 SINGH, S.; SØRENSEN, K.; CONDRA, T.; BATZ, S. S.; KRISTENSEN, K. Investigation on transient performance of a large-scale packed-bed thermal energy storage. **Applied Energy**, Elsevier, v. 239, p. 1114–1129, 2019.

34 KELLY, B. D. **Advanced thermal storage for central receivers with supercritical coolants**. [S.l.], 2010.

35 ENERGYPLUS website. Available at: <<https://energyplus.net/weather>>. Accessed in: Aug 20$^{th}$, 2019.

36 HO, C. K.; IVERSON, B. D. Review of high-temperature central receiver designs for concentrating solar power. **Renewable and Sustainable Energy Reviews**, Elsevier, v. 29, p. 835–846, 2014.

37 BESARATI, S. M.; GOSWAMI, D. Y.; STEFANAKOS, E. K. Development of a solar receiver based on compact heat exchanger technology for supercritical carbon dioxide power cycles. **Journal of Solar Energy Engineering**, American Society of Mechanical Engineers, v. 137, n. 3, p. 031018, 2015.

38 IVERSON, B. D.; CONBOY, T. M.; PASCH, J. J.; KRUIZENGA, A. M. Supercritical $CO_2$ brayton cycles for solar-thermal energy. **Applied Energy**, Elsevier, v. 111, p. 957–970, 2013.

39 WINKLER, J. M. **Development of a component based simulation tool for the steady state and transient analysis of vapor compression systems**. Dissertation (Ph.D.), 2009.

40 PEARSON, A. Carbon dioxide – new uses for an old refrigerant. **International Journal of Refrigeration**, v. 28, n. 8, p. 1140 – 1148, 2005.

41 MONTAGNER, G. **Um estudo da aplicação de ciclos transcríticos de $CO_2$ em sistemas comerciais de refrigeração**. Dissertation (Ph.D.) — Federal University of Santa Catarina, 2013.

42 LORENTZEN, G. Revival of carbon dioxide as a refrigerant. **International Journal of Refrigeration**, v. 17, n. 5, p. 292 – 301, 1994.

43 HEJZLAR, P.; DOSTAL, V.; DRISCOLL, M. J.; DUMAZ, P.; POULLENNEC, G.; ALPY, N. Assessment of gas cooled fast reactor with indirect supercritical $CO_2$ cycle. **Nuclear Engineering and and Technology**, v. 38, n. 2, p. 109–118, 2006.

44 ANGELINO, G. Carbon dioxide condensation cycles for power production. **Journal of Engineering for Gas Turbines and Power**, American Society of Mechanical Engineers, v. 90, n. 3, p. 287–295, 1968.

45 ANGELINO, G. Real gas effects in carbon dioxide cycles. ASME Paper No. 69-GT-103, v. 91, n. 7, p. 68, 1969.

46 FEHER, E. G. The supercritical thermodynamic power cycle. **Energy conversion**, Pergamon, v. 8, n. 2, p. 85–90, 1968.

47 CHEN, Y. **Thermodynamic Cycles using Carbon Dioxide as Working Fluid: $CO_2$ transcritical power cycle study**. Dissertation (Ph.D.) — KTH Royal Institute of Technology, 2011.

48 DE LA TOUR, C. C. Exposée de quelques résultats obtenu par l'action combinée de la chaleur et de la compression sur certains liquides, tels que l'eau, l'alcool, l'éther sulfurique et l′essence de pétrole rectifiée. **Annales de Chimie et de Physique**, v. 21, n. 178-182, p. 127–132, 1822.

49 DE LA TOUR, C. C. Nouvelle note sur les effets qu'on obtient par l'application simultané de la chaleur et de la compression a certains liquides. **Annales de Chimie et de Physique**, v. 22, p. 410–415, 1823.

50 BERCHE, B.; HENKEL, M.; KENNA, R. Fenômenos críticos: 150 anos desde Cagniard de la Tour. **Revista Brasileira de Ensino de Física**, v. 31, n. 2, p. 2602.1–2602.4, 2009.

51 ANDREWS, T. Bakerian lecture: On the continuity of the gaseous and liquid states of matter. **Proceedings of the Royal Society of London**, The Royal Society, v. 18, n. 114-122, p. 42–45, 1869.

52 STANLEY, H. E. **Introduction to phase transitions and critical phenomena**. Oxford: Oxford University Press, 1971.

53 HALL, W.; JACKSON, J. Heat transfer near the critical point. **Advances in Heat Transfer**, Academia Press, v. 7, n. 1, p. 86, 1971.

54 BOLMATOV, D.; BRAZHKIN, V.; TRACHENKO, K. Thermodynamic behaviour of supercritical matter. **Nature communications**, Nature Publishing Group, v. 4, 2013.

55 PETUKHOV, B. S. Heat transfer and friction in turbulent pipe flow with variable physical properties. **Advances in heat transfer**, Academic Press, New York, v. 6, n. 503, p. i565, 1970.

56 KURGANOV, V. A.; KAPTILNYI, A. G. Flow structure and turbulent transport of a supercritical pressure fluid in a vertical heated tube under the conditions of mixed convection. experimental data. **International journal of heat and mass transfer**, v. 36, n. 13, p. 3383–3392, 1993.

57 KRASNOSHCHEKOV, E.; KURAEVA, I.; PROTOPOPOV, V. Local heat transfer of carbon dioxide at supercritical pressure under cooling conditions. **High Temperature (translated from Teplofizika Vysokikh Temperatur)**, v. 7, n. 5, p. 856–862, 1970.

58 PITLA, S. S.; GROLL, E. A.; RAMADHYANI, S. New correlation to predict the heat transfer coefficient during in-tube cooling of turbulent supercritical $CO_2$. **International Journal of Refrigeration**, v. 25, n. 7, p. 887 – 895, 2002.

59 YOON, S. H.; KIM, J. H.; HWANG, Y. W.; KIM, M. S.; MIN, K.; KIM, Y. Heat transfer and pressure drop characteristics during the in-tube cooling process of carbon dioxide in the supercritical region. **International Journal of Refrigeration**, v. 26, n. 8, p. 857 – 864, 2003.

60 CHENG, L.; RIBATSKI, G.; THOME, J. R. Analysis of supercritical $CO_2$ cooling in macro- and micro-channels. **International Journal of Refrigeration**, v. 31, n. 8, p. 1301 – 1316, 2008.

61 SPAN, R.; WAGNER, W. A new equation of state for carbon dioxide covering the fluid region from the triple-point temperature to 1100 K at pressures up to 800 MPa. **Journal of Physical and Chemical Reference Data**, NIST, v. 25, n. 6, p. 1509–1596, 1996.

62 SCALABRIN, G.; MARCHI, P.; FINEZZO, F.; SPAN, R. A reference multiparameter thermal conductivity equation for carbon dioxide with an optimized functional form. **Journal of Physical and Chemical Reference Data**, NIST, v. 35, n. 4, p. 1549–1575, 2006.

63 VESOVIC, V.; WAKEHAM, W.; OLCHOWY, G.; SENGERS, J.; WATSON, J.; MILLAT, J. The transport properties of carbon dioxide. **Journal of physical and chemical reference data**, NIST, v. 19, n. 3, p. 763–808, 1990.

64 XU, L.; KUMAR, P.; BULDYREV, S. V.; CHEN, S.-H.; POOLE, P. H.; SCIORTINO, F.; STANLEY, H. E. Relation between the widom line and the dynamic crossover in systems with a liquid-liquid phase transition. **Proceedings of the National Academy of Sciences**, National Acad Sciences, v. 102, n. 46, p. 16558–16562, 2005.

65 KULHANEK, M.; DOSTAL, V. Supercritical carbon dioxide cycles thermodynamic analysis and comparison. **Supercritical $CO_2$ Power Cycle Symposium**, p. 24–25, 2011.

66 UTAMURA, M. Thermal-hydraulic characteristics of microchannel heat exchanger and its application to solar gas turbines. American Society of Mechanical Engineers, p. 287–294, 2007.

67 UTAMURA, M. Thermodynamic analysis of part-flow cycle supercritical $CO_2$ gas turbines. **Journal of Engineering for Gas Turbines and Power**, v. 132, n. 11, p. 111701, 2010.

68 ZHANG, X.; YAMAGUCHI, H.; FUJIMA, K.; ENOMOTO, M.; SAWADA, N. Theoretical analysis of a thermodynamic cycle for power and heat production using supercritical carbon dioxide. **Energy**, v. 32, n. 4, p. 591 – 599, 2007.

69 ZHANG, X.; YAMAGUCHI, H.; UNENO, D.; FUJIMA, K.; ENOMOTO, M.; SAWADA, N. Analysis of a novel solar energy-powered rankine cycle for combined power and heat generation using supercritical carbon dioxide. **Renewable Energy**, v. 31, n. 12, p. 1839 – 1854, 2006.

70 HEFNI, B. E.; SOLER, R. Dynamic multi-configuration model of a 145 MWe concentrated solar power plant with the thermosyspro library (tower receiver, molten salt storage and steam generator). **Energy Procedia**, Elsevier, v. 69, p. 1249–1258, 2015.

71 NIKNIA, I.; YAGHOUBI, M. Transient simulation for developing a combined solar thermal power plant. **Applied Thermal Engineering**, Elsevier, v. 37, p. 196–207, 2012.

72 AL-MALIKI, W. A. K.; ALOBAID, F.; KEZ, V.; EPPLE, B. Modelling and dynamic simulation of a parabolic trough power plant. **Journal of Process Control**, Elsevier, v. 39, p. 123–138, 2016.

73 SINGH, R.; MILLER, S. A.; ROWLANDS, A. S.; JACOBS, P. A. Dynamic characteristics of a direct-heated supercritical carbon-dioxide brayton cycle in a solar thermal power plant. **Energy**, Elsevier, v. 50, p. 194–204, 2013.

74 SINGH, R.; ROWLANDS, A. S.; MILLER, S. A. Effects of relative volume-ratios on dynamic performance of a direct-heated supercritical carbon dioxide closed brayton cycle in a solar-thermal power plant. **Energy**, Elsevier, v. 55, p. 1025–1032, 2013.

75 SYSTEMES, D. **Dassault Systemes website**. Available at: <<http://www.3ds.com/products-services/catia/products/dymola/>>. Accessed in: November 28$^{th}$, 2016.

76 SINGH, R.; KEARNEY, M. P.; MANZIE, C. Extremum-seeking control of a supercritical carbon-dioxide closed brayton cycle in a direct-heated solar thermal power plant. **Energy**, Elsevier, v. 60, p. 380–387, 2013.

77 LI, X.; SHU, G.; TIAN, H.; SHI, L.; WANG, X. Dynamic modeling of $CO_2$ transcritical power cycle for waste heat recovery of gasoline engines. **Energy Procedia**, Elsevier, v. 105, p. 1576–1581, 2017.

78 NALLUSAMY, N.; SAMPATH, S.; VELRAJ, R. Experimental investigation on a combined sensible and latent heat storage system integrated with constant/varying (solar) heat sources. **Renewable Energy**, Elsevier, v. 32, n. 7, p. 1206–1227, 2007.

79 SALOMONI, V. A.; MAJORANA, C. E.; GIANNUZZI, G. M.; MILIOZZI, A.; MAGGIO, R. D.; GIRARDI, F.; MELE, D.; LUCENTINI, M. Thermal storage of sensible heat using concrete modules in solar power plants. **Solar Energy**, Elsevier, v. 103, p. 303–315, 2014.

80 HOBOLD, G. M.; da SILVA, A. Critical phenomena and their effect on thermal energy storage in supercritical fluids. **Applied energy**, Elsevier, v. 205, p. 1447–1458, 2017.

81 MILANI, D.; LUU, M. T.; MCNAUGHTON, R.; ABBAS, A. A comparative study of solar heliostat assisted supercritical $CO_2$ recompression brayton cycles: dynamic modelling and control strategies. **The Journal of Supercritical Fluids**, Elsevier, v. 120, p. 113–124, 2017.

82 OSORIO, J. D.; HOVSAPIAN, R.; ORDONEZ, J. C. Dynamic analysis of concentrated solar supercritical $CO_2$-based power generation closed-loop cycle. **Applied Thermal Engineering**, Elsevier, v. 93, p. 920–934, 2016.

83 OSORIO, J. D.; HOVSAPIAN, R.; ORDONEZ, J. C. Effect of multi-tank thermal energy storage, recuperator effectiveness, and solar receiver conductance on the performance of a concentrated solar supercritical $CO_2$-based power plant operating under different seasonal conditions. **Energy**, Elsevier, v. 115, p. 353–368, 2016.

84 ZHU, H.-H.; WANG, K.; HE, Y.-L. Thermodynamic analysis and comparison for different direct-heated supercritical $CO_2$ brayton cycles integrated into a solar thermal power tower system. **Energy**, Elsevier, v. 140, p. 144–157, 2017.

85 MA, Z.; TURCHI, C. S. **Advanced supercritical carbon dioxide power cycle configurations for use in concentrating solar power systems**. [S.l.], 2011.

86 CHACARTEGUI, R.; ALOVISIO, A.; ORTIZ, C.; VALVERDE, J.; VERDA, V.; BECERRA, J. Thermochemical energy storage of concentrated solar power by integration of the calcium looping process and a $CO_2$ power cycle. **Applied energy**, Elsevier, v. 173, p. 589–605, 2016.

87 ZHANG, Y.; YANG, K.; HONG, H.; ZHONG, X.; XU, J. Thermodynamic analysis of a novel energy storage system with carbon dioxide as working fluid. **Renewable Energy**, Elsevier, v. 99, p. 682–697, 2016.

88 DE ARAUJO PASSOS, L.; ABREU, S. de; da SILVA, A. A short-and long-term demand based analysis of a $CO_2$ concentrated solar power system with backup heating. **Applied Thermal Engineering**, Elsevier, p. 114003, 2019.

89 LIU, J.; CHEN, H.; XU, Y.; WANG, L.; TAN, C. A solar energy storage and power generation system based on supercritical carbon dioxide. **Renewable Energy**, Elsevier, v. 64, p. 43–51, 2014.

90 BUENO, P.; BATES, L.; ANDERSON, R.; BINDRA, H. Thermal energy storage for the supercritical $co_2$ brayton cycle. In: AMERICAN SOCIETY OF MECHANICAL ENGINEERS. **Turbo Expo: Power for Land, Sea, and Air**. [S.l.], 2015. v. 56802, p. V009T36A017.

91 JOHNSON, E.; BATES, L.; DOWER, A.; BUENO, P. C.; ANDERSON, R. Thermal energy storage with supercritical carbon dioxide in a packed bed: Modeling charge-discharge cycles. **The Journal of Supercritical Fluids**, Elsevier, v. 137, p. 57–65, 2018.

92 ZANGANEH, G.; KHANNA, R.; WALSER, C.; PEDRETTI, A.; HASELBACHER, A.; STEINFELD, A. Experimental and numerical investigation of combined sensible–latent heat for thermal energy storage at 575°C and above. **Solar Energy**, Elsevier, v. 114, p. 77–90, 2015.

93 OSTERMAN, K.; GUILLEN, D.; GOSWAMI, D. Y. Numerical investigation of combined sensible/latent heat thermal energy storage with supercritical carbon dioxide as heat transfer fluid at 650°C. In: AMERICAN SOCIETY OF MECHANICAL ENGINEERS. **ASME International Mechanical Engineering Congress and Exposition**. [S.l.], 2019. v. 59438, p. V006T06A101.

94 HERNÁNDEZ-JIMÉNEZ, F.; SORIA-VERDUGO, A.; ACOSTA-IBORRA, A.; SANTANA, D. Exergy recovery from solar heated particles to supercritical $CO_2$. **Applied Thermal Engineering**, Elsevier, v. 146, p. 469–481, 2019.

95 HO, C. K.; CARLSON, M.; GARG, P.; KUMAR, P. Technoeconomic analysis of alternative solarized s-$CO_2$ brayton cycle configurations. **Journal of Solar Energy Engineering**, American Society of Mechanical Engineers Digital Collection, v. 138, n. 5, 2016.

96 MEYBODI, M. A.; BEATH, A.; GWYNN-JONES, S.; VEERARAGAVAN, A.; GURGENCI, H.; HOOMAN, K. Techno-economic analysis of supercritical carbon dioxide power blocks. In: AIP PUBLISHING LLC. **AIP Conference Proceedings**. [S.l.], 2017. v. 1850, n. 1, p. 060001.

97 TREVISAN, S.; GUÉDEZ, R.; LAUMERT, B. Supercritical $CO_2$ brayton power cycle for CSP with packed bed tes integration and cost benchmark evaluation. In: AMERICAN SOCIETY OF MECHANICAL ENGINEERS DIGITAL COLLECTION. **ASME 2019 Power Conference**. [S.l.].

98 MANZOLINI, G.; BINOTTI, M.; BONALUMI, D.; INVERNIZZI, C.; IORA, P. $CO_2$ mixtures as innovative working fluid in power cycles applied to solar plants. techno-economic assessment. **Solar Energy**, Elsevier, v. 181, p. 530–544, 2019.

99 CALLE, A. de la; BAYON, A.; PYE, J. Techno-economic assessment of a high-efficiency, low-cost solar-thermal power system with sodium receiver, phase-change material storage, and supercritical $CO_2$ recompression brayton cycle. **Solar Energy**, Elsevier, v. 199, p. 885–900, 2020.

100 ZHAO, Y.; HONG, H.; JIN, H. Optimization of the solar field size for the solar–coal hybrid system. **Applied energy**, Elsevier, v. 185, p. 1162–1172, 2017.

101 LI, Y.; ZHANG, N.; LIOR, N. Performance comparison of two low-$CO_2$ emission solar/methanol hybrid combined cycle power systems. **Applied energy**, Elsevier, v. 155, p. 740–752, 2015.

102 CARDEMIL, J. M.; da SILVA, A. K. Parametrized overview of $CO_2$ power cycles for different operation conditions and configurations – An absolute and relative performance analysis. **Applied Thermal Engineering**, Elsevier, v. 100, p. 146–154, 2016.

103 NELLIS, G.; KLEIN, S. **Heat Transfer**. New York: Cambridge University Press, 2009.

104 The MathWorks Inc. **MATLAB, 2017b**. Available at: <<http://mathworks.com>>.

105 F-CHART. **Engineering Equation Solver**. Available at: <<http://www.fchart.com/ees/>>. Accessed in: June 16$^{th}$, 2019.

106 ÇENGEL, Y. A.; BOLES, M. A.; KANOĞLU, M. **Thermodynamics: an engineering approach**. New York: McGraw-Hill, 2011.

107 BEJAN, A. **Advanced Engineering Thermodynamics**. 3$^{rd}$. ed. New York: John Wiley & Sons, Inc, 2006.

108 PATANKAR, S. **Numerical heat transfer and fluid flow**. [S.l.]: CRC press, 1980.

109 BEJAN, A. **Convection Heat Transfer**. 3rd. ed. New York: John Wiley & Sons, Inc, 2004.

110 INCROPERA, F. P.; BERGMAN, T. L.; LAVINE, A. S.; DEWITT, D. P. **Fundamentals of heat and mass transfer**. 7th ed. ed. Hoboken, NJ: John Wiley & Sonns, 2011.

111 JACKSON, J. Fluid flow and convective heat transfer to fluids at supercritical pressure. **Nuclear Engineering and Design**, Elsevier, v. 264, p. 24–40, 2013.

112 FANG, X.; XU, Y. Modified heat transfer equation for in-tube supercritical $CO_2$ cooling. **Applied Thermal Engineering**, Elsevier, v. 31, n. 14, p. 3036–3042, 2011.

113 THERMINOL. **Therminol website**. Available at: <<https://www.therminol.com/resources/QandA>>. Accessed in: June 16th, 2019.

114 BEJAN, A.; KRAUS, A. D. **Heat transfer handbook**. [S.l.]: John Wiley & Sons, 2003.

115 ANSYS. **Ansys website**. Available at: <<http://www.ansys.com/Products/Fluids/ANSYS-Fluent>>. Accessed in: November 28th, 2016.

116 RAO, N. T.; OUMER, A.; JAMALUDIN, U. State-of-the-art on flow and heat transfer characteristics of supercritical $CO_2$ in various channels. **The Journal of supercritical fluids**, Elsevier, v. 116, p. 132–147, 2016.

117 CHENG, X.; KUANG, B.; YANG, Y. Numerical analysis of heat transfer in supercritical water cooled flow channels. **Nuclear Engineering and Design**, Elsevier, v. 237, n. 3, p. 240–252, 2007.

118 LEE, S. H.; HOWELL, J. R. Turbulent developing convective heat transfer in a tube for fluids near the critical point. **International Journal of Heat and Mass Transfer**, Elsevier, v. 41, n. 10, p. 1205–1218, 1998.

119 YOO, J. Y. The turbulent flows of supercritical fluids with heat transfer. **Annual review of fluid mechanics**, Annual Reviews, v. 45, p. 495–525, 2013.

120 BEJAN, A. **Shape and Structure, from Engineering to Nature**. Cambridge: Cambridge University Press, 2000.

121 BATTISTI, F. G.; CARDEMIL, J. M.; MILLER, F. M.; da SILVA, A. K. Normalized performance optimization of supercritical, $CO_2$-based power cycles. **Energy**, Elsevier, v. 82, p. 108–118, 2015.

122 DYREBY, J. J. **Modeling the supercritical carbon dioxide Brayton cycle with recompression**. Dissertation (Ph.D.) — The University of Wisconsin-Madison, 2014.

123 DE ARAUJO PASSOS, L.; ABREU, S. de; da SILVA, A. Time-dependent behavior of a recompression cycle with direct $CO_2$ heating through a parabolic collector array. **Applied Thermal Engineering**, Elsevier, v. 140, p. 593–603, 2018.

124 ARIS, R. **Vectors, Tensors and the Basic Equations of Fluid Mechanics**. [S.l.]: Dover Publications, Inc., 1962.

125 Kunii, D.; Smith, J. M. Heat transfer characteristics of porous rocks. **Aiche Journal**, v. 6, n. 1, p. 71–78, 1960.

126 YAGI, S.; KUNII, D. Studies on effective thermal conductivities in packed beds. **AIChE Journal**, Wiley Online Library, v. 3, n. 3, p. 373–381, 1957.

127 PFEFFER, R. Heat and mass transport in multiparticle systems. **Industrial & Engineering Chemistry Fundamentals**, ACS Publications, v. 3, n. 4, p. 380–383, 1964.

128 MACDONALD, I.; EL-SAYED, M.; MOW, K.; DULLIEN, F. Flow through porous media–the ergun equation revisited. **Industrial & Engineering Chemistry Fundamentals**, ACS Publications, v. 18, n. 3, p. 199–208, 1979.

129 YANG, S.; WANG, J.; LUND, P. D.; JIANG, C.; LI, X. High performance integrated receiver-storage system for concentrating solar power beam-down system. **Solar Energy**, v. 187, p. 85–94, 2019.

130 OFUCHI, K.; KUNII, D. Heat-transfer characteristics of packed beds with stagnant fluids. **International Journal of Heat and Mass Transfer**, Elsevier, v. 8, n. 5, p. 749–757, 1965.

131 JIANG, P.-X.; SHI, R.-F.; ZHAO, C.-R.; XU, Y.-J. Experimental and numerical study of convection heat transfer of $CO_2$ at supercritical pressures in vertical porous tubes. **International Journal of Heat and Mass Transfer**, Elsevier, v. 51, n. 25-26, p. 6283–6293, 2008.

132 BRUN, K.; FRIEDMAN, P.; DENNIS, R. **Fundamentals and applications of supercritical carbon dioxide ($sCO_2$) based power cycles**. [S.l.]: Woodhead publishing, 2017.

133 KELLEY, K. K. Contributions to the data on theoretical metallurgy, xiii. high-temperature heat-content, heat-capacity, and entropy data for the elements and inorganic compounds. **Bulletin 584 Bureau of Mines**, US Government Printing Office, 1960.

134 FURUKAWA, G. T.; DOUGLAS, T. B.; MCCOSKEY, R. E.; GINNINGS, D. C. Thermal properties of aluminum oxide from 0 to 1,200 k. **Journal of Research of the National Bureau of Standards**, v. 57, n. 2, p. 67–82, 1956.

135 Whitson Jr, M. E. **Handbook of the Infrared Optical Properties of Al2O3. Carbon, MGO and ZrO2. Volume 1**. El Segundo/CA, 1975.

136 AETG – UC San Diego website. Available at: <<http://www-ferp.ucsd.edu/LIB/PROPS/PANOS/al2o3.html>>. Accessed in: August 24th, 2019.

137 KINGERY, W. D. Thermal conductivity: Xii, temperature dependence of conductivity for single-phase ceramics. **Journal of the American Ceramic Society**, Wiley Online Library, v. 38, n. 7, p. 251–255, 1955.

138 DALLAIRE, J.; GOSSELIN, L.; da SILVA, A. K. Conceptual optimization of a rotary heat exchanger with a porous core. **International Journal of Thermal Sciences**, Elsevier, v. 49, n. 2, p. 454–462, 2010.

139 BEEK, J. Design of packed catalytic reactors. In: **Advances in Chemical Engineering**. [S.l.]: Elsevier, 1962. v. 3, p. 203–271.

140 LATIFI, M. Numerical modeling of thermal-fluid behavior of the s-$CO_2$ cooled pebble bed reactor. **Alexandria engineering journal**, Elsevier, v. 57, n. 4, p. 3995–4001, 2018.

141 ASME. Power piping: ASME code for pressure piping, B31.1-2001. 2002.

142 FAROUKI, O. T. Thermal properties of soils. CRREL Monograph 81-1. **US Army Cold Regions Research and Engineering Laboratory, Hanover, New Hampshire**, v. 3755, 1981.

143 MCWHIRTER, J. D.; CRAWFORD, M. E.; KLEINS, D. E. Wall region porosity distributions for packed beds of uniform spheres with modified and unmodified walls. **Transport in porous media**, Springer, v. 27, n. 1, p. 99–118, 1997.

144 YING, A. Y.; ABDOU, M. A. Solid breeder thermal transient under purge-line-break accidents. **Nuclear engineering and design**, Elsevier, v. 146, n. 1-3, p. 349–362, 1994.

145 BARRIENTOS, M. A. I. **Heat transfer and thermal storage in fixed and fluidized beds of phase change materials**. Dissertation (Ph.D.) — Universidad Carlos III de Madrid, 2014.

146 Pritchard, P. J.; Leylegian, J. C.; Fox, R. W.; McDonald, A. T. **Fox and McDonald's Introduction to Fluid Mechanics**. [S.l.: s.n.], 2011.

147 MCTIGUE, J.; WHITE, A. A comparison of radial-flow and axial-flow packed beds for thermal energy storage. **Applied Energy**, Elsevier, v. 227, p. 533–541, 2018.

148 ZAVATTONI, S.; BARBATO, M. C.; PEDRETTI, A.; ZANGANEH, G.; STEINFELD, A. High temperature rock-bed tes system suitable for industrial-scale csp plant–cfd analysis under charge/discharge cyclic conditions. **Energy Procedia**, Elsevier, v. 46, p. 124–133, 2014.

149 Dinçer İbrahim; Rosen, M.; Bejan, A. **Thermal energy storage: systems and applications**. [S.l.: s.n.], 2010.

150 BURTSEVA, L.; SALAS, B. V.; WERNER, F.; PETRANOVSKII, V. Packing of monosized spheres in a cylindrical container: models and approaches. **Revista mexicana de física E**, Sociedad Mexicana de Física, v. 61, n. 1, p. 20–27, 2015.

151 ROGERS, C. A. The packing of equal spheres. **Proceedings of the London Mathematical Society**, Wiley Online Library, v. 3, n. 4, p. 609–620, 1958.

152 GARDNER, M. New mathematical diversions from scientific american. Simon and Schuster, 1966.

153 DIXON, A. G. Correlations for wall and particle shape effects on fixed bed bulk voidage. **The Canadian Journal of Chemical Engineering**, Wiley Online Library, v. 66, n. 5, p. 705–708, 1988.

154 BENYAHIA, F.; O'NEILL, K. Enhanced voidage correlations for packed beds of various particle shapes and sizes. **Particulate science and technology**, Taylor & Francis, v. 23, n. 2, p. 169–177, 2005.

155 LUU, M. T.; MILANI, D.; MCNAUGHTON, R.; ABBAS, A. Dynamic modelling and start-up operation of a solar-assisted recompression supercritical $CO_2$ brayton power cycle. **Applied energy**, Elsevier, v. 199, p. 247–263, 2017.

156 DE ARAUJO PASSOS, L. **Uma análise de ciclos de potência operando com CO2 supercrítico e concentradores solares**. Dissertation (Ph.D.) — Federal University of Santa Catarina, 2018.

157 FORRISTALL, R. **Heat transfer analysis and modeling of a parabolic trough solar receiver implemented in engineering equation solver**. [S.l.], 2003.

158 BUOL, S. Tropical soils| humid tropical. Elsevier, 2013.

159 BEJAN, A.; TSATSARONIS, G.; MORAN, M. **Thermal Design and Optimization**. [S.l.: s.n.], 1996.

160 AHMADI, P.; DINCER, I.; ROSEN, M. A. Exergy, exergoeconomic and environmental analyses and evolutionary algorithm based multi-objective optimization of combined cycle power plants. **Energy**, Elsevier, v. 36, n. 10, p. 5886–5898, 2011.

161 WORLD Steel Prices website. Available at: <<https://worldsteelprices.com/>>. Accessed in: Jan 6$^{th}$, 2020.

162 USF Energy Information Administration website. Available at: <<https://www.eia.gov/dnav/ng/hist/n3050ca3m.htm>>. Accessed in: Jan 10$^{th}$, 2020.

163 INDEXMUNDI. Available at: <<https://www.indexmundi.com/commodities/glossary/mmbtu>>. Accessed in: Jan 10$^{th}$, 2020.

164 SCIENCEDIRECT website. Available at: <<https://www.sciencedirect.com/topics/engineering/calorific-value>>. Accessed in: Jan 10$^{th}$, 2020.

165 AMINYAVARI, M.; NAJAFI, B.; SHIRAZI, A.; RINALDI, F. Exergetic, economic and environmental (3e) analyses, and multi-objective optimization of a $CO_2/NH_3$ cascade refrigeration system. **Applied Thermal Engineering**, Elsevier, v. 65, n. 1-2, p. 42–50, 2014.

166 DOWLING, A. W.; ZHENG, T.; ZAVALA, V. M. Economic assessment of concentrated solar power technologies: A review. **Renewable and Sustainable Energy Reviews**, Elsevier, v. 72, p. 1019–1032, 2017.

167 WRIGHT, S. A.; DAVIDSON, C. S.; SCAMMELL, W. O. Thermo-economic analysis of four $sCO_2$ waste heat recovery power systems. In: **Fifth International $sCO_2$ Symposium, San Antonio, TX**. [S.l.: s.n.], 2016. p. 28–31.

168 FLEMING, E.; WEN, S.; SHI, L.; da SILVA, A. K. Experimental and theoretical analysis of an aluminum foam enhanced phase change thermal storage unit. **International Journal of Heat and Mass Transfer**, Elsevier, v. 82, p. 273–281, 2015.

# Appendix A – ENERGY CONSERVATION EQUATION

This appendix presents in detail the process for obtaining the fluid energy conservation equation used throughout all studies composing this dissertation, which is obtained from the expression given by Refs. [114, 124] as

$$\rho\frac{De}{Dt} = \vec{\nabla}\cdot\left(k\vec{\nabla}T\right) - P\left(\vec{\nabla}\cdot\vec{u}\right) + \mu\Phi + \Omega, \tag{A.1}$$

for which $\rho$ is the volume-specific mass, $e$ the mass-specific internal energy, $t$ the time, $k$ the thermal conductivity, $T$ the temperature, $P$ the thermodynamic pressure, $\vec{u}$ the velocity vector, $\mu$ the dynamic viscosity, $\Phi$ the dissipation function, and $\Omega$ the generation term.

Now, considering the definition of the mass-specific enthalpy $i$ as

$$i \equiv e + Pv \rightarrow e = i - Pv, \tag{A.2}$$

for which $v$ is the mass-specific volume, it is possible to rewrite Eq. A.1 as

$$\rho\frac{Di}{Dt} - \rho P\frac{Dv}{Dt} - \rho v\frac{DP}{Dt} = \vec{\nabla}\cdot\left(k\vec{\nabla}T\right) - P\left(\vec{\nabla}\cdot\vec{u}\right) + \mu\Phi + \Omega. \tag{A.3}$$

Moreover, because $v = 1/\rho$, then

$$\frac{Dv}{Dt} = \left(\frac{-1}{\rho^2}\right)\frac{D\rho}{Dt}, \tag{A.4}$$

which may be used to rewrite Eq. A.3 as

$$\rho\frac{Di}{Dt} + \frac{P}{\rho}\frac{D\rho}{Dt} - \frac{DP}{Dt} = \vec{\nabla}\cdot\left(k\vec{\nabla}T\right) - P\left(\vec{\nabla}\cdot\vec{u}\right) + \mu\Phi + \Omega, \tag{A.5}$$

which may be reorganized as

$$\rho\frac{Di}{Dt} + P\left[\frac{1}{\rho}\frac{D\rho}{Dt} + \left(\vec{\nabla}\cdot\vec{u}\right)\right] = \vec{\nabla}\cdot\left(k\vec{\nabla}T\right) + \frac{DP}{Dt} + \mu\Phi + \Omega. \tag{A.6}$$

So, multiplying the second term on the LHS of Eq. A.6 by $\rho/\rho$ and further reorganizing the equation, it yields

$$\rho\frac{Di}{Dt} + \frac{P}{\rho}\left[\frac{D\rho}{Dt} + \rho\left(\vec{\nabla}\cdot\vec{u}\right)\right] = \vec{\nabla}\cdot\left(k\vec{\nabla}T\right) + \frac{DP}{Dt} + \mu\Phi + \Omega. \tag{A.7}$$

Now, considering that mass conservation (continuity) equation reads

$$\left[\frac{D\rho}{Dt} + \rho\left(\vec{\nabla}\cdot\vec{u}\right)\right] = \left[\frac{\partial\rho}{\partial t} + \vec{\nabla}\cdot(\rho\vec{u})\right] = 0, \tag{A.8}$$

the second term on the LHS of Eq. A.7 is canceled. Hence, Eq. A.7 becomes

$$\rho\frac{Di}{Dt} = \vec{\nabla}\cdot\left(k\vec{\nabla}T\right) + \frac{DP}{Dt} + \mu\Phi. + \Omega, \tag{A.9}$$

which may also be found in Ref. [114].

Now, focusing specifically on the first term on the LHS of Eq. A.9, it may be shown that

$$\frac{D(\rho i)}{Dt} = \rho\frac{Di}{Dt} + i\frac{D\rho}{Dt} \rightarrow \rho\frac{Di}{Dt} = \frac{D(\rho i)}{Dt} - i\frac{D\rho}{Dt}, \tag{A.10}$$

and, from the definition of the material derivative,

$$\frac{D(\rho i)}{Dt} = \frac{\partial(\rho i)}{\partial t} + \vec{u}\cdot\vec{\nabla}(\rho i). \tag{A.11}$$

Then, combining Eqs. A.10 and A.11, it yields

$$\rho\frac{Di}{Dt} = \frac{\partial(\rho i)}{\partial t} + \vec{u}\cdot\vec{\nabla}(\rho i) - i\frac{D\rho}{Dt}. \tag{A.12}$$

Also, it may be shown that

$$\vec{\nabla}\cdot(\vec{u}\rho i) = \rho i\vec{\nabla}\cdot\vec{u} + \vec{u}\cdot\vec{\nabla}(\rho i) \rightarrow \vec{u}\cdot\vec{\nabla}(\rho i) = \vec{\nabla}\cdot(\vec{u}\rho i) - \rho i\vec{\nabla}\cdot\vec{u}. \tag{A.13}$$

Hence, using Eq. A.13, Eq. A.12 may be rewritten as

$$\rho\frac{Di}{Dt} = \frac{\partial(\rho i)}{\partial t} + \vec{\nabla}\cdot(\vec{u}\rho i) - \rho i\vec{\nabla}\cdot\vec{u} - i\frac{D\rho}{Dt}, \tag{A.14}$$

which, then, may be reorganized as

$$\rho\frac{Di}{Dt} = \frac{\partial(\rho i)}{\partial t} + \vec{\nabla}\cdot(\vec{u}\rho i) - i\left[\frac{D\rho}{Dt} + \rho\left(\vec{\nabla}\cdot\vec{u}\right)\right]. \tag{A.15}$$

Once again recognizing the continuity (i.e., Eq. A.8), the last term on the RHS of Eq. A.15 is canceled, thus

$$\rho\frac{Di}{Dt} = \frac{\partial(\rho i)}{\partial t} + \vec{\nabla}\cdot(\rho\vec{u}i). \tag{A.16}$$

Then, substituting Eq. A.16 in Eq. A.9, it becomes

$$\frac{\partial\left(\rho i\right)}{\partial t}+\vec{\nabla}\cdot\left(\rho\vec{u}i\right)=\vec{\nabla}\cdot\left(k\vec{\nabla}T\right)+\frac{DP}{Dt}+\mu\Phi+\Omega, \tag{A.17}$$

which is the general conservative form for the energy equation in terms of the mass-specific enthalpy used throughout all studies developed in this dissertation. From the LHS to the RHS of Eq. A.17, the terms are related to temporal variation, advection, diffusion and/or convection heat transfer with a wall, pressure variation, viscous dissipation, and generation.

Now, focusing on the second term on the RHS of Eq. A.17, the pressure material derivative is given by

$$\frac{DP}{Dt}=\frac{\partial P}{\partial t}+\vec{u}\cdot\vec{\nabla}P, \tag{A.18}$$

and, similar to Eq. A.13,

$$\vec{\nabla}\cdot\left(\vec{u}P\right)=\left(\vec{\nabla}\cdot\vec{u}\right)P+\vec{u}\cdot\vec{\nabla}\left(P\right)\rightarrow\vec{u}\cdot\vec{\nabla}\left(P\right)=\vec{\nabla}\cdot\left(\vec{u}P\right)-P\left(\vec{\nabla}\cdot\vec{u}\right). \tag{A.19}$$

So, with Eq. A.19, Eq. A.18 may be rewritten as

$$\frac{DP}{Dt}=\frac{\partial P}{\partial t}+\vec{\nabla}\cdot\left(\vec{u}P\right)-P\left(\vec{\nabla}\cdot\vec{u}\right), \tag{A.20}$$

which may substituted in Eq. A.17, yielding

$$\frac{\partial\left(\rho i\right)}{\partial t}+\vec{\nabla}\cdot\left(\rho\vec{u}i\right)=\vec{\nabla}\cdot\left(k\vec{\nabla}T\right)+\frac{\partial P}{\partial t}+\vec{\nabla}\cdot\left(\vec{u}P\right)-P\left(\vec{\nabla}\cdot\vec{u}\right)+\mu\Phi+\Omega. \tag{A.21}$$

Now, adopting the finite-volumes approach for numerically dealing with Eq. A.21, considering a volume $V$ bounded by a surface $S$ whose outward normal is $\hat{n}$, disregarding generation, neglecting the influence of viscous dissipation – which is arguably expected to be negligible for all cases considered in this dissertation –, and integrating Eq. A.21 over

the volume $V$ and the time $t$, it yields

$$\int_t \int_V \frac{\partial\left(\rho i\right)}{\partial t}\, dVdt + \int_t \int_V \vec{\nabla}\cdot\left(\rho\vec{u}i\right)\, dVdt = \int_t \int_V \vec{\nabla}\cdot\left(k\vec{\nabla}T\right)\, dVdt + \int_t \int_V \frac{\partial P}{\partial t}\, dVdt + \int_t \int_V \vec{\nabla}\cdot\left(\vec{u}P\right)\, dVdt - P\int_t \int_V \left(\vec{\nabla}\cdot\vec{u}\right)\, dVdt. \tag{A.22}$$

Then, applying the divergence theorem to the second term on the LHS and on the first, third, and fourth terms on the RHS of Eq. A.22, it yields

$$\int_t \int_V \frac{\partial\left(\rho i\right)}{\partial t}\, dVdt + \int_t \int_S \left(\rho\vec{u}i\right)\cdot\hat{n}\, dSdt = \int_t \int_S \left(k\vec{\nabla}T\right)\cdot\hat{n}\, dSdt + \int_t \int_V \frac{\partial P}{\partial t}\, dVdt \int_t \int_S \left(\vec{u}P\right)\cdot\hat{n}\, dSdt - P\int_t \int_S \vec{u}\cdot\hat{n}\, dSdt. \tag{A.23}$$

Throughout this dissertation, for the one-dimensional models, the node nomenclature presented by Ref. [108] was adopted, i.e., the center of a control volume is indicated by $P$, the center of the volume to the left (west) of $P$ is indicated by $W$, the center of the volume to the right (east) of $P$ is indicated by $E$, the interface between nodes $W$ and $P$ is indicated by $w$, and the interface between nodes $P$ and $E$ is indicated by $e$.

Now, specifically for one-dimensional horizontal plug flows, focusing on the last three terms on the RHS of Eq. A.23 (which are related to the pressure variation term) and using the aforementioned node nomenclature, it may be written that

$$\int_t \int_V \frac{DP}{Dt}\, dVdt \approx V_{\mathrm{P}}\left(P_{\mathrm{P}} - P_{\mathrm{P}}^{0}\right) + \left[\left(AuP\right)_{\mathrm{e}} - \left(AuP\right)_{\mathrm{w}}\right]\Delta t + -P_{\mathrm{P}}\left[\left(Au\right)_{\mathrm{e}} - \left(Au\right)_{\mathrm{w}}\right]\Delta t. \tag{A.24}$$

Then, using that the total mass flow rate is given by $\dot{m} = \rho u A \rightarrow (Au) = \dot{m}/\rho$, Eq. A.24 may be rewritten as

$$\int_t \int_V \frac{dP}{dt}\, dVdt \approx V_{\mathrm{P}}\left(P_{\mathrm{P}} - P_{\mathrm{P}}^{0}\right) + \left[\left(\frac{\dot{m}P}{\rho}\right)_{\mathrm{e}} - \left(\frac{\dot{m}P}{\rho}\right)_{\mathrm{w}}\right]\Delta t + -P_{\mathrm{P}}\left[\left(\frac{\dot{m}}{\rho}\right)_{\mathrm{e}} - \left(\frac{\dot{m}}{\rho}\right)_{\mathrm{w}}\right]\Delta t. \tag{A.25}$$

And, reorganizing the last two terms on the RHS of Eq. A.25, it finally becomes

$$\int_t \int_V \frac{dP}{dt}\, dVdt \approx V_{\mathrm{P}}\left(P_{\mathrm{P}} - P_{\mathrm{P}}^{0}\right) + \left[\left(\frac{\dot{m}}{\rho}\right)_{\mathrm{e}}\left(P_{\mathrm{e}} - P_{\mathrm{P}}\right) - \left(\frac{\dot{m}}{\rho}\right)_{\mathrm{w}}\left(P_{\mathrm{P}} - P_{\mathrm{w}}\right)\right]\Delta t. \tag{A.26}$$

An important aspect regarding the modeling for considering the effects of the pressure variation on the energy conservation (i.e., Eq. A.26) is that it is not inherently conservative. Nonetheless, for the case of linear pressure drop distribution along the fluid flow direction – which is arguably expected to be the case for the studies developed in this dissertation –, if the pressure evaluation at the nodes centers is performed according to arithmetic means of the pressures at the respective nodes interfaces, the approach shown in Eq. A.26 becomes conservative.

Finally, it is worth remembering that Eqs. A.23 and A.26 were obtained regarding the finite-volumes approach in a general form for a one-dimensional horizontal plug flow while disregarding generation and neglecting viscous dissipation.